Title	Tuning Reactivity and Mechanisms of Oxidation with Nonheme Manganese(IV)-Oxo Complexes
Author(s)	Yoon, Heejung
Citation	大阪大学, 2015, 博士論文
Version Type	VoR
URL	https://doi.org/10.18910/52123
rights	
Note	

Doctoral Dissertation

Tuning Reactivity and Mechanisms of Oxidation with Nonheme Manganese(IV)-Oxo Complexes

Heejung Yoon

January 2015

Department of Material and Life Science
Division of Advanced Science and Biotechnology
Graduate School of Engineering
Osaka University

Contents

General Introduction

Oxygenic photosynthesis, the process by which plants convert carbon dioxide to carbohydrates using solar energy, has generated most of the dioxygen in the atmosphere, sustaining life on Earth.[1] Dioxygen is produced when water is oxidized in a complex chemical reaction involving the transfer of four electrons and four protons.[1,2] Photosynthetic anabolic pathways use chemical energy in the form of ATP and NADH or NADPH to synthesize cellular components from simple precursor molecules.[1,2] Anabolic pathways are generally reductive rather than oxidative.[2] Anabolism and catabolism proceed simultaneously in a dynamic steady state, so the energy-yielding degradation of cellular components is counterbalanced by biosynthetic processes, which create and maintain the intricate orderliness of living cells.[3]

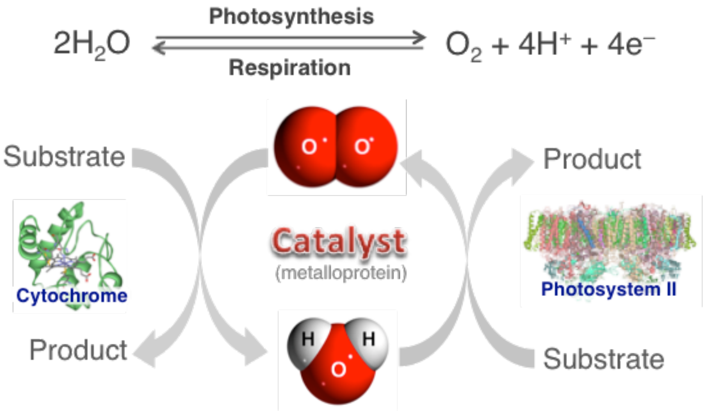

Figure 1. Complementary photosynthesis and respiration processes in the living world.

Atmospheric dioxygen naturally exists as a diradical in its ground state as triplet oxygen.[4] The low reactivity of dioxygen is due to its diradical state.[4] Relative stability of dioxygen results from the spin-forbidden reactions with singlet molecules.[5] Therefore, reaction pathways for spin-allowed O_2 binding occur through involving catalysts in the form of transition metal complexes. Especially, high-valent metal-oxo complexes are in the high capacity of reacting factors in both respiration and photosynthesis.[6,11]

In biological systems, the respiration process requires a catalytic element in the form of an active oxidant in oxygen activating iron enzymes, which is implicated as high-valent iron-oxo intermediates. For example, cytochrome *c* oxidase (CcO) performs a four-electron reduction of oxygen to water in the last step of respiration.[2] The active site in CcO consists of a heme/Cu site having a post-translationally modified tyrosine residue covalently bound to one of the histidine ligands of the distal Cu.[7] A series of iron porphyrins have been synthesized as models of cytochrome *c* oxidase. Cytochrome c (Cytc), a small electron transfer protein, is the source of electrons for CcO and has a coordinatively saturated low-spin heme active site.[8,9] Cytochrome P450 enzymes (CYP 450) are also good target for biomimetic model studies involving iron-oxo intermediates. P450s bind molecular oxygen on a heme center and transfer one of its oxygen atoms to a substrate, while the other oxygen atom originating from O_2 is reduced to a water molecule.[10,11] The P450s are versatile monooxygenation catalysts that perform substrate aliphatic and aromatic hydroxylation, epoxidation, heteroatom oxidation and dehydrogenation processes.[10,11] In the catalytic cycle of dioxygen activation and oxygen atom transfer by cytochrome P450 enzymes (CYP 450), high-valent iron(IV)–oxo porphyrin π-radical cations, termed compound I and two oxidizing equivalents above the resting ferric state, are believed to transfer the oxygen atom to organic substrates.[11]

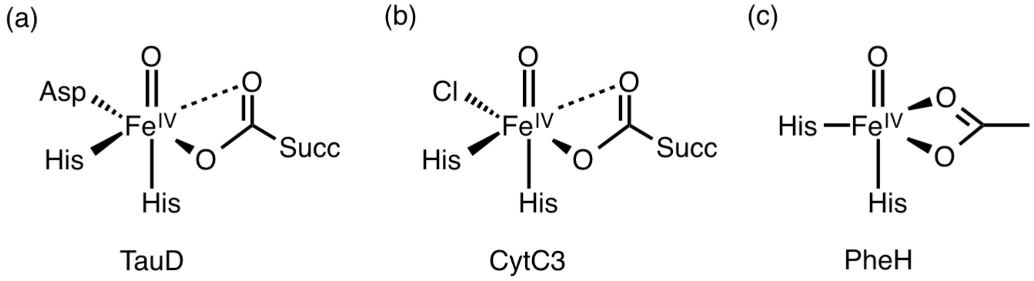

Figure 2. Proposed structures of iron(IV)-oxo intermediates of (a) TauD, (b) CytC3, and (c) PheH.

Nonheme high-valent iron-oxo intermediates have also been implicated and identified in some cases, as the active oxidant in oxygen activating nonheme iron enzymes in that activate O_2 to carry out metabolically vital oxidative transformations.[12,13] Most of these enzymes utilize an iron center coordinated to a 2-His-1-carboxylate facial triad motif to catalyze substrate oxidations, including hydroxylation, halogenation, desaturation, epoxidation and *cis*-dihydroxylation.[14] Electron donors for O_2 activation include the commonly used reductant NADH, as well as α-ketoglutarate (α-KG), tetrahydrobiopterin, and ascorbate.[15] For some enzymes like isopenicillin N synthase (IPNS), the substrate undergoes $4e^-$ oxidation, providing all necessary electrons required for O_2 activation.[16] An iron(IV)-oxo species is the oxidant most commonly postulated for these enzymes, while a *cis*-HO iron(IV)-oxo oxidant is proposed for the Rieske dioxygenases that catalyze *cis*-dihydroxylation of arene double bonds.[12,17,18]

The energetically opposite to respiration is photosynthesis. This crucial reaction requires the precise and timely transfer of four protons and four electrons as part of the conversion of two water molecules to dioxygen.[19] The biological water oxidation in the natural system is conducted in photosynthetic protein complex Photosystem II (PSII) where the oxidation of water molecule to dioxygen at embedded tetra manganese-calcium cluster indicating oxygen-evolving center (OEC) in PSII.[19] There are many known varieties of the PSII enzyme but the OEC seems to be identical in each case.[19] This conservation of the active-site structure has led to the idea that the specific combination and coordination of metal ions present in the OEC is necessary for its function.[19] However, our understanding of how the structural environment and physical properties of these ions are linked to water oxidation remains incomplete.[20] Increasing the knowledge in this area requires a combination of several different approaches that range from protein crystallography to the study of synthetic analogs of the OEC.[19]

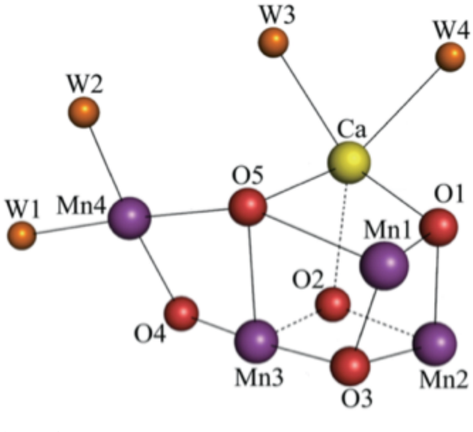

Figure 3. Structure of OEC in PS II.

The structure of the OEC cluster can be approximated as a Mn_3O_4Ca cubane that supports a fourth, dangling, manganese center (Figure 3).[19] Calcium ion was found in the 1980s to be an essential cofactor in oxygen evolution.[21] One calcium is required per OEC.[22,23] The incorporation of a calcium ion within a cuboid structure is unique to the OEC, and it’s inclusion is also rare in synthetic chemistry. Although it has been proposed that calcium ion acts in water splitting by binding a substrate water molecule,[24-27] the role of Ca^{2+} in the O–O bond-forming reaction has yet to be clarified.

It is well known that redox-inactive metal ions and proton act important roles in controlling biological electron-transfer processes of coenzymes such as flavins, quinones in photosynthesis and respiration.[28-33] Binding redox-inactive metal ions to electron acceptors (A) results in enhancement of an electron-acceptor ability of A, because the one-electron reduction potential of A is shifted to a positive direction by the stronger binding of metal ions to the radical anion ($A^{\bullet-}$) as compared to the binding to A.[34-41] According to the Nernst equation, the positive shift of E_{red} (ΔE_{red}) of A due to the complex formation with a metal ion (M^{n+}) is determined by the difference in the binding constants between M^{n+} complexes with A (K_{ox}) and $A^{\bullet-}$ (K_{red}) as given by eq 1 under the conditions that $K_{red}[M^{n+}] > 1$.[41]

$$\Delta E_{\mathrm{red}} = \frac{RT}{F}\ln\left[\frac{K_{red}[\mathrm{M}^{n+}]}{K_{ox}[\mathrm{M}^{n+}]+1}\right] \qquad (1)$$

Thus, electron-transfer reactions from electron donors (D) to electron acceptors (A), which are not thermodynamically feasible to occur ($\Delta G_{et} > 0$), would occur in the presence of M^{n+} provided that the $F\Delta E_{red}$ value is larger than ΔG_{et} ($\Delta G_{et} < F\Delta E_{red}$). In such a case, the free energy change of electron transfer becomes negative ($\Delta G_{et} < 0$ in the presence of M^{n+}) as shown in Scheme1. Under the conditions that $K_{ox}[M^{n+}] < 1$, eq 1 is rewritten by eq 2.

$$\Delta E_{\mathrm{red}} = \frac{RT}{F}\ln(K_{red}[\mathrm{M}^{n+}]) \qquad (2)$$

In this case, M^{n+} binds only to $A^{\bullet-}$ when virtually no binding of M^{n+} occurs to A. In such a case there are two reaction pathways. One is electron transfer followed by binding of M^{n+} to $A^{\bullet-}$, when electron transfer and binding of M^{n+} to $A^{\bullet-}$ occurs is a stepwise pathway. One is electron transfer followed by binding of M^{n+} to $A^{\bullet-}$, when electron transfer and binding of M^{n+} to $A^{\bullet-}$ occurs is a stepwise pathway. The other is a concerted pathway when electron transfer is coupled with binding of M^{n+} to $A^{\bullet-}$. The latter pathway is normally energetically more feasible because the binding of M^{n+} is coupled with electron transfer. This is defined as metal ion-coupled electron transfer (MCET) on analogy of proton-coupled electron transfer (PCET) where protonation is coupled with electron transfer.[42-45]

The general concent of MCET in Scheme 1 may play important roles in tuning the reactivity of high-valent metal-oxo complexes in biological redox reactions including respiration and photosynthesis. The first spectroscopic evidence for mononuclear no nheme iron(IV)-oxo species was reported by Wieghardt and co-workers in the ozonolysis of $[Fe^{III}(cyclamacetato)(CF_3SO_3)]^+$ (cyclam-acetato = 1-(carboxymethyl)-1,4,8,11-tetraazacyclotetradecane).[46] In 2003, the first X-ray crystal structure of a mononuclear nonheme iron(IV)-oxo complex bearing a macrocyclic TMC ligand, $[(TMC)Fe^{IV}(O)]^{2+}$, was reported with a thorough spectroscopic characterization.[46] Since then, a large number of mononuclear nonheme iron(IV)-oxo complexes have been synthesized using various supporting ligands and used in the structural and spectroscopic characterization and reactivity studies in oxidation reactions.[11,47] The most striking observation made in the oxidation of organic substrates by nonheme iron(IV)-oxo complexes was the hydroxylation of alkanes by $[(N4Py)Fe^{IV}(O)]^{2+}$ and $[(Bn\text{-}TPEN)Fe^{IV}(O)]^{2+}$.[48] The iron(IV)-oxo complexes bearing pentadentate N5 ligands were thermally stable even at room temperature but capable of activating the C−H bonds of unactivated hydrocarbons. Recently, the reactivity and mechanisms of iron(IV)-oxo complexes bearing pentadentate N5 ligands, $[(N4Py)Fe^{IV}(O)]^{2+}$, in oxidation reactions and the factors that modulate their reactivities and change their reaction mechanisms have been examined.[49,50]

Fukuzumi, Nam and coworker reported the first crystal structure of a non-heme $Fe^{IV}(O)–Sc^{3+}$ complex, in which Sc^{3+} ion is bound to the oxo group.[47] Binding of Sc^{3+} and protons to non-heme iron(IV)-oxo complexes resulted in ramakable enhancement of the reactivity in the electron-transfer reduction.[49,50] Agapie and coworkers also reported that one possible role of the Ca^{2+} ion in OEC is to modulate the reduction potential of the manganese center.[51]

There have been enormous efforts to elucidate reactive intermediates in case of synthetic iron-oxo field.[11,16] Heme and nonheme iron enzymes catalyze a diverse array of important metabolic transformations that require the binding and activation of dioxygen.[10,11,52-55] Our understanding of the catalytic reactions of the enzymes, especially the nature of active oxidizing species, has improved recently with the intensive mechanistic studies of the enzymes and their model compounds.[11,16]

Although not as ubiquitous as iron(IV)- oxo and manganese(IV)-oxo still performs very important reaction specifically in OEC in PS II. However, it is only recently that a nonheme synthetic manganese(IV)-oxo was shown to be powerful enough to oxidize

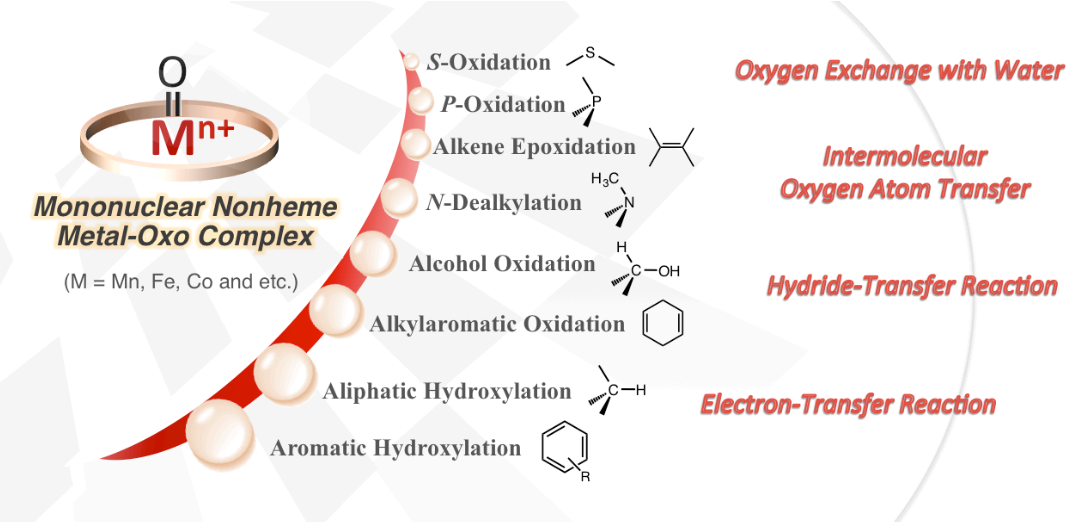

Figure 4. Oxidation reactions mediated by mononuclear nonheme metal-oxo complexes.

organic substrateactivate the C–H nond of cyclohexane.[56] However, tuning reactivity and mechanisms of oxidation of substrates with manganese(IV)-oxo complexes have yet to be reported as compared wth those described above for iron(IV)-oxo complexes.

In this thesis, the author focusses on tuning reactivity and mechanisms of oxidation of substrates with manganese(IV)-oxo complexes supported by pentadentate ligands. The factors that tune the redox reactivity of the oxo intermediates were thoroughly investigated especially with regard to the effects of Lewis acids (i.e., redox-inactive metal ions and proton) on the redox reactivity of nonheme manganese(IV)-oxo complexes. The compositions of the thesis are electron-transfer properties of a high-valent mononuclear nonheme manganese(IV)-oxo complex (chapter 1), an electron-transfer mechanisms in hydride transfer reactions of a manganese(IV)-oxo complex (chaper 2), characterization and electron-transfer properties of scandium ion-bound nonheme manganese(IV)-oxo complexes (chapter 3-4), and characterization and electron-transfer properties of protonated nonheme manganese(IV)-oxo (chapter 5).

In chapter 1, basic electron-transfer (ET) properties of a nonheme manganese(IV)-oxo complex have been investigated. In chapter 2, the reactivity of a nonheme manganese(IV)-oxo complex in hydride transfer from NADH analogs is compared with that of the corresponding ion(IV)-oxo complex. In chapter 3, a mononuclear nonheme manganese(IV)-oxo complex binding redox-inactive scandium ion has been synthesized and characterized by using various spectroscopic methods.

The change in the reactivity of the nonheme manganese(IV)-oxo complex in the absence and presence of Sc^{3+} was studied in the oxygen atom transfer (OAT) and hydrogen atom transfer (HAT) reactions. In chapter 4, the effects of binding of Sc^{3+} ions to nonheme manganese(IV)-oxo complexes on the redox properties were thoroughly inverstigated to clarfy the mechanistic difference between OAT and HAT reactions of nonheme manganese(IV)-oxo complexes in the presence of Sc^{3+}. In chapter 5, diprotonated nonheme manganese(IV)-oxo complexes were synthesized by adding HOTf (trifluoromethanesulfonic acid) to manganese(IV)-oxo complexes and characterized by using various spectroscopic methods and DFT calculations. The change in the reactivity of the nonheme manganese(IV)-oxo complex in the absence and presence of HOTf was studied in the ET, OAT and HAT reactions.

This thesis provides will provide valuable insights into fine tuning of the reactivity of high-valent metal-oxo complexes and mechanisms by binding metal ions and protons to the oxo moiety.

References

(1) (a) Hoff A. J.; Deisenhofer, *J. Phys. Rep.* **1997**, *287*, 1. (b) Blankenship, R. E.; Madigan, M. T.; Bauer, C. E., Eds; *Anoxygenic Photo-synthetic Bacteria*; Kluwer Academic Publishers: Dordrecht, The Netherlands, **1995**. (c) Woodrow, I. R.; Berry, J. A. *Annu. Rev. Plant Physiol. Plant Mol. Biol.* **1988**, *39*, 533. (d) Brugnoli, E; Farquhar, G. D. *Adv. Photosynth.* **2000**, *9*, 399. (e) Conlan, B.; Hillier, W.; Wydrzynski, T. *Engineering model proteins for Photosystem II function, Photosynth. Res.* **2007**, *94*, 225.

(2) (a) Hosler, J. P.; Ferguson-Miller, S.; Mills, D. A. *Annu. Rev. Biochem*. **2006**, *75*, 165. (b) Pereira, M. M.; Santana, M.; Teixeira, M. *Biochim. Biophys. Acta* **2001**, *1505*, 185. (c) Ferguson-Miller, S.; Babcock, G. T. *Chem. Rev*. **1996**, *96*, 2889. (d) Winter, M.; Brodd, R. J. *Chem. Rev*. **2004**, *104*, 4245. (e) Kaila, V. R. I.; Verkhovsky, M. I.; Wikström, M. *Chem. Rev*. **2010**, *110*, 7062.

(3) Nelson, D. L.; Cox, M. M *Lehninger Principles of Biochemistry*, 5th ed.; W. H. Freeman and Company: New York, **2008**.

(4) Taube, H. *J. Gen. Physiol*. **1965**, *49*, 29.

(5) Schweitzer, C.; Schmidt, R. *Chem. Rev.*, **2003**, *103*, 1685.

(6) Meelich, K.; Zaleski, C. M.; Pecoraro, V. L. *Phil. Trans. R. Soc. B*, **2008**, *363*, 1271.

(7) Collman, J. P.; Ghosh, S.; Dey, A.; Decreau, R. A.; Yang, Y. J. *J. Am. Chem. Soc*. **2009**, *131*, 5034.

(8) Ferguson-Miller, S.; Babcock, G. T. *Chem. Rev.* **1996**, *96*, 2889.

(9) (a) Iwata, S.; Ostermeier, C.; Ludwig, B.; Michel, H. *Nature* **1995**, *376*, 660. (b) Yoshikawa, S.; Shinzawa-Itoh, K.; Nakashima, R.; Yaono, R.; Yamashita, E.; Inoue, N.; Yao, M.; Fei, M. J.; Libeu, C. P.; Mizushima, T.; Yamaguchi, H.; Tomizaki, T.; Tsukihara, T. *Science* **1998**, *280*, 1723. (c) Fei, M. J.; Yamashita, E.; Inoue, N.; Yao, M.; Yamaguchi, H.; Tsukihara, T.; Shinzawa-Itoh, K.; Nakashima, R.; Yoshikawa, S. *Acta Crystallogr.Sect. D: Biol. Crystallogr.* **2000**, *56*, 529.

(10) (a) Ortiz de Montellano, P.R. *Cytochrome P450: Structure, Mechanism and Biochemistry*, 3rd ed., Kluwer Academic/Plenum Publishers, New York, **2005**, Chapter 1, 1–44. (b) Groves, J. T.; Haushalter, R. C.; Nakamura, M.; Nemo, T. E.; Evans, B. J. *J. Am. Chem. Soc.* **1981**, *103*, 2884.

(11) Nam, W. *Acc. Chem. Res.* **2007**, *40*, 522.

(12) Solomon, E. I.; Brunold, T. C.; Davis, M .I.; Kemsley, J. N.; Lee, S.-K.; Lehnert, N.; Neese, F.; Skulan, A. J.; Yang, Y.-S.; Zhou, J. *Chem. Rev.* **2000**, *100*, 235.

(13) Costas, M.; Mehn, M. P.; Jensen, M. P.; Que, L. Jr., *Chem. Rev*. **2005**, *104*, 939.

(14) Krebs, C.; Fujimori, D. G.; Walsh, C. T.; Bollinger, J. M., Jr. *Acc. Chem. Res.* **2007**, *40*, 484.

(15) Kovaleva, E. G.; Lipscomb, J. D. *Nat. Chem. Biol.* **2008**, *4*, 186.

(16) Mcdonald, A. R.; Que, L., Jr. *Coord. Chem. Rev.* **2013**, *257*, 414.

(17) Wolfe, M. D.; Lipscomb, J. D. *J. Biol. Chem.* **2003**, *278*, 829.

(18) Neibergall, M. B.; Stubna, A.: Mekmouche, Y.; Münck, E.; Lipscomb, J. D. *Biochemistry* **2007,** *46*, 8004.

(19) Umena, Y.; Kawakami, K.; Shen, J.-R.; Kamiya, N. *Nature*, **2011**, *473*, 55.

(20) Brudvig, G. W. *Philos. Transf. R. Soc. B* **2008**, *363*, 1211.

(21) Ghanotakis, D. F.; Babcock, G. T.; Yocum, C. F. *FEBS Lett.* **1984**, *167*, 127.

(22) Han, K.; Katoh, S. *Plant Cell Physiol*. **1993**, *34*, 585.

(23) Adelroth, P.; Lindberg, K.; Andreasson, L. E. *Biochemistry* **1995**, *34*, 9021.

(24) Pecoraro, V. L.; Baldwin, M. J.; Caudle, M. T.; Hsieh, W. Y.; Law, N. A. *Pure Appl. Chem*. **1998**, *70*, 925.

(25) Vrettos, J. S.; Limburg, J.; Brudvig, G. W. *Biochim. Biophys. Acta* **2001**, *1503*, 229.

(26) Rutherford, A. W. *Trends Biochem. Sci.* **1989**, *14*, 227.

(27) Limburg, J.; Szalai, V. A.; Brudvig, G. W. *J. Chem. Soc., Dalton Trans*. **1999**, 1353.

(28) Fukuzumi, S.; Okubo, K. *Coord. Chem. Rev.* **2008***, 252*, 296.

(29) Kaim, W.; Schwederski, B. *Bioinorganic Chemistry: Inorganic Elements in the Chemistry of Life*; John Wiley & Son: Chichester, **1994**.

(30) Hoff, A. J.; Deisenhofer, J. *Phys. Rep.* **1997**, *287*, 2.

(31) J. Deisenhofer, J.R. Norris (Eds.), The Photosynthetic Reaction Center, Academic Press, San Diego, **1993**.

(32) Ferguson-Miller, S.; Babcock, G. T. *Chem. Rev.* **1996**, *96*, 2889.

(33) Yocum, C. F. *Coord. Chem. Rev.* **2008**, *252*, 296.

(34) Fukuzumi, S; *Electron Transfer in Chemistry*, vol. 4, ed. V. Balzani; Wiley-VCH: Weinheim, Germany, **2001**, pp. 3–59.

(35) Fukuzumi, S. *Bull. Chem. Soc. Jpn.* **1997**, *70*, 1.

(36) Fukuzumi, S.; Itoh, S. in *Advances in Photochemistry*; Neckers, D. C.; Volman, D. H.; von Bünau, G., Eds.; Wiley: New York, **1998**, Vol. 25, pp. 107-172.

(37) Fukuzumi, S.; Itoh, S *Antioxid. Redox Signal*. **2001**, *3*, 807.

(38) Fukuzumi, S. *Org. Biomol. Chem.* **2003**, *1*, 609.

(39) Fukuzumi, S. *Bull. Chem. Soc. Jpn.* **2006**, *79*, 177.

(40) Fukuzumi, S. *Prog. Inorg. Chem.* **2009**, *56*, 49.

(41) Marcus, R.A.; Eyring, H. *Annu. Rev. Phys. Chem.* **1964**, *15*, 155.

(42) Cukier, R. I.; Nocera, D. G. *Annu. Rev. Phys. Chem.* **1998**, *49*, 337.

(43) Chang, C. J.; Chang, M. C. Y.; Damrauer, N. H.; Nocera, D. G. *Biochim. Biophys. Acta*. **2004**, *1655*, 13.

(44) Mayer, J. M.; Rhile, I. J. *Biochim. Biophys. Acta* **2004**, *1655*, 51.

(45) Huynh, M. H. V.; Meyer, T. J. *Chem. Rev.* **2007**, *107*, 5004.

(46) Rohde, J.-U.; In, J.-H.; Lim, M. H.; Brennessel, W. W.; Bukowski, M. R.; Stubna, A.; Münck, E.; Nam, W.; Que, L. Jr. *Science* **2003**, *299*, 1037.

(47) Hohenberger, J.; Ray, K.; Meyer, K. *Nat. Commun.* **2012**, *3*, xDOI: 10.1038/ncomms1718.

(48) Kaizer, J.; Klinker, E. J.; Oh, N. Y.; Rohde, J.-U.; Song, W. J.; Stubna, A.; Kim, J.; Münck, E.; Nam, W.; Que, L. Jr. *J. Am. Chem. Soc.* **2004**, *126*, 472.

(49) Morimoto, M.; Kotani, H.; Park, J.; Lee, Y.-M.; Nam, W.; Fukuzumi, S. *J. Am. Chem. Soc.* **2011**, *133*, 403.

(50) (a) Park, J.; Morimoto, Y.; Lee, Y.-M.; Nam, W.; Fukuzumi, S. *J. Am. Chem. Soc.* **2011**, *133*, 5236. (b) Park, J.; Morimoto, Y.; Lee, Y.-M.; Nam, W.; Fukuzumi, S. *J. Am. Chem. Soc.* **2012**, *134*, 3903. (c) Park, J.; Lee, Y.-M.; Nam, W.; Fukuzumi, S. *J. Am. Chem. Soc.*, **2013**, 135, 5052. (d) Park, J.; Morimoto, Y.; Lee, Y.-M.; Nam, W.; Fukuzumi, S. *Inorg. Chem.*, **2014**, 53, 3618.

(51) (a) Kanady, J. S.; Tsui, E. Y.; Day, M. W.; Agapie, T. *Science* **2011**, *333*, 733. (b) Tsui, E. Y.; Tran, R.; Yano, J.; Agapie, T., *Nat. Chem.* **2013**, *5*, 293.

(52) Denisov, I. G.; Makris, T. M.; Sligar, S. G.; Schlichting, I. *Chem. Rev.* **2005**, *105*, 2253.

(53) Meunier, B.; de Visser, S. P.; Shaik, S. *Chem. Rev.* **2004**, *104*, 3947.

(54) Abu-Omar, M. M.; Loaiza, A.; Hontzeas, N. *Chem. Rev.* **2005**, *105*, 2227.

(55) Costas, M.; Mehn, M. P.; Jensen, M. P.; Que, L. Jr. *Chem. Rev.* **2004**, *104*, 939.

(56) Wu, X.; Seo, M. S.; Davis, K. M.; Lee, Y.-M.; Chen, J.; Cho, K.-B.; Pushkar, Y. N.; Nam, W. *J. Am. Chem. Soc.* **2011**, *133*, 20088.

Chapter 1

Electron-Transfer Properties of a Nonheme Manganese(IV)-Oxo Complex Acting as a Stronger One-Electron Oxidant than the Iron(IV)-Oxo Analog

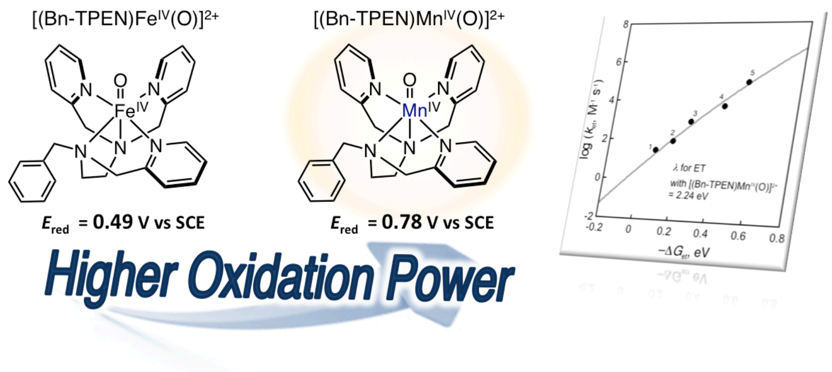

Abstract: Electron-transfer properties of a nonheme manganese(IV)-oxo complex, $[(\mathrm{Bn\text{-}TPEN})\mathrm{Mn}^{\mathrm{IV}}(\mathrm{O})]^{2+}$, reveals that manganese(IV)-oxo complex acts as a stronger one-electron oxidant than the iron(IV)-oxo analog. As a result, an electron transfer process in *N*-dealkylation has been detected by a transient radical cation intermediate, *para*-methyl-DMA$^{\bullet+}$, in the oxidation of *para*-methyl-DMA by $[(\mathrm{Bn\text{-}TPEN})\mathrm{Mn}^{\mathrm{IV}}(\mathrm{O})]^{2+}$.

Introduction

High-valent metal-oxo complexes play pivotal roles as reactive intermediates in a wide range of heme (e.g., cytochromes P450 and peroxidases)[1] and nonheme metalloenzymes[2] as well as in their biomimetic catalytsts.[3] In particular, manganese-oxo complexes have attracted much attention recently as a key intermediate in oxygen-evolving center (OEC) in Photosystem II,[4] in which four-electron oxidation of H_2O to O_2 is efficiently catalyzed. Although extensive efforts have been devoted to elucidate the structural and electronic properties as well as the reactivities of manganese-oxo complexes in oxidation reactions,[5-9] it is quite important to understand the factors that control the redox reactivity of the intermediates since electron transfer is the most fundamental process among a variety of redox reactions, including hydrogen atom transfer (HAT) and oxygen atom transfer (OAT). With regard to nonheme

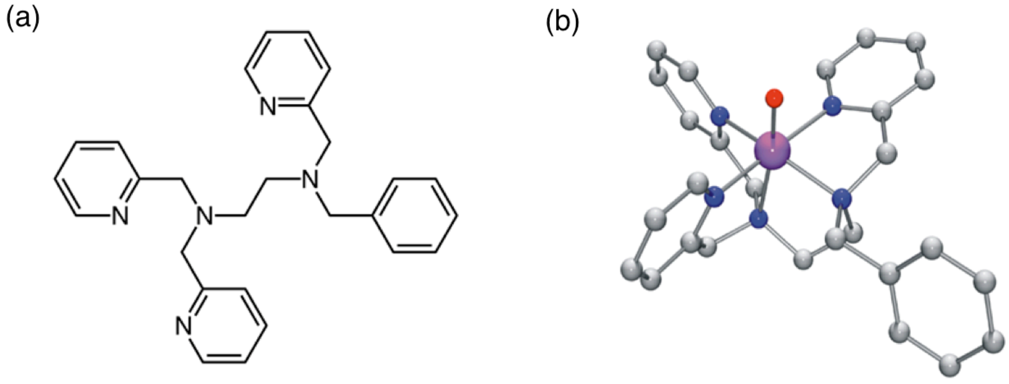

Figure 1. (a) Bn-TPEN lignad and (b) DFT-optimized structure of $[(\text{Bn-TPEN})\text{Mn}^{\text{IV}}(\text{O})]^{2+}$

iron(IV)-oxo complexes, electron-transfer properties have been reported in relation with the redox reactivity.[10] However, electron-transfer properties of manganese(IV)-oxo complexes have yet to be studied in comparison with those of nonheme iron(IV)-oxo analogs.

We report herein thermodynamic and kinetic data for electron transfer from a series of electron donors to a nonheme manganese(IV)-oxo complex, $[(\text{Bn-TPEN})\text{Mn}^{\text{IV}}(\text{O})]^{2+}$ (Bn-TPEN = *N*-benzyl-*N*,*N*’,*N*’-tris(2-pyridylmethyl)-1,2-diaminoethane) (Figure 1).[11] The driving force dependence of the electron-transfer rate is analyzed in light of the Marcus theory of electron transfer,[12] leading to the evaluation of the fundamental electron-transfer properties, such as the reorganization energy and the one-electron reduction potential of $[(\text{Bn-TPEN})\text{Mn}^{\text{IV}}(\text{O})]^{2+}$ in comparison with the iron(IV)-oxo analog, $[(\text{Bn-TPEN})\text{Fe}^{\text{IV}}(\text{O})]^{2+}$. The reactivity of $[(\text{Bn-TPEN})\text{Mn}^{\text{IV}}(\text{O})]^{2+}$ is also investigated in *N*-dealkylation of *N*,*N*-dialkylamines to compare its reactivity with nonheme iron(IV)-oxo species.

Experimental Section

Materials. Commercially available chemicals were used without further purification unless otherwise indicated. Solvents were dried according to published procedures and distilled under Ar prior to use. Iodosylbenzene (PhIO) was prepared by a literature method.[21] Ligand (Bn-TPEN= *N*-benzyl-*N*,*N*',*N*'-tris(2-pyridylmethyl)-1,2-diaminoethane) and manganese(II) complex, $[\text{Mn(II)}(\text{CF}_3\text{SO}_3)_2]\cdot 2\text{CH}_3\text{CN}$, were prepared by literature methods.[22] The synthesis of

$Mn(Bn\text{-}TPEN)(CF_3SO_3)_2$ was carried out in a glove box. Bn-TPEN (0.47 mmol, 200 mg) and $[Mn(II)(CF_3SO_3)_2]\cdot 2CH_3CN$ (0.57 mmol, 250 mg) were dissolved in CH_3CN and stirred at ambient temperature overnight. The resulting solution was filtered and added to a large volume of Et_2O. The product was obtained as a white solid with 85% yield (0.38 g). $[(Bn\text{-}TPEN)Mn(IV)(O)]^{2+}$ was generated by literature methods.[23]

Spectral Redox Titration. Redox titration of electron-transfer from Br_2Fc to $[(Bn\text{-}TPEN)Mn^{IV}(O)]^{2+}$ (2.5×10^{-4} M) was examined in the various concentration of Br_2Fc (7.5×10^{-5} M – 5.0×10^{-4} M) in $CF_3CH_2OH\text{-}CH_3CN$ (*v/v* = 1:1) at 273 K using a Hewlett Packard 8453 photodiode-array spectrometer with a quarts cuvette (path length = 10 mm). Typically, a deaerated MeCN solution of Br_2Fc (7.5×10^{-5} M–5.0×10^{-4} M) was added to a deaerated 2,2,2-trifluoroethanol solution containing $[(Bn\text{-}TPEN)Mn^{IV}(O)]^{2+}$ (2.5×10^{-4} M).

Kinetic Measurements. Kinetic measurements were performed on a UNISOKU RSP-601 stopped-flow spectrometer equipped with a MOS-type highly sensitive photodiode array or a Hewlett Packard 8453 photodiode-array spectrophotometer at 273 K. Rates of electron-transfer from ferrocene derivatives to $[(Bn\text{-}TPEN)Mn^{IV}(O)]^{2+}$ (2.5×10^{-4} M) were monitored by the formation and decay of absorption bands due to ferrocenium ions and $[(Bn\text{-}TPEN)Mn^{IV}(O)]^{2+}$ respectively. All kinetic measurements except dimethylferrocene were carried out under pseudo-first-order conditions where concentrations of ferrocene derivatives were maintained to be more than 10-folds excess of that of $[(Bn\text{-}TPEN)Mn^{IV}(O)]^{2+}$. The k_{et} value for dimethylferrocene was determined under second-order conditions, where both concentrations of Me_2Fc and $[(Bn\text{-}TPEN)Mn^{IV}(O)]^{2+}$ were 8.0×10^{-5} M, because electron transfer rate from Me_2Fc to $[(Bn\text{-}TPEN)Mn^{IV}(O)]^{2+}$ was too fast to follow under pseudo-first-order conditions even with stopped-flow equipment.

Instrumentation. UV-vis spectra were recorded on a Hewlett Packard 8453 diode array spectrophotometer equipped with a UNISOKU Scientific Instruments Cryostat USP-203A for low-temperature experiments or on a UNISOKU RSP-601 stopped-flow spectrometer equipped with a MOS-type highly sensitive photodiode-array. Electrochemical measurements were performed on a CH Instrument (CHI630B) electrochemical analyzer in deaerated $CF_3CH_2OH\text{-}CH_3CN$ (*v/v* = 1:1) containing 0.1M

Bu_4NPF_6 as a supporting electrolyte at 273 K for ferrocene derivatives. A conventional three-electrode cell was used with a platinum working electrode (surface area of 0.3 cm^2) and a platinum wire as a counter electrode. The platinum working electrodes (BAS) were routinely polished with BAS polishing alumina suspension and rinsed with CF_3CH_2OH-CH_3CN (*v/v* = 1:1) prior to use. The measured potentials were recorded as a function of $Ag/AgNO_3$ (0.01 M) reference electrode. All potentials (vs Ag/Ag^+) were converted to the values vs SCE by adding 0.29 V.[24] All electrochemical measurements were performed under Ar atmosphere.

Results and Discussion

$[(Bn\text{-}TPEN)Mn^{IV}(O)]^{2+}$ was prepared by the reaction of $[(Bn\text{-}TPEN)Mn^{II}]^{2+}$ with four equiv of iodosylbenzene (PhIO) in trifluoroethanol (CF_3CH_2OH) according to the reported procedure.[11] The iron(IV)-oxo analog, $[(Bn\text{-}TPEN)Fe^{IV}(O)]^{2+}$, was also prepared by the literature method.[10a] We then performed electron-transfer reactions with a series of electron donors, such as ferrocene (Fc) and its derivatives, and the metal-oxo complexes, such as $[(Bn\text{-}TPEN)Mn^{IV}(O)]^{2+}$ and $[(Bn\text{-}TPEN)Fe^{IV}(O)]^{2+}$, in 1:1 (*v/v*) mixture of CF_3CH_2OH and MeCN at 273 K. The solvent mixture was chosen to optimize the solubility of electron donors and the stability of $[(Bn\text{-}TPEN)Mn^{IV}(O)]^{2+}$

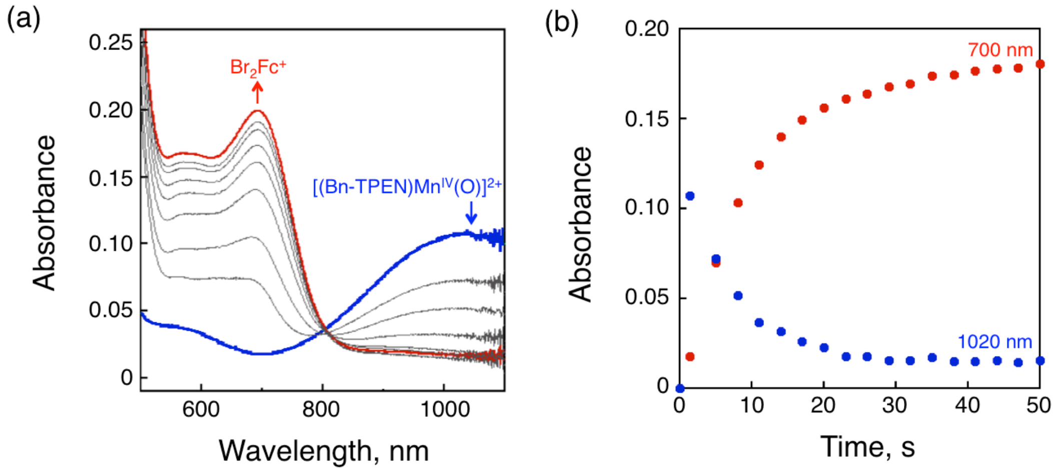

Figure 2. (a) Absorption spectral changes observed in electron transfer from Br_2Fc (2.5×10^{-3} M) to $[(Bn\text{-}TPEN)Mn^{IV}(O)]^{2+}$ (2.5×10^{-4} M) in CF_3CH_2OH-CH_3CN (*v/v* = 1:1) at 273 K. (b) Time profiles of the absorbance at 700 nm (blue circle) and 1020 nm (red circle) due to the formation of Br_2Fc^+ and disappearance of $[(Bn\text{-}TPEN)Mn^{IV}(O)]^{2+}$, respectively.

and $[(\text{Bn-TPEN})\text{Fe}^{\text{IV}}(\text{O})]^{2+}$; both of the metal-oxo complexes are quite stable at 273 K under the reaction conditions. Although no electron transfer from dibromoferrocene (Br_2Fc) to $[(\text{Bn-TPEN})\text{Fe}^{\text{IV}}(\text{O})]^{2+}$ occurred at 273 K, we observed the occurrence of electron transfer from Br_2Fc to $[(\text{Bn-TPEN})\text{Mn}^{\text{IV}}(\text{O})]^{2+}$ under the identical reaction conditions (Figure 2), where the NIR absorption band at 1020 nm due to $[(\text{Bn-TPEN})\text{Mn}^{\text{IV}}(\text{O})]^{2+}$ disappears[11], accompanied by appearance of the absorption band at 700 nm due to dibromoferrocenium ion (Br_2Fc^+). This observation suggests that $[(\text{Bn-TPEN})\text{Mn}^{\text{IV}}(\text{O})]^{2+}$ is a stronger one-electron oxidant than $[(\text{Bn-TPEN})\text{Fe}^{\text{IV}}(\text{O})]^{2+}$. The electron transfer from Br_2Fc to $[(\text{Bn-TPEN})\text{Mn}^{\text{IV}}(\text{O})]^{2+}$ is also found to be in equilibrium eq 1, where the final concentration of Br_2Fc^+ produced increases with increasing the initial concentration of Br_2Fc (Figure 3). The equilibrium constant (K_{et}) is determined to be 23 at 273 K by fitting the plot in Figure 4.

$$[(\text{Bn-TPEN})\text{Mn}^{\text{IV}}(\text{O})]^{2+} + \text{Br}_2\text{Fc} \xrightleftharpoons{K_{\text{et}}} [(\text{Bn-TPEN})\text{Mn}^{\text{III}}(\text{O})]^{+} + \text{Br}_2\text{Fc}^{+} \quad (1)$$

The apparent one-electron reduction potential, E_{red}, of $[(\text{Bn-TPEN})\text{Mn}^{\text{IV}}(\text{O})]^{2+}$ is determined from the K_{et} value and the E_{ox} value of Br_2Fc (0.71 V vs SCE: see Table 1) using the Nernst equation (eq 2) to be 0.78 V.[13] This E_{red} value of $[(\text{Bn-TPEN})\text{Mn}^{\text{IV}}(\text{O})]^{2+}$ is significantly more positive than the E_{red} value of $[(\text{Bn-TPEN})\text{Fe}^{\text{IV}}(\text{O})]^{2+}$ (0.49 V vs SCE),[10a] which is consistent with the result that no electron transfer from Br_2Fc to $[(\text{Bn-TPEN})\text{Fe}^{\text{IV}}(\text{O})]^{2+}$ occurs because the electron t

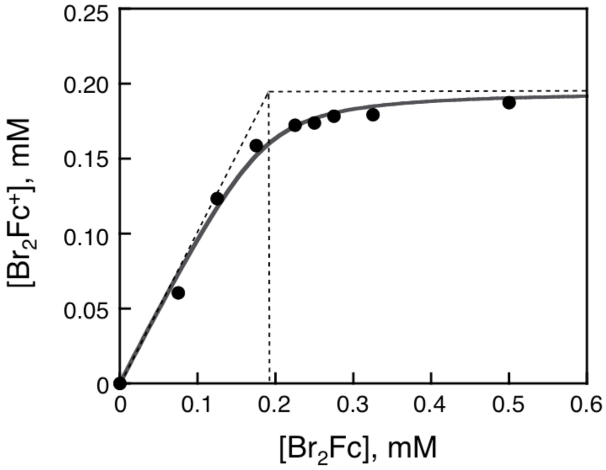

Figure 3. Plot of concentration of Br_2Fc^+ produced in electron transfer from Br_2Fc to $[(\text{Bn-TPEN})\text{Mn}^{\text{IV}}(\text{O})]^{2+}$ vs initial concentration of Br_2Fc, $[\text{Br}_2\text{Fc}]_0$.

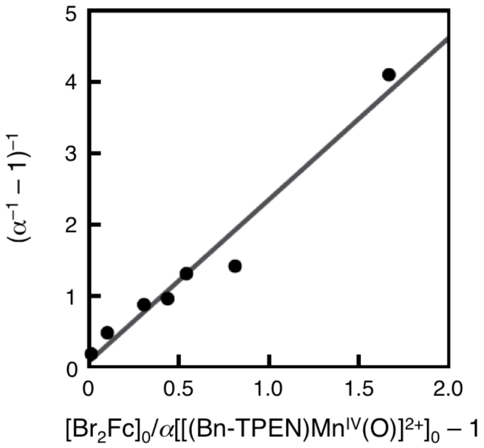

Figure 4. Plot of $(\alpha^{-1} - 1)^{-1}$ vs $[Br_2Fc]_0/\alpha[[(Bn\text{-}TPEN)Mn^{IV}(O)]^{2+}]_0 - 1$ to determine the equilibrium constants (K_{et}) in the electron transfer from Br_2Fc to $[(Bn\text{-}TPEN)Mn^{IV}(O)]^{2+}$ upon addition of Br_2Fc (0.0 – 0.5 mM) into the solution of $[(Bn\text{-}TPEN)Mn^{IV}(O)]^{2+}$ (0.20 mM) in $CF_3CH_2OH\text{-}CH_3CN$ (*v/v* = 1:1) at 273 K.

ransfer is endergonic (ΔG_{et} = –0.07 eV). The higher E_{red} value of $[(Bn\text{-}TPEN)Mn^{IV}(O)]^{2+}$ than those of the corresponding nonheme iron(IV)-oxo complexes was also reported for the case of manganese(IV)-oxo porphyrins with electron-donating and withdrawing substituents, which have significantly higher E_{red} values (E_{red} = 0.95–1.20 V vs SCE)[14] than the E_{red} value of an iron(IV)-oxo porphyrin (Horseradish peroxidase compound II: 0.62 V vs SCE).[15,16]

$$E_{red} = E_{ox} + (RT/F)\ln K_{xet} \tag{3}$$

Rates of electron transfer from Br_2Fc to $[(Bn\text{-}TPEN)Mn^{IV}(O)]^{2+}$ were determined

Table 1. Oxidation Potentials (E_{ox}) of Electron Donors Rate Constant (k_{et}), and Driving Force ($-\Delta G_{et}$) for One-Electron Reduction of $[(Bn\text{-}TPEN)Mn^{IV}(O)]^{2+}$ by Electron Donors in Deaerated $CF_3CH_2OH\text{-}CH_3CN$ (*v/v* = 1:1) at 273 K.

electron donor	E_{ox}, V vs SCE[a]	k_{et}, M^{-1} s^{-1}	$-\Delta G_{et}$, eV
Dimethylferrocene (Me_2Fc)	0.26	1.6×10^4	0.52
Ferrocene (Fc)	0.37	6.1×10^3	0.41
Bromoferrocene (BrFc)	0.54	9.3×10^2	0.24
Acetylferrocene (AcFc)	0.62	9.3×10	0.16
Dibromoferrocene (Br_2Fc)	0.71	3.1×10	0.07

[a] One-electron oxidation potentials of electron donors were measured in $CF_3CH_2OH\text{-}CH_3CN$ (*v/v* = 1:1) at 273 K.

from the increase in the absorption band at 700 nm due to Br_2Fc^+ (Figure 2a). The electron-transfer rates obeyed pseudo-first-order kinetics in large excess of Br_2Fc (Figure 2b). The pseudo-first-order rate constants (k_{obs}) increased linearly with increasing concentration of Br_2Fc (Figure 5). The second-order rate constant of the electron transfer (k_{et}) was determined from the slope of the linear plot of k_{obs} vs concentration of Br_2Fc to be 3.1 × 10 M^{-1} s^{-1}. Similarly, the k_{et} values of electron transfer from a series of electron donors to $[(Bn\text{-}TPEN)Mn^{IV}(O)]^{2+}$ were determined, and the k_{et} values obtained are listed in Table 1 (also see Figure 5 and Figure 6),[13] together with the E_{ox} values of electron donors and the driving force of electron transfer, which was determined using eq 3, where e is the elementary charge. The k_{et} value for dimethylferrocene is obtained by the kinetic measurement carried out under second-order conditions because the reaction is too fast to follow even with stopped-flow equipment under pseudo-first-order conditions (Figure 6).

$$-\Delta G_{et}\ (\mathrm{eV}) = e(E_{red} - E_{ox}) \qquad (3)$$

The driving force dependence of the electron-transfer rate constants is shown in Figure 7, where the log k_{et} values are plotted against the $-\Delta G_{et}$ values. The driving force dependence of k_{et} is well fitted by the solid line in Figure 7 in light of the Marcus theory of adiabatic outer-sphere electron transfer eq 4, where Z is the collision frequency taken as 1 × 10^{11} M^{-1} s^{-1}, λ is the reorganization energy of electron transfer, k_B is the Boltzmann constant, and T is the absolute temperature.[10,12] The λ value is determined to

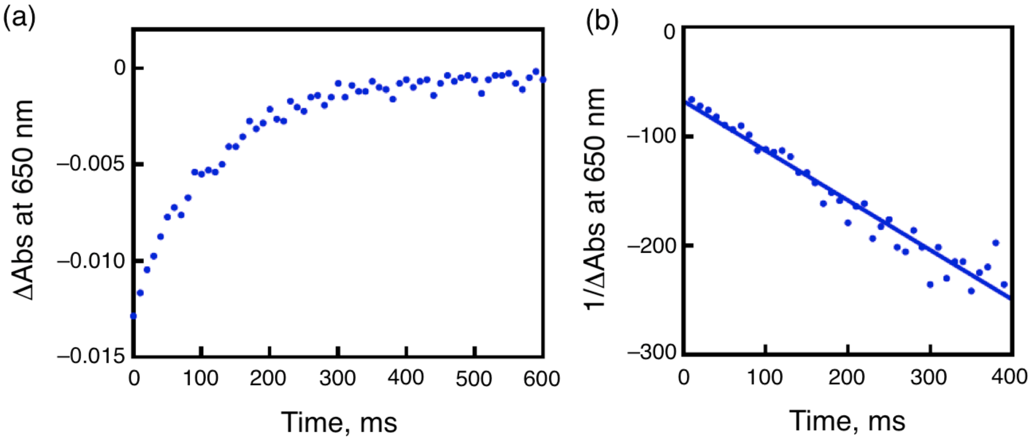

Figure 6. (a) A time course of the absorbance monitored at 650 nm due to Me_2Fc^+ (λ_{max} = 650 nm; ε = 340 M^{-1} cm^{-1}) observed in the oxidation reaction of Me_2Fc (8.0 × 10^{-5} M) by $[(Bn\text{-}TPEN)Mn^{IV}(O)]^{2+}$ (8.0 × 10^{-5} M) in CF_3CH_2OH-MeCN (1:1 *v*/*v*) at 273 K. (b) Second-order-plot of the spectral change.

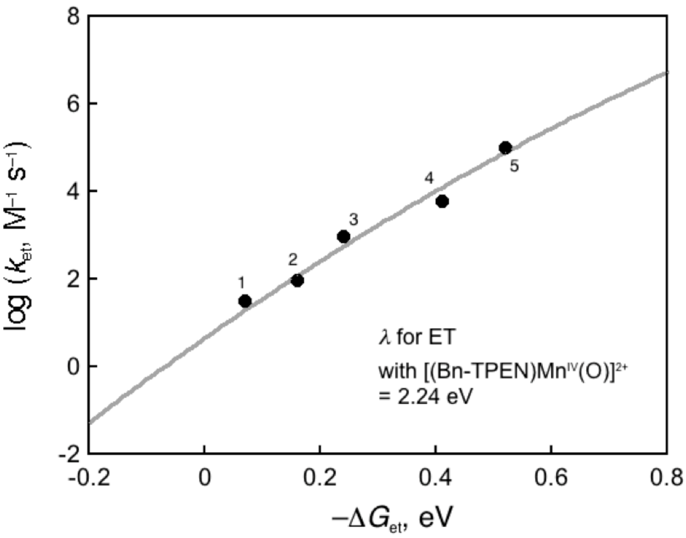

Figure 7. ET driving force ($-\Delta G_{et}$) dependence of rate constants (log k_{et}) from one-electron donors (1: dibromoferrocene, 2: acethylferrocene, 3: bromoferrocene, 4: ferrocene, 5: dimethylferrocene) to $[(\text{Bn-TPEN})\text{Mn}^{IV}(\text{O})]^{2+}$ in CF_3CH_2OH-CH_3CN (v/v = 1:1) at 273 K. The gray line is the Marcus line calculated with λ value of 2.24 eV.

be 2.24 eV as the best fit value of eq 4 and this value is compared with λ values of iron(IV)-oxo complexes in Table 2, where the E_{red} values are also listed.[10]

$$k_{et} = Z \exp[-(\lambda/4)(1 + \Delta G_{et}/\lambda)^2/k_BT] \qquad (4)$$

The λ value of the electron-transfer reduction of $[(\text{Bn-TPEN})\text{Mn}^{IV}(\text{O})]^{2+}$ (2.24 eV) is similar to those determined for the electron-transfer reduction of nonheme iron(IV)-oxo complexes. This indicates that one-electron reduction of high-valent metal-oxo complexes generally requires large reorganization energy probably due to significant

Table 2. One-electron reduction potentials (E_{red}) and reorganization energies (λ) of electron-transfer reduction of manganese(IV)-oxo and iron(IV)-oxo complexes.

complex	E_{red}, V vs SCE	λ, eV
$[(\text{Bn-TPEN})\text{Mn}^{IV}(\text{O})]^{2+}$	0.78 ± 0.01	2.37 ± 0.03
$[(\text{TMC})\text{Fe}^{IV}(\text{O})]^{2+}$	0.39 ± 0.01^a	2.37 ± 0.04
$[(\text{Bn-TPEN})\text{Fe}^{IV}(\text{O})]^{2+}$	0.49 ± 0.02^a	2.55 ± 0.05
$[(\text{N4Py})\text{Fe}^{IV}(\text{O})]^{2+}$	0.51 ± 0.02^a	2.74 ± 0.06
$[(\text{N2Py2})\text{Fe}^{IV}(\text{O})]^{2+}$	0.73^b	2.05

[a] Taken from ref. 10a. [b] Taken from ref. 10c.

elongation of metal-oxo bond upon a one-electron reduction. $[(\mathrm{Bn\text{-}TPEN})\mathrm{Mn^{IV}(O)}]^{2+}$ has the most positive E_{red} value as compared with those of iron(IV)-oxo complexes, suggesting that $[(\mathrm{Bn\text{-}TPEN})\mathrm{Mn^{IV}(O)}]^{2+}$ is the strongest one-electron oxidant among nonheme metal-oxo complexes reported so far.

We also investigated the reactivity of $[(\mathrm{Bn\text{-}TPEN})\mathrm{Mn^{IV}(O)}]^{2+}$ in *N*-dealkylation and then compared its reactivity with an iron(IV)-oxo complex, $[(\mathrm{N4Py})\mathrm{Fe^{IV}(O)}]^{2+}$.[10d,17,18] We examined the oxidation of *para*-methyl-*N,N*-dimethylaniline (*para*-methyl-DMA; E_{ox} = 0.69 V vs SCE) by $[(\mathrm{Bn\text{-}TPEN})\mathrm{Mn^{IV}(O)}]^{2+}$. The *N*-dealkylation of DMA derivatives by metal-oxo species are known to consist of an electron transfer coupled with a proton transfer from DMA derivatives to metal-oxo species.[10d,17,19] In the case of oxidation of *para*-methyl-DMA by $[(\mathrm{N4Py})\mathrm{Fe^{IV}(O)}]^{2+}$, the intermediate $\mathrm{DMA}^{\bullet+}$ resulted from an electron transfer process is not detected because the initial ET process is the rate-determining step.[10d,17] In contrast, addition of a *para*-methyl-DMA to a deaerated $\mathrm{CF_3CH_2OH\text{-}CH_3CN}$ (v/v = 1:1) solution of $[(\mathrm{Bn\text{-}TPEN})\mathrm{Mn^{IV}(O)}]^{2+}$ resulted in the immediate generation of a transient absorption band at λ_{max} = 460 nm (Figure 8). The absorption band was identical to the *para*-methyl-$\mathrm{DMA}^{\bullet+}$, given by the reaction of *para*-methyl-DMA (2.5×10^{-3} M) with cerium(IV) ammonium nitrate (2.5×10^{-3} M) in $\mathrm{CF_3CH_2OH\text{-}CH_3CN}$ (v/v = 1:1) at 273 K (Figure 9). The transient absorption band of *para*-methyl-$\mathrm{DMA}^{\bullet+}$ appears, accompanied by a decrease in the absorption band at 725 nm[20] due to $[(\mathrm{Bn\text{-}TPEN})\mathrm{Mn^{IV}(O)}]^{2+}$ (Figure 8b). Electron transfer from *para*-methyl-DMA to $[(\mathrm{Bn\text{-}TPEN})\mathrm{Mn^{IV}(O)}]^{2+}$ proceeds via fast electron transfer from

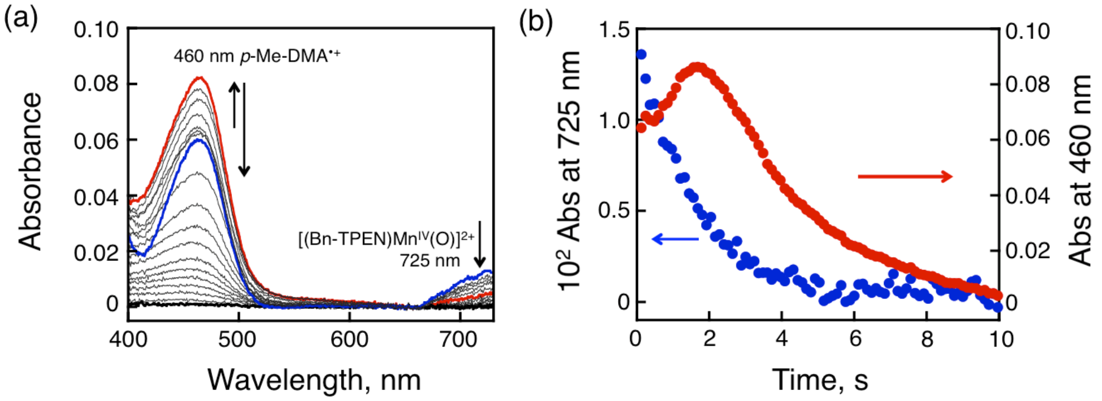

Figure 8. (a) Optical spectral changes in the reaction of 1 (2.5×10^{-4} M) and *para*-methyl-DMA (2.5×10^{-3} M) in $\mathrm{CF_3CH_2OH\text{-}CH_3CN}$ (v/v = 1:1) at 273 K. (b) The time course of the decay of $[(\mathrm{Bn\text{-}TPEN})\mathrm{Mn^{IV}(O)}]^{2+}$ (blue line) and the formation and decay of *para*-methyl-$\mathrm{DMA}^{\bullet+}$ (red line) monitored at 725 nm and 460 nm, respectively.

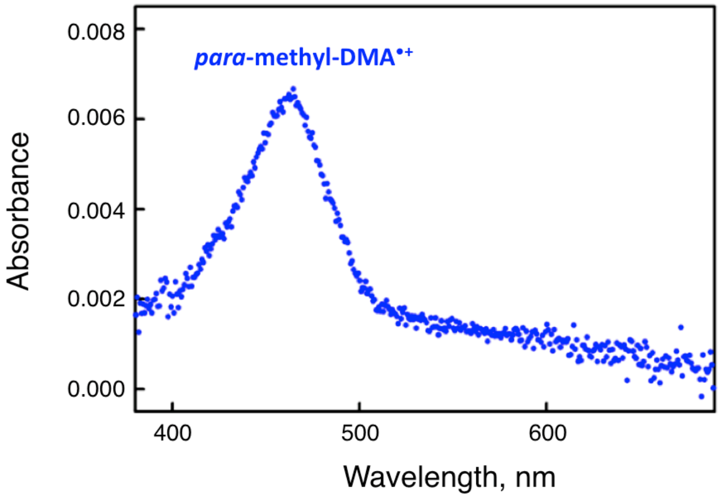

Figure 9. Absorption spectrum of *para*-methyl-DMA$^{•+}$ observed in the reaction of *para*-methyl-DMA (2.5×10^{-3} M) with cerium (IV) ammonium nitrate (2.5×10^{-3} M) in CF_3CH_2OH-CH_3CN (*v/v* = 1:1) at 273 K.

DMA to [(Bn-TPEN)Mn^{IV}(O)]$^{2+}$ to produce *para*-methyl-DMA$^{•+}$, followed by slower proton transfer from *para*-methyl-DMA$^{•+}$ to [(Bn-TPEN)Mn^{III}(O)]$^{+}$ in a stepwise manner. The initial electron transfer becomes energetically feasible due to the highly positive E_{red} value of [(Bn-TPEN)Mn^{IV}(O)]$^{2+}$. The rate constant was evaluated to be 2.6×10^2 M^{-1} s^{-1} in CF_3CH_2OH-CH_3CN (*v/v* = 1:1) at 273 K. Thus, to the best of our knowledge, this is the first example of detecting the radical cation intermediate in electron-transfer reactions of metal-oxo complexes without acids or metal ion effect.

Conclusion

In summary, we have determined for the first time the fundamental electron-transfer properties of a nonheme manganese(IV)-oxo complex, which is featured by a highly positive one-electron reduction potential, as compared with those of nonheme iron(IV)-oxo complexes. As a result of the highly positive one-electron reduction potential, the occurrence of electron transfer in the *N*-dealkylation of DMA derivatives has been confirmed by the detection of radical cation intermediate, *para*-methyl-DMA$^{•+}$, in the oxidation of *para*-methyl-DMA by the nonheme manganese(IV)-oxo complex.

References

(1) Ortiz de Montellano, P. R. *Cytochrome P450: Structure, Mechanism, and Biochemistry*, 3rd ed.; Kluwer Academic/Plenum Publishers: New York, **2005**.

(2) (a) Bruijnincx, P. C. A.; van Koten, G.; Klein Gebbink, R. J. M. *Chem. Soc. Rev.* **2008**, *37*, 2716. (b) Krebs, C.; Fujimori, D. G.; Walsh, C. T.; Bollinger, J. M., Jr. *Acc. Chem. Res*. **2007**, *40*, 484.

(3) (a) Hohenberger, J.; Ray, K.; Meyer, K. *Nature Commun.* **2012**, *3*, 720. (b) Borovik, A. S. *Acc. Chem. Res.* **2005**, *38*, 54. (c) Nam, W. *Acc. Chem. Res.* **2007**, *40*, 522.

(4) (a) McEvoy, J. P.; Brudvig, G. W. *Chem. Rev*. **2006**, *106*, 4455. (b) Umena, Y.; Kawakami, K.; Shen, J.-R.; Kamiya, N. *Nature* **2011**, *473*, 55.

(5) (a) Groves, J. T.; Kruper, W. J. Jr.; Haushalter, R. C. *J. Am. Chem. Soc.*, **1980**, *102*, 6375. (b) Jin, N.; Bourassa, J. L.; Tizio, S. C.; Groves, J. T. *Angew. Chem., Int. Ed.*, **2000**, *39*, 3849. (c) Umile, T. P.; Groves, J. T. *Angew. Chem., Int. Ed*., **2011**, *50*, 695.

(6) (a) Gross, Z.; Golubkov, G.; Simkhovich, L. *Angew. Chem., Int. Ed.*, **2000**, *39*, 4045. (b) Kumar, A.; Goldberg, I.; Botoshansky, M.; Buchman, Y.; Gross, Z. *J. Am. Chem. Soc*. **2010**, *132*, 15233.

(7) (a) Liua, H.-Y.; HR Mahmooda, M.: Qiuc, S.-X.; Chang, C. K. *Coord. Chem. Rev*. **2013**, *257*, 1306. (b) Zhao, H.; Pierloot, K.; Langner, E. H. G.; Swarts, J. C.; Conradie, J.; Ghosh, A. *Inorg. Chem*., **2012**, *51*, 4002.

(8) (a) Goldberg, D. P. *Acc. Chem. Res*. **2007**, *40,* 626. (b) Prokop, K. A.; de Visser, S. P.; Goldberg, D. P. *Angew. Chem., Int. Ed.* **2010**, *49*, 5091. (c) Prokop, K. A.; Neu, H. M.; de Visser, S. P.; Goldberg, D. P. *J. Am. Chem. Soc.* **2011**, *133*, 15874. (d) Fukuzumi, S.; Kotani, H.; Prokop, K. A.; Goldberg, D. P. *J. Am. Chem. Soc.* **2011**, *133*, 1859.

(9) (a) Nam, W.; Kim, I.; Lim, M. H.; Choi, H. J.; Lee, J. S.; Jang, H. G. *Chem.–Eur. J.*, **2002**, *8*, 2067. (b) Song, W. J.; Seo, M. S.; George, S. D.; Ohta, T.; Song, R.; Kang, M.-J.; Tosha, T.; Kitagawa, T.; Solomon, E. I.; Nam, W. *J. Am. Chem. Soc.*, **2007**, *129*, 1268. (c) Lee, J. Y.; Lee, Y.-M.; Kotani, H.; Nam, W.; Fukuzumi, S. *Chem. Commun.*, **2009**, *704*. (d) Han, Y.; Lee, Y.-M.; Mariappan, M.; Fukuzumi, S.; Nam, W. *Chem. Commun*., **2010**, *46*, 8160. (e) Kim, S. H.; Park, H.; Seo, M. S.; Kubo, M.; Ogura, T.; Klajn, J.; Gryko, D. T.; Valentine, J. S.; Nam, W. *J. Am. Chem. Soc*., **2010**, *132*, 14030. (f) Fukuzumi, S.; Kishi, T.; Kotani, H.; Lee, Y.-M.; Nam, W. *Nature Chem.*, **2011**, *3*, 38.

(10) (a) Lee, Y.-M.; Kotani, H.; Suenobu, T.; Nam, W.; Fukuzumi, S. *J. Am. Chem. Soc*. **2008**, *130*, 434. (b) Park, J.; Morimoto, Y.; Lee, Y.-M.; Nam, W.; Fukuzumi, S. *J. Am. Chem. Soc.* **2011**, *133*, 5236. (c) Comba, P.; Fukuzumi, S.; Kotani, H.; Wunderlich, S. *Angew. Chem., Int. Ed*. **2010**, *49*, 2622. (d) Park, J.; Morimoto, Y.; Lee, Y.-M.; Nam, W.; Fukuzumi, S. *Inorg. Chem*. **2011**, *50*, 11612. (e) Takahashi, A.; Kurahashi, T.; Fujii, H. *Inorg. Chem.*, **2011**, *50*, 6922.

(11) The manganese(IV)-oxo species could be generated by use of a stoichiometrical amount of PhIO. However, 4 equiv of PhIO was used in this work to shorten the reaction time and also to make sure the complete conversion to the manganese(IV) species; see: Wu, X.; Seo, M. S.; Davis, K. M.; Lee, Y.-M.; Chen, J.; Cho, K.-B.; Pushkar, Y. N.; Nam, W. *J. Am. Chem. Soc.* **2011**, *133*, 20088.

(12) Marcus, R. A. *Angew. Chem. Int. Ed. Engl.* **1993**, *32*, 1111.

(13) Oxidation potentials of electron donors in CF_3CH_2OH-MeCN (*v*/*v* = 1:1) were determined in this work (see Table 1).

(14) Fukuzumi, S.; Mizuno, T.; Ojiri, T. *Chem.–Eur. J.*, **2012**, *18*, 15794.

(15) Fukuzumi, S. *Coord. Chem. Rev*. **2013**, *257*, 1564.

(16) The reason why the E_{red} value of $[(\text{N2Py2})\text{Fe}^{\text{IV}}(\text{O})]^{2+}$ is higher than those of other nonheme $\text{Fe}^{\text{IV}}(\text{O})$ complexes may result from the less electron-donating coordination of the tentradendentate N2Py2 ligand as compared with pentadentate ligands of other nonheme $\text{Fe}^{\text{IV}}(\text{O})$ complexes.

(17) Nehru, K.; Seo, M. S.; Kim, J.; Nam, W. *Inorg. Chem.*, **2007**, *46*, 293.

(18) It has been reported that $[(\text{Bn-TPEN})\text{Fe}^{\text{IV}}(\text{O})]^{2+}$ exhibits similar reactivity to $[(\text{N4Py})\text{Fe}^{\text{IV}}(\text{O})]^{2+}$; see ref 10a.

(19) Montellano, P. R. Ortiz de; De Voss, J. J. *Nat. Prod. Rep.*, **2002**, *19*, 477.

(20) Due to the range limitation of stopped-flow spectrometer (350 – 750 nm), the absorbance at 725 nm was monitored.

(21) *Organic Syntheses*; Saltzman, H.; Sharefkin, J. G., Eds.; Wiley: New York, **1973**, Vol. V, pp. 658.

(22) Lubben,M.; Meetsma, A.; Wilkinson, E. C.; Feringa, B.; Que, L., Jr., *Angew. Chem. Int. Ed.* **1995**, *34*, 1512.

(23) Wu, X.; Seo, M. S.; Davis, K. M.; Lee, Y.-M.; Chen, J.; Cho, K-B.; Pushkar, Y. N.; Nam, W. *J. Am. Chem. Soc.* **2011**, *133*, 20088.

(24) *Electrochemical Reactions in Non-aqueous Systems*, Mann, C. K.; Barnes, K. K., Mercel Dekker: New York, **1970**.

Chapter 2

Hydride Transfer from NADH Analogs to a Nonheme Manganese(IV)-Oxo Complex via Rate-Determining Electron Transfer

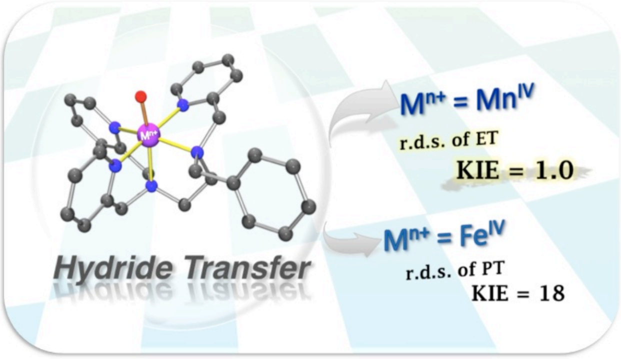

Abstract: Hydride transfer from NADH analogs to a nonheme manganese(IV)-oxo complex, $[(\text{Bn-TPEN})\text{Mn}^{\text{IV}}(\text{O})]^{2+}$, proceeds *via* a rate-determining electron-transfer step with no deuterium kinetic isotope effect (KIE = 1.0 ± 0.1); a charge-transfer complex formed between the manganese(IV)-oxo complex and NADH analogs is involved in the hydride-transfer reaction.

Introduction

An important objective in biological oxidation reactions is to understand the nature of reactive intermediates and their reaction mechanisms occurring at the active sites of enzymes.[1] High-valent metal-oxo complexes play pivotal roles as reactive intermediates in a wide range of heme[2] and nonheme metalloenzymes[3] as well as in their biomimetic catalysts.[4] In particular, manganese-oxo complexes have attracted much attention as key intermediates in oxygen-evolving complex (OEC) in photosystem II,[5] in which four-electron oxidation of H_2O to O_2 is efficiently catalyzed. We have previously reported electron-transfer properties of a nonheme manganese(IV)–oxo complex, which revealed that manganese(IV)–oxo complex is a

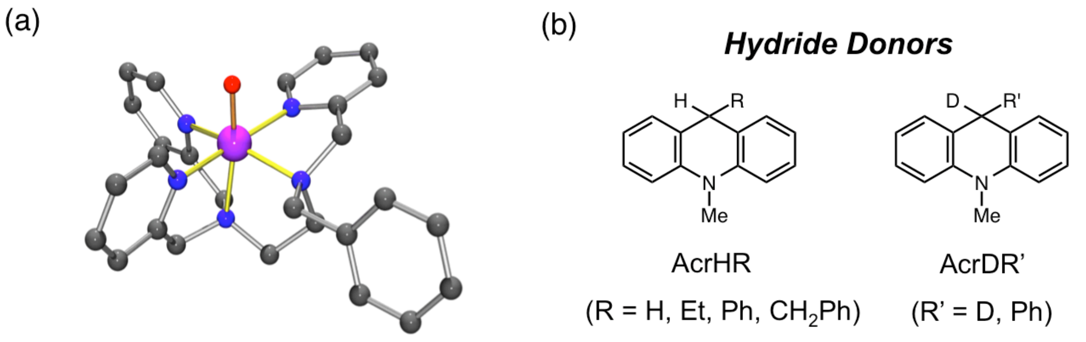

Figure 1. (a) Chemical structures of (a) $[(\text{Bn-TPEN})\text{Mn}^{\text{IV}}(\text{O})]^{2+}$ and (b) NADH analogs used in HT reactions.

stronger one-electron oxidant than the iron(IV)–oxo analogs.[6,7] Hydride transfer from dihydronicotinamide adenine dinucleotide (NADH) analogs,[8] such as 10-methyl-9,10-dihydroacridine (AcrH_2) and its derivatives, to nonheme iron(IV)-oxo complexes has been reported to occur via electron transfer followed by proton and electron transfer, exhibiting large deuterium kinetic effects (KIEs) to yield the corresponding NAD^+ analogs and nonheme Fe(II) complexes.[7] In contrast to iron(IV)-oxo complexes, hydride transfer from NADH analogs to nonheme manganese(IV)–oxo complexes, which are stronger oxidants than the corresponding iron(IV)-oxo complexes may proceed via a rate-determining electron transfer step, which should exhibit no KIE. However, there has been no report on hydride-transfer reactions via a rate-determining electron-transfer step despite extensive studies on hydride-transfer reactions of NADH analogs.[9-13]

We report herein the first example of hydride transfer (HT) from a series of NADH analogs and their deuterated compounds to a mononuclear nonheme manganese(IV)–oxo complex, $[(\text{Bn-TPEN})\text{Mn}^{\text{IV}}(\text{O})]^{2+}$ (Bn-TPEN = *N*-benzyl-*N*,*N*′,*N*′-tris(2-pyridylmethyl)ethane-1,2-diamine) (Figure 1)[6] via a rate-determining electron-transfer step. The difference in the rate-determining steps of HT from NADH analogs to nonheme iron(IV)-oxo[7b] and manganese(IV)–oxo complexes is clarified by carrying out kinetic studies, including the determination of deuterium kinetic isotope effect (KIE).

Experimental Section

Materials. Commercially available reagents, such as 10-methylacridone, acridine, 10-methylacridinium iodide ($AcrH^+I^-$), methyl iodide (MeI), $NaBH_4$, $LiAlD_4$ and $NaBD_4$, were the best available purity and were used without further purification unless otherwise noted. Solvents were dried according to published procedures and distilled under Ar prior to use. Iodosylbenzene (PhIO) was prepared by a literature method. Ligand (Bn-TPEN= *N*-benzyl-*N*,*N'*,*N'*-tris(2-pyridylmethyl)-1,2-diaminoethane), $[Mn^{II}(CF_3SO_3)_2]\cdot 2CH_3CN$ and $[Mn^{II}(Bn\text{-}TPEN)](CF_3SO_3)_2$ were prepared by literature methods. The synthesis of $[Mn^{II}(Bn\text{-}TPEN)](CF_3SO_3)_2$ was carried out in a glove box. Bn-TPEN (0.47 mmol, 200 mg) and $[Mn^{II}(CF_3SO_3)_2]\cdot 2CH_3CN$ (0.57 mmol, 250 mg) were dissolved in CH_3CN and stirred at ambient temperature overnight. The resulting solution was filtered and added to a large volume of Et_2O. The product was obtained as a white solid with 85% yield (0.38 g). $[(Bn\text{-}TPEN)Mn^{IV}(O)]^{2+}$ was generated by literature methods. 9,10-Dihydro-10-methylacridine ($AcrH_2$) was prepared by reducing 10-methylacridinium iodide ($AcrH^+I^-$) with $NaBH_4$ in methanol and purified by recrystallization from ethanol. For the preparation of $AcrH^+I^-$, acridine was treated with MeI in acetone, and then the mixture was refluxed for 7 days. 9-Alkyl-9,10-dihydro-10-methylacridine (AcrHR; R = Et, CH_2Ph, Ph) was prepared by the reduction of $AcrH^+I^-$ with the corresponding Grignard reagents (RMgX) and purified by recrystallization from ethanol.[17] The dideuterated compound, $[9,9'\text{-}^2H_2]$-10-methylacridine ($AcrD_2$), was prepared from 10-methylacridone by reduction with $LiAlD_4$ in ether.

Kinetic and Reactivity Measurements. UV-vis spectra were recorded on a Hewlett Packard 8453 diode array spectrophotometer at 273 K equipped with a UNISOKU Scientific Instruments Cryostat USP-203A for low-temperature experiments. All kinetic measurements were carried out under pseudo-first-order conditions where concentrations of NADH analogs were maintained to be more than 10-folds excess of that of **1**. Rates of hydride-transfer from NADH analogs to $[(Bn\text{-}TPEN)Mn^{IV}(O)]^{2+}$ (5.0×10^{-5} M) were monitored by the formation due to 10-methylacridinium ion ($AcrH^+$). After the completion of reactions, k_{obs} values were calculated by pseudo-first-order fitting of the kinetic data. By using dideuterated compound, $AcrD_2$, kinetic isotope effect (KIE) value was determined. To determine the formation constant of precursor complexes between electron donor and $[(Bn\text{-}TPEN)Mn^{IV}(O)]^{2+}$, pseudo-first-order rate constant of electron transfer from dibromoferrocene derivatives to

$[(\text{Bn-TPEN})\text{Mn}^{\text{IV}}(\text{O})]^{2+}$ were monitored by the formation of absorption bands at λ_{max} = 700 nm due to Br_2Fc^+. Electron transfer from Br_2Fc to $[(\text{Bn-TPEN})\text{Mn}^{\text{IV}}(\text{O})]^{2+}$ (1.3×10^{-4} M) was examined from the spectral change in the presence of various concentrations of dibromoferrocene ($6.3 \times 10^{-4} - 5.0 \times 10^{-2}$ M) using UNISOKU RSP-601 stopped-flow spectrometer equipped with a MOS-type highly sensitive photodiode array or a Hewlett Packard 8453 photodiode-array spectrophotometer at 273 K.

EPR measurements. CW-EPR spectra were taken at 5 K using an X-band Bruker EMX-plus spectrometer equipped with a dual mode cavity (ER 4116DM). Low temperatures were achieved and controlled with an Oxford Instruments ESR900 liquid He quartz cryostat with an Oxford Instruments ITC503 temperature and gas flow controller. The magnitude of modulation was chosen to optimize the resolution and signal-to-noise (S/N) ratio of the observed spectra under non-saturating microwave power conditions. The experimental parameters for EPR spectra were as follows: Microwave frequency = 9.647 GHz, microwave power = 1.0 mW, modulation amplitude = 10 G, gain = 1×10^4, time constant = 10.24 ms, conversion time = 81.96 ms.

Results and Discussion

In order to compare the HT reactivities of nonheme iron(IV)-oxo and manganese(IV)–oxo complexes, we determined the rate constants of HT reactions from the same series of NADH analogs to nonheme manganese(IV)–oxo complexes, as employed in the reactions of nonheme iron(IV)-oxo complexes.[7b] The visible absorption changes in HT from AcrH_2 to $[(\text{Bn-TPEN})\text{Mn}^{\text{IV}}(\text{O})]^{2+}$ in deaerated $\text{CF}_3\text{CH}_2\text{OH-CH}_3\text{CN}$ (*v/v* = 1:1) at 273 K are shown in Figure 2a, where the absorption band at 358 nm due to 10-methylacridinium ion (AcrH^+) increases. The rates obeyed pseudo-first-order kinetics in the presence of large excess of AcrH_2, and the pseudo-first-order rate constants (k_{obs}) increased linearly with the increase of the AcrH_2 concentration (Figure 2b). The second-order rate constant (k_{H}) of HT from AcrH_2 to $[(\text{Bn-TPEN})\text{Mn}^{\text{IV}}(\text{O})]^{2+}$ in deaerated $\text{CF}_3\text{CH}_2\text{OH-CH}_3\text{CN}$ (*v/v* = 1:1) at 273 K was determined from the slope of the linear plot in Figure 2b (blue) to be 1.4×10^2 M^{-1} s^{-1}. When AcrH_2 was replaced by the deuterated compound (AcrD_2), the same second-order rate constant was obtained as

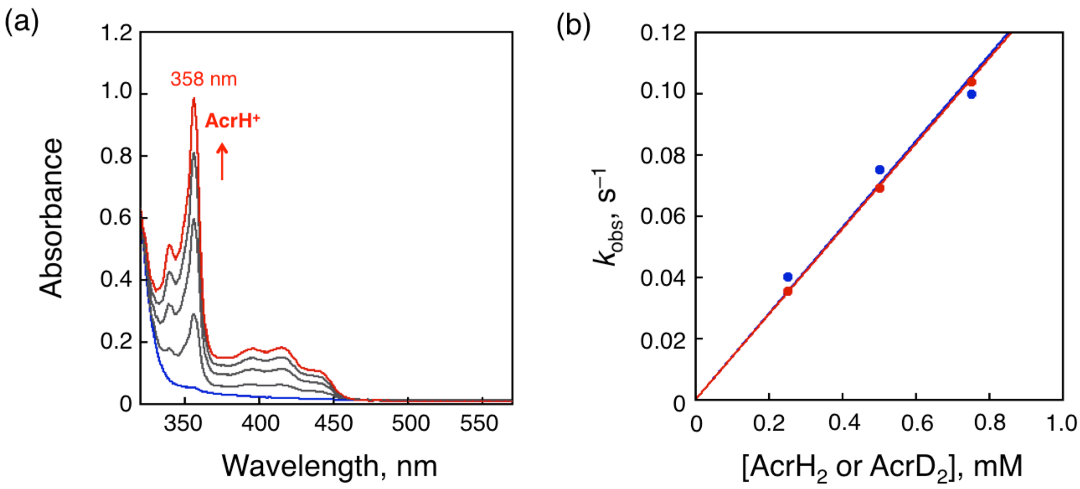

Figure 2. (a) UV-vis spectral changes observed in HT from $AcrH_2$ (5.0×10^{-4} M) to $[(Bn\text{-}TPEN)Mn^{IV}(O)]^{2+}$ (5.0×10^{-5} M) in CF_3CH_2OH-CH_3CN (v/v = 1:1) at 273 K. (b) Plots of the pseudo-first-order constants (k_{obs}) of $[(Bn\text{-}TPEN)Mn^{IV}(O)]^{2+}$ vs $AcrH_2$ (blue) or $AcrD_2$ (red).

shown in Figure 2b (red), exhibiting no deuterium kinetic isotope effect in the HT reaction (KIE = k_H/k_D = 1.0 ± 0.1). This is in sharp contrast to HT reactions by $[(Bn\text{-}TPEN)Fe^{IV}(O)]^{2+}$, in which a large KIE value of 18 was obtained.[7b] In the case of $[(Bn\text{-}TPEN)Mn^{IV}(O)]^{2+}$, which has a higher one-electron reduction potential (E_{red} = 0.78 V vs SCE)[6c] than $[(Bn\text{-}TPEN)Fe^{IV}(O)]^{2+}$ (E_{red} = 0.49 V vs SCE),[7a] electron transfer (ET) from $AcrH_2$ (E_{ox} = 0.81 V vs SCE)[14] to $[(Bn\text{-}TPEN)Mn^{IV}(O)]^{2+}$ is thermodynamically feasible, whereas ET from $AcrH_2$ to $[(Bn\text{-}TPEN)Fe^{IV}(O)]^{2+}$ is endergonic ($\Delta G_{et} > 0$). Thus, HT from $AcrH_2$ to $[(Bn\text{-}TPEN)Mn^{IV}(O)]^{2+}$ occurs via rate-determining ET, followed by fast proton and electron transfer to yield $AcrH^+$ and $[(Bn\text{-}TPEN)Mn^{II}(OH)]^{2+}$ (Figure 3); we have shown previously that HT from $AcrH_2$ to $[(Bn\text{-}TPEN)Fe^{IV}(O)]^{2+}$ occurs via uphill ET followed by rate-determining proton transfer (PT) in competition with the back ET, followed by fast ET to yield $AcrH^+$ and $[(Bn\text{-}TPEN)Fe^{II}(OH)]^{2+}$.[7b]

The k_H values of HT from other NADH analogs (AcrHR: R = Ph, CH_2Ph, Et and AcrDPh) were also determined (Table 1, Figure 4). The substitution of one H by Ph in $AcrH_2$ (i.e., AcrHPh) results in the higher E_{ox} value (0.88 V vs SCE) than $AcrH_2$ (0.81 V vs SCE), thus a slower deprotonation from $AcrHPh^{\bullet+}$ occurs compared to $AcrH_2^{\bullet+}$.[7b,14] In such a case, ET from AcrHPh to $[(Bn\text{-}TPEN)Mn^{IV}(O)]^{2+}$ becomes endergonic,

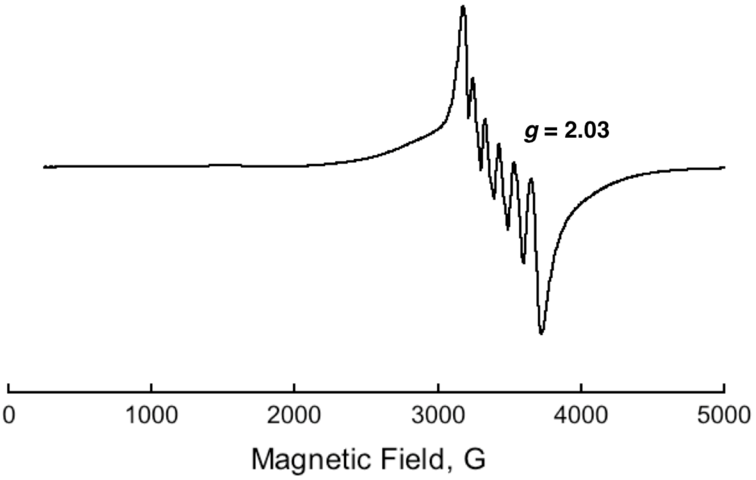

Figure 3. X-band EPR spectrum of the reaction products obtained in the reaction between $[(\text{Bn-TPEN})\text{Mn}^{\text{IV}}(\text{O})]^{2+}$ (1.0×10^{-3} M)) and $AcrH_2$ (1.0×10^{-2} M). The spectrum was recorded in CF_3CH_2OH-MeCN (1:1 v/v) at 5 K. The yield of low-spin Mn(II) complex produced is ~ 95%, which was calculated by comparing with the EPR spectrum of an authentic low-spin Mn(II) complex, $\text{Mn}^{\text{II}}(\text{TMC})(\text{OTf})_2$ (TMC = 1,4,8,11-tetramethyl-1,4,8,11-tetraazacyclotetradecane) (see Nam *et al. Angew. Chem.*, *Int. Ed.,* 2007, **46**, 377).

Table 1. Oxidation potentials (E_{ox}) of NADH analogs and electron donors, rate constants for hydride transfer (k_{H}) from NADH analogs and electron transfer (k_{et}) from electron donors to $[(\text{Bn-TPEN})\text{Mn}^{\text{IV}}(\text{O})]^{2+}$ in deaerated CF_3CH_2OH-MeCN (1:1 *v/v*) at 273 K.

NADH analog	E_{ox}, V vs SCE[a]	k_{et}, M^{-1} s^{-1}	$-\Delta G_{\text{et}}$, eV
$AcrH_2$	0.81	1.4×10^2	–0.03
$AcrD_2$	0.81	1.4×10^2	–0.03
AcrHEt	0.84	6.4×10	–0.06
$AcrHCH_2Ph$	0.84	4.0×10	– 0.06
AcrHPh	0.88	4.1×10	–0.10
AcrDPh	0.88	2.1×10	–0.10
electron donor	E_{ox}, V vs SCE[b]	k_{H}, M^{-1} s^{-1}[b]	$-\Delta G_{\text{et}}$, eV
Dimethylferrocene (Me_2Fc)	0.26	1.0×10^5	0.52
Ferrocene (Fc)	0.37	6.1×10^3	0.41
Bromoferrocene (BrFc)	0.54	9.3×10^2	0.24
Acetylferrocene (AcFc)	0.62	9.3×10	0.16
Dibromoferrocene (Br_2Fc)	0.71	3.1×10	0.07

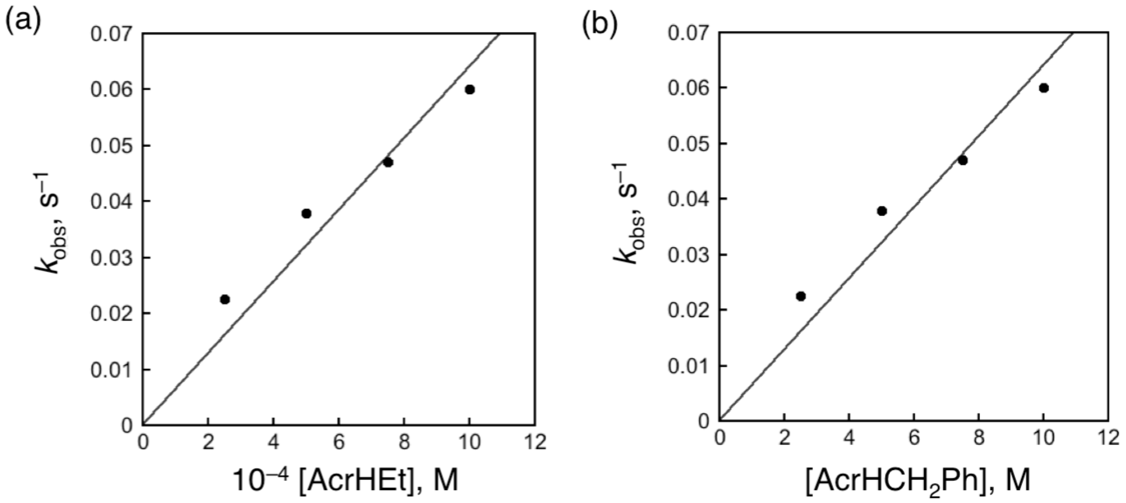

Figure 4. Plots of pseudo-first-order rate constants (k_f) for HT from (a) AcrHEt and (b) $AcrHCH_2Ph$ to $[(Bn\text{-}TPEN)Mn^{IV}(O)]^{2+}$ (5.0×10^{-5} M) to determine the second-order rate constant (k_{obs}) in CF_3CH_2OH-MeCN (1:1 *v*/*v*) at 273 K (see also Table 1).

followed by slower PT from $AcrHPh^{\bullet+}$ to $[(Bn\text{-}TPEN)Mn^{III}(O)]^{+}$ as compared with the case of $AcrH_2$. Thus, the rate constant of HT from AcrHPh and AcrDPh to $[(Bn\text{-}TPEN)Mn^{IV}(O)]^{2+}$ exhibits a KIE value of $k_H/k_D = 1.9$ (Figure 5). In this case, PT from $AcrDPh^{\bullet+}$ to $[(Bn\text{-}TPEN)Mn^{III}(O)]^{+}$ becomes partially a rate-determining step in competition with the back ET from $[(Bn\text{-}TPEN)Mn^{III}(O)]^{+}$ to $AcrDPh^{\bullet+}$ following endergonic ET from AcrDPh to $[(Bn\text{-}TPEN)Mn^{IV}(O)]^{2+}$.

We have previously reported that the rate constant of outer-sphere electron transfer

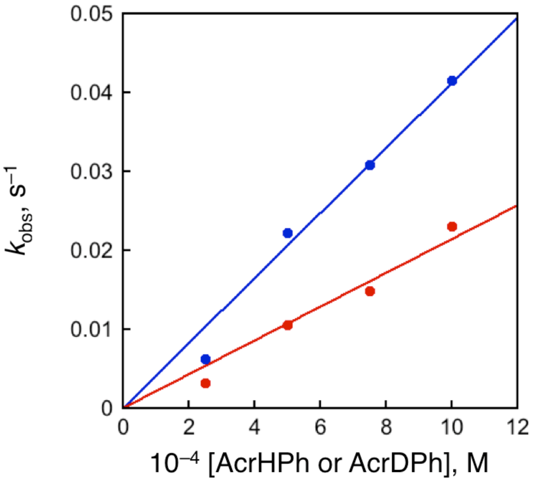

Figure 5. Plots of the pseudo-first-order constants (k_{obs}) of $[(Bn\text{-}TPEN)Mn^{IV}(O)]^{2+}$ (5.0×10^{-5} M) vs concentration of AcrHPh (blue) or AcrDPh (red) in CF_3CH_2OH-MeCN (1:1 *v*/*v*) at 273 K. The KIE value of k_H/k_D was determined to be 1.9.

from ferrocene derivatives to $[(\mathrm{Bn\text{-}TPEN})\mathrm{Mn^{IV}(O)}]^{2+}$ is well fitted by the Marcus theory of outer-sphere electron transfer[15] eq 1,

$$k_{\mathrm{et}} = Z\exp[-(\lambda/4)(1 + \Delta G_{\mathrm{et}}/\lambda)^2/k_{\mathrm{B}}T] \qquad (1)$$

where Z is the collision frequency taken as 1×10^{11} $\mathrm{M^{-1}\ s^{-1}}$, λ is the reorganization energy of ET, k_{B} is the Boltzmann constant, and T is the absolute temperature.[6,7,15] The driving force dependence of logarithm of the rate constants of outer-sphere electron transfer is shown in Figure 6 (red circles), where the log k_{et} values are plotted against the $-\Delta G_{\mathrm{et}}$ values. The driving force dependence of k_{et} is well fitted by the red line in Figure 6 using eq 1 with the λ value of 2.24 eV.[6c] The rate constants (k_{H}) of HT from AcrHR to $[(\mathrm{Bn\text{-}TPEN})\mathrm{Mn^{IV}(O)}]^{2+}$ are also plotted in Figure 6 (blue circles), where the k_{H} values are much larger than those expected from outer-sphere electron transfer (red line). Such difference in the k_{H} and k_{et} values at the same driving force results from the difference in the equilibrium constants of precursor complexes formed prior to ET (vide infra).[16]

The dependence of the pseudo-first-order rate constant (k_{f}) on concentration of $\mathrm{AcrH_2}$ at larger concentrations is shown in Figure 7a, where the k_{f} value increases with

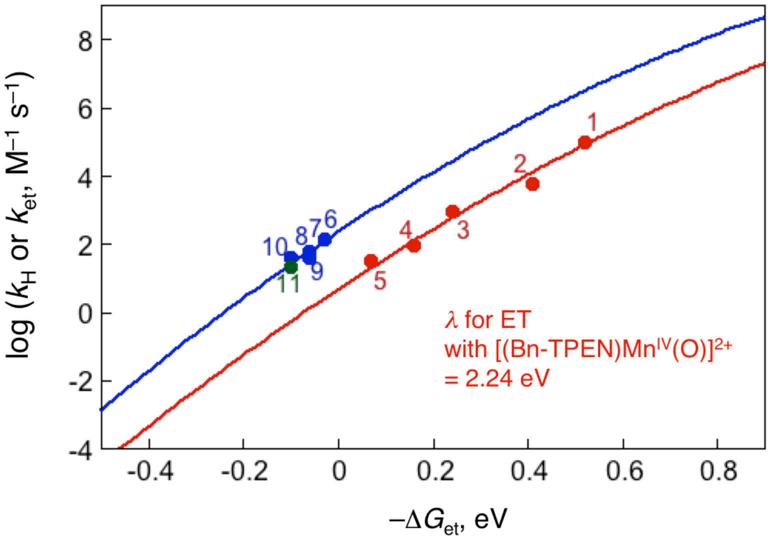

Figure 6. ET driving force ($-\Delta G_{\mathrm{et}}$) dependence of log k_{et} of ET from one electron donors (1, dimethylferrocene; 2, ferrocene; 3, bromoferrocene; 4, acetylferrocene; 5, dibromoferrocene) to $[(\mathrm{Bn\text{-}TPEN})\mathrm{Mn^{IV}(O)}]^{2+}$ (red) and the HT from NADH analogs (6, $\mathrm{AcrH_2}$; 7, $\mathrm{AcrD_2}$; 8, AcrHEt; 9, $\mathrm{AcrHCH_2Ph}$; 10, AcrHPh; 11, AcrDPh) to $[(\mathrm{Bn\text{-}TPEN})\mathrm{Mn^{IV}(O)}]^{2+}$ (blue) in $\mathrm{CF_3CH_2OH}$-MeCN (1:1 *v*/*v*) at 273 K. The red line is drawn according to eq 1 with the λ value of 2.24 eV.

increasing concentration of $AcrH_2$ to approach the constant value. Such a saturation behaviour of k_f on concentration of NADH analogs is given by eq 2, where k_{ET} is the rate constant in the precursor complex, K is the formation constant of the precursor complex, and [S] is the concentration of a substrate.[16] Eq 2 is rewritten by eq 3, which predicts a linear correlation between k_f^{-1} vs $[S]^{-1}$, which was confirmed in Figure 7b.

$$k_f = k_{ET}K[S]/(1 + K[s]) \quad (2)$$

$$k_f^{-1} = (k_{ET}K[S])^{-1} + k_{ET}^{-1} \quad (3)$$

The K value was determined from linear plot of k_f^{-1} vs $[S]^{-1}$ (Figure 7b) to be 2.1 ×

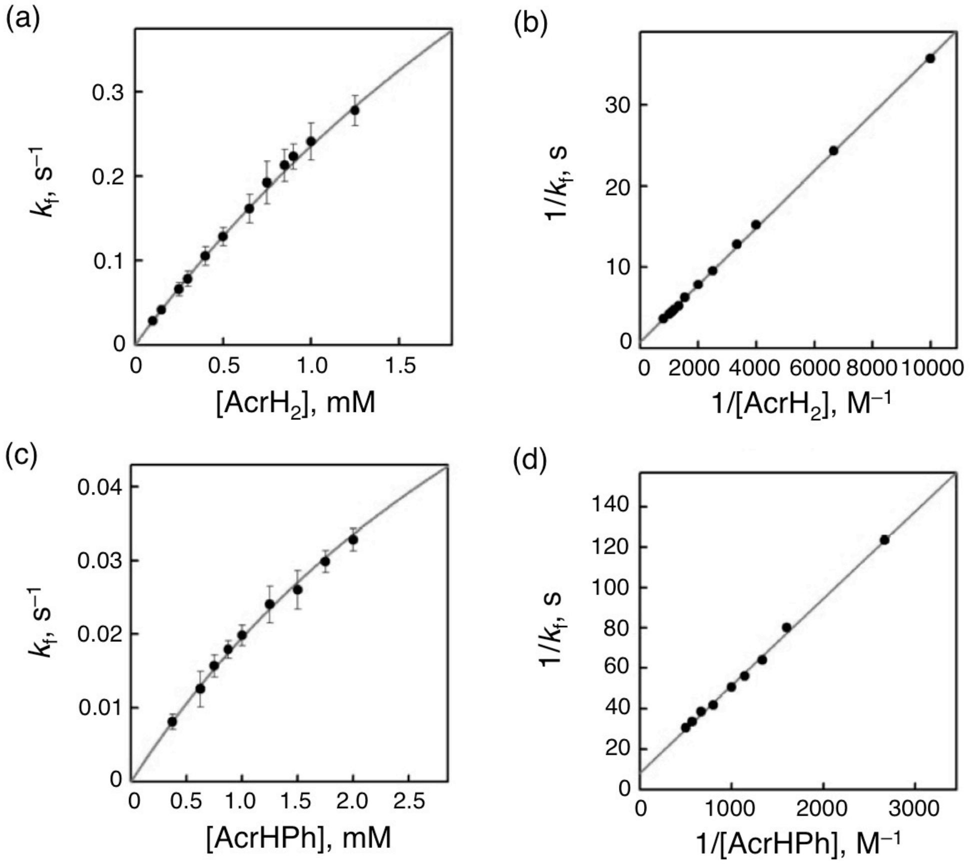

Figure 7. (a) Plot of first-order rate constant (k_f) vs concentration of $AcrH_2$ in the reaction of $[(Bn\text{-}TPEN)Mn^{IV}(O)]^{2+}$ (5.0×10^{-5} M) with $AcrH_2$ in CF_3CH_2OH-MeCN (1:1 *v*/*v*) at 273 K. (b) Plot of $1/k_f$ vs $1/[AcrH_2]$ where the values of slope and intercept were determined to be 3.5×10^{-3} M s and 0.72 s, respectively. (c) Plot of first-order rate constant (k_f) vs concentration of AcrHPh in oxidation of AcrHPh by $[(Bn\text{-}TPEN)Mn^{IV}(O)]^{2+}$ (5.0×10^{-5} M) in CF_3CH_2OH-MeCN (1:1 *v*/*v*) at 273 K. (b) Plot of $1/k_f$ vs 1/[AcrHPh] where the values of slope and intercept were determined to be 4.3×10^{-2} M s and 8.2 s, respectively.

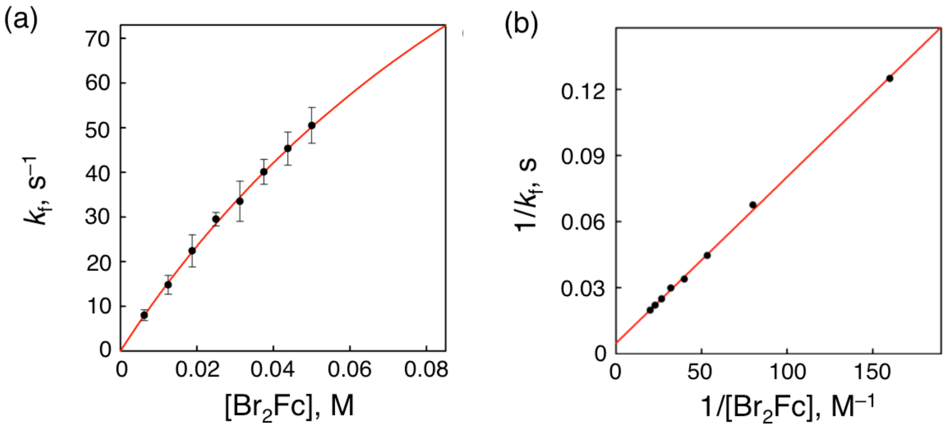

Figure 8. (a) Plot of first-order rate constant (k_f) vs concentration of Br_2Fc in oxidation of Br_2Fc by $[(Bn\text{-}TPEN)Mn^{IV}(O)]^{2+}$ (1.3×10^{-4} M) in CF_3CH_2OH-MeCN (1:1 *v*/*v*) at 273 K. (b) Plot of 1/k_f vs 1/[Br_2Fc] where the values of slope and intercept were determined to be 7.5×10^{-4} M s and 4.8×10^{-3} s, respectively.

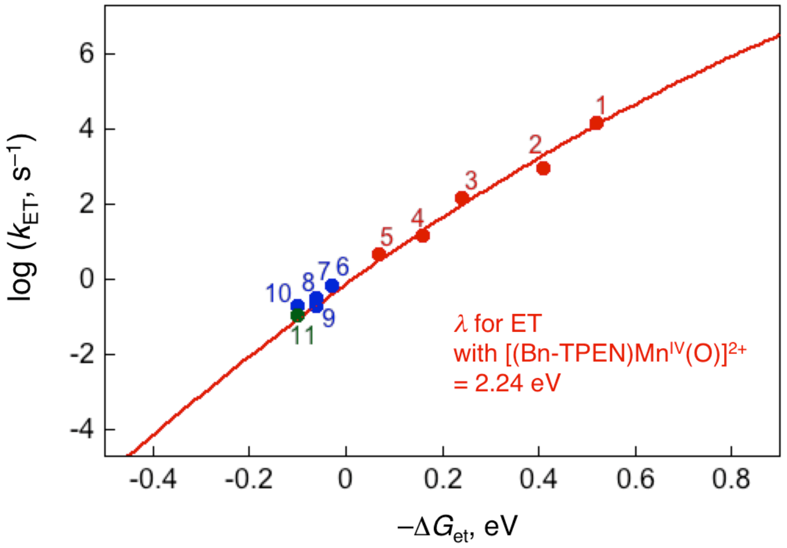

Figure 9. ET driving force ($-\Delta G_{et}$) dependence of log k_{ET} of ET from one electron donors (1, dimethylferrocene; 2, ferrocene; 3, bromoferrocene; 4, acetylferrocene; 5, dibromoferrocene) to $[(Bn\text{-}TPEN)Mn^{IV}(O)]^{2+}$ (red) and the HT from NADH analogs (6, $AcrH_2$; 7, $AcrD_2$; 8, AcrHEt; 9, $AcrHCH_2Ph$; 10, AcrHPh; 11, AcrDPh) to $[(Bn\text{-}TPEN)Mn^{IV}(O)]^{2+}$ (blue) in CF_3CH_2OH-CH_3CN (*v*/*v* = 1:1) at 273 K. The red line is the Marcus line calculated with λ value of 2.24 eV.

10^2 M^{-1}, which is much larger than that expected from outer-sphere electron transfer. The larger *K* value of the precursor complex prior to ET results in the larger k_{et} values than those expected from outer-sphere electron transfer in Figure 6.

The K values may be different depending on the E_{ox} values of NADH analogs; therefore, the k_{ET} values were evaluated as 2.0×10^2 M^{-1} by using average K values with $AcrH_2$ (2.1×10^2 M^{-1}) and AcrHPh (1.9×10^2 M^{-1}; Figure 7). The K value of the precursor complexes of $[(Bn\text{-}TPEN)Mn^{IV}(O)]^{2+}$ with Br_2Fc, which is adapted as one-electron donor, was determined to be 6.4 M^{-1} (Figure 8), indicating that the K values of NADH analogs are much larger than that of a ferrocene derivative. Figure 9 shows unified plots of log k_{ET} of ET and HT from ferrocene derivatives and NADH analogs to $[(Bn\text{-}TPEN)Mn^{IV}(O)]^{2+}$, respectively. The driving force dependence of log k_{ET} of ET in deaerated $CF_3CH_2OH\text{-}CH_3CN$ (v/v = 1:1) at 273 K is unified as a single red line using the same λ value of 2.24 eV,[6c] confirming that the HT of NADH analogs by $[(Bn\text{-}TPEN)Mn^{IV}(O)]^{2+}$ proceeds via the rate-determining ET step.

Conclusion

In summary, HT from $AcrH_2$ to $[(Bn\text{-}TPEN)Mn^{IV}(O)]^{2+}$ occurs via rate-determining ET, followed by rapid PT and ET with no KIE. In contrast, HT from $AcrH_2$ to $[(Bn\text{-}TPEN)Fe^{IV}(O)]^{2+}$ occurs via rate-determining PT from $AcrH_2^{\bullet+}$ to $[(Bn\text{-}TPEN)Fe^{III}(O)]^{+}$ in competition with back ET from $[(Bn\text{-}TPEN)Fe^{III}(O)]^{+}$ to $AcrH_2^{\bullet+}$ following endergonic ET with a large KIE value of 18.[7b] Such a change in the rate-determining step was also observed when $AcrH_2$ is replaced by AcrDPh, which exhibits KIE of 1.9 because of the higher one-electron oxidation potential of AcrDPh and slower deprotonation from $AcrDPh^{\bullet+}$ as compared with $AcrH_2^{\bullet+}$.[14] ET from $AcrH_2$ to $[(Bn\text{-}TPEN)Mn^{IV}(O)]^{2+}$ occurs via formation of a precursor complex between $AcrH_2$ and $[(Bn\text{-}TPEN)Mn^{IV}(O)]^{2+}$ with a much larger formation constant (K) in Scheme 1 as compared with outer-sphere electron transfer from ferrocene derivatives to

Scheme 1. Proposed Mechanism of HT from AcrHR to $[(Bn\text{-}TPEN)Mn^{IV}(O)]^{2+}$.

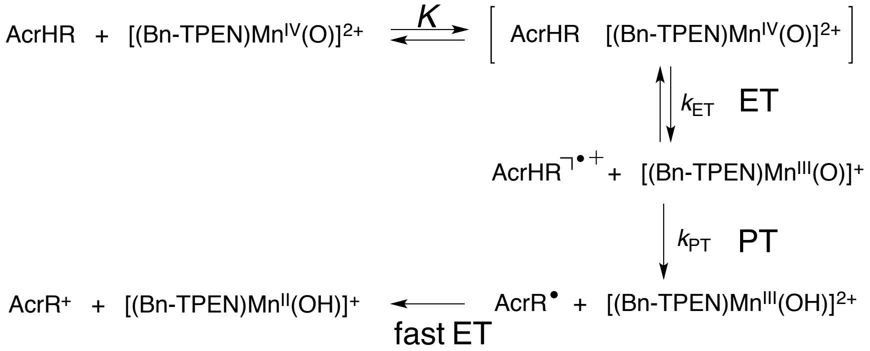

$[(\text{Bn-TPEN})\text{Mn}^{\text{IV}}(\text{O})]^{2+}$. This study has revealed the switch of the rate-determining step in HT from NADH analogs to high-valent metal-oxo complexes, depending on the one-electron redox potentials of NADH analogs and the metal-oxo complexes.

References

(1) Nam, W. *Acc. Chem. Res.*, **2007**, *40*, 465 and review articles in the special issue.

(2) Ortiz de Montellano, P. R. *Cytochrome P450: Structure, Mechanism, and Biochemistry*, 3rd ed.; Kluwer Academic/Plenum Publishers: New York, **2005**.

(3) (a) Bruijnincx, P. C. A.; van Koten, G.; Klein Gebbink, R. J. M. *Chem. Soc. Rev.* **2008**, *37*, 2716. (b) Krebs, C.; Fujimori, D. G.; Walsh, C. T.; Bollinger, J. M., Jr. *Acc. Chem. Res*. **2007**, *40*, 484.

(4) Nam, W.; Lee, Y.-M.; Fukuzumi, S. *Acc. Chem. Res*., **2014**, *47*, 1146.

(5) (a) McEvoy, J. P.; Brudvig, G. W. *Chem. Rev*. **2006**, *106*, 4455. (b) Umena, Y.; Kawakami, K.; Shen, J.-R.; Kamiya, N. *Nature* **2011**, *473*, 55.

(6) (a) Yoon, H.; Morimoto, Y.; Lee, Y.-M.; Nam, W.; Fukuzumi, S. *Chem. Commun*. **2012**, *48*, 11187. (b) Wu, X.; Seo, M. S.; Davis, K. M.; Lee, Y.-M.; Chen, J.; Cho, K.-B.; Pushkar, Y. N.; Nam, W. *J. Am. Chem. Soc.* **2011**, *133*, 20088. (c) Yoon, H.; Lee, Y.-M.; Wu, X.; Cho, K.-B.; Sarangi, R.; Nam, W.; Fukuzumi, S. *J. Am. Chem. Soc*. **2013**, *135*, 9186.

(7) (a) Lee, Y.-M.; Kotani, H.; Suenobu, T.; Nam, W.; Fukuzumi, S. *J. Am. Chem. Soc*. **2008**, *130*, 434. (b) Fukuzumi, S.; Kotani, H.; Lee, Y.-M.; Nam, W. *J. Am. Chem. Soc.*, **2008**, *130*, 15134.

(8) (a) Stout, D. M.; Meyers, A. I. *Chem. Rev.* **1982**, *82*, 223. (b) Gebicki, J.; Marcinek, A.; Zielonka, J. *Acc. Chem. Res.* **2004**, *37*, 379.

(9) (a) Pestovsky, O.; Bakac, A.; Espenson, J. H. *J. Am. Chem. Soc*., **1998**, *120*, 13422. (b) Pestovsky, O.; Bakac, A.; Espenson, J. H. *Inorg. Chem.,* **1998**, *37*, 1616. (c) Song, N.; Zhang, M.-T.; Binstead, R. A.; Fang, Z.; Meyer, T. J. *Inorg. Chem*., **2014**, *53*, 4100.

(10) (a) Carlson, B. W.; Miller, L. L. *J. Am. Chem. Soc*., **1985**, *107*, 479. (b) Miller, L. L.; Valentine, J. R. *J. Am. Chem. Soc*., **1988**, *110*, 3982. (c) Fukuzumi, S.; Koumitsu, S.; Hironaka, K.; Tanaka, T. *J. Am. Chem. Soc*., **1987**, *109*, 305.

(11) (a) Lee, I.-S.; Jeoung, E. H.; Kreevoy, M. M. *J. Am. Chem. Soc*., **1997**, *119*, 2722. (b) Liu, Z.; Deeth, R. J.; Butler, J. S.; Habtemariam, A.; Newton, M. E.; Sadler, P. J. *Angew. Chem., Int. Ed*., **2013**, 52, 4194.

(12) (a) Zhu, X.-Q.; Yang, Y.; Zhang, M.; Cheng, J.-P. *J. Am. Chem. Soc*., **2003**, *125*, 15298. (b) Zhu, X.-Q.; Cao, L.; Liu, Y.; Yang, Y.; Lu, J.-Y.; Wang, J.-S.; Cheng, J.-P. *Chem.-Eur. J.,* **2003**, *9*, 3937. (c) Zhu, X.-Q.; Zhang, J.-Y.; Cheng, J.-P. *J. Org. Chem.,* **2006**, *71*, 7007. (d) Zhu, X.-Q.; Mu, Y.-Y.; Li, X.-T. *J. Phys. Chem. B*, **2011**, *115*, 14794.

(13) (a) Afanasyeva, M. S.; Taraban, M. B.; Purtov, P. A.; Leshina, T. V.; Grissom, C. B. *J. Am. Chem. Soc.,* **2006**, *128*, 8651. (b) Yuasa, J.; Yamada, S.; Fukuzumi, S. *J. Am. Chem. Soc*., **2008**, *130*, 5808.

(14) Fukuzumi, S.; Tokuda, Y.; Kitano, T.; Okamoto, T.; Otera, J. *J. Am. Chem. Soc*., **1993**, *115*, 8960.

(15) Marcus, R. A. *Angew. Chem., Int. Ed. Engl.,* **1993**, *32*, 1111.

(16) (a) Park, J.; Lee, Y.-M.; Nam, W.; Fukuzumi, S. *J. Am. Chem. Soc*., **2013**, *135*, 5052. (b) Park, J.; Morimoto, Y.; Lee, Y.-M.; Nam, W.; Fukuzumi, S. *Inorg. Chem*., **2014**, *53*, 3618.

(17) Fukuzumi, S.; Koumitsu, S.; Hironaka, K.; Tanaka, T.; Otera, J. *J. Am. Chem. Soc*., **1987**, *109*, 305.

Chapter 3

A Mononuclear Nonheme Manganese(IV)–Oxo Complex Binding Redox-Inactive Metal Ions

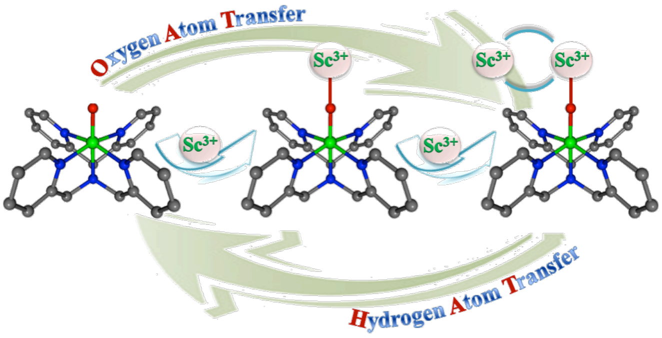

Abstract: Redox-inactive metal ions play pivotal roles in regulating reactivities of high-valent metal-oxo species in a variety of enzymatic and chemical reactions. A mononuclear nonheme manganese(IV)-oxo complex bearing a pentadentate N5 ligand has been synthesized and used in the synthesis of a manganese(IV)-oxo complex binding scandium ions. The manganese(IV)-oxo complexes are characterized with various spectroscopic methods. The reactivities of the manganese(IV)-oxo complex are markedly influenced by binding Sc^{3+} ions in oxidation reactions, such as ~2500-fold increase in the oxidation of thioanisole (i.e., oxygen atom transfer) but ~180-fold decrease in the C–H bond activation of 1,4-cyclohexadiene (i.e., hydrogen atom transfer). The present results provide the first example of a nonheme manganese(IV)-oxo complex binding redox-inactive metal ions that shows a contrasting effect of redox-inactive metal ions on the reactivities of metal-oxo species in the oxygen atom transfer and hydrogen atom transfer reactions.

Introduction

High-valent metal-oxo species have been invoked as key intermediates in the dioxygen O–O bond-cleaving and bond-forming reactions by a number of metalloenzymes, such as heme and nonheme iron oxygenases for the oxidation of organic substrates and Photosystem II (PS II) for the oxidation of water.[1-3] In

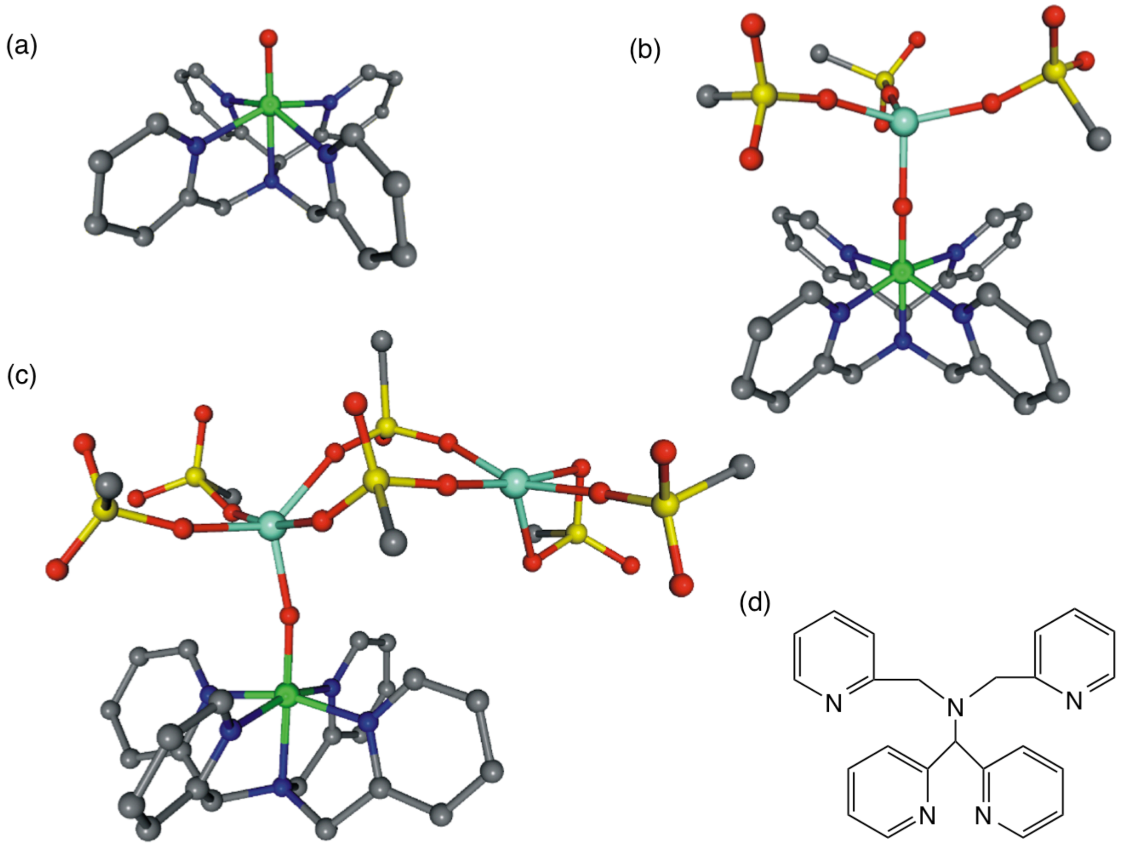

Figure 1. DFT-optimized structures of (a) $[(N4Py)Mn^{IV}(O)]^{2+}$ (**2**), (b) $[(N4Py)Mn^{IV}(O)–Sc(CF_3SO_3)_3]^{2+}$ (**3**), and (c) $[(N4Py)Mn^{IV}(O)–Sc(CF_3SO_3)_3–Sc(CF_3SO_3)_3]^{2+}$ (**4**), calculated at B3LYP/LACVP level in solvent phase. The Mn-O bond lengths of **2**, **3**, and **4** are calculated to be 1.67, 1.74 and 1.74 Å, respectively (see SI, DFT Calculations Section for computational details). Hydrogen atoms in N4Py and fluorine atoms in the counter ion ($CF_3SO_3^-$) have been omitted for clarity (Mn, green; N, blue; O, red; C, black; Sc, aquamarine; S, yellow). (d) N4Py ligand.

biomimetic studies, a number of iron-oxo and manganese-oxo complexes bearing porphyrin, corrole, corrolazine, and non-porphyrin ligands have been synthesized and characterized with various spectroscopic techniques and X-ray crystallography.[4] Their reactivities have also been investigated in a variety of oxygen atom transfer (OAT), hydrogen atom transfer (HAT), and electron-transfer (ET) reactions.[4]

Metal ions that function as Lewis acids play pivotal roles in tuning reactivities of metal-oxo complexes in a variety of chemical transformations, such as OAT and ET reactions.[5] In PS II, it is widely accepted that a redox-inactive Ca^{2+} ion acts as an essential cofactor for the oxidation of water to evolve dioxygen at the manganese-calcium (Mn_4CaO_5) active site.[6] Although the exact functional role of the

Ca^{2+} ion remains elusive, it has been proposed that the presence of a redox-inactive Ca^{2+} ion facilitates the O-O bond formation step by a presumed manganese(V)-oxo species.[7]

Recently, we have reported the first crystal structure of a nonheme iron(IV)-oxo complex binding a scandium ion (Sc^{3+}).[8] We have also shown that the reaction rates of OAT and ET by nonheme iron(IV)-oxo complexes are markedly increased upon addition of redox-inactive metal ions.[9] More recently, Goldberg and co-workers reported the influence of a redox-inactive Zn^{2+} ion on a valence tautomerization of a manganese(V)-oxo corrolazine complex and its enhanced ET and HAT reactivity.[10] As our ongoing efforts to understand the effects of redox-inactive metal ions on the reactivities of metal-oxo species, we synthesized, characterized, and investigated reactivities of a nonheme manganese(IV)-oxo complex and its Sc^{3+} ion-binding species (Figure 1). We now report the first spectroscopic evidence of binding Sc^{3+} ions by a mononuclear nonheme manganese(IV)-oxo complex and the contrasting effect of metal ions in OAT and HAT reactions by the Sc^{3+} ion-binding manganese(IV)-oxo complex.

Experimental Section

Materials. Commercially available chemicals were used without further purification unless otherwise indicated. Solvents were dried according to published procedures and distilled under Ar prior to use.[19] Scandium triflate, $Sc(OTf)_3$ (OTf = $CF_3SO_3^-$), was purchased from Aldrich and used as received. $H_2{}^{18}O$ (95% ^{18}O-enriched) was purchased from ICON Services Inc. (Summit, NJ, USA). Iodosylbenzene (PhIO), N4Py ligand (N4Py = *N*,*N*-bis(2-pyridylmethyl)-*N*-bis(2-pyridyl)methylamine), and $Mn^{II}(OTf)_2 \cdot 2CH_3CN$ were prepared by literature methods.[20] The preparation of $Mn^{II}(N4Py)(CF_3SO_3)_2$ (**1**) was carried out in a glove box. N4Py (0.54 mmol, 0.20 g) and $Mn^{II}(OTf)_2 \cdot 2CH_3CN$ (0.82 mmol, 0.32 g) were dissolved in CH_3CN, and the reaction solution was stirred at ambient temperature overnight. The resulting solution was filtered and added to a large volume of Et_2O. The product was obtained as a white solid with 60% yield (0.24 g). Colorless plate crystals suitable for X-ray analysis were obtained by diffusion of dry Et_2O into a saturated CH_3CN solution of **1**. Anal. Calcd. for $C_{25}H_{21}F_6MnN_5O_6S_2$: C, 41.67; H, 2.94; N, 9.72. Found: C, 41.86; H, 2.98; N, 9.84 %.

Instrumentation. UV-vis spectra were recorded on a Hewlett Packard 8453 diode array spectrophotometer equipped with a UNISOKU Scientific Instruments Cryostat

USP-203A for low-temperature experiments or on a Hi-Tech Scientific (U.K.) SF-61 DX2 cryogenic stopped-flow spectrophotometer equipped with a Xe arc lamp and a KinetaScan diode array rapid scanning unit. Electrospray ionization mass spectra (ESI MS) were collected on a Thermo Finnigan (San Jose, CA, USA) LCQ^{TM} Advantage MAX quadrupole ion trap instrument, by infusing samples directly into the source using a manual method. The spray voltage was set at 3.7 kV and the capillary temperature at 150 °C. X-band EPR spectra were recorded at 5 K using X-band Bruker EMX-plus spectrometer equipped with a dual mode cavity (ER 4116DM). Low temperature was achieved and controlled with an Oxford Instruments ESR900 liquid He quartz cryostat with an Oxford Instruments ITC503 temperature and gas flow controller. The experimental parameters for EPR measurement were as follows: Microwave frequency = 9.646 GHz, microwave power = 1.0 mW, modulation amplitude = 10 G, gain = 1×10^3, modulation frequency = 100 kHz, time constant = 40.96 ms, and conversion time = 81.00 ms. ^{1}H NMR spectra were measured with a Bruker model digital AVANCE III 400 FT-NMR spectrometer.

X-ray structural analysis. Single crystals of **1** suitable for X-ray analysis were obtained by slow diffusion of Et_2O into a saturated CH_3CN solution of **1**. These crystals were taken from the solution by a nylon loop (Hampton Research Co.) on a hand made cooper plate and mounted on a goniometer head in a N_2 cryostream. The diffraction data for **1** were collected at 170 K on a Bruker SMART AXS diffractometer equipped with a monochromator in the Mo $K\alpha$ (λ = 0.71073 Å) incident beam. The CCD data were integrated and scaled using the Bruker-SAINT software package, and the structure was solved and refined using SHEXTL V 6.12.[21] Hydrogen atoms were located in the calculated positions. The crystallographic data and selected bond distances and angles for **1** are listed in Tables S1 and S2, respectively. CCDC 914701 contains the supplementary crystallographic data for this paper. These data can be obtained free of charge via www.ccdc.cam.ac.uk/data_request/cif (or from the Cambridge Crystallographic Data Center, 12, Union Road, Cambridge CB2 1EZ, UK; fax: (+44) 1223-336-033; or deposit@ccdc.cam.ac.uk).

XAS and EXAFS measurements. X-ray absorption spectra were collected at the Advanced Photon Source (APS) at Argonne National Laboratory on bending magnet beamline 20 at electron energy 6 keV and average current of 100 mA. The radiation was monochromatized by a Si(110) crystal monochromator. The intensity of the x-rays was monitored by three ion chambers (I_0, I_1, and I_2) filled with 20% nitrogen and 80% helium and placed before the sample (I_0) and after the sample (I_1 and I_2). $KMnO_4$ powder was placed between the I_1 and I_2 and its absorption was recorded with each scan for energy calibration. Plastic (Lexan) EXAFS sample holders (inner dimensions of 12 mm × 2 mm × 3 mm) filled with frozen solutions were inserted into a cryostat pre-cooled to 20 K. The samples were kept at 20 K in an He atmosphere at ambient pressure. Data were recorded as fluorescence excitation spectra using a 13-element energy-resolving detector. In order to reduce the risk of sample damage by x-radiation, 80% flux was used in the defocused mode (beam size 1 × 2 mm) and no damage was observed during first five scans used in data analysis. The samples were in addition protected from the X-ray beam during the spectrometer movements by a shutter synchronized with the scan program. Mn XAS energy was calibrated by the maximum of the pre-edge feature of the potassium permanganate powder XANES spectrum (6543.3 eV), which was placed between I_1 and I_2 ionization chambers. EXAFS scans with 5 eV steps in the pre-edge region (6437.67 – 6529.67 eV), 0.5 eV steps (6529.67 – 6637.67 eV) through the edge and 0.05 $Å^{-1}$ steps from k = 2.0 – 12 $Å^{-1}$ were used.

EXAFS data analysis. Athena software was used for data processing.[22] Energy scale for each scan was normalized using potassium permanganate powder standard and scans for same samples were added. Data in energy space were pre-edge corrected, normalized, and background corrected. The processed data were next converted to the photoelectron wave vector (k) space and weighted by k^3. The electron wave number is defined as $k = \left[2m(E - E_0)/\hbar^2\right]^{1/2}$, E_0 is the energy origin or the threshold energy. K-space data were truncated near the zero crossings (k = 3.381 – 11.362 $Å^{-1}$) before Fourier transformation in R space. The k-space data were transferred into the Artemis Software for curve fitting. In order to fit the data, the Fourier peaks were isolated separately, or entire experimental spectrum was fitted. The individual Fourier peaks were isolated by applying a Hanning window to the first and last 15 % of the chosen range, leaving the middle 70 % untouched. Curve fitting was performed using *ab initio*-calculated phases and amplitudes from the FEFF8 program from the University of Washington.

Ab initio-calculated phases and amplitudes were used in the EXAFS equation:[23]

$$\chi(k) = S_0^2 \sum_j \frac{N_j}{kR_j^2} f_{eff_j}(\pi, k, R_j) e^{-2\sigma_j^2 k^2} e^{\frac{-2R_j}{\lambda_j(k)}} \sin(2kR_j + \phi_{ij}(k)) \qquad (1)$$

where NN_j is the number of atoms in the j^{th} shell; R_j the mean distance between the absorbing atom and the atoms in the j^{th} shell; *feffj* (π□,*k*, *Rj*) is the *ab initio* amplitude function for shell *j*, and the Debye-Waller term $e^{-2\sigma_j^2 k^2}$ accounts for damping due to static and thermal disorder in absorber-backscatterer distances. The mean free path term $e^{\frac{-2R_j}{\lambda_j(k)}}$ reflects losses due to inelastic scattering, where $\lambda_j(k)$, is the electron mean free path. The oscillations in the EXAFS spectrum are reflected in the sinusoidal term $\sin(2kR_j + \phi_{ij}(k))$, where $\phi_{ij}(k)$ is the *ab initio* phase function for shell *j*. This sinusoidal term shows the direct relation between the frequency of the EXAFS oscillations in k-space and the absorber-backscatterer distance. S_0^2 is an amplitude reduction factor representing central atom shake-up and shake-off effects. The mean free path of the electron (λ) is due to the finite core hole lifetime and interactions with the valence electrons.

The EXAFS equation (Eq 1) was used to fit the experimental data using N, S_o^2, E_0, R, and σ^2 as variable parameters (See fit results in Tables S3). N refers to the number of coordination atoms surrounding Mn in each shell. The quality of fit was evaluated by R-factor, and the reduced Chi-Square value. R-factor is used to denote closeness of fit. An R-factor less than 2% denotes that the fit is good enough whereas R-factor between 2% and 5% denotes that the fit is correct within a consistently broad model.[24] The reduced Chi Square value is used to compare fits as more absorber-backscatter shells are included to fit the data. Reduced chi-square value justifies the inclusion of additional shell.

Spin state measurements. The effective magnetic moments (μ_{eff}, BM) of the Mn$^{\text{II}}$ complex (**1**) and its Mn$^{\text{IV}}$(O) intermediates (**2**, **3**, and **4**) were determined using the modified ^{1}H NMR method of Evans at room temperature and 253 K, respectively.[25] A WILMAD® coaxial insert (sealed capillary) tube containing the blank trifluoroethanol-d_3 solvent only was inserted into the normal NMR tube containing the complexes (2.0 mM) dissolved in trifluoroethanol-d_3. The chemical shift of the solvent peak in the presence of the paramagnetic metal complexes was compared to that of the solvent peak in the inner coaxial insert tube. The magnetic moment was calculated using the following equation,

$$\mu = 0.0618(\Delta v T/2fM)^{1/2}$$

where f is the oscillator frequency (MHz) of the superconducting spectrometer, T is the absolute temperature, M is the molar concentration of the metal ion, and Δv is the difference in frequency (Hz) between the two reference signals.[25] The magnetic moments of 4.3, 4.2, and 4.3 μ_B for **2**, **3**, and **4**, respectively, indicate that these intermediates possess $S = 3/2$ spin state in CF_3CD_2OD solution, whereas that of 6.2 μ_B for **1** indicates that the Mn^{II} complex possesses $S = 5/2$ spin state in CF_3CD_2OD solution.

Electrochemical measurements. Electrochemical measurements were performed on a CH Instrument (CHI630B) electrochemical analyzer in deaerated CF_3CH_2OH-CH_3CN (*v/v* 19:1) containing 0.10 M (n-hexyl)$_4$NPF$_6$ as a supporting electrolyte. A conventional three-electrode cell was used with a platinum working electrode (surface area of 0.3 cm^2) and a platinum wire as a counter electrode. The platinum working electrodes (BAS) were routinely polished with BAS polishing alumina suspension and rinsed with CH_3CN prior to use. The measured potentials were recorded as a function of Ag/AgNO$_3$ (0.010 M) reference electrode. All potentials (vs Ag/Ag$^+$) were converted to the values vs SCE by adding 0.29 V.[26] All electrochemical measurements were performed under Ar atmosphere.

Generation and kinetic studies of manganese(IV)-oxo intermediates. Reactions were run at least in triplicate, and the data reported represent the average of these reactions. The nonheme manganese(IV)-oxo complex, $[Mn^{IV}(O)(N4Py)]^{2+}$ (**2**), was prepared by reacting $Mn^{II}(N4Py)(OTf)_2$ (**1**-CF_3SO_3, 1.0 mM) with 4 equiv of PhIO in CF_3CH_2OH at 298 K. The Sc^{3+} ion-binding manganese(IV)-oxo complexes, $[Mn^{IV}(O)(N4Py)]^{2+}$–Sc^{3+} (**3**) and $[Mn^{IV}(O)(N4Py)]^{2+}$–$2Sc^{3+}$ (**4**), were prepared by adding 1.0 and 6.0 equiv of Sc^{3+} ions to the solution of **2** in CH_3CN at 298 K, respectively. Subsequently, appropriate amounts of substrates (e.g. *para*-X-substituted thioanisoles and 1,4-cyclohexadine) were added to a reaction solution of **2**, **3** or **4**, respectively, in CF_3CH_2OH-CH_3CN (*v/v* 19:1) at 273 K for sulfoxidation and 298 K for C-H activation reactions. All reactions were monitored by the decay of absorption bands at 940 nm for **2**, 680 nm for **3**, and 635 nm for **4**. Pseudo-first-order fitting of the kinetic data allowed us to determine k_{obs} (s^{-1}) values. For the single-mixing experiments by a stopped-flow spectrophotometer for the reactions of **3** and **4** with *para*-X-substituted thioanisoles, a syringe was charged with **3** or **4**, and then a second syringe was charged with substrates in CF_3CH_2OH-CH_3CN (*v/v* 19:1). The solutions were loaded into the stopped-flow spectrophotometer and triggered by simultaneous injection of 120 μL of each syringe. The final concentrations of intermediate, substrates, and Sc^{3+} were 1.0, 10 – 80, and 6.0 mM, respectively. All reaction traces were collected at 635 nm due to **4** and 680 nm due to **3**, using a 1.0 cm optical path length at 273 K. The raw kinetic data were treated with KinetAsyst 3 (Hi-Tech Scientific) and Specfit/32 Global Analysis System software from Spectrum Software Associates.

Results and Discussion

The starting manganese complex, $[Mn^{II}(N4Py)(CF_3SO_3)]^+$ (**1**) [N4Py = *N*,*N*–bis(2–pyridylmethyl)–*N*–bis(2–pyridyl)-methylamine, Figure 1d], was synthesized and characterized with electrospray ionization mass spectrometry (ESI MS), electron paramagnetic resonance (EPR) spectroscopy, and X-ray crystallography (See the experimental section, Figure S1 and Figure 2, and Tables S1 and S2). Addition of 4 equiv iodosylbenzene (PhIO) to a solution of **1** (1 mM) in CF_3CH_2OH at 298 K afforded a greenish yellow complex **2** with an absorption band at 940 nm (ε ~250 M^{-1} cm^{-1}) (Figure 3). The metastable intermediate ($t_{1/2}$ ~2 h at 298 K) was characterized with various spectroscopic techniques. The X-band EPR spectrum of **2** shows signals that are characteristic of S = 3/2 Mn^{IV} (Figure 4),[11] and the spin state of S = 3/2 for **2** was confirmed using the modified NMR method of Evans (SI, Experimental Section).[12] The ESI MS of **2** exhibits a prominent ion peak at *m/z* 587.0 (SI, Figure S4), whose mass and isotope distribution patterns correspond to $[(N4Py)Mn^{IV}(O)(CF_3SO_3)]^+$ (calculated *m/z* 587.1). Upon introduction of ^{18}O into **2** using $PhI^{18}O$, a mass shift from *m/z* 587.0 to 589.0 was observed (Figure 5), indicating that **2** contains an oxygen atom.

Comparison of X-ray absorption near edge structure (XANES) at the Mn K-edge for compounds **1** and **2** shows a large high energy shift confirming the Mn^{IV} oxidation state in **2** (Figure 6a).[11] Extended X-ray absorption fine structure (EXAFS) shows that the first peak corresponding to Mn–O,N interactions in the first coordination sphere is shifted to a shorter apparent distance in **2** as compared to **1**. This change can be

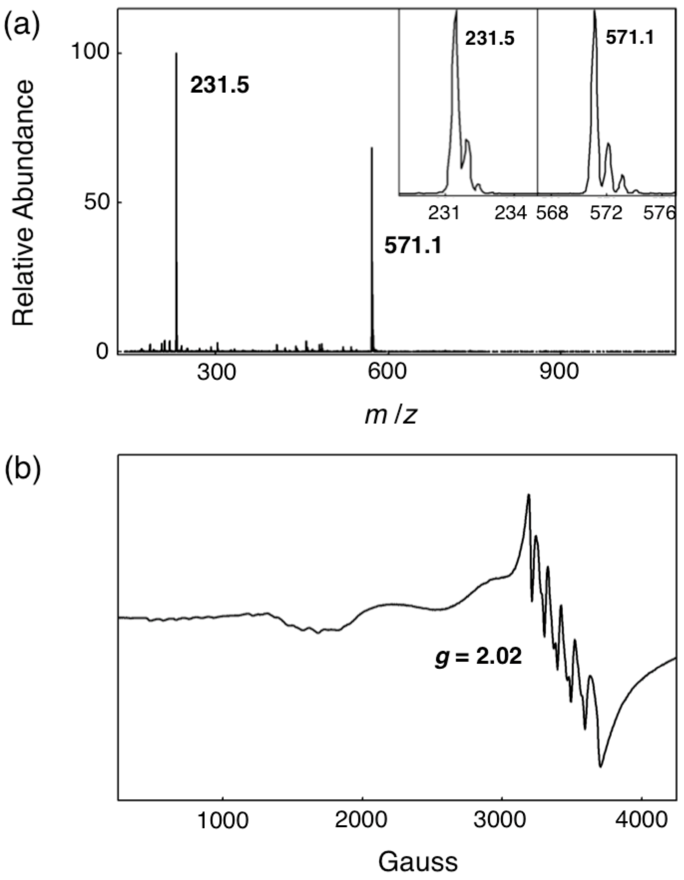

Figure 2. (a) ESI MS spectrum of $[Mn^{II}(N4Py)(CF_3SO_3)](CF_3SO_3)$ (**1**-CF_3SO_3) in CF_3CH_2OH. Peaks at *m*/*z* = 231.5 and 571.1 correspond to $[Mn^{II}(N4Py)(CH_3CN)]^{2+}$ (*calcd. m*/*z* = 231.5) and $[Mn^{II}(N4Py)(CF_3SO_3)]^{+}$ (*calcd. m*/*z* = 571.1), respectively. Insets show the observed isotope distribution patterns for $[Mn^{II}(N4Py)(CH_3CN)]^{2+}$ (left panel) and $[Mn^{II}(N4Py)(CF_3SO_3)]^{+}$ (right panel). (b) X-band CW-EPR spectrum of **1**-CF_3SO_3 recorded in CF_3CH_2OH at 5 K.

rationalized as shortening of the Mn–O,N bond distances in **2**, and fits to the EXAFS data indeed indicate the presence of a 1.70 Å Mn=O interaction as well as shortening of the Mn–N distance (SI, Table S3; also see the 1.67 Å Mn–O distance obtained from DFT calculations in Figure 1a).[11,13] Based on the spectroscopic characterization presented above, **2** is assigned as a mononuclear manganese(IV)-oxo complex, $[(N4Py)Mn^{IV}(O)]^{2+}$ (**2**) (Figure 1a).

Addition of Sc^{3+} ions to the solution of **2** resulted in a stepwise change in the absorption spectrum of **2** (Figure 3; SI, Figure S2a). The absorption band at 940 nm due to **2** changed to a new absorption band at 680 nm with a well-defined isosbestic point at

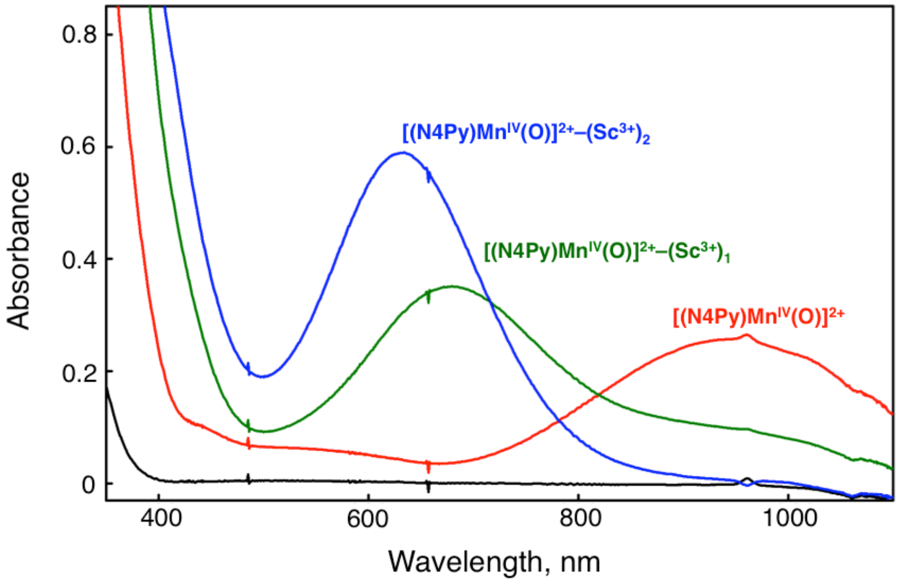

Figure 3. UV-vis spectra of $[Mn^{II}(N4Py)]^{2+}$ (**1**, black line; 1.0 mM), $[Mn^{IV}(O)(N4Py)]^{2+}$ (**2**, red line; addition of 4 equiv PhIO to **1**), $[(N4Py)Mn^{IV}(O)]^{2+}–Sc^{3+}$ (**3**, green line; addition of 1 equiv Sc^{3+} to **2**), and $[(N4Py)Mn^{IV}(O)]^{2+}–2Sc^{3+}$ (**4**, blue line; addition of 5 equiv Sc^{3+} to **3**) in CF_3CH_2OH at 298 K.

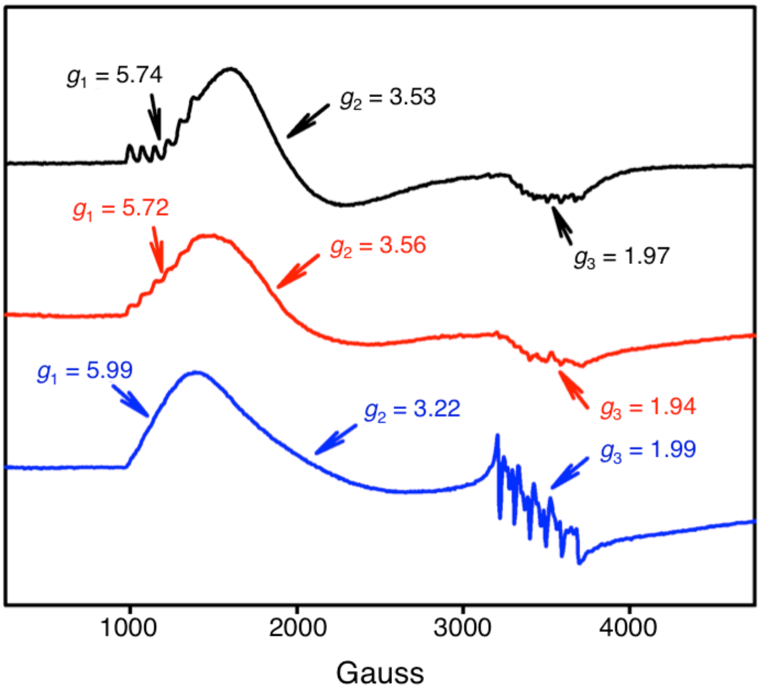

Figure 4. X-band CW-EPR spectra of $[(N4Py)Mn^{IV}(O)]^{2+}$ (**2**) (2.0 mM, black line), $[Mn^{IV}(O)(N4Py)]^{2+}–Sc^{3+}$ (**3**) (2.0 mM, red line), and $[(N4Py)Mn^{IV}(O)]^{2+}–2Sc^{3+}$ (**4**) (2.0 mM, blue line) in CF_3CH_2OH-CH_3CN (*v/v* 19:1) at 5 K.

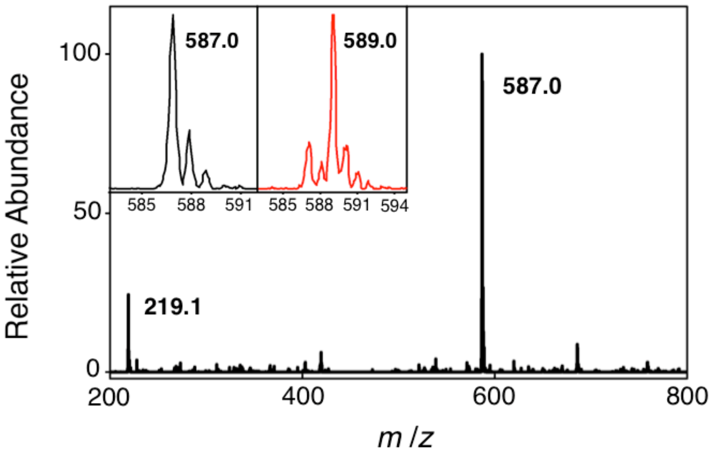

Figure 5. ESI MS spectrum of $[Mn^{IV}(O)(N4Py)]^{2+}$ (**2**) in CF_3CH_2OH. Peaks at m/z = 219.1 and 587.0 correspond to $[(N4Py)Mn^{IV}(O)]^{2+}$ (*calcd.* m/z = 219.1) and $[(N4Py)Mn^{IV}(O)(CF_3SO_3)]^+$ (*calcd.* m/z = 587.1), respectively. Insets show the observed isotope distribution patterns for **2**–^{16}O (left panel, prepared with $PhI^{16}O$) and **2**–^{18}O (right panel, prepared with $PhI^{18}O$).

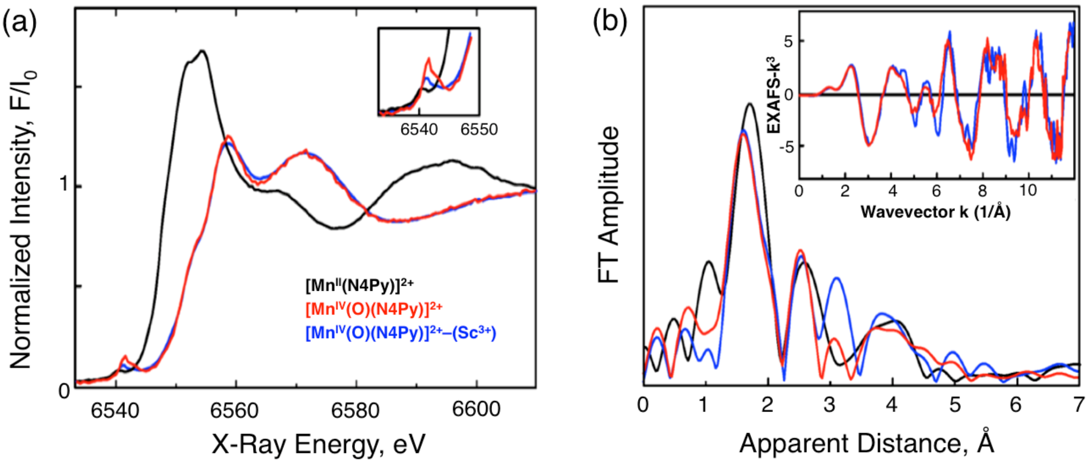

Figure 6. (a) Normalized Mn K-edge XANES of **1** (black), **2** (red), and **4** (blue). Inset shows magnified pre-edge features. (b) Overlay of the Fourier transforms (k = 3.5 – 11.3 Å^{-1}) of **1** (black), **2** (red), and **4** (blue). Inset shows k-space data of **2** and **4** (Fits are in SI, Table S3 and Figure S3).

817 nm by adding up to 1 equiv of Sc^{3+} ion (Figure 3; SI, Figure S2b). Further addition of Sc^{3+} ions (up to ~5 equiv of Sc^{3+}) to the resulting solution changed the absorption band from 680 nm to 635 nm (Figure 2; SI, Figure S2b). Such spectral changes of **2** upon addition of Sc^{3+} ions suggest that one Sc^{3+} ion binds to **2** to produce a manganese(IV)-oxo complex binding one Sc^{3+} ion (**3**), followed by the binding of the second Sc^{3+} to **3** to yield a manganese(IV)-oxo complex with two Sc^{3+} ions (**4**) (eqs 1

and 2). The equilibrium constant of K_2 for the second Sc^{3+} ion binding to **3** to give **4** was determined to be 6.1×10^3 M^{-1} from the titration experiment (SI, Figure S2b), although the binding constant of K_1 for the first Sc^{3+} ion binding to **2** was too large to be determined accurately ($K_1 >> 10^4$ M^{-1}).

$$[(\mathrm{N4Py})\mathrm{Mn}^{\mathrm{IV}}(\mathrm{O})]^{2+} + \mathrm{Sc}^{3+} \overset{K_1}{\rightleftharpoons} [(\mathrm{N4Py})\mathrm{Mn}^{\mathrm{IV}}(\mathrm{O})]^{2+}\text{–}\mathrm{Sc}^{3+} \tag{1}$$

$$[(\mathrm{N4Py})\mathrm{Mn}^{\mathrm{IV}}(\mathrm{O})]^{2+}\text{–}\mathrm{Sc}^{3+} + \mathrm{Sc}^{3+} \overset{K_2}{\rightleftharpoons} [(\mathrm{N4Py})\mathrm{Mn}^{\mathrm{IV}}(\mathrm{O})]^{2+}\text{–}2\mathrm{Sc}^{3+} \tag{2}$$

The highly stable intermediates **3** ($t_{1/2}$ ~12 h at 298 K) and **4** ($t_{1/2}$ ~1 day at 298 K) were characterized with various spectroscopic techniques. The EPR spectra of **3** and **4** (Figure 4), along with the modified NMR method of Evans (Experimental Section),[12] indicate the spin state of $S = 3/2$ Mn^{IV}.[11] The ESI MS of **3** exhibits ion peaks at *m/z* 1028.9 and 1078.9, which shift to 1030.9 and 1080.9 upon using $PhI^{18}O$ (Figure 7), suggesting that **3** contains one oxygen atom and binds one Sc^{3+} ion (Figure 1b). The ESI MS of **4** exhibits ion peaks at *m/z* 1028.9, 1078.9, 1520.6, and 1570.5 (Figure 8); the latter two peaks correspond to $[(N4Py)Mn^{IV}(O)]^{2+}$ with two Sc^{3+} ions. Upon introduction of ^{18}O into **4** using $PhI^{18}O$, two mass units shift in the ion peaks was observed (Figure 8b), supporting that **4** contains one oxygen atom (Figure 1c).

4 was further characterized with XANES/EXAFS. The binding of Sc^{3+} with the formation of compound **4** does not change the position of the Mn K-edge (Figure 6a), confirming an unchanged Mn^{IV} oxidation state, as shown in the EPR results (Figure 4). However, the pre-edge intensity is slightly lower in **4** as compared to **2** (see Figure 6a inset), indicating differences in the electronic structure due to Sc^{3+} binding. Because 1s to 3d transitions are dipole forbidden, pre-edge intensity mostly arises from quadrupole transitions and transitions to orbitals with mixed Mn 3d and ligand 2p characters. From the decreased pre-edge intensity in **4**, one can suggest that Sc^{3+} binding decreases the mixing of Mn 3d and O 2p orbitals. EXAFS analysis (Table S3) did not show elongation of the Mn–O distance in **4** and changes in the pre-edge. This is likely due to a small distance change that is within the resolution of our measurements. EXAFS in

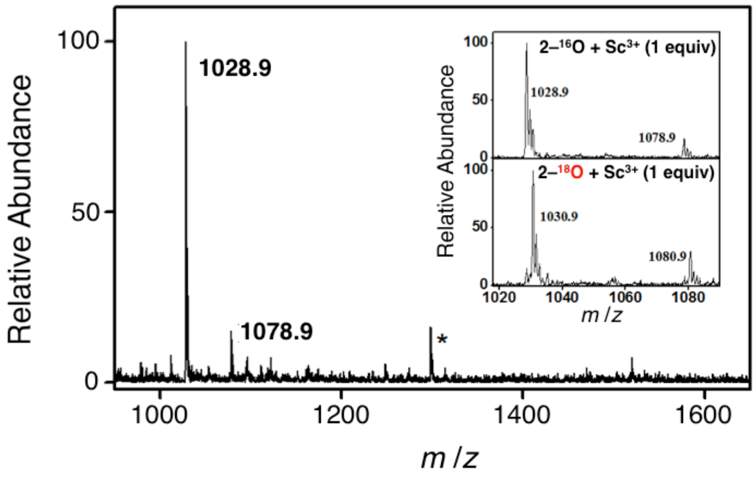

Figure 7. ESI MS spectrum of a solution containing $[Mn^{IV}(O)(N4Py)]^{2+}$ (1.0 mM) and $Sc(CF_3SO_3)_3$ (1.0 mM) in CF_3CH_2OH-CH_3CN (*v/v* 19:1) at 298 K. The mass and isotope distribution patterns of prominent ion peaks at *m/z* = 1028.9 and 1078.9 correspond to $[Mn^{IV}(O)(N4Py)(Sc^{III})(CF_3SO_3)(CF_3CH_2O)_3(CF_3CH_2OH)]^+$ (*calcd. m/z* = 1029.0) and $[Mn^{IV}(O)(N4Py)(Sc^{III})(CF_3SO_3)_2(CF_3CH_2O)_2(CF_3CH_2OH)]^+$ (*calcd. m/z* = 1079.0), respectively. The peak marked with * is not assigned. Insets show the observed isotope distribution patterns for samples prepared with $[Mn^{IV}(^{16}O)(N4Py)]^{2+}$ (**2**–^{16}O) plus Sc^{3+} (1 equiv) (upper panel) and $[Mn^{IV}(^{18}O)(N4Py)]^{2+}$ (**2**–^{18}O) plus Sc^{3+} (1 equiv) (lower panel). **2**–^{16}O (1.0 mM) and **2**-^{18}O (1.0 mM) were prepared by reacting **1** (1.0 mM) with $PhI^{16}O$ (4.0 mM) and $PhI^{18}O$ (4.0 mM), respectively.

Figure 6b show the presence of an additional peak in **4**. This peak was assigned to a Mn–Sc distance at 3.5 Å, as was confirmed by fits in Table S3. EXAFS fit quality is better for the model with one Mn–Sc interaction. DFT calculations support a similar geometry around the Mn center in **3** and **4**, suggesting one direct Mn–Sc interaction. As shown in the DFT-optimized structures (Figures 1b and 1c), there is one direct binding between the Sc^{3+} ion and the Mn–O moiety in **3** and **4**.[14] In addition, the Mn–Sc distances in **3** and **4** were calculated to be 3.65 and 3.66 Å, respectively, which are in good agreement with the EXAFS result (vide supra). Based on the spectroscopic characterization discussed above, **3** is proposed to have one direct binding of Sc^{3+} ion by the $[(N4Py)Mn^{IV}(O)]^{2+}$ complex (Figure 1b), whereas **4** contains two Sc^{3+} ions, such as one Sc^{3+} ion binding directly to the manganese-oxo moiety and the second Sc^{3+} ion being in the secondary coordination sphere (Figure 1c).[14]

We then compared the reactivities of **2**, **3**, and **4** in OAT and HAT reactions. The reactivities of the manganese(IV)-oxo complexes were first investigated kinetically in OAT, such as the oxidation of thioanisole. Upon addition of thioanisole to the solutions

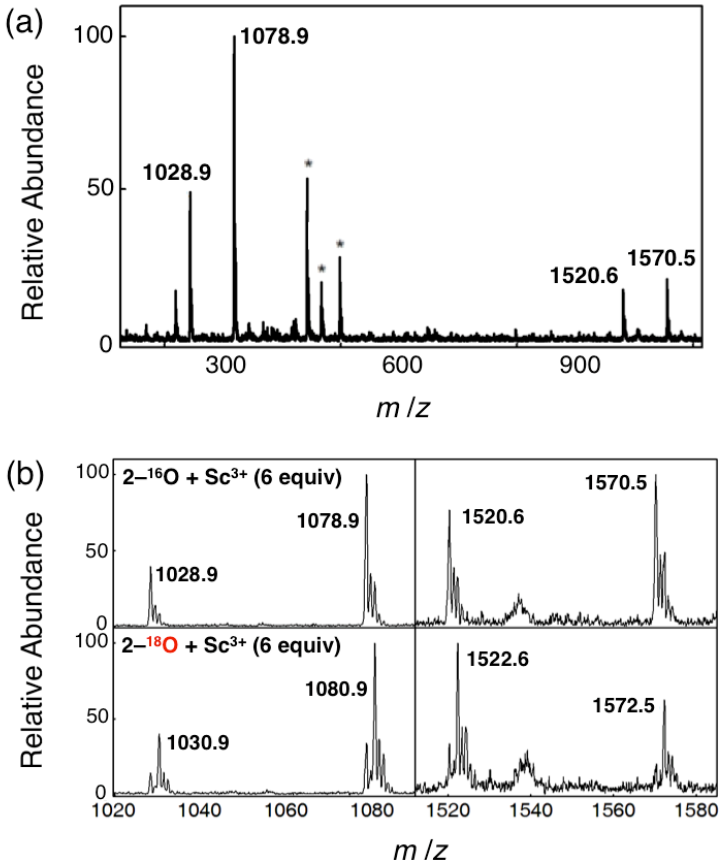

Figure 8. ESI MS spectrum of a solution containing $[Mn^{IV}(O)(N4Py)]^{2+}$ (1.0 mM) and $Sc(CF_3SO_3)_3$ (1.0 mM) in CF_3CH_2OH-CH_3CN (*v/v* 19:1) at 298 K. The mass and isotope distribution patterns of prominent ion peaks at *m/z* = 1028.9 and 1078.9 correspond to $[Mn^{IV}(O)(N4Py)(Sc^{III})(CF_3SO_3)(CF_3CH_2O)_3(CF_3CH_2OH)]^+$ (*calcd. m/z* = 1029.0) and $[Mn^{IV}(O)(N4Py)(Sc^{III})(CF_3SO_3)_2(CF_3CH_2O)_2(CF_3CH_2OH)]^+$ (*calcd. m/z* = 1079.0), respectively. The peak marked with * is not assigned. Insets show the observed isotope distribution patterns for samples prepared with $[Mn^{IV}(^{16}O)(N4Py)]^{2+}$ (**2**–^{16}O) plus Sc^{3+} (1 equiv) (upper panel) and $[Mn^{IV}(^{18}O)(N4Py)]^{2+}$ (**2**–^{18}O) plus Sc^{3+} (1 equiv) (lower panel). **2**–^{16}O (1.0 mM) and **2**-^{18}O (1.0 mM) were prepared by reacting **1** (1.0 mM) with PhI^{16}O (4.0 mM) and PhI^{18}O (4.0 mM), respectively.

of **2**, **3**, and **4**, the intermediates reverted back to the starting Mn^{II} complex with the reactivity showing that **4** is much more reactive than **2** (Figure 9; Figures 11 and 12 for EPR and ESI MS, respectively, for the Mn(II) product formation).[15] The conversion of manganese(IV)-oxo to Mn(II) species indicates that the oxidation of sulfide by the manganese(IV)-oxo complexes occurs via a two-electron oxidation process.[11] Product analysis of the reaction solutions revealed the formation of methyl phenyl sulfoxide in a quantitative yield. The second-order rate constants determined in the reactions of **2** and **4** were 9.2×10^{-3} and 2.0×10 M^{-1} s^{-1} at 273 K, respectively (Figure 13),[15]

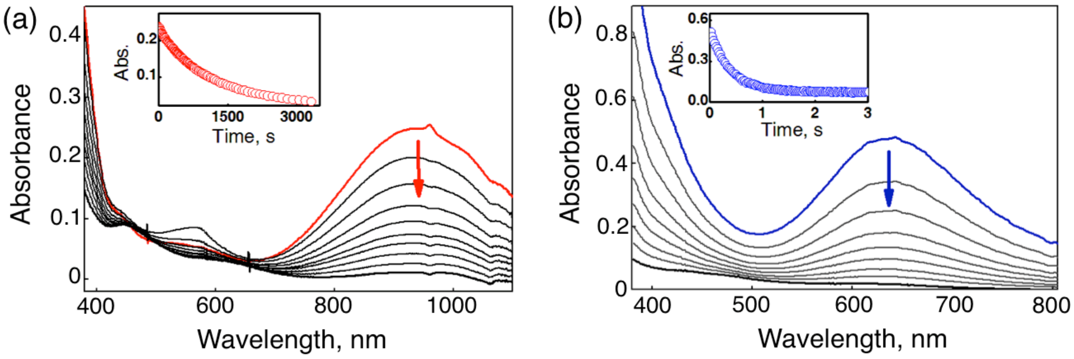

Figure 9. UV-vis spectral changes of (a) **2** (1.0 mM) and (b) **4** (1.0 mM) upon addition of thioanisole (0.10 M) at 273 K. Insets show the time trace monitored at 940 nm for **2** (a) and at 635 nm for **4** (b).

demonstrating that the reactivity of the manganese(IV)-oxo complex in the OAT reaction is markedly enhanced upon binding Sc^{3+} ions (i.e., ~2200-fold increase in reactivity). The high reactivity of the manganese(IV)-oxo species binding Sc^{3+} ions was also observed in the reactions of *para*-substituted thioanisoles, and the ρ values of –4.6 and –5.6 were obtained in the reactions of **2** and **4**, respectively (Table 1 and Figure 14).

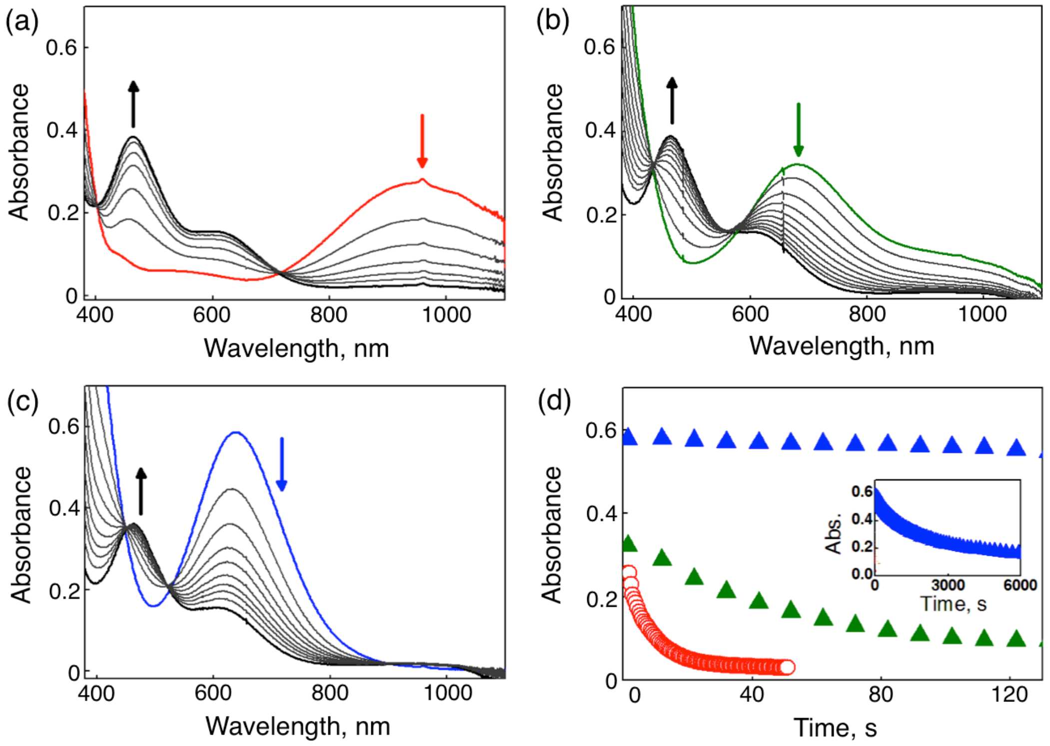

Figure 10. (a–c) UV-vis spectral changes of (a) **2**, (b) **3**, and (c) **4** (each 1.0 mM) upon addition of CHD (20 mM) at 298 K. (d) Time traces monitored at 940 nm for **2** (red ○), at 680 nm for **3** (green ▲), and at 635 nm for **4** (blue ▲). Inset shows the time trace for **4** longer time.

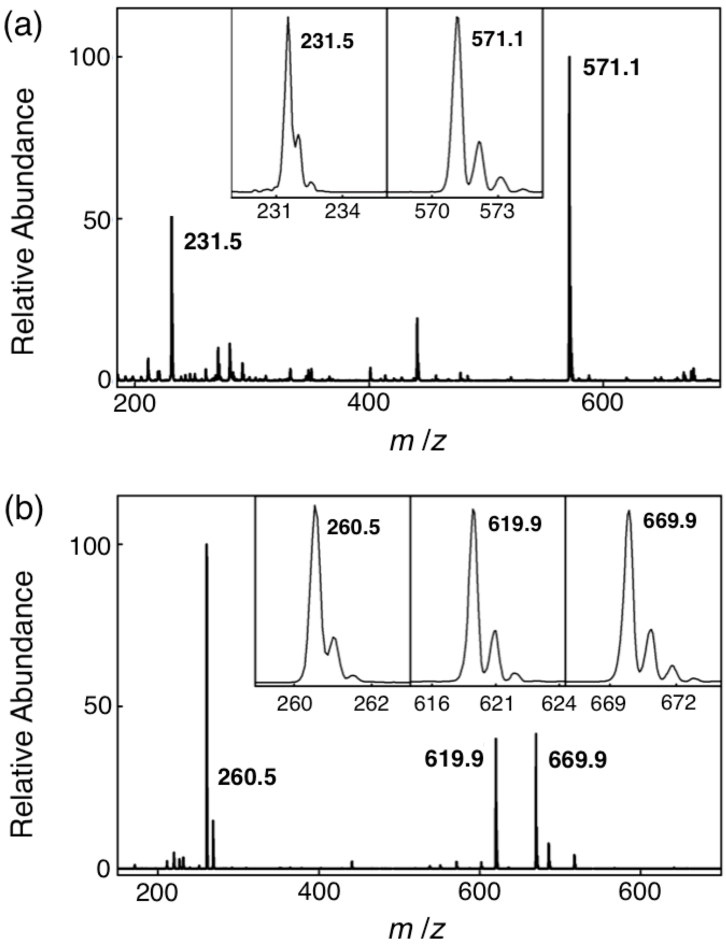

Figure 11. (a) ESI MS spectrum of the reaction solution of **2** (1.0 mM) and thioanisole (100 mM) in CF_3CH_2OH-CH_3CN (*v/v* 19:1) in a glove box at 298 K. Peaks at *m/z* = 231.5 and 571.1 correspond to $[Mn^{II}(N4Py)(CH_3CN)]^{2+}$ (*calcd. m/z* = 231.5) and $[Mn^{II}(N4Py)(CF_3SO_3)]^+$ (*calcd. m/z* = 571.1), respectively. Insets show the observed isotope distribution patterns for $[Mn^{II}(N4Py)(CH_3CN)]^{2+}$ (left panel) and $[Mn^{II}(N4Py)(CF_3SO_3)]^+$ (right panel). (b) ESI MS spectrum of the reaction solution of **2** (1.0 mM) and 1,4-cyclohexadiene (10 mM) in CF_3CH_2OH-CH_3CN (*v/v* 19:1) at 298 K. Peaks at *m/z* = 260.5, 619.9, and 669.9 correspond to $[Mn^{III}(N4Py)(CF_3CH_2O)]^{2+}$ (*calcd. m/z* = 260.5), $[Mn^{III}(N4Py)(CF_3CH_2O)_2]^+$ (*calcd. m/z* = 620.1), and $[Mn^{III}(N4Py)(CF_3CH_2O)(CF_3SO_3)]^+$ (*calcd. m/z* = 670.1), respectively. Insets show the observed isotope distribution patterns for $[Mn^{III}(N4Py)(CF_3CH_2O)]^{2+}$ (left panel), $[Mn^{III}(N4Py)(CF_3CH_2O)_2]^+$ (middle panel), and $[Mn^{III}(N4Py)(CF_3CH_2O)(CF_3SO_3)]^+$ (right panel).

In addition, plots of the logarithm of the second-order constants vs one-electron oxidation potentials of thioanisoles afforded a good linear correlation (Table 1 and Figure 15).

The reactivities of **2**, **3**, and **4** were also investigated kinetically in HAT, such as the

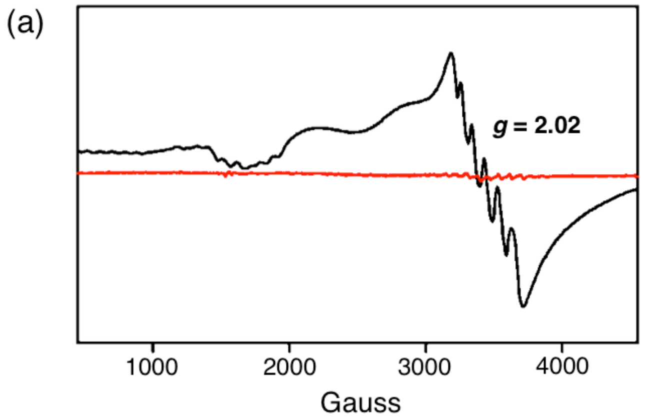

Figure 12. X-band CW-EPR spectra of reaction solutions of (a) $[Mn^{IV}(O)(N4Py)]^{2+}$ (**2**, 2.0 mM) with thioanisole (50 mM, black lines) and 1,4-cyclohexadiene (50 mM, red lines) and (b) $[Mn^{IV}(O)(N4Py)]^{2+}$–$(2Sc^{3+})$ (**4**, 2.0 mM) with thioanisole (50 mM, black lines) and 1,4-cyclohexadiene (50 mM, red lines) in CF_3CH_2OH-CH_3CN (*v/v* 19:1) at 25 °C. EPR spectra were recorded at 5 K.

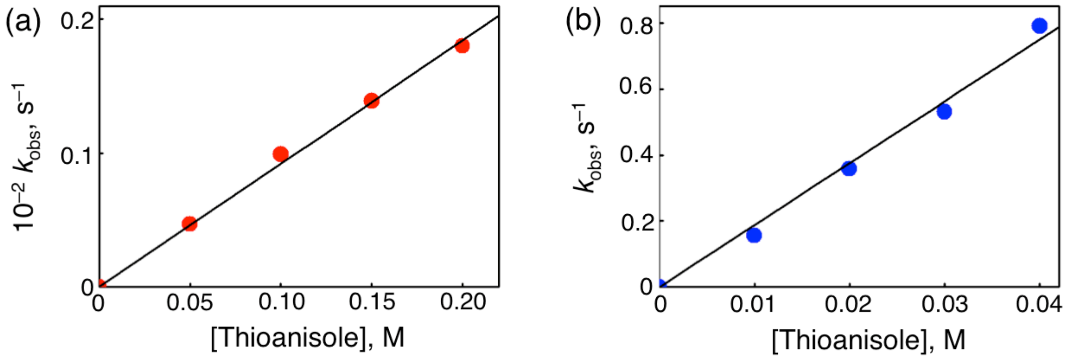

Figure 13. Plots of k_{obs} against the concentration of thioanisole to determine a second-order rate constant in the oxidation of thioanisole by (a) **2** (1.0 mM) and (b) **4** (1.0 mM) in CF_3CH_2OH-CH_3CN (*v/v* 19:1) at 273 K.

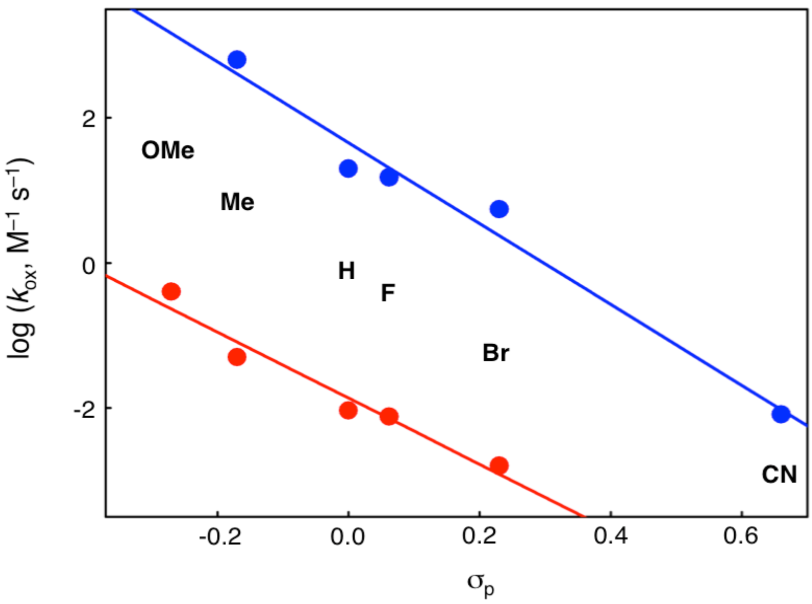

Figure 14. Hammett plots of the log k_2 against σ$_p$ of *para*-X-thioanisoles (X = MeO, Me, H, F, Br, and CN) by **2** (1.0 mM, red squares, slope = –4.6) and **4** (1.0 mM, blue squares, slope = –5.6) in CF_3CH_2OH-CH_3CN (*v/v* 19:1) at 273 K.

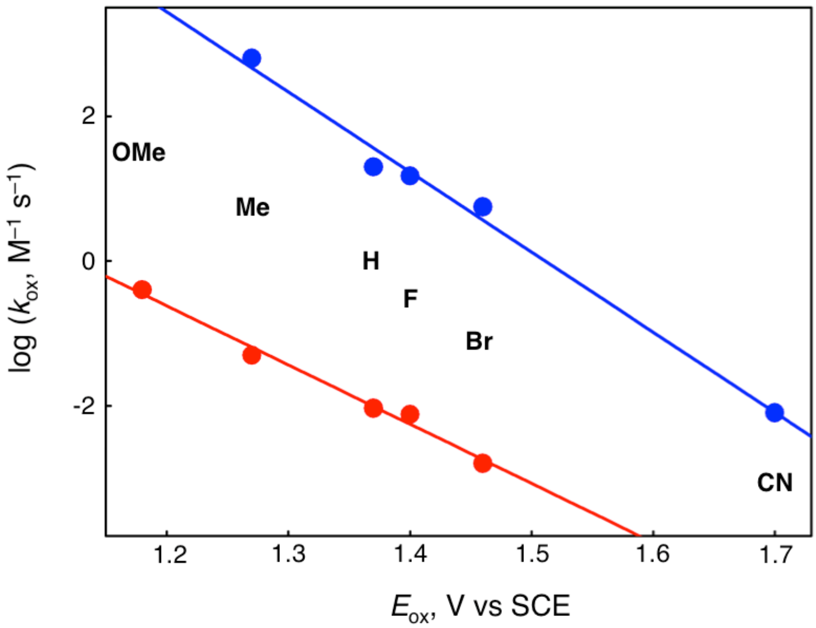

Figure 15. Plots of the log k_2 against the oxidation potentials (E_{ox}) of *para*-X-thioanisoles (X = MeO, Me, H, F, Br, and CN) by **2** (1.0 mM, red squares, slope = –8.2) and **4** (1.0 mM, blue squares, slope = –11) in CF_3CH_2OH-CH_3CN (*v/v* 19:1) at 273 K

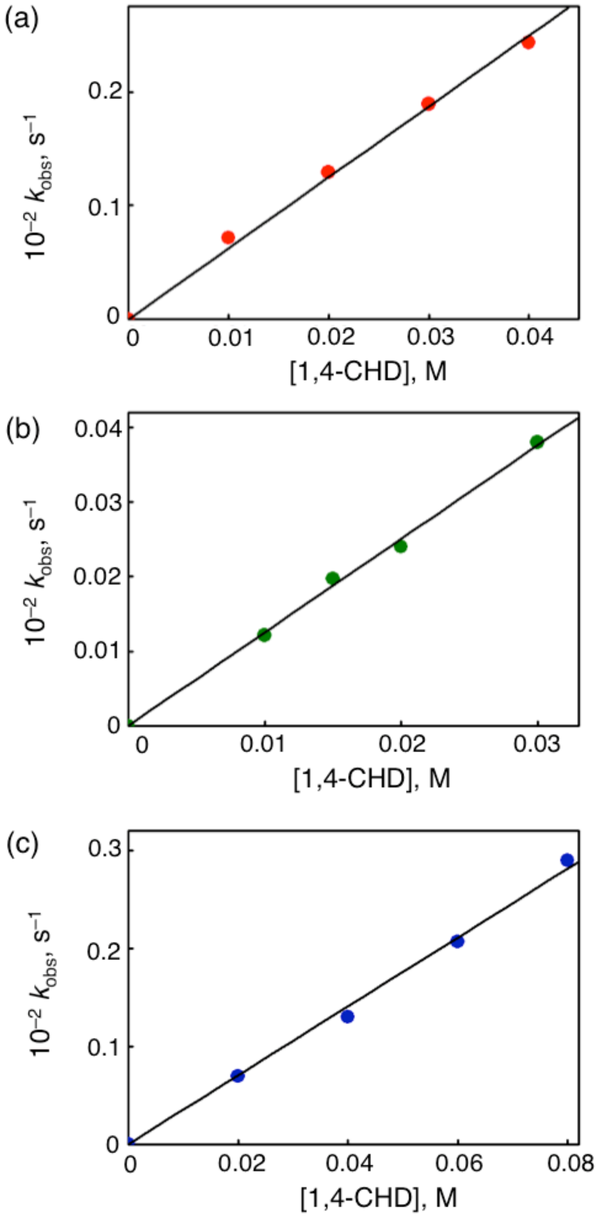

Figure 16. Plots of k_{obs} against the concentration of 1,4-cyclohexadiene (CHD) to determine a second-order rate constant in the oxidation of CHD by (a) **2** (1.0 mM), (b) **3** (1.0 mM), and (c) **4** (1.0 mM) in CF_3CH_2OH-CH_3CN (*v/v* 19:1) at 298 K.

C–H bond activation of 1,4-cyclohexadiene (CHD). Addition of CHD to the solutions of **2**, **3**, and **4** afforded the formation of a Mn(III) species with the reactivity order of **2** > **3** > **4** and with isosbestic points at 400 and 715 nm for **2**, at 433 and 575 nm for **3**, and at 450 and 525 nm for **4** (Figure 10; Figures 11 and 12 for EPR and ESI MS, respectively, for the Mn(III) product formation); we have reported recently experimental and theoretical results on the formation of Mn(III) products in the C–H bond activation of alkanes by nonheme manganese(IV)-oxo complexes.[11,13] Product analysis of the reaction solutions of **2**, **3**, and **4** revealed the formation of benzene as the sole product, as observed in the oxidation of CHD by other metal-oxo complexes.[16] The second-order rate constants determined in the reactions of **2**, **3**, and **4** were 6.2, 1.2, and 3.5×10^{-2} M^{-1} s^{-1} at 298 K, respectively (Figure 16), indicating that the reactivity of the manganese(IV)-oxo complex diminished by a factor of ~5 and ~180 upon binding one Sc^{3+} ion and two Sc^{3+} ions, respectively. This result is in sharp contrast to that of the OAT reaction, in which the binding of Sc^{3+} ions increased the reactivity of the manganese(IV)-oxo species markedly (vide supra). In addition, such a significant deceleration of reaction rate in the C–H bond activation by a Sc^{3+}–binding manganese(IV)-oxo complex ions is different from the results reported in HAT reactions by a Zn^{2+}–binding manganese(IV)-oxo complex[10] and a Sc^{3+}–binding $[(N4Py)Fe^{IV}(O)]^{2+}$ complex.[17]

The contrasting effect observed in the OAT and HAT reactions by Sc^{3+} ion-binding manganese(IV)-oxo species might be explained with the difference in their reaction mechanisms. In the case of OAT, electron transfer from thioanisoles to **4** may be the rate-determining step, followed by a fast oxygen atom transfer, as shown in

Table 1. Second-Order Rate Constants, k_2, Determined in the Sulfoxidation of *para*-X-Thioanisoles by **2** and **4**[a].

para-X	σ_ρ	E_{ox}[b] (V vs SCE)	Second-order rate constant, k_2, M^{-1} s^{-1}	
			2	**4**
MeO	-0.27	1.18	4.0×10^{-1}	ND[c]
Me	-0.17	1.27	5.0×10^{-2}	6.3×10^{2}
H	0.0	1.37	9.2×10^{-3}	2.0×10^{1}
F	0.062	1.40	7.6×10^{-3}	1.5×10^{1}
Br	0.23	1.46	1.6×10^{-3}	5.6
CN	0.66	1.70	ND[d]	8.0×10^{-3}

[a]Reaction conditions: All reactions were performed in CF_3CH_2OH-CH_3CN (*v/v* 19:1) at 273 K. [b]The oxidation potentials of *para*-X-thioanisoles were determined by second harmonic A.C. voltammetry (SHACV) in $CF_3CH_2OH:CH_3CN$ (*v/v* 19:1) containing 0.10 M $(n\text{-hexyl})_4NPF_6$ as a supporting electrolyte at 0 °C. [c]Too fast to be measured even with stopped-flow spectrophotometer. [d]Too slow to be measured.

Sc^{3+}-promoted OAT reactions by $[(N4Py)Fe^{IV}(O)]^{2+}$.[9] The proposed electron-transfer pathway is supported by a good linear correlation between reaction rates and E_{ox} of *para*-substituted thioanisoles (Figure 15).[9b,18] Such an electron-transfer pathway requires only little interaction between **4** and thioanisoles, which is rather insensitive to the steric effect caused by the Sc^{3+} ions bound to the manganese-oxo moiety. In contrast, the HAT reaction requires significant interaction in the substrate C–H bond activation by the manganese-oxo moiety in **3** and **4**, which is hindered by the Sc^{3+} ions bound to the manganese-oxo moiety in **3** and **4** (see Figure 1).

Conclusion

In summary, we have reported the synthesis, characterization, and reactivity of mononuclear nonheme manganese(IV)-oxo complexes binding Sc^{3+} ions and the contrasting metal ion effect on the reactivities of the manganese(IV)-oxo species in OAT and HAT reactions. The increased reactivity in OAT is rationalized with the involvement of an electron-transfer pathway, whereas the decreased reactivity in HAT is interpreted with the steric hindrance caused by the Sc^{3+} ions bound to the manganese-oxo moiety. The present results provide an example demonstrating a diverse redox-inactive metal ion effect on the reactivities of high-valent metal-oxo species in oxidation reactions.

References

(1) Nam, W. *Acc. Chem. Res.* **2007**, *40*, 465, and references therein.

(2) Hammarström, L.; Hammes-Schiffer, S. *Acc. Chem. Res.* **2009**, *42*, 1859, and references therein.

(3) (a) Rittle, J.; Green, M. T. *Science* **2010**, *330*, 933. (b) Abu-Omar, M. M.; Loaiza, A.; Hontzeas, N. *Chem. Rev.* **2005**, *105*, 2227. (c) Krebs, C.; Fujimori, D. G.; Walsh, C. T.; Bollinger, J. M., Jr. *Acc. Chem. Res*. **2007**, *40*, 484. (d) Bruijnincx, P. C. A.; van Koten, G.; Klein Gebbink, R. J. M. *Chem. Soc. Rev.* **2008**, *37*, 2716.

(4) (a) Nam, W. *Acc. Chem. Res.* **2007**, *40*, 522. (b) Goldberg, D. P. *Acc. Chem. Res.* **2007**, *40*, 626. (c) Aviv, I.; Gross, Z. *Chem. Commun.* **2007**, 1987. (d) Gunay, A.; Theopold, K. H. *Chem. Rev.* **2010**, *110*, 1060. (e) Borovik, A. S. *Chem. Soc. Rev.* **2011**, *40*, 1870. (f) Mayer, J. M. *Acc. Chem. Res.* **2011**, *44*, 36. (g) de Visser, S. P.; Rohde, J.-U.; Lee, Y.-M.; Cho, J.; Nam, W. *Coord. Chem. Rev.* **2013**, *257*, 381. (h) Mcdonald, A. R.; Que, L., Jr. *Coord. Chem. Rev.* **2013**, *257*, 414.

(5) (a) Pfaff, F. F.; Kundu, S.; Risch, M.; Pandian, S.; Heims, F.; Pryjomska-Ray, I.; Haack, P.; Metzinger, R.; Bill, E.; Dau, H.; Comba, P.; Ray, K. *Angew. Chem., Int. Ed.* **2011**, *50*, 1711. (b) Yiu, S.-M.; Man, W.-L.; Lau, T.-C. *J. Am. Chem. Soc.* **2008**, *130*, 10821. (c) Lam, W. W. Y.; Yiu, S.-M.; Lee, J. M. N.; Yau, S. K. Y.; Kwong, H.-K.; Lau, T.-C.; Liu, D.; Lin, Z. *J. Am. Chem. Soc.* **2006**, *128*, 2851. (d) Yiu, S.-M.; Wu, Z.-B.; Mak, C.-K.; Lau, T.-C. *J. Am. Chem. Soc.* **2004**, *126*, 14921. (e) Miller, C. G.; Gordon-Wylie, S. W.; Horwitz, C. P.; Strazisar, S. A.; Peraino, D. K.; Clark, G. R.; Weintraub, S. T.; Collins, T. J. *J. Am. Chem. Soc.* **1998**, *120*, 11540. (f) Du, H.; Lo, P.-K.; Hu, Z.; Liang, H.; Lau, K.-C.; Wang, Y.-N.; Lam, W. W. Y.; Lau, T.-C. *Chem. Commun.* **2011**, *47*, 7143.

(6) (a) Umena, Y.; Kawakami, K.; Shen, J.-R.; Kamiya, N. *Nature* **2011**, *473*, 55. (b) Gatt, P.; Patrie, S.; Stranger, R.; Pace, R. J. *Angew. Chem., Int. Ed.* **2012**, *51*, 12025.

(7) (a) Kanady, J. S.; Tsui, E. Y.; Day, M. W.; Agapie, T. *Science* **2011**, *333*, 733. (b) Park, Y. J.; Ziller, J. W.; Borovik, A. S. *J. Am. Chem. Soc.* **2011**, *133*, 9258.

(8) Fukuzumi, S.; Morimoto, Y.; Kotani, H.; Naumov, P.; Lee, Y.-M.; Nam, W. *Nature Chem.* **2010**, *2*, 756.

(9) (a) Morimoto, Y.; Kotani, H.; Park, J.; Lee, Y.-M.; Nam, W.; Fukuzumi, S. *J. Am. Chem. Soc.* **2011**, *133*, 403. (b) Park, J.; Morimoto, Y.; Lee, Y.-M.; Nam, W.; Fukuzumi, S. *J. Am. Chem. Soc.* **2011**, *133*, 5236.

(10) Leeladee, P.; Baglia, R. A.; Prokop, K. A.; Latifi, R.; de Visser, S. P.; Goldgerg, D. P. *J. Am. Chem. Soc.* **2012**, *134*, 10397.

(11) Wu, X.; Seo, M. S.; Davis, K. M.; Lee, Y.-M.; Chen, J.; Cho, K-B.; Pushkar, Y. N.; Nam, W. *J. Am. Chem. Soc.* **2011**, *133*, 20088.

(12) Evans, D. F.; Jakubovic, D. A. *J. Chem. Soc. Dalton Trans.* **1988**, 2927.

(13) Cho, K.-B.; Shaik, S.; Nam, W. *J. Phys. Chem. Lett.* **2012**, *3*, 2851.

(14) Direct binding of two Sc^{3+} ions to the Mn-O moiety in **4** may be unlikely to occur, since it is 40 kcal/mol higher in energy than the one with only one Sc^{3+} binding (see SI, Figure S15).

(15) Although **3** showed reactivity between **2** and **4** in the oxidation of thioanisole, we were not able to determine an accurate rate constant due to a poor kinetic fitting in the first-order decay profile of the thioanisole oxidation by **3**.

(16) (a) Garcia-Bosch, I.; Company, A.; Cady, C. W.; Styring, S.; Browne, W. R.; Ribas, X.; Costas, M. *Angew. Chem., Int. Ed.* **2011**, *50*, 5648. (b) Sawant, S. C.; Wu, X.; Cho, J.; Cho, K.-B.; Kim, S. H.; Seo, M. S.; Lee, Y.-M.; Kubo, M.; Ogura, T.; Shaik, S.; Nam, W. *Angew. Chem., Int. Ed.* **2010**, *49*, 8190. (c) Jeong, Y. J.; Kang, Y.; Han, A.-R.; Lee, Y.-M.; Kotani, H.; Fukuzumi, S.; Nam, W. *Angew. Chem., Int. Ed.* **2008**, *47*, 7321.

(17) Morimoto, Y.; Park, J.; Suenobu, T.; Lee, Y.-M.; Nam, W.; Fukuzumi, S. *Inorg. Chem.* **2012**, *51*, 10025.

(18) (a) Goto, Y.; Matsui, T.; Ozaki, S.; Watanabe, Y.; Fukuzumi, S. *J. Am. Chem. Soc.* **1999**, *121*, 9497. (b) Taki, M.; Itoh, S.; Fukuzumi, S. *J. Am. Chem. Soc.* **2002**, *124*, 998. (c) Arias, J.; Newlands, C. R.; Abu-Omar, M. M. *Inorg. Chem.* **2001**, *40*, 2185. (d) McPherson, L. D.; Drees, M.; Khan, S. I.; Strassner, T.; Abu-Omar, M. M. *Inorg. Chem.* **2004**, *43*, 4036. (e) Kumar, A.; Goldberg, I.; Botoshansky, M.; Buchman, Y.; Gross, Z. *J. Am. Chem. Soc.* **2010**, *132*, 15233.

(19) Armarego, W. L. F.; Chai, C. L. L. *Purification of Laboratory Chemicals*, 6th ed.; Pergamon Press, Oxford, U.K., 2009.

(20) (a) Saltzman, H.; Sharefkin, J. G., Eds.; *Organic Syntheses*; Wiley: New York, 1973, Vol. V, pp. 658. (b) Kaizer, J.; Klinker, E. J.; Oh, N. Y.; Rohde, J.-U.; Song, W. J.; Stubna, A.; Kim, J.; Münck, E.; Nam, W.; Que, L., Jr. *J. Am. Chem. Soc.* **2004**, *126*, 472. (c) Wu, X.; Seo, M. S.; Davis, K. M.; Lee, Y.-M.; Chen, J.; Cho, K.-B.; Pushkar, Y. N.; Nam, W. *J. Am. Chem. Soc.* **2011**, *133*, 20088.

(21) Sheldrick, G. M. *SHELXTL/PC Version 6.12 for Windows XP*; Bruker AXS Inc.: Madison, Wisconsin, USA, 2001.

(22) Ravel, B.; Newville, M. *J. Synchrot. Radiat.* **2005**, *12*, 537.

(23) Rehr, J. J.; Albers, R. C. *Rev. Mod. Phys.* **2000**, *72*, 621.

(24) Koningsberger, D. C.; Prins, R. *X-Ray Absorption: Principles, Applications, Techniques of EXAFS, SEXAFS and XANES*; John Wiley & Sons, 1988.

(25) (a) Evans, D. F. *J. Chem. Soc.* **1959**, 2003. (b) Löliger, J.; Scheffold, R. *J. Chem. Edu.* **1972**, 646. (c) Evans, D. F.; Jakubovic, D. A. *J. Chem. Soc. Dalton Trans.* **1988**, 2927.

(26) Mann, C. K.; Barnes, K.K. *Electrochemical Reactions in Non-aqueous Systems*; Mercel Dekker: New York, 1970.

Supporting Information for Chapter 3

Table S1. Crystal Data and Structure Refinement for [Mn^{II}(N4Py)(CF_3SO_3)](CF_3SO_3).

Empirical formula	C25 H21 F6 Mn N5 O6 S2
Formula weight	720.53
Temperature (K)	100(2)
Wavelength (Å)	0.71073
Crystal system/space group	Tetragonal / *P4(3)*
Unit cell dimensions	
a (Å)	10.05280(10)
b (Å)	10.05280(10)
c (Å)	28.2357(4)
α (°)	90.00
β (°)	90.00
γ (°)	90.00
Volume (Å^3)	2853.47(6)
Z	4
Calculated density (g/cm^{-3})	1.677
Absorption coefficient (mm^{-1})	0.699
F(000)	1460
Reflections collected	51369
Independent reflections [*R*(int)]	6575 [0.0328]
Refinement method	Full-matrix least-squares on F^2
Data/restraints/parameters	6575 / 1 / 433
Goodness-of-fit on F^2	1.040
Final *R* indices [$I > 2$sigma(I)]	0.0514
Final *wR* indices [$I > 2$sigma(I)]	0.1296
Largest difference peak and hole (e/Å^3)	1.239 and –0.665

Table S2. Selected Bond Lengths (Å) and Angles (°) for [Mn^{II}(N4Py)(CF$_3$SO$_3$)](CF$_3$SO$_3$).

Distances (Å)			
Mn1-O1	2.128(3)	Mn1-N3	2.288(3)
Mn1-N1	2.237(3)	Mn1-N4	2.297(3)
Mn1-N2	2.248(3)	Mn1-N5	2.285(3)
Angles (°)			
O1-Mn1-N1	114.28(13)	N1-Mn1-N5	76.47(10)
O1-Mn1-N2	91.39(12)	N2-Mn1-N3	90.03(11)
O1-Mn1-N3	94.70(13)	N2-Mn1-N4	150.48(11)
O1-Mn1-N4	116.87(11)	N2-Mn1-N5	75.88(12)
O1-Mn1-N5	162.95(13)	N3-Mn1-N4	79.85(11)
N1-Mn1-N2	85.32(11)	N3-Mn1-N5	74.34(11)
N1-Mn1-N3	150.71(12)	N4-Mn1-N5	74.70(11)
N1-Mn1-N4	90.12(11)		

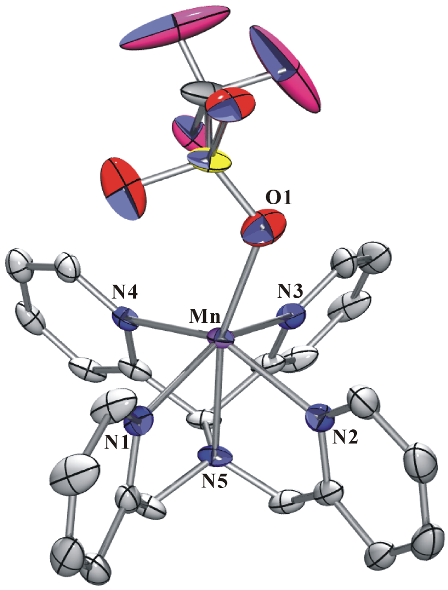

Figure S1. X-ray structure of [Mn^{II}(N4Py)(CF$_3$SO$_3$)]$^+$ moiety in [Mn^{II}(N4Py)(CF$_3$SO$_3$)]-(CF$_3$SO$_3$) (**1**-CF$_3$SO$_3$), showing 50% probability thermal ellipsoids. Crystallographic and structural data are summarized in Tables S1 and S2.

Table S3. Structural Parameters from EXAFS Fits.

Sample	Fit #	Shell	R, Å	N*	$\sigma^2 \times 10^3$	R-factor	Reduced $\mathrm{Chi}^2 \times 10^4$
$[\mathrm{Mn^{IV}(O)(N4Py)}]^{2+}$ Peak 1	1	Mn-N	1.94	6	7.2	0.38	1.7444
	2	Mn-O	1.70	5	5.6	0.193	2.2168
		Mn-N	1.98	1			
$[\mathrm{Mn^{IV}(O)(N4Py)}]^{2+}$ Peak 1+2	3	Mn-N	1.95	6	6.9	0.4856	0.7324
	4	Mn-O	1.70	1	4.8	0.3349	0.6374
		Mn-N	1.96	5			
	5	Mn-O	1.71	1	5.6	0.096	0.3826
		Mn-N	1.99	5			
		Mn-C	2.92	7	11.9		
	6	Mn-O	1.72	1	4.2	0.0182	0.1614
		Mn-N	2.02	4			
		Mn-N	2.28	1			
		Mn-C	2.97	7	13.6		
	7	Mn-O	1.72	1	4.8	0.0013	0.0949
		Mn-N	2.02	4			
		Mn-N	2.28	1			
		Mn-C	2.97	7	10.5		
		Mn-C	3.29	4			
$[\mathrm{Mn^{IV}(O)(N4Py)}]^{2+}$–$2\mathrm{Sc}^{3+}$ Peak 1	8	Mn-N	1.89	6	5.2	0.42	1.7129
	9	Mn-O	1.70	1	5.3	0.276	2.8200
		Mn-N	1.97	5			
$[\mathrm{Mn^{IV}(O)(N4Py)}]^{2+}$–$2\mathrm{Sc}^{3+}$ Peak 1+2+3	10	Mn-N	1.89	6	5.1	0.6739	0.5573
	11	Mn-O	1.70	1	5.3	0.5518	0.5231
		Mn-N	1.98	5			
	12	Mn-O	1.71	1	5.9	0.3540	0.4746
		Mn-N	2.01	5			
		Mn-C	2.94	7	13.0		
	13	Mn-O	1.72	1	4.9	0.0500	0.1145
		Mn-N	2.03	4			
		Mn-N	2.32	1			
		Mn-C	2.97	7	15.4		
		Mn-Sc	3.51	1	4.9		
	14	Mn-O	1.72	1	4.4	0.0156	0.055
		Mn-N	2.02	4			
		Mn-N	2.31	1			
		Mn-C	2.97	7	12.8		
		Mn-C	3.30	4			
		Mn-Sc	3.51	1	4.4		
	15	Mn-O	1.69	1	6.6	0.054	0.1912
		Mn-N	2.03	4			
		Mn-N	2.34	1			
		Mn-C	2.99	7	9.4		
		Mn-C	3.25	4			
		Mn-Sc	3.53	1	6.6		
$[\mathrm{Mn^{IV}(O)(N4Py)}]^{2+}$–$2\mathrm{Sc}^{3+}$ peak 3	16	Mn-Sc	3.52	1	4.0	0.0015	0.0119
	17	Mn-Sc	3.51	2	10.0	0.0328	0.2559
$[\mathrm{Mn^{II}(N4Py)}]^{2+}$ Peak 1	18	Mn-N	2.24	6	7.7	0.0005	0.0042
$[\mathrm{Mn^{II}(N4Py)}]^{2+}$ Peak 1+2	19	Mn-N	2.26	6	7.7	0.228	1.2980
	20	Mn-N	2.25	6	7.9	0.0405	0.1242
		Mn-C	3.17	11	13.3		

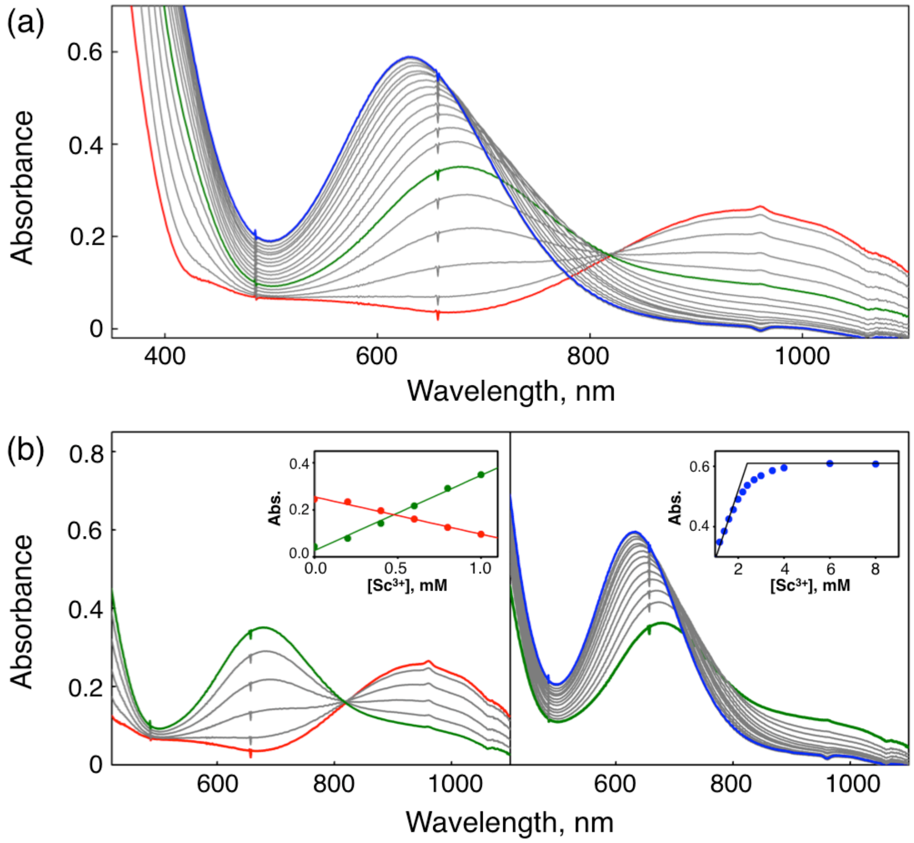

Figure S2. (a) UV-vis spectral changes observed in the titration of **2** (red line) with Sc^{3+} upon addition of Sc^{3+} (0.0 – 8.0 mM) into the solution of **2** (1.0 mM) in CF_3CH_2OH-CH_3CN (*v/v* 19:1) at 298 K. (b) Left panel: UV-vis spectral changes showing the conversion from **2** (red line) to **3** (green line), observed in the titration experiment upon addition of Sc^{3+} (from 0.0 to 1.0 mM with 0.2 mM interval) into the solution of **2** (1.0 mM, red line) in increments of 0.2 equiv in CF_3CH_2OH-CH_3CN (*v/v* 19:1) at 298 K. The absorption band at 940 nm due to **2** changed to absorption band at 680 nm due to **3** with an isosbestic point at 817 nm. Inset shows the spectroscopic titration monitored at 940 nm (●) due to the decay of **2** and 680 nm (▲) due to formation of **3**. Crossing point between two lines at 940 nm and 680 nm was shown at 0.50 equiv of Sc^{3+}. This crossing point at 0.5 equiv of Sc^{3+} together with an isosbestic point in the spectral changes strongly indicates that 1:1 complex between **2** and Sc^{3+} was formed with a very high binding constant. Right panel: UV-vis spectral changes showing the conversion from **3** (green line) to **4** (blue line), observed in the titration of **3** with Sc^{3+} upon addition of Sc^{3+} (from 1.0 to 8.0 mM) into the solution of **3** (1.0 mM) in CF_3CH_2OH-CH_3CN (*v/v* 19:1) at 298 K. The no observation of an isosbestic point for the conversion from **3** to **4** might be due to the existence of the second Sc^{3+} ion in the secondary coordination sphere with an equilibrium between **3** and **4** and with a fast exchange rate for the binding of the second Sc^{3+} ion by **3**. Inset shows the spectroscopic titration monitored at 635 nm (▲) due to **4**.

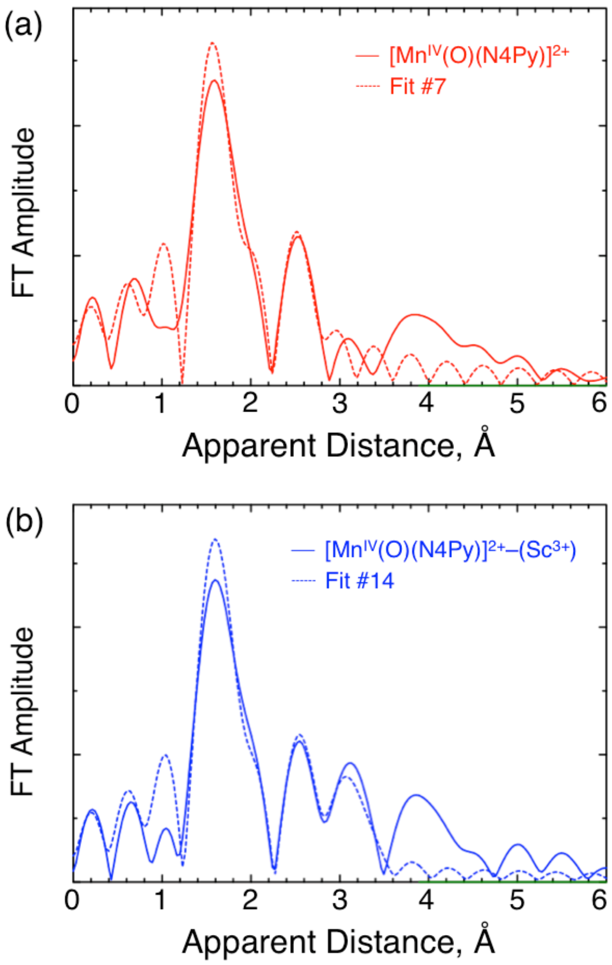

Figure S3. Overlay of the Fourier transforms (k = 3.5 – 11.3 Å^{-1}) of **2** (a) and **4** (b) and results of Fits #7 and #14 from Table S3.

Chapter 4

Enhanced Electron-Transfer Reactivity of Nonheme Manganese(IV)-Oxo Complexes by Binding Scandium Ions

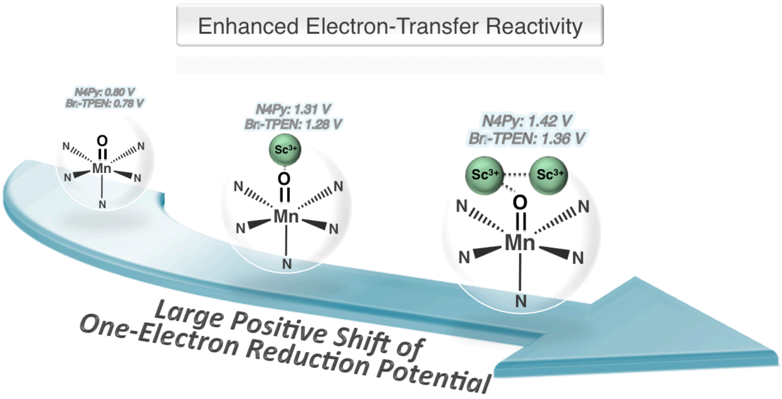

Abstract: One and two scandium ions (Sc^{3+}) are bound strongly to nonheme manganese(IV)-oxo complexes, $[(N4Py)Mn^{IV}(O)]^{2+}$ (N4Py = *N*,*N*-bis(2-pyridylmethyl)-*N*-bis(2-pyridyl)methylamine) and $[(Bn\text{-}TPEN)Mn^{IV}(O)]^{2+}$ (Bn-TPEN = *N*-benzyl-*N*,*N'*,*N'*-tris(2-pyridylmethyl)-1,2-diaminoethane), to form $Mn^{IV}(O)–(Sc^{3+})_1$ and $Mn^{IV}(O)–(Sc^{3+})_2$ complexes, respectively. The binding of Sc^{3+} ions to the $Mn^{IV}(O)$ complexes was examined by spectroscopic methods as well as by DFT calculations. The one-electron reduction potentials of the manganese(IV)-oxo complexes were markedly shifted to a positive direction by binding of Sc^{3+} ions. Accordingly, rates of the electron transfer reactions of the manganese(IV)-oxo complexes were enhanced as much as 10^7–fold by binding of two Sc^{3+} ions. The driving force dependence of electron transfer from various electron donors to the $Mn^{IV}(O)$ and $Mn^{IV}(O)–(Sc^{3+})_2$ complexes was examined and analyzed in light of the Marcus theory of electron transfer to determine the reorganization energies of electron transfer. The smaller reorganization energies and much more positive reduction potentials of the $Mn^{IV}(O)–(Sc^{3+})_2$ complexes resulted in remarkable enhancement of the electron-transfer reactivity of the manganese(IV)-oxo complexes. Such a dramatic enhancement of the electron-transfer reactivity of the manganese(IV)-oxo complexes by binding of Sc^{3+} ions resulted in the change of mechanism in the sulfoxidation of thioanisoles by

manganese(IV)-oxo complexes from a direct oxygen atom transfer pathway without metal ion binding to an electron-transfer pathway with binding of Sc^{3+} ions.

Introduction

High-valent metal-oxo complexes play pivotal roles as reactive intermediates in the reactions of heme (cytochromes P450 and peroxidases)[1-3] and nonheme metalloenzymes (taurine/α-ketoglutarate dioxygenase (TauD),[4] soluble methane monooxygenase (sMMO)[5] and oxygen-evolving center (OEC) in Photosystem II[6,7]) as well as in their biomimetic oxidation catalysis.[8-13] A number of synthetic high-valent metal-oxo complexes have been synthesized and characterized by various spectroscopic techniques as well as by X-ray crystallography.[8-17] The oxidizing reactivity of the high-valent metal-oxo complexes has so far been finely controlled by the oxidation state of metals and the supporting and axial ligands.[8-28] Alternatively, binding of redox-inactive metal ions acting as Lewis acids to the metal-oxo moiety of high-valent metal-oxo complexes has also been reported to enhance the oxidizing power of the metal-oxo complexes.[29-32] For example, Lau and co-workers have shown that rates of oxidation of alkanes by MnO_4^- are accelerated dramatically by addition of Lewis acids.[33] We have reported the first X-ray crystal structure of a Sc^{3+} ion-bound iron(IV)-oxo complex[34] and found that the binding of Sc^{3+} ions to iron(IV)-oxo complexes resulted in the remarkable enhancement of the oxidizing reactivity of the iron-oxo complexes in various oxidation reactions.[29] Those findings are reminiscent of the indispensable role of Ca^{2+} in the manganese-oxo-calcium (Mn_4CaO_5) active site in OEC, which catalyzes four-electron oxidation of water to dioxygen, although the exact function of Ca^{2+} has yet to be clarified.[35,36] In this context, we have recently communicated preliminary results that binding of redox-inactive metal ions to a nonheme manganese(IV)-oxo complex affected the oxidizing ability significantly.[37] Goldberg and co-workers also reported the influence of a redox-inactive Zn^{2+} ion on a valence tautomerization of a manganese(V)-oxo corrolazine complex.[38] More recently, Agapie and co-workers reported that the redox potentials of tetranuclear heterometallic trimanganese dioxo clusters [$Mn_3M(\mu_4\text{-}O)(\mu_2\text{-}O)$] containing a redox-inactive metal ion, which were synthesized as an excellent structural model of the OEC active site,[39] were systematically controlled by the Lewis acidity of the redox-inactive metal ions.[40] The positive shift in the redox potentials of an iron(IV)-oxo complex was also observed in the presence of various redox-inactive metal ions, showing a correlation between the reactivity of the iron(IV)-oxo complex and the Lewis acidity of the redox-inactive metal ions.[29a] However, the electron-transfer properties of metal ion-bound manganese(IV)-oxo complexes, which are the most fundamental factor in controlling the reactivity of metal-oxo species in oxidation reactions, have yet to be clarified.

We report herein not only the synthesis and characterization of nonheme manganese(IV)-oxo complexes binding one and two Sc^{3+} ions, $Mn^{IV}(O)–(Sc^{3+})_1$ and $Mn^{IV}(O)–(Sc^{3+})_2$, but also the detailed kinetic data on electron transfer from various electron donors to $Mn^{IV}(O)$, $Mn^{IV}(O)–(Sc^{3+})_1$, and $Mn^{IV}(O)–(Sc^{3+})_2$ complexes. The large positive shifts in one-electron reduction potentials of manganese(IV)-oxo complexes by binding of one and two Sc^{3+} ions have also been determined for the first time by carrying out redox titration experiments using electron donors with known one-electron oxidation potentials. Rates of the electron-transfer reactions by manganese(IV)-oxo complexes were remarkably enhanced by binding of Sc^{3+} ions. The driving force dependence of the rate constants of electron-transfer reactions has been analyzed in light of the Marcus theory of electron transfer[41] to determine the reorganization energies of electron transfer of Sc^{3+} ion-bound manganese(IV)-oxo complexes in comparison with those of manganese(IV)-oxo complexes without Sc^{3+} ions. We have also shown that binding of redox-inactive metal ions enhances the reactivity of manganese(IV)-oxo complexes in sulfoxidation of thioanisoles and changes the sulfoxidation mechanism from direct oxygen atom transfer to electron transfer.

Experimental Section

Materials. Commercially available chemicals were used without further purification unless otherwise indicated. Solvents were dried according to published procedures and distilled under Ar prior to use.[48] Scandium triflate, $Sc(OTf)_3$ (OTf = $SO_3CF_3^-$), was purchased from Aldrich and used as received. Iodosylbenzene (PhIO) was prepared by a literature method.[49] N4Py and Bn-TPEN ligands and $Mn^{II}(OTf)_2 \cdot 2CH_3CN$ were prepared by literature methods.[20b,50] The $[(N4Py)Mn^{II}(CH_3CN)](CF_3SO_3)_2$ and $[(Bn\text{-}TPEN)Mn^{II}(CH_3CN)](CF_3SO_3)_2$ complexes were prepared in a dry box.[37,41] N4Py

(0.54 mmol, 0.20 g) and $Mn^{II}(OTf)_2 \cdot 2CH_3CN$ (0.82 mmol, 0.32 g) were dissolved in CH_3CN, and the reaction solution was stirred at ambient temperature overnight. The resulting solution was filtered and added to a large volume of Et_2O. The product was obtained as a white solid with 60% yield (0.24 g). Bn-TPEN (0.47 mmol, 200 mg) and $Mn^{II}(CF_3SO_3)_2 \cdot 2CH_3CN$ (0.57 mmol, 250 mg) were dissolved in CH_3CN and stirred at ambient temperature overnight. The resulting solution was filtered and added to a large volume of Et_2O. The product was obtained as a white solid in 85% yield (0.38 g). One-electron reductants, such as $[Fe^{II}(Me_2\text{-phen})_3]^{2+}$, $[Fe^{II}(Ph_2\text{-phen})_3]^{2+}$, $[Fe^{II}(bpy)_3]^{2+}$, $[Fe^{II}(5\text{-Cl-phen})_3]^{2+}$, and $[Ru^{II}(bpy)_3]^{2+}$, were synthesized according to literature methods.[51]

DFT Calculations. Calculations were done with Density Functional Theory (DFT)[44] using the Gaussian 09 package[52] and the B3LYP functional.[53] Optimizing and single-point frequency calculations were done with the LACVP basis set[54] (except for S, which required 6-311+G*), while a single-point evaluation was done using the LACV3P*$^+$ basis set[54] in order to obtain more accurate Mulliken spin density distribution. All calculations (including the optimizations) were done in solvent (acetonitrile) using the CPCM scheme.[55]

Redox Titrations. Electron transfer from dibromoferrocene to $[Mn^{IV}(O)]^{2+}$ (5.0×10^{-4} M) was examined from the spectral change in the various concentration of dibromoferrocene ($1.5 \times 10^{-4} - 5.0 \times 10^{-2}$ M) at 273 K. Typically, a deaerated CH_3CN solution of dibromoferrocene ($7.5 \times 10^{-5} - 5.0 \times 10^{-4}$ M) was added to a deaerated trifluoroethanol solution containing $[Mn^{IV}(O)]^{2+}$ (5.0×10^{-4} M). The concentration of dibromoferrocenium ion (Br_2Fc^+) was determined from the absorption band at $\lambda = 700$ nm due to Br_2Fc^+ ($\varepsilon = 4.0 \times 10^2$ M^{-1} cm^{-1}). The ε value of Br_2Fc^+ was determined by the electron-transfer oxidation of Br_2Fc with cerium (IV) ammonium nitrate (5.0×10^{-3} M) in CF_3CH_2OH-MeCN (v/v = 1:1) at 273 K. Likewise, electron transfer from $[Ru^{II}(bpy)_3]^{2+}$ to $[Mn^{IV}(O)]^{2+}-(Sc^{3+})_1$ (5.0×10^{-4} M) and $[Ru^{II}(5\text{-Cl-phen})_3]^{2+}$ to $[Mn^{IV}(O)]^{2+}-(Sc^{3+})_2$ (5.0×10^{-4} M) were examined from the spectral change in the various concentration of $[Ru^{II}(bpy)_3]^{2+}$ ($1.5 \times 10^{-4} - 5.0 \times 10^{-2}$ M) and $[Ru^{II}(5\text{-Cl-phen})_3]^{2+}$ at 273 K.

Kinetic Measurements. Kinetic measurements were performed in

CF_3CH_2OH-CH_3CN (v/v = 1:1) at 273 K. Rates of electron transfer from ferrocene derivatives to $[Mn^{IV}(O)]^{2+}$ (2.5×10^{-4} M) were investigated by the formation and decay of absorption bands due to ferrocenium ion and $[Mn^{IV}(O)]^{2+}$, respectively. Kinetic measurements for rates of electron transfer from various electron donors to $[Mn^{IV}(O)]^{2+}$–$(Sc^{3+})_1$ and $[Mn^{IV}(O)]^{2+}$–$(Sc^{3+})_2$ were carried out under second-order conditions, where both concentrations of electron donors and $[Mn^{IV}(O)]^{2+}$–$(Sc^{3+})_1$ or $[Mn^{IV}(O)]^{2+}$–$(Sc^{3+})_2$ were 1.25×10^{-4} M, because electron transfer rates were too fast to follow under pseudo-order conditions even with the use of a stopped-flow equipment.

Instrumentation. UV-vis spectra were recorded on a Hewlett Packard 8453 diode array spectrophotometer equipped with a UNISOKU Scientific Instruments Cryostat USP-203A for low-temperature experiments or on a UNISOKU RSP-601 stopped-flow spectrometer equipped with a MOS-type highly sensitive photodiode-array. X-band EPR spectra were recorded at 5 K using X-band Bruker EMX-plus spectrometer equipped with a dual mode cavity (ER 4116DM). Low temperature was achieved and controlled with an Oxford Instruments ESR900 liquid He quartz cryostat with an Oxford Instruments ITC503 temperature and gas flow controller. The experimental parameters for EPR measurement were as follows: Microwave frequency = 9.646 GHz, microwave power = 1.0 mW, modulation amplitude = 10 G, gain = 1.0×10^4, modulation frequency = 100 kHz, time constant = 40.96 ms, and conversion time = 81.00 ms.

Results and Discussion

Binding of Sc^{3+} Ions to Nonheme Manganese(IV)-Oxo Complexes. $[(Bn\text{-}TPEN)Mn^{IV}(O)]^{2+}$ (**1**) and its scandium-bound species were synthesized and characterized spectroscopically, as reported for binding of Sc^{3+} ions to $[(N4Py)Mn^{IV}(O)]^{2+}$ (**2**) (see Chart 1).[37,41] Addition of up to two equiv of $Sc(OTf)_3$ to a solution of **1** in a solvent mixture of CF_3CH_2OH-CH_3CN (v/v =

Chart 1

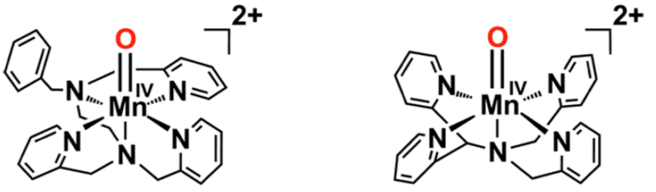

1 **2**

19:1) resulted in a blue shift of the absorption band of **1** at λ_{max} = 1020 nm to that at λ_{max} = 740 nm with an isosbestic point at 900 nm (Figure 1a). Such a blue shift suggests that the ground state of **1** is more stabilized by binding of Sc^{3+} ions. Further addition of $Sc(OTf)_3$ resulted in a more blue-shift to give the absorption band at λ_{max} = 690 nm (Figure 1c). No further spectral change was observed by addition of more than nine equiv of $Sc(OTf)_3$. Such stepwise spectral changes indicate the binding of one and two Sc^{3+} ions to **1** to produce $Mn^{IV}(O)–(Sc^{3+})_1$ and $Mn^{IV}(O)–(Sc^{3+})_2$ complexes, respectively. The X-band EPR spectra of $[(Bn\text{-}TPEN)Mn^{IV}(O)]^{2+}–(Sc^{3+})_1$ and $[(Bn\text{-}TPEN)Mn^{IV}(O)]^{2+}–(Sc^{3+})_2$ exhibit signals that are characteristic of S = 3/2 Mn^{IV} (Figure 2). This result is the same as that reported previously for the complexes of **2** with Sc^{3+} ions.[37] The magnetic moments of $[(Bn\text{-}TPEN)Mn^{IV}(O)]^{2+}–(Sc^{3+})_1$ and

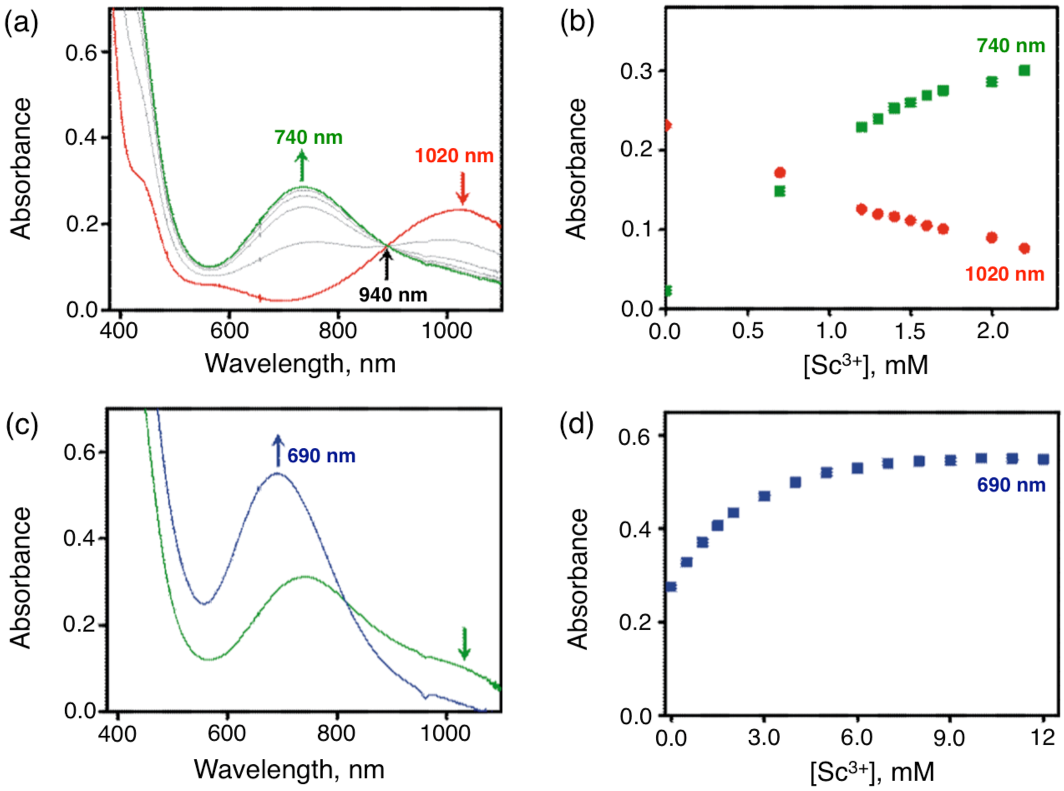

Figure 1. (a) UV-vis spectral changes showing the conversion from $[(Bn\text{-}TPEN)Mn^{IV}(O)]^{2+}$ (red line) to $[(Bn\text{-}TPEN)Mn^{IV}(O)]^{2+}–(Sc^{3+})_1$ (green line) upon addition of incremental amounts of Sc^{3+} (from 0.0 to 2.0 mM) in the titration experiment. (b) Spectroscopic titration monitored at 1020 nm (red rhombuses) due to the decay of $[(Bn\text{-}TPEN)Mn^{IV}(O)]^{2+}$ and at 740 nm (green squares) due to the formation of $[(Bn\text{-}TPEN)Mn^{IV}(O)]^{2+}–(Sc^{3+})_1$. (c) UV-vis spectral changes showing the conversion from $[(Bn\text{-}TPEN)Mn^{IV}(O)]^{2+}–(Sc^{3+})_1$ (green line) to $[(Bn\text{-}TPEN)Mn^{IV}(O)]^{2+}–(Sc^{3+})_2$ (blue line) observed upon addition of Sc^{3+} ions (from 0.0 to 12 mM). (d) Spectroscopic titration monitored at 690 nm (blue squares) due to $[(Bn\text{-}TPEN)Mn^{IV}(O)]^{2+}–(Sc^{3+})_2$.

$[(\mathrm{Bn\text{-}TPEN})\mathrm{Mn}^{\mathrm{IV}}(\mathrm{O})]^{2+}$– $(\mathrm{Sc}^{3+})_2$ were also determined to be 4.4 and 4.3 μ_{B} by the modified NMR technique of Evans,[42] respectively, confirming the spin state of $S = 3/2$ for both complexes.[41a]

The formation constant of the $[(\mathrm{Bn\text{-}TPEN})\mathrm{Mn}^{\mathrm{IV}}(\mathrm{O})]^{2+}$–$(\mathrm{Sc}^{3+})_1$ complex was determined to be 4.0×10^3 M^{-1}, by analyzing the spectral change in Figure 1b (see the linear plot to determine the formation constant in Figure 3a).[43] The formation constant of the $[(\mathrm{Bn\text{-}TPEN})\mathrm{Mn}^{\mathrm{IV}}(\mathrm{O})]^{2+}$–$(\mathrm{Sc}^{3+})_2$ complex was also determined to be 1.2×10^3 M^{-1} from the titration curve in Figure 1d (see also Figure 3b for the linear plot to determine the formation constant), which is somewhat smaller than that of the

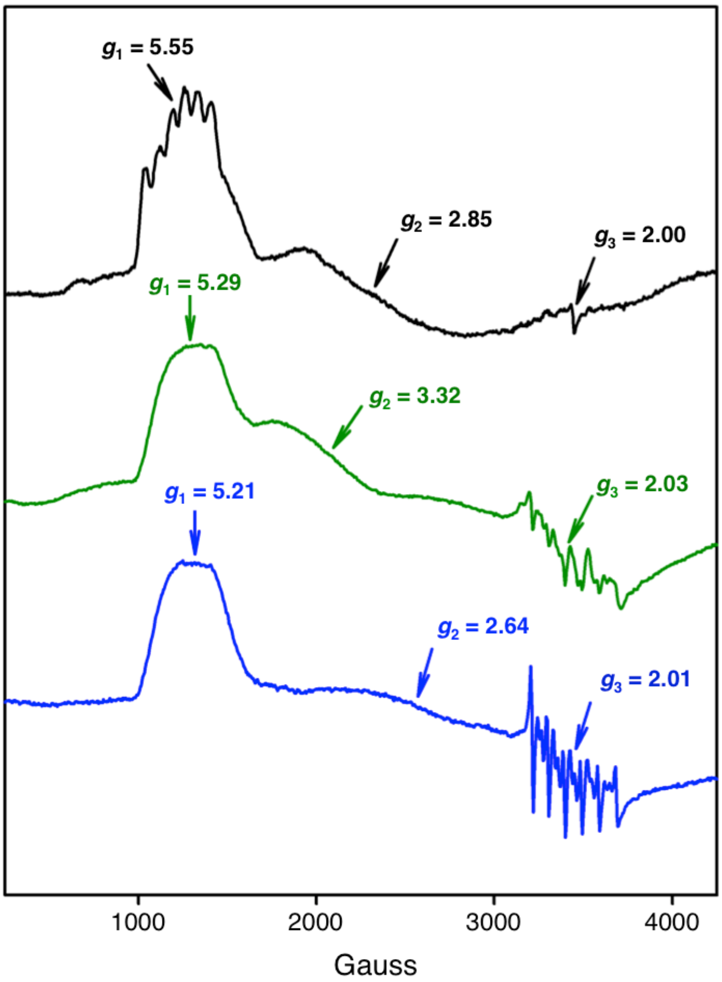

Figure 2. X-band CW-EPR spectra of $[(\mathrm{Bn\text{-}TPEN})\mathrm{Mn}^{\mathrm{IV}}(\mathrm{O})]^{2+}$ (1.0 mM, black line), $[(\mathrm{Bn\text{-}TPEN})\mathrm{Mn}^{\mathrm{IV}}(\mathrm{O})]^{2+}$–$(\mathrm{Sc}^{3+})_1$ (1.0 mM, green line), and $[(\mathrm{Bn\text{-}TPEN})\mathrm{Mn}^{\mathrm{IV}}(\mathrm{O})]^{2+}$–$(\mathrm{Sc}^{3+})_2$ (1.0 mM, blue line). Spectra were recorded in $\mathrm{CF_3CH_2OH\text{-}CH_3CN}$ (v/v = 19:1) at 5 K.

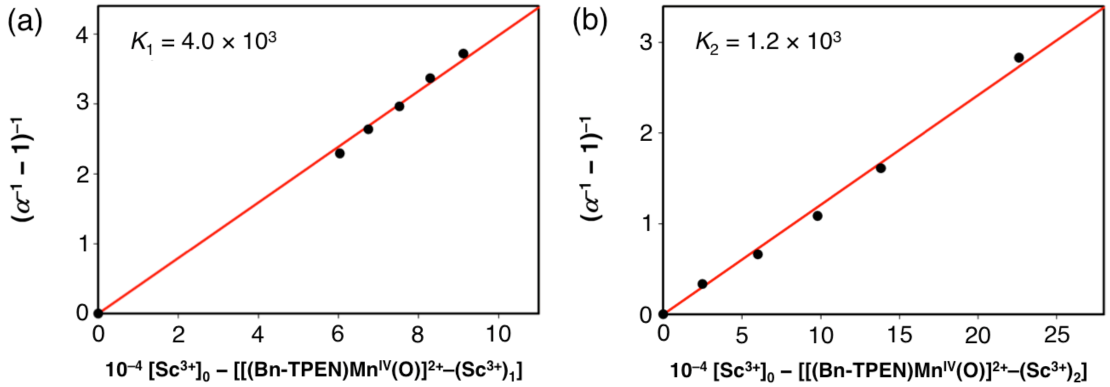

Figure 3. (a) Plot of $(\alpha^{-1} - 1)^{-1}$ vs $[Sc^{3+}]_0 - [[(BnTPEN)Mn^{IV}(O)]^{2+}\text{–}(Sc^{3+})_1]$ to determine the first binding constant ($K_1 = [[Mn^{IV}(O)]^{2+}\text{–}(Sc^{3+})_1]/[[Mn^{IV}(O)]^{2+}][Sc^{3+}]$) upon addition of Sc^{3+} (0.0 – 2.0 mM) into the solution of $[(BnTPEN)Mn^{IV}(O)]^{2+}$ (1.0 mM) in $CF_3CH_2OH\text{-}CH_3CN$ (v/v = 1:1) at 298 K; $\alpha = [[(BnTPEN)Mn^{IV}(O)]^{2+}\text{–}(Sc^{3+})_1]/[[(BnTPEN)Mn^{IV}(O)]^{2+}]_0$. (b) Plot of $(\alpha^{-1} - 1)^{-1}$ vs $[Sc^{3+}]_0 - [[(BnTPEN)Mn^{IV}(O)]^{2+}\text{–}(Sc^{3+})_2]$ to determine the second binding constant ($K_2 = [[Mn^{IV}(O)]^{2+}\text{-}(Sc^{3+})_2]/[[Mn^{IV}(O)]^{2+}\text{–}(Sc^{3+})_1][Sc^{3+}]$) upon addition of Sc^{3+} (0.0 – 12 mM) into the solution of $[(BnTPEN)Mn^{IV}(O)]^{2+}\text{–}(Sc^{3+})_1$ (1.0 mM) in $CF_3CH_2OH\text{-}CH_3CN$ (v/v = 1:1) at 298 K; $\alpha = [[(BnTPEN)Mn^{IV}(O)]^{2+}\text{–}(Sc^{3+})_2]/[[(BnTPEN)Mn^{IV}(O)]^{2+}\text{–}(Sc^{3+})_1]_0$. The expression used for the determination of K_1 and K_2 was derived according to ref 43 in the text.

$[(N4Py)Mn^{IV}(O)]^{2+}\text{–}(Sc^{3+})_2$ complex (6.1 × 10^3 M^{-1}).[37]

The structural details of Sc^{3+} binding was investigated using Mn K-edge EXAFS on **1**, $[(Bn\text{-}TPEN)Mn^{IV}(O)]^{2+}\text{–}(Sc^{3+})_1$ and $[(Bn\text{-}TPEN)Mn^{IV}(O)]^{2+}\text{–}(Sc^{3+})_2$ (see SI, Experimental section for X-ray absorption spectroscopy, Figure S1 and Table S1). The EXAFS results show that on going from no Sc^{3+} binding in **1** to one and two Sc^{3+} binding, the Mn=O bond elongates from 1.69 to 1.74 (2) Å, which is consistent with a weakening of the Mn=O bond. The EXAFS data also reveal a short Mn–Sc distance (3.45 (10) Å), which clearly indicates that Sc^{3+} ions bind to the manganese(IV)-oxo moiety in both $[(Bn\text{-}TPEN)Mn^{IV}(O)]^{2+}\text{–}(Sc^{3+})_1$ and $[(Bn\text{-}TPEN)Mn^{IV}(O)]^{2+}\text{–}(Sc^{3+})_2$. Density functional theory (DFT)[44] calculations of the $Mn^{IV}(O)\text{–}(Sc^{3+})_2$ complex suggested that one Sc^{3+} ion binds directly to the oxo moiety of the manganese(IV)-oxo complex but the second Sc^{3+} ion is located at the secondary coordination sphere (see the DFT-optimized structures in Figure 4).[37,45] As shown previously, the Mn–O bond is elongated upon one Sc^{3+} binding (from 1.68 Å to 1.75 Å), but no further elongation is seen upon binding of the second Sc^{3+} ion (Table S2 in SI). This result is in a good agreement with that obtained from EXAFS experiments. This is also in line with what has been observed previously with $[(N4Py)Mn^{IV}(O)]^{2+}$ (**2**).[37] The significant blue shift

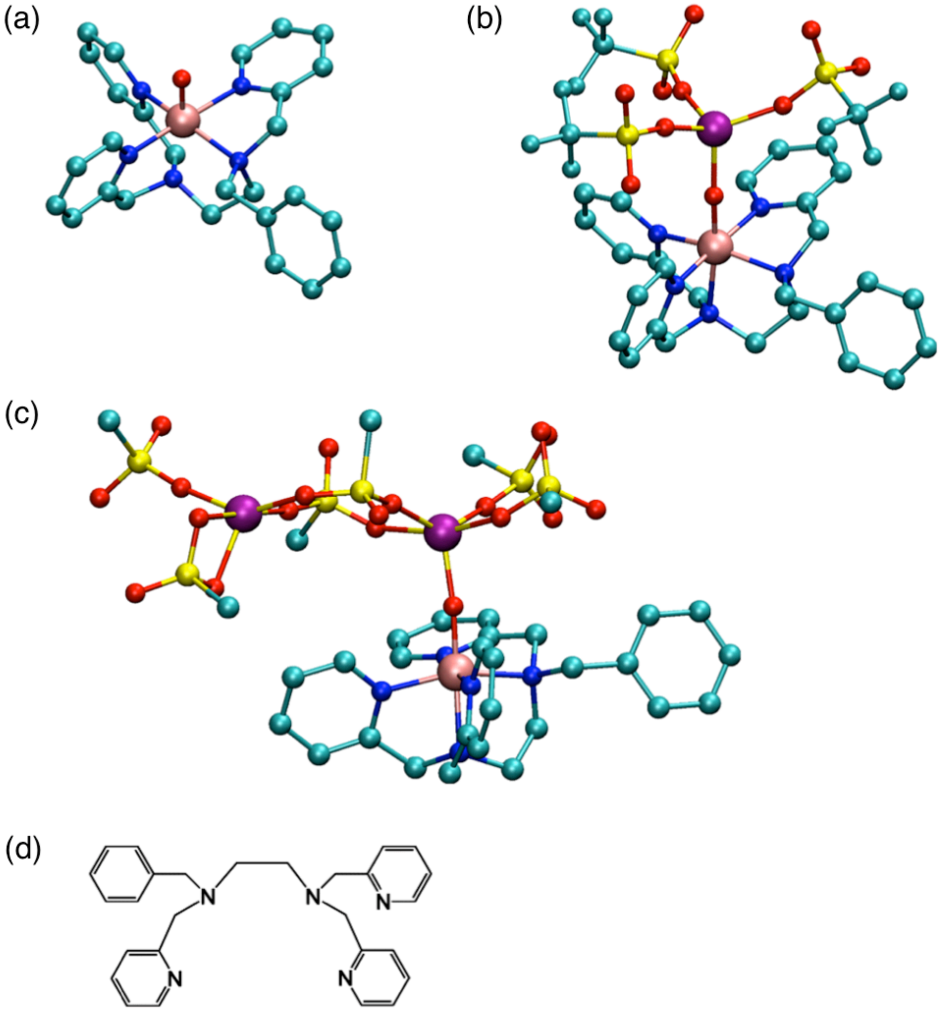

Figure 4. DFT-optimized structures of (a) $[(\text{Bn-TPEN})\text{Mn}^{\text{IV}}(\text{O})]^{2+}$ (**1**), (b) $[(\text{Bn-TPEN})\text{Mn}^{\text{IV}}(\text{O})\text{–Sc}(\text{OTf})_3]^{2+}$, and (c) $[(\text{Bn-TPEN})\text{Mn}^{\text{IV}}(\text{O})\text{–}[\text{Sc}(\text{OTf})_3]_2]^{2+}$, calculated at the B3LYP/LACVP level in the solvent phase. The Mn–O bond lengths of $[\text{Mn}^{\text{IV}}(\text{O})]^{2+}$, $[\text{Mn}^{\text{IV}}(\text{O})]^{2+}\text{–Sc}^{3+}$, and $[\text{Mn}^{\text{IV}}(\text{O})]^{2+}\text{–}(\text{Sc}^{3+})_2$ were calculated to be 1.68, 1.75, and 1.75 Å, respectively (see the DFT Calculations Section in the SI for computational details). H atoms in Bn-TPEN and F atoms in the OTf– counterions have been omitted for clarity (Mn, pink; N, blue; O, red; C, green; Sc, purple; S, yellow). (d) Schematic drawing of the Bn-TPEN ligand.

in the absorption band of the $\text{Mn}^{\text{IV}}(\text{O})\text{–}(\text{Sc}^{3+})_2$ complex as compared with that of the $\text{Mn}^{\text{IV}}(\text{O})\text{–}(\text{Sc}^{3+})_1$ complex indicates that the electronic state of the $\text{Mn}^{\text{IV}}(\text{O})$ moiety is somewhat perturbed by binding of the second Sc^{3+} ion, but the conservation of the core geometry in $\text{Mn}^{\text{IV}}(\text{O})\text{–}(\text{Sc}^{3+})_2$, compared to $\text{Mn}^{\text{IV}}(\text{O})\text{–}(\text{Sc}^{3+})_1$, suggests that the changes mostly affect the unoccupied virtual orbitals (such as σ^*_{xy}). The blue-shift indicates that the virtual orbitals are shifted higher in energy, hence stabilizing the occupied orbitals.[46]

The Mulliken spin density distribution shows negligible spin on the Sc^{3+} or counter-anion atoms in all cases, while showing around three radicals in total for the Mn(O)-5xN moiety (Table S3 in SI), indicating that the manganese(IV)-oxo configuration is kept after Sc^{3+} binding. Indeed, natural orbital analysis showed that the valence orbital occupation was (δ, π^*_{xz}, π^*_{yz}) corresponding to high-spin manganese(IV)-oxo. In addition, none of the nine valence manganese(IV)-oxo orbitals with Mn *d*-orbital elements in it is mixing with Sc^{3+} orbitals, indicating a pure ionic $Mn^{IV}(O)–Sc^{3+}$ bond despite the short distance (1.94 Å). Hence, the $Mn^{IV}–O$ bond elongation can be attributed to pure Coulomb interactions rather than to changes in the electronic structure.

Positive Shifts in One-Electron Reduction Potentials of Nonheme Manganese(IV)-Oxo Complexes by Binding of Sc^{3+} Ions. Electron transfer from ferrocene derivatives to manganese(IV)-oxo complexes **1** and **2** occurred to completion in CF_3CH_2OH-CH_3CN (v/v = 1:1) at 273 K (Figure 5a). The solvent mixture was used due to the solubility of electron donors and the stability of **1** and **2**; both of which are quite stable at 273 K. The redox titration for formation of Br_2Fc^+ in Figure 3b indicates only one-electron reduction of **2** occurred without further reduction by Br_2Fc (see Table 1 for E_{ox} values of electron donors). This result is in agreement with the result of the redox titration of **1** with Br_2Fc reported previously.[41b]

When ferrocene derivatives were replaced by a weaker reductant such as $[Ru^{II}(bpy)_3]^{2+}$ (bpy = 2.2'-bipyridine; E_{ox} = 1.24 V vs SCE), no electron transfer was observed. This is consistent with the lower one-electron reduction potential of **1** (E_{red} = 0.78 V vs SCE), as reported previously.[41b] The E_{red} value of **2** was also determined to be 0.80 V vs SCE by the redox titration using Br_2Fc (E_{ox} = 0.71 V vs SCE) (Figure 5b).

When the $Mn^{IV}(O)–(Sc^{3+})_1$ complex of **1** was employed with two equiv of $Sc(OTf)_3$ (2.0 mM), electron transfer from $[Ru^{II}(bpy)_3]^{2+}$ to the $Mn^{IV}(O)–(Sc^{3+})_1$ complex became energetically feasible to occur as shown in Figure 6a, where the absorption band (λ_{max} = 650 nm) due to $[Ru^{III}(bpy)_3]^{3+}$ increased. In this case, however, the electron transfer from $[Ru^{II}(bpy)_3]^{2+}$ to the $Mn^{IV}(O)–(Sc^{3+})_1$ complex was not complete with two equiv of $[Ru^{II}(bpy)_3]^{2+}$. Figure 6b shows the titration curve of the electron-transfer reaction, suggesting that electron transfer from $[Ru^{II}(bpy)_3]^{2+}$ to the $Mn^{IV}(O)–(Sc^{3+})_1$ complex is in equilibrium with back electron transfer from the $Mn^{III}(O)–(Sc^{3+})_1$ complex to

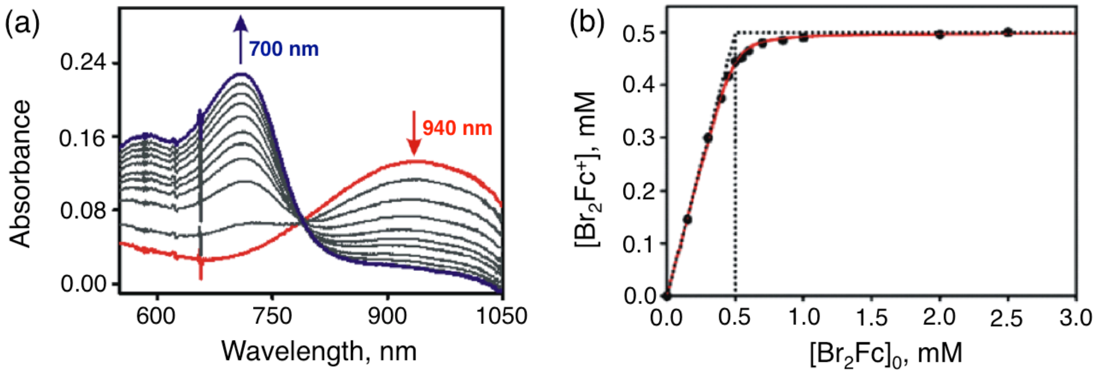

Figure 5. Absorption spectral changes observed in electron transfer from dibromoferrocene (Br_2Fc; 5.0 × 10^{-3} M) to $[(N4Py)Mn^{IV}(O)]^{2+}$ (**2**; 5.0 × 10^{-4} M) in CF_3CH_2OH-CH_3CN (v/v = 1:1) at 273 K. (b) Plot of concentration of Br_2Fc^+ produced in electron transfer from Br_2Fc to **2** vs initial concentration of Br_2Fc, $[Br_2Fc]_0$.

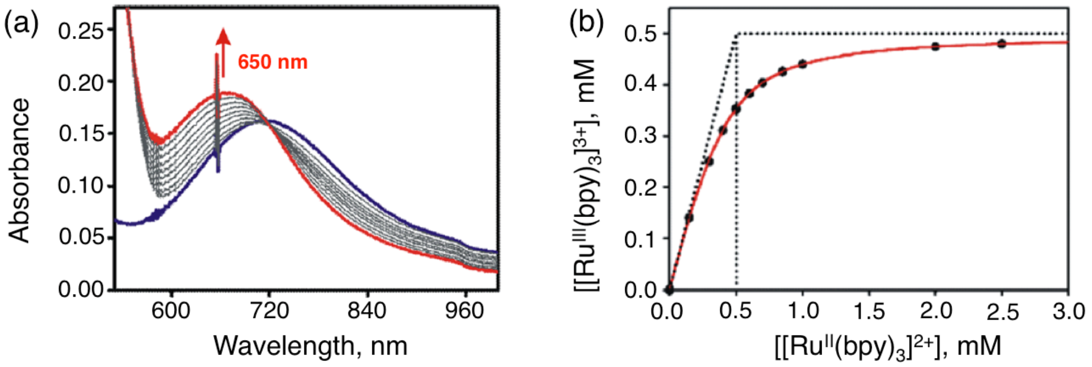

Figure 6. (a) Absorption spectral changes observed in electron transfer from $[Ru^{II}(bpy)]^{2+}$ (5.0 × 10^{-3} M) to $[(Bn\text{-}TPEN)Mn^{IV}(O)]^{2+}$–$Sc^{3+}$ (5.0 × 10^{-4} M) in CF_3CH_2OH-CH_3CN (v/v = 1:1) at 273 K. (b) Plot of concentration of $[Ru^{III}(bpy)_3]^{3+}$ produced in electron transfer from $[Ru^{II}(bpy)_3]^{2+}$ to $[(Bn\text{-}TPEN)Mn^{IV}(O)]^{2+}$–$Sc^{3+}$ vs initial concentration of $[Ru^{II}(bpy)_3]^{2+}$, $[[Ru^{II}(bpy)_3]^{2+}]_0$.

$[Ru^{III}(bpy)_3]^{3+}$ (eq 1, where K_{et} is the electron-transfer equilibrium constant).

$$[Ru^{II}(bpy)]^{2+} + [Mn^{IV}(O)]^{2+}\text{–}Sc^{3+} \overset{K_{et}}{\rightleftharpoons} [Ru^{III}(bpy)]^{3+} + [Mn^{III}(O)]^{+}\text{–}Sc^{3+} \quad (1)$$

From the redox titration curve in Figure 6b, the K_{et} value was determined to be 5.7 (see a linear plot to determine the K_{et} value in Figure 7d).[43] The E_{red} value of 1.28 V vs SCE for $[(Bn\text{-}TPEN)Mn^{IV}(O)]^{2+}$–$(Sc^{3+})_1$ was determined from the K_{et} value and the E_{ox} value of $[Ru^{II}(bpy)_3]^{2+}$ (1.24 V vs SCE) using the Nernst equation (eq 2). This E_{red} value

Table 1. One-Electron Oxidation Potentials (E_{ox}) of Electron Donors and Second-Order Rate Constants of Electron Transfer from Electron Donors to $[(\mathrm{N4Py})\mathrm{Mn}^{\mathrm{IV}}(\mathrm{O})]^{2+}$ in the Absence and Presence of $\mathrm{Sc(OTf)_3}$ (10 mM) with Driving Force of Electron Transfer ($-\Delta G_{\mathrm{et}}$) in $\mathrm{CF_3CH_2OH}$-$\mathrm{CH_3CN}$ (v/v = 1:1) at 273 K.

electron donor	E_{ox} (V vs SCE)[a]	$[(\mathrm{Bn\text{-}TPEN})\mathrm{Mn}^{\mathrm{IV}}(\mathrm{O})]^{2+\,a}$		$[(\mathrm{N4Py})\mathrm{Mn}^{\mathrm{IV}}(\mathrm{O})]^{2+}$	
		k_{obs}, $\mathrm{M^{-1}\,s^{-1}}$	$-\Delta G_{\mathrm{et}}$, eV	k_{obs}, $\mathrm{M^{-1}\,s^{-1}}$	$-\Delta G_{\mathrm{et}}$, eV
dimethylferrocene	0.26	$(1.0 \pm 0.1) \times 10^5$	0.52	-	
ferrocene	0.37	$(6.1 \pm 0.3) \times 10^3$	0.41	$(8.2 \pm 0.1) \times 10^3$	0.43
bromoferrocene	0.54	$(9.3 \pm 0.1) \times 10^2$	0.24	$(8.4 \pm 0.3) \times 10^2$	0.26
acetylferrocene	0.62	$(9.3 \pm 0.2) \times 10$	0.16	$(8.2 \pm 0.2) \times 10$	0.18
dibromoferrocene	0.71	$(3.1 \pm 0.1) \times 10$	0.07	$(4.3 \pm 0.1) \times 10$	0.09
electron donor	E_{ox} (V vs SCE)[b]	$[(\mathrm{Bn\text{-}TPEN})\mathrm{Mn}^{\mathrm{IV}}(\mathrm{O})]^{2+}$–$(\mathrm{Sc}^{3+})_2$		$[(\mathrm{N4Py})\mathrm{Mn}^{\mathrm{IV}}(\mathrm{O})]^{2+}$–$(\mathrm{Sc}^{3+})_2$	
		k_{obs}, $\mathrm{M^{-1}\,s^{-1}}$	$-\Delta G_{\mathrm{et}}$, eV	k_{obs}, $\mathrm{M^{-1}\,s^{-1}}$	$-\Delta G_{\mathrm{et}}$, eV
$[\mathrm{Fe^{II}(Me_2\text{-}phen)_3}]^{2+}$	0.94	$(1.7 \pm 0.2) \times 10^5$	0.42	$(2.3 \pm 0.1) \times 10^5$	0.48
$[\mathrm{Fe^{II}(Ph_2\text{-}phen)_3}]^{2+}$	1.02	$(2.1 \pm 0.1) \times 10^4$	0.34	$(2.4 \pm 0.4) \times 10^4$	0.40
$[\mathrm{Fe^{II}(bpy)_3}]^{2+}$	1.06	$(3.6 \pm 0.1) \times 10^3$	0.30	$(6.9 \pm 0.1) \times 10^3$	0.36
$[\mathrm{Fe^{II}(5\text{-}Cl\text{-}phen)_3}]^{2+}$	1.20	$(4.1 \pm 0.8) \times 10^2$	0.16	$(4.1 \pm 0.2) \times 10^2$	0.22
$[\mathrm{Ru^{II}(bpy)_3}]^{2+}$	1.24	$(7.3 \pm 0.1) \times 10$	0.12	$(6.4 \pm 0.3) \times 10$	0.18

[a]Taken from ref 41b. b Taken from ref 30b.

is significantly more positive than the E_{red} value of **1** (0.78 V vs SCE), which was reported previously.[41b]

$$E_{\mathrm{red}} = E_{\mathrm{ox}} + (RT/F)\ln K_{\mathrm{xet}} \qquad (2)$$

Similarly, the E_{red} values of **1** and **2** in the presence of various concentrations of $\mathrm{Sc(OTf)_3}$ were determined from the K_{et} values obtained by the redox titrations with $[\mathrm{Ru^{II}(bpy)_3}]^{2+}$ (E_{ox} = 1.24 V vs SCE) and $[\mathrm{Ru^{II}(5\text{-}Cl\text{-}phen)_3}]^{2+}$ (5-Cl-phen = 5-chloro-1,10-phenanthroline; E_{ox} = 1.36 V vs SCE) (see Figures 7 and 8). Figure 9 shows plots of E_{red} of **1** and **2** in the presence of various concentrations of $\mathrm{Sc(OTf)_3}$. The E_{red} values of **1** and **2** were shifted from 0.78 and 0.80 V vs SCE in the absence of $\mathrm{Sc(OTf)_3}$ to 1.28 and 1.31 V vs SCE in the presence of one equiv (for N4Py) or two equiv (for Bn-TPEN) of $\mathrm{Sc(OTf)_3}$, which correspond to the E_{red} values of the $[\mathrm{Mn^{IV}(O)}]^{2+}$–$\mathrm{Sc}^{3+}$ complexes of **1** and **2**, respectively. The E_{red} values increase with increasing concentration of $\mathrm{Sc(OTf)_3}$ to reach constant values with more than six equiv

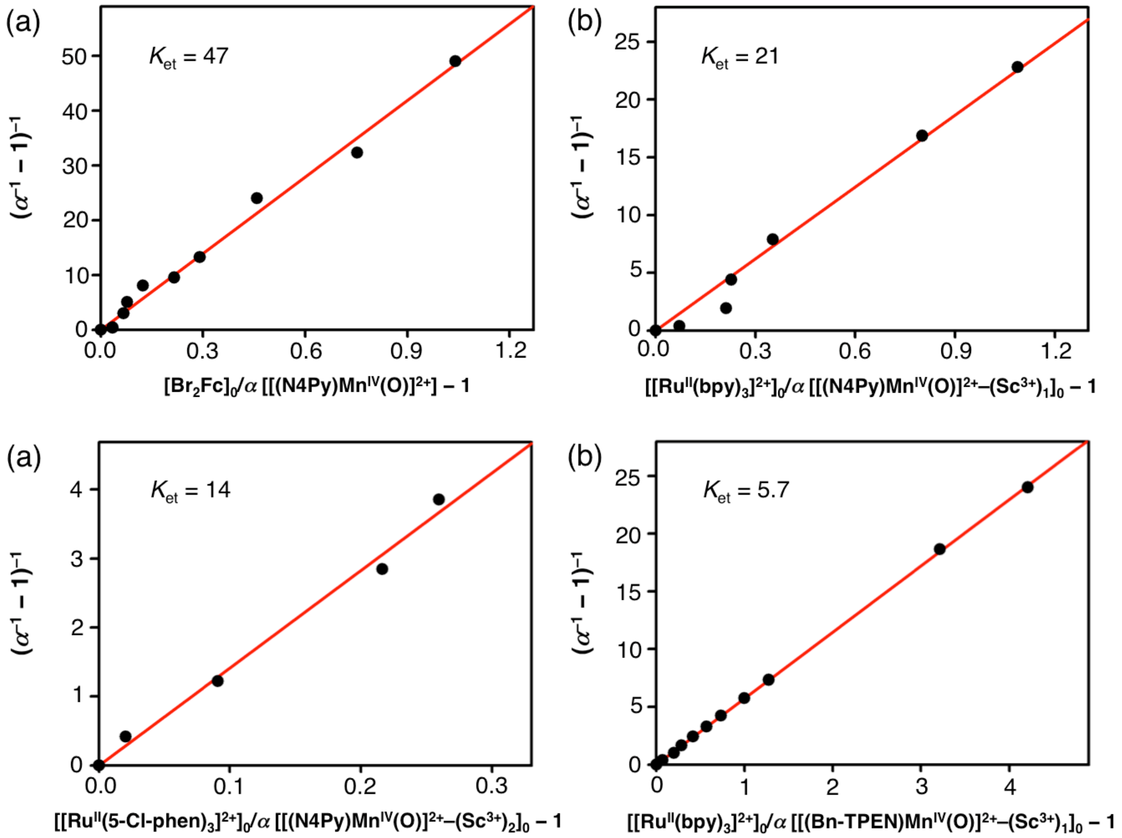

Figure 7. (a) Plot of $(\alpha^{-1} - 1)^{-1}$ vs $[\mathrm{Br_2Fc}]_0/\alpha[[(\mathrm{N4Py})\mathrm{Mn^{IV}(O)}]^{2+}]_0 - 1$ to determine equilibrium constants ($K_{\mathrm{et}} = [\mathrm{Br_2Fc^+}][[\mathrm{Mn^{III}(O)}]^+]/[\mathrm{Br_2Fc}][[\mathrm{Mn^{IV}(O)}]^{2+}]$) for electron transfer from $\mathrm{Br_2Fc}$ to $[(\mathrm{N4Py})\mathrm{Mn^{IV}(O)}]^{2+}$ upon addition of $\mathrm{Br_2Fc}$ (0.0 – 2.5 mM) into the solution of $[(\mathrm{N4Py})\mathrm{Mn^{IV}(O)}]^{2+}$ (0.50 mM) in $\mathrm{CF_3CH_2OH\text{-}CH_3CN}$ (v/v = 1:1) at 273 K ($\alpha = [\mathrm{Br_2Fc^+}]/[[(\mathrm{N4Py})\mathrm{Mn^{IV}(O)}]^{2+}]_0$). The slope of the linear plot corresponds to K_{et}. The linear correlation can be derived from the electron-transfer equilibrium in eq 1. The same analyses were performed to determine the K_{et} values for $(\mathrm{N4Py})\mathrm{Mn^{IV}(O)}]^{2+}\text{–}(\mathrm{Sc^{3+}})_1$ (b), $[(\mathrm{N4Py})\mathrm{Mn^{IV}(O)}]^{2+}\text{–}(\mathrm{Sc^{3+}})_2$ (c), and $(\mathrm{Bn\text{-}TPEN})\mathrm{Mn^{IV}(O)}]^{2+}\text{–}(\mathrm{Sc^{3+}})_1$ (d). (b) Plot of $(\alpha^{-1} - 1)^{-1}$ vs $[[\mathrm{Ru^{II}(bpy)_3}]^{2+}]_0/\alpha[[(\mathrm{N4Py})\mathrm{Mn^{IV}(O)}]^{2+}\text{–}(\mathrm{Sc^{3+}})_1]_0 - 1$ ($\alpha = [[\mathrm{Ru^{III}(bpy)_3}]^{3+}]/[[(\mathrm{N4Py})\mathrm{Mn^{IV}(O)}]^{2+}\text{–}(\mathrm{Sc^{3+}})_1]_0$). (c) Plot of $(\alpha^{-1} - 1)^{-1}$ vs $[[\mathrm{Ru^{II}(5\text{-}Cl\text{-}phen)_3}]^{2+}]_0/\alpha[[(\mathrm{N4Py})\mathrm{Mn^{IV}(O)}]^{2+}\text{–}(\mathrm{Sc^{3+}})_2]_0 - 1$ ($\alpha = [[\mathrm{Ru^{III}(5\text{-}Cl\text{-}phen)_3}]^{3+}]/[[(\mathrm{N4Py})\mathrm{Mn^{IV}(O)}]^{2+}\text{–}(\mathrm{Sc^{3+}})_2]_0$). (d) Plot of $(\alpha^{-1} - 1)^{-1}$ vs $[[\mathrm{Ru^{II}(bpy)_3}]^{2+}]_0/\alpha[[(\mathrm{BnTPEN})\mathrm{Mn^{IV}(O)}]^{2+}\text{–}(\mathrm{Sc^{3+}})_1]_0 - 1$ ($\alpha = [[\mathrm{Ru^{III}(bpy)_3}]^{3+}]/[[(\mathrm{BnTPEN})\mathrm{Mn^{IV}(O)}]^{2+}\text{–}(\mathrm{Sc^{3+}})_1]_0$.

of $\mathrm{Sc(OTf)_3}$. This is consistent with the UV-vis spectral change to produce the $[\mathrm{Mn^{IV}(O)}]^{2+}\text{–}(\mathrm{Sc^{3+}})_2$ complex in Figure 1b. The saturated E_{red} values of 1.36 and 1.42 V vs SCE in the presence of large excess $\mathrm{Sc(OTf)_3}$ correspond to those of the $[\mathrm{Mn^{IV}(O)}]^{2+}\text{–}(\mathrm{Sc^{3+}})_2$ complexes of **1** and **2**, respectively. These E_{red} values are summarized in Table 2. There is a large difference in the E_{red} values between

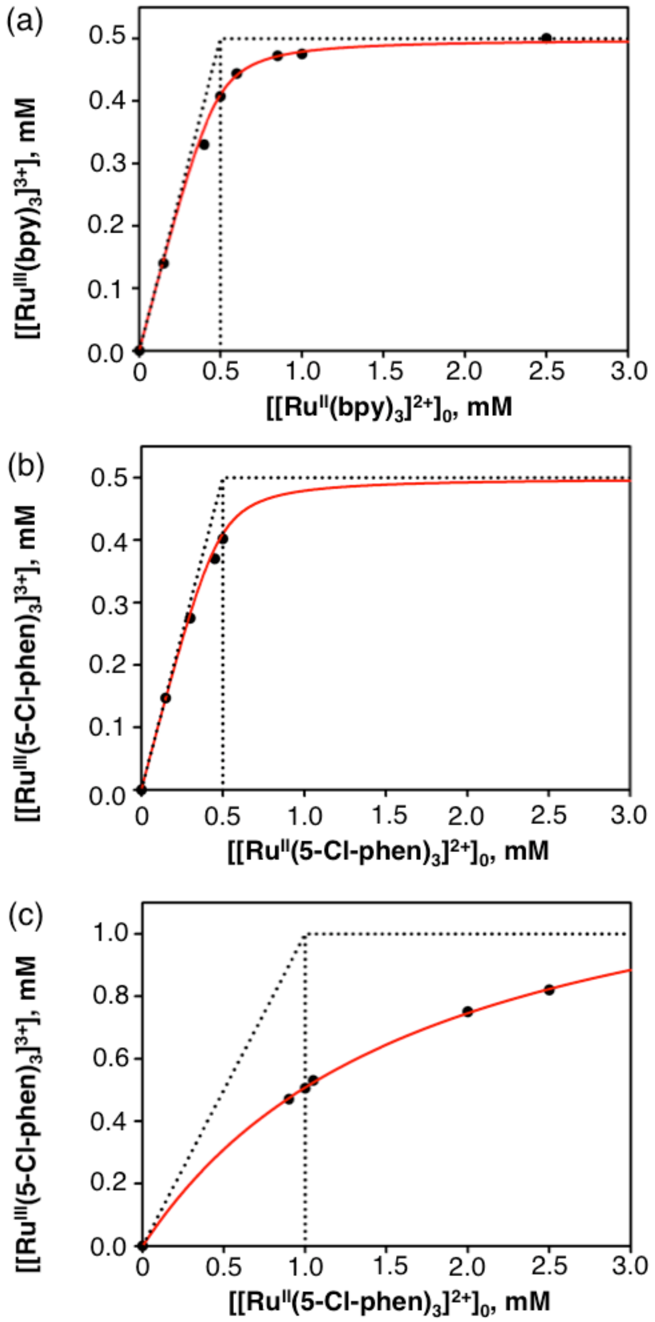

Figure 8. (a) Plot of concentration of $[Ru^{III}(bpy)_3]^{3+}$ produced in electron transfer from $[Ru^{II}(bpy)_3]^{2+}$ (1.24 V vs SCE) to $[(N4Py)Mn^{IV}(O)]^{2+}$–$(Sc^{3+})_1$ vs initial concentration of $[Ru^{II}(bpy)_3]^{2+}$ in CF_3CH_2OH-CH_3CN (*v*/*v* = 1:1) at 273 K. (b) Plot of concentration of $[Ru^{III}(5\text{-Cl-phen})_3]^{3+}$ produced in electron transfer from $[Ru^{II}(5\text{-Cl-pehn})_3]^{2+}$ (1.36 V vs SCE) to $[(N4Py)Mn^{IV}(O)]^{2+}$–$(Sc^{3+})_2$ vs initial concentration of $[Ru^{II}(5\text{-Cl-phen})_3]^{2+}$ in CF_3CH_2OH-CH_3CN (*v*/*v* = 1:1) at 273 K. (c) Plot of concentration of $[Ru^{III}(5\text{-Cl-phen})_3]^{3+}$ produced in electron transfer from $[Ru^{II}(5\text{-Cl-phen})_3]^{2+}$ to $[(Bn\text{-}TPEN)Mn^{IV}(O)]^{2+}$–$(Sc^{3+})_2$ vs initial concentration of $[Ru^{II}(5\text{-Cl-phen})_3]^{2+}$ in CF_3CH_2OH-CH_3CN (*v*/*v* = 1:1) at 273 K.

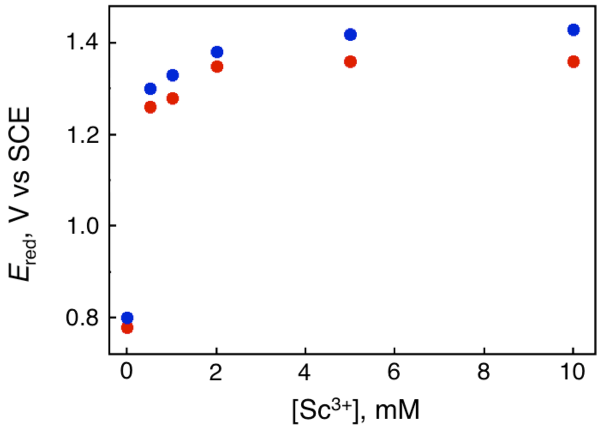

Figure 9. Dependence of E_{red} of $[(N4Py)Mn^{IV}(O)]^{2+}$ (blue circles) and $[(Bn\text{-}TPEN)Mn^{IV}(O)]^{2+}$ (red circles) on [Sc^{3+}] in CF_3CH_2OH-CH_3CN (*v*/*v* = 1:1) at 273 K. The E_{red} values were determined from the equilibrium constants (K_{et}) between one electron donors and $[(N4Py)Mn^{IV}(O)]^{2+}$.

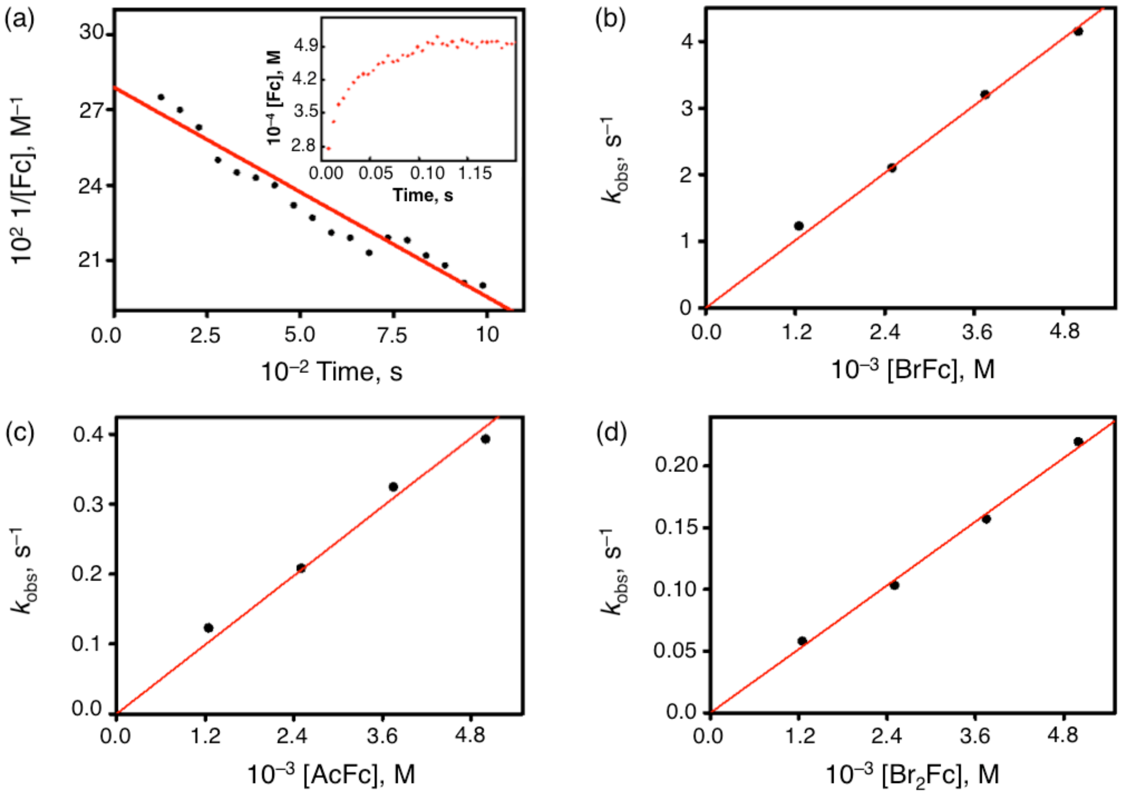

Figure 10. (a) Second-order-plot of 1/[Fc] vs time for electron transfer from ferrocene (5.0×10^{-3} M) to $[(N4Py)Mn^{IV}(O)]^{2+}$ (5.0×10^{-3} M). Inset shows time course of the absorbance change monitored at 615 nm due to ferrocenium ion (ε_{615} = 400 M^{-1} cm^{-1}). (b, c, d) Plots of pseudo-first-order rate constant (k_{obs}) vs concentrations of ferrocene derivatives to determine the second-order rate constants of electron transfer from ferrocene derivatives [(b) bromoferrocene (BrFc), (c) acetylferrocene (AcFc), and (d) dibromoferrocene (Br_2Fc)] to $[(N4Py)Mn^{IV}(O)]^{2+}$ (5.0×10^{-3} M) in CF_3CH_2OH-CH_3CN (*v*/*v* = 1:1) at 273 K.

$[\mathrm{Mn^{IV}(O)}]^{2+}$ and $[\mathrm{Mn^{IV}(O)}]^{2+}$–$\mathrm{Sc^{3+}}$, indicating that the binding of $\mathrm{Sc^{3+}}$ to $[\mathrm{Mn^{III}(O)}]^{+}$ is much stronger than that to $[\mathrm{Mn^{IV}(O)}]^{2+}$ as expected from the increased basicity of the oxo moiety in $[\mathrm{Mn^{III}(O)}]^{+}$. The smaller difference in E_{red} between $[\mathrm{Mn^{IV}(O)}]^{2+}$–$(\mathrm{Sc^{3+}})_1$ and $[\mathrm{Mn^{IV}(O)}]^{2+}$–$(\mathrm{Sc^{3+}})_2$ may support the previous conclusion based on XANES/EXAFS analysis together with DFT calculations: second $\mathrm{Sc^{3+}}$ ion is located at the secondary coordination sphere rather than direct binding to the oxo moiety.[37]

Comparison of Electron-Transfer Reactivity of Nonheme $\mathrm{Mn^{IV}(O)}$ Complexes with and without $\mathrm{Sc^{3+}}$ Ions. A remarkable positive shift of E_{red} values of $[\mathrm{Mn^{IV}(O)}]^{2+}$ complexes by binding one or two $\mathrm{Sc^{3+}}$ ions predicts the much enhanced electron-transfer reactivity. Rate constants of electron transfer from various electron donors to **1** and **2** in the absence and presence of $\mathrm{Sc^{3+}}$ were determined by monitoring the absorbance changes in reaction solutions due to the oxidized electron donors. Rates of electron transfer in the absence of $\mathrm{Sc^{3+}}$ obeyed pseudo-first-order kinetics in the presence of large excess of electron donors, and the observed pseudo-first-order rate constants (k_{obs}) increased linearly with no intercept with concentrations of electron donors (Figure 10). Rate constants of electron transfer from one-electron reductants to **1** and **2** in the presence of $\mathrm{Sc^{3+}}$ were determined under second-order reaction conditions (Figures 11 and 12). The k_{et} values increased with increasing concentration of $\mathrm{Sc^{3+}}$ in the conversion of $[\mathrm{Mn^{IV}(O)}]^{2+}$ to $[\mathrm{Mn^{IV}(O)}]^{2+}$–$(\mathrm{Sc^{3+}})_2$ (Figure 13). The k_{et} values thus determined are listed in Table 1 along with the one-electron oxidation potentials (E_{ox}) of donors and the driving force of electron transfer ($-\Delta G_{\mathrm{et}}$).

Figure 14 shows comparison of dependence of k_{et} on E_{ox} of electron donors for electron transfer from electron donors to $[(\text{Bn-TPEN})\mathrm{Mn^{IV}(O)}]^{2+}$ (**1**) with that of electron transfer to $[(\text{Bn-TPEN})\mathrm{Mn^{IV}(O)}]^{2+}$–$(\mathrm{Sc^{3+}})_2$ in the absence and presence of $\mathrm{Sc(OTf)_3}$ (5.0 mM) in $\mathrm{CF_3CH_2OH}$-$\mathrm{CH_3CN}$ (v/v = 1:1) at 273 K. The k_{et} values of $[\mathrm{Mn^{IV}(O)}]^{2+}$–$(\mathrm{Sc^{3+}})_2$ are much larger than those of $[\mathrm{Mn^{IV}(O)}]^{2+}$.

The driving force dependences of the rate constants of electron transfer from electron donors to $[\mathrm{Mn^{IV}(O)}]^{2+}$ and $[\mathrm{Mn^{IV}(O)}]^{2+}$–$(\mathrm{Sc^{3+}})_2$ for **1** are shown in Figure 15, where two different plots in Figure 14 are largely unified. The driving force dependence of log k_{et} is well fitted by the solid line in Figure 15 in light of the Marcus theory of adiabatic outer-sphere electron transfer (eq 3),[47]

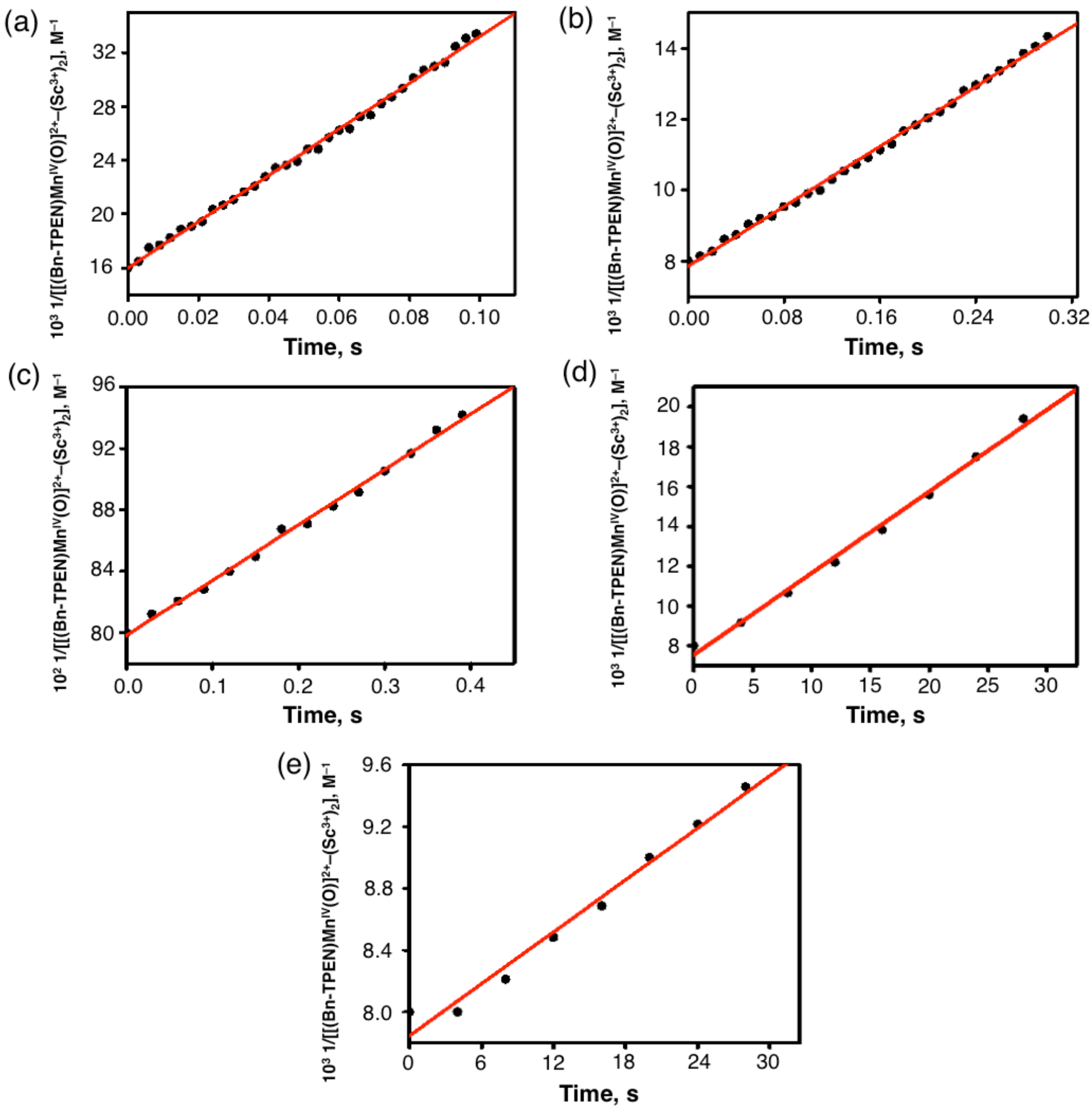

Figure 11. Second-order-plots of 1/[[(Bn-TPEN)Mn^{IV}(O)]$^{2+}$–(Sc^{3+})$_2$] vs time for electron transfer from one-electron reductants (1.25 × 10^{-5} M; (a) [Fe^{II}(Me$_2$-bpy)$_3$]$^{2+}$, (b) [Fe^{II}(Ph$_2$-phen)$_3$]$^{2+}$, (c) [Fe^{II}(bpy)$_3$]$^{2+}$, (d) [Fe^{II}(5-Cl-phen)$_3$]$^{2+}$, and (e) [Ru^{II}(bpy)$_3$]$^{2+}$) to [(Bn-TPEN)Mn^{IV}(O)]$^{2+}$–(Sc^{3+})$_2$ (1.25 × 10^{-5} M) in CF$_3$CH$_2$OH-CH$_3$CN (v/v = 1:1) at 273 K.

$$k_{\mathrm{et}} = Z\exp[-(\lambda/4)(1 + \Delta G_{\mathrm{et}}/\lambda)^2/k_{\mathrm{B}}T] \qquad (3)$$

where Z is the collision frequency taken as 1 × 10^{11} M^{-1} s^{-1}, λ is the reorganization energy of electron transfer, k_{B} is the Boltzmann constant, and T is the absolute temperature. The closer look of the fitting afforded slightly different λ values, such as one for [(Bn-TPEN)Mn^{IV}(O)]$^{2+}$ (2.24 ± 0.03 eV) and the other for

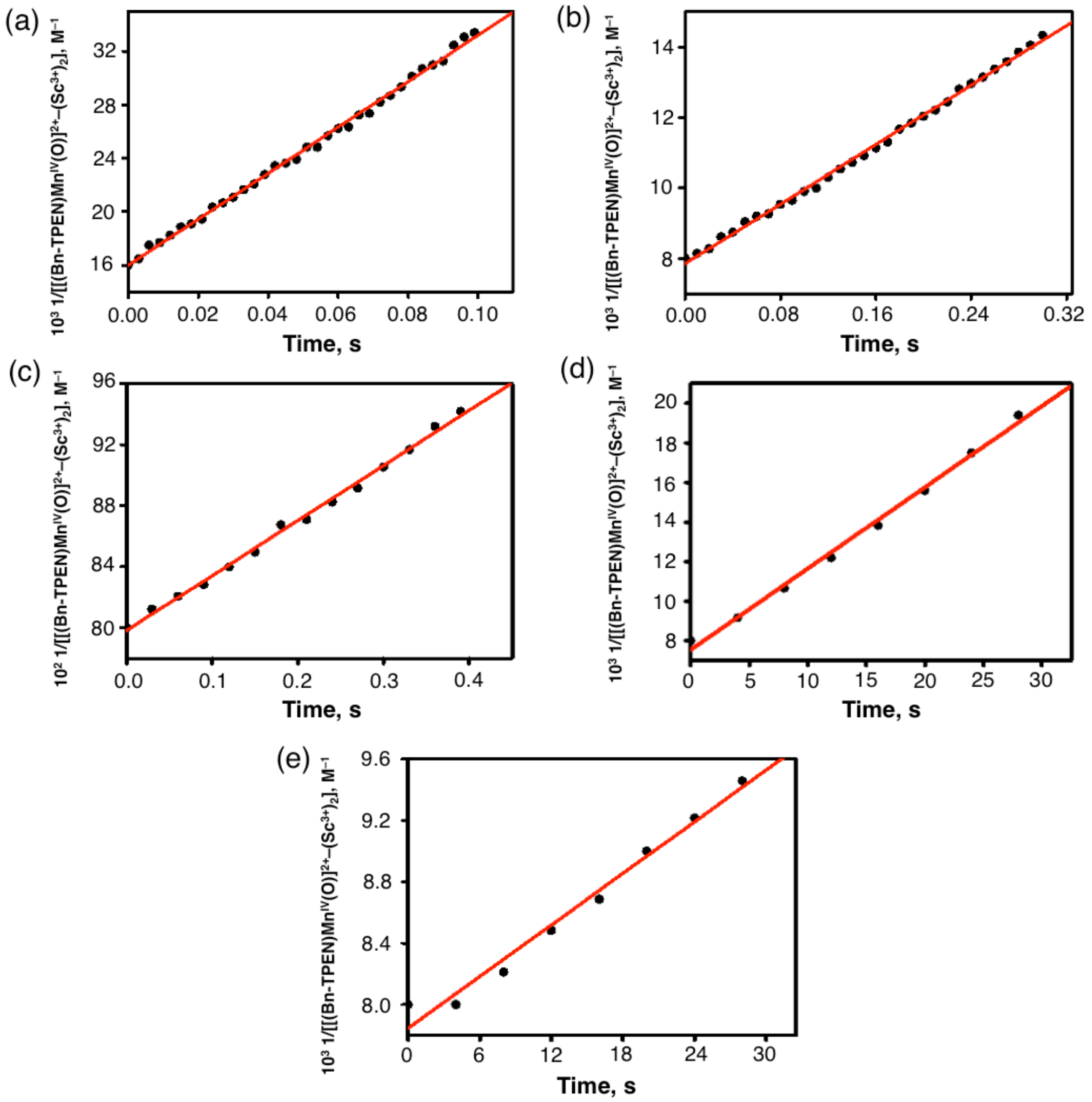

Figure 11. Second-order-plots of 1/[[(Bn-TPEN)Mn^{IV}(O)]$^{2+}$–(Sc^{3+})$_2$] vs time for electron transfer from one-electron reductants (1.25×10^{-5} M; (a) [Fe^{II}(Me_2-bpy)$_3$]$^{2+}$, (b) [Fe^{II}(Ph_2-phen)$_3$]$^{2+}$, (c) [Fe^{II}(bpy)$_3$]$^{2+}$, (d) [Fe^{II}(5-Cl-phen)$_3$]$^{2+}$, and (e) [Ru^{II}(bpy)$_3$]$^{2+}$) to [(Bn-TPEN)Mn^{IV}(O)]$^{2+}$–(Sc^{3+})$_2$ (1.25×10^{-5} M) in CF_3CH_2OH-CH_3CN (*v*/*v* = 1:1) at 273 K.

[(Bn-TPEN)Mn^{IV}(O)]$^{2+}$–(Sc^{3+})$_2$ (2.12 ± 0.02 eV). Similarly, the other λ values were determined with the E_{red} values, as listed in Table 2.

The λ values of the electron-transfer reduction of [Mn^{IV}(O)]$^{2+}$ are similar to those determined for the electron-transfer reduction of iron(IV)-oxo complexes.[23b] This indicates that the one-electron reduction of high-valent metal-oxo complexes generally requires a large reorganization energy probably due to the significant elongation of

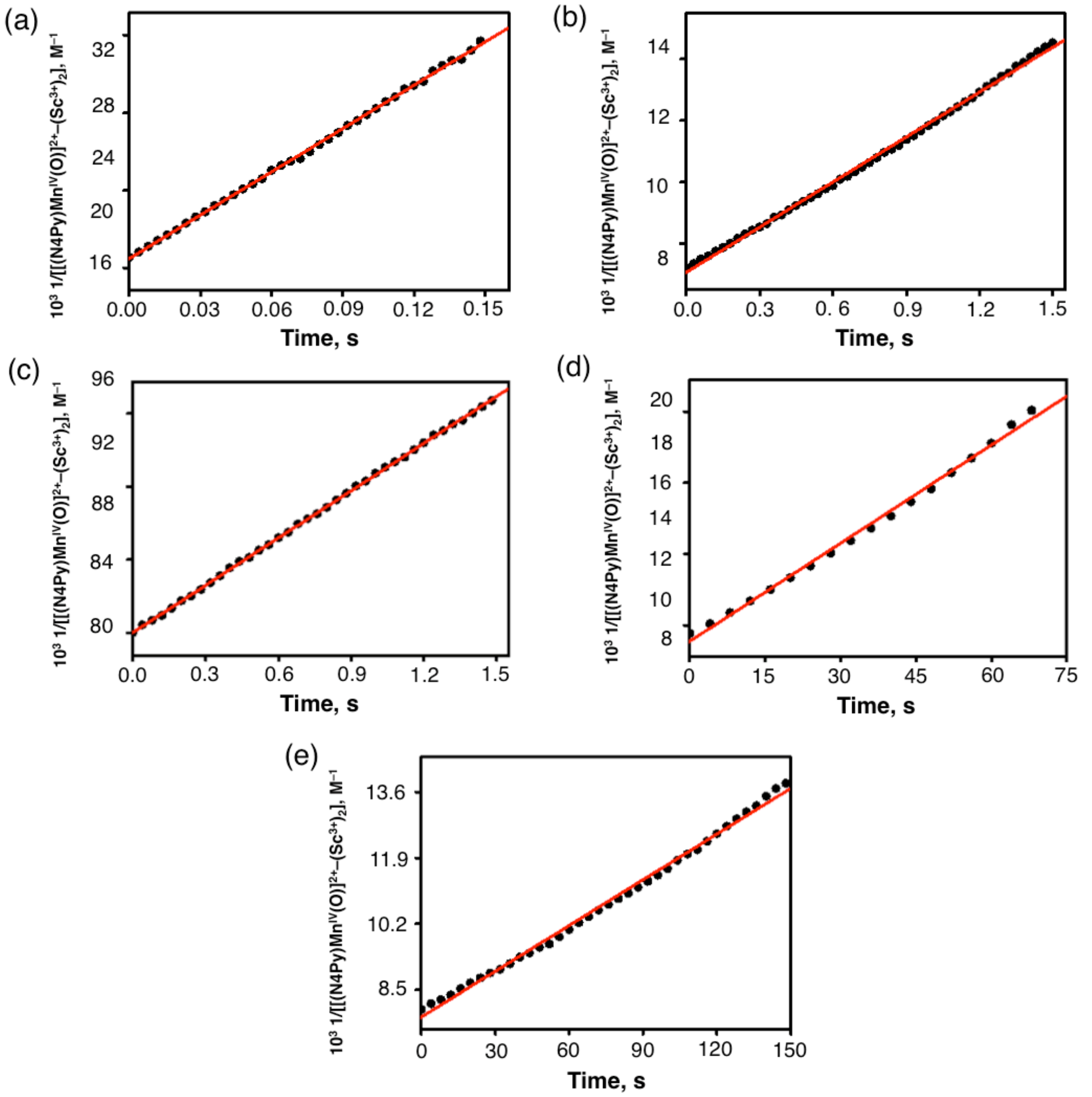

Figure 12. Second-order-plots of 1/[[(Bn-TPEN)Mn^{IV}(O)]$^{2+}$–(Sc^{3+})$_2$] vs time for electron transfer from one-electron reductants (1.25 × 10^{-5} M; (a) [Fe^{II}(Me$_2$-bpy)$_3$]$^{2+}$, (b) [Fe^{II}(Ph$_2$-phen)$_3$]$^{2+}$, (c) [Fe^{II}(bpy)$_3$]$^{2+}$, (d) [Fe^{II}(5-Cl-phen)$_3$]$^{2+}$, and (e) [Ru^{II}(bpy)$_3$]$^{2+}$) to [(Bn-TPEN)Mn^{IV}(O)]$^{2+}$–(Sc^{3+})$_2$ (1.25 × 10^{-5} M) in CF$_3$CH$_2$OH-CH$_3$CN (*v*/*v* = 1:1) at 273 K.

metal-oxo bond upon one-electron reduction. The smaller λ value of [Mn^{IV}(O)]$^{2+}$–(Sc^{3+})$_2$, as compared with [Mn^{IV}(O)]$^{2+}$, may be explained by the elongation of the Mn^{IV}–O bond prior to electron transfer because of binding of two Sc^{3+} ions, which results in smaller change in the Mn–O bond distance upon the electron transfer. It should be noted that [(N4Py)Mn^{IV}(O)]$^{2+}$–(Sc^{3+})$_2$ has the most positive E_{red} value as compared with those of iron(IV)-oxo complexes.[23] Thus, [(N4Py)Mn^{IV}(O)]$^{2+}$–(Sc^{3+})$_2$ is regarded as the strongest oxidant among high-valent metal-oxo complexes reported so far.

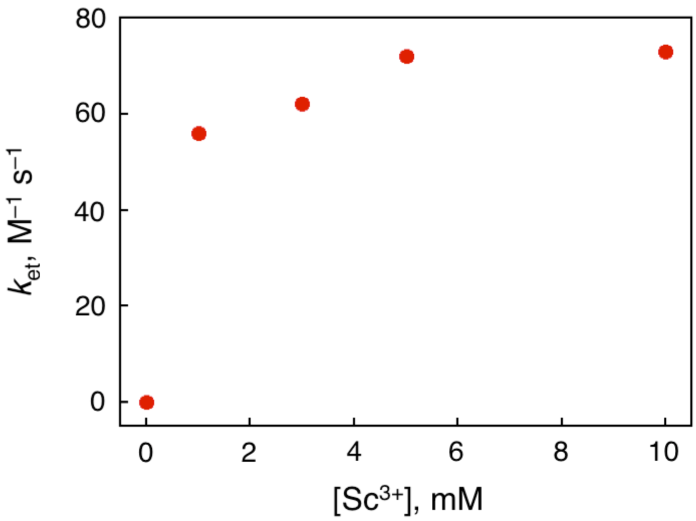

Figure 13. Dependence of k_{et} on [Sc^{3+}] for electron transfer from [$Ru^{II}(bpy)_3$]$^{2+}$ to [(Bn-TPEN)Mn^{IV}(O)]$^{2+}$ in CF_3CH_2OH-CH_3CN (*v*/*v* 1:1) at 273 K.

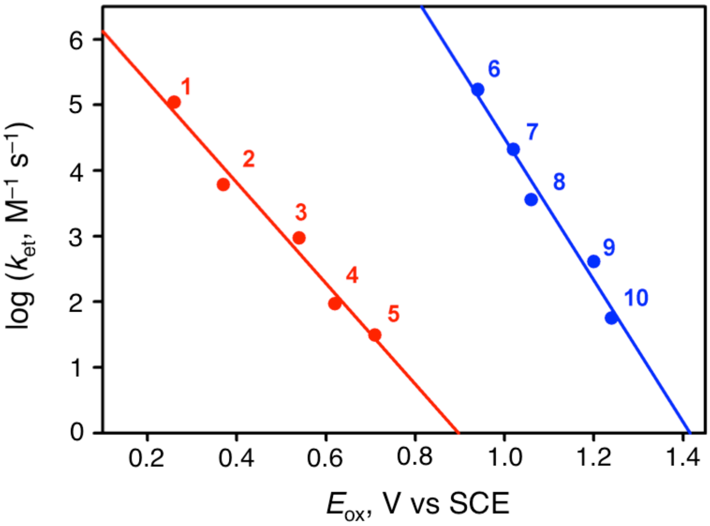

Figure 14. Plots of log k_{et} vs the one-electron oxidation potentials of electron donors (E_{ox}) for electron transfer from various electron donors [(1) dimethylferrocene, (2) ferrocene, (3) bromoferrocene, (4) acetylferrocene, (5) Br_2Fc, (6) [$Fe^{II}(Me_2$-phen$)_3$]$^{2+}$, (7) [$Fe^{II}(Ph_2$-phen$)_3$]$^{2+}$, (8) [$Fe^{II}(bpy)_3$]$^{2+}$, (9) [Fe^{II}(5-Cl-phen$)_3$]$^{2+}$, and (10) [$Ru^{II}(bpy)_3$]$^{2+}$] to [(Bn-TPEN)Mn^{IV}(O)]$^{2+}$ (red line) and [(Mn^{IV}(O)]$^{2+}$–(Sc^{3+})$_2$ (blue line) in CF_3CH_2OH-CH_3CN (*v*/*v* = 1:1) at 273 K.

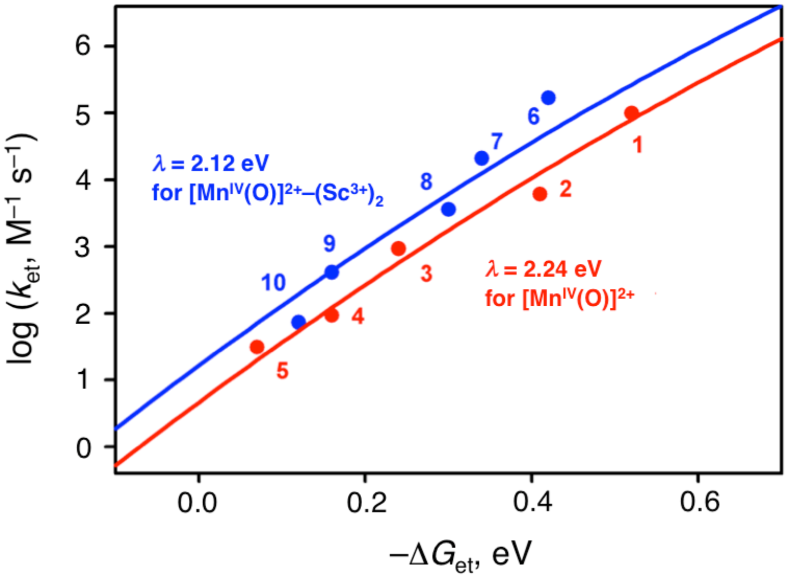

Figure 15. Driving force ($-\Delta G_{et}$) dependence of rate constants (log k_{et}) of electron transfer from one-electron donors [(1) dimethylferrocene, (2) ferrocene, (3) bromoferrocene, (4) acetylferrocene, (5) Br_2Fc, (6) $[Fe^{II}(Me_2\text{-phen})_3]^{2+}$, (7) $[Fe^{II}(Ph_2\text{-phen})_3]^{2+}$, (8) $[Fe^{II}(bpy)_3]^{2+}$, (9) $[Fe^{II}(5\text{-Cl-phen})_3]^{2+}$, and (10) $[Ru^{II}(bpy)_3]^{2+}$] to $[(Bn\text{-TPEN})Mn^{IV}(O)]^{2+}$ (red circles) and $[(Bn\text{-TPEN})Mn^{IV}(O)]^{2+}–(Sc^{3+})_2$ (blue circles) in $CF_3CH_2OH\text{-}CH_3CN$ (v/v = 1:1) at 273 K. The blue and red lines are the Marcus lines calculated with λ values of 2.12 and 2.24 eV, respectively.

Change in Mechanism from Direct Oxygen Atom Transfer to Electron Transfer in Sulfoxidation of Thioanisoles with Nonheme $Mn^{IV}(O)$ Complexes by Binding of Sc^{3+} Ions. We have suggested previously that the mechanism of sufoxidation of thioanisoles with $[(N4Py)Mn^{IV}(O)]^{2+}$ is changed from direct oxygen atom transfer (DOT) to electron transfer (ET) when Sc^{3+} ions are bound to $[(N4Py)Mn^{IV}(O)]^{2+}$.[37] This proposal is now verified by the electron-transfer driving force dependence of log k_{obs} for sulfoxidation of thioanisoles with $[(N4Py)Mn^{IV}(O)]^{2+}$ vs $[(N4Py)Mn^{IV}(O)]^{2+}–(Sc^{3+})_2$ (Figure 16). The k_{obs} values of sulfoxidation of thioanisoles with $[(N4Py)Mn^{IV}(O)]^{2+}$ are much larger than the predicted values of the solid line drawn based on eq 3 for outer-sphere electron-transfer reactions. This implies that much stronger interaction between thioanisoles and $[(N4Py)Mn^{IV}(O)]^{2+}$ is required in the sulfoxidation reaction as compared with outer- sphere electron transfer from thioanisoles to $[(N4Py)Mn^{IV}(O)]^{2+}$. Thus, the sulfoxidation reaction with $[(N4Py)Mn^{IV}(O)]^{2+}$ proceeds via direct oxygen atom transfer. In contrast, the rate constants of sulfoxidation of thioanisoles with $[(N4Py)Mn^{IV}(O)]^{2+}–(Sc^{3+})_2$ fit well in the Marcus line for electron transfer from one-electron reductants to $[(N4Py)Mn^{IV}(O)]^{2+}–(Sc^{3+})_2$. Such an agreement clearly

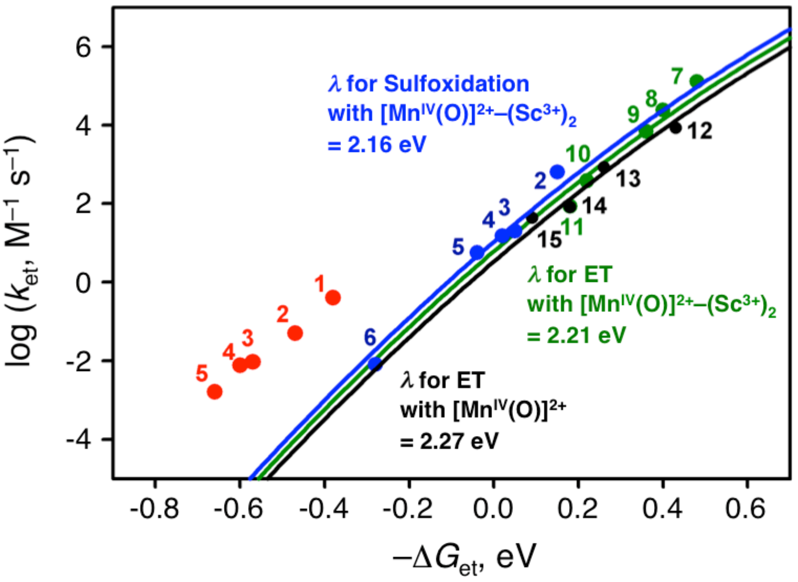

Figure 16. Plots of log k_{obs} for sulfoxidation of *para*-X-substituted thioanisoles [X = (1) MeO, (2) Me, (3) H, (4) F, (5) Br, (6) CN] with [(N4Py)Mn^{IV}(O)]$^{2+}$ (0.50 mM) in CF_3CH_2OH-CH_3CN (v/v = 19:1) at 273 K vs the driving force of electron transfer [$-\Delta G_{et} = e(E_{red} - E_{ox})$] from the thioanisoles to [(N4Py)Mn^{IV}(O)]$^{2+}$ in the absence of Sc^{3+} (red circles) and the presence of 5.0 mM Sc^{3+} (blue circles). The k_{obs} values for the sulfoxidation were taken from ref 37. The black and green circles show the driving-force dependence of the rate constants (log k_{et}) for electron transfer from one-electron reductants [(7) [Fe^{II}(Me$_2$-phen)$_3$]$^{2+}$, (8) [Fe^{II}(Ph$_2$-phen)$_3$]$^{2+}$, (9) [Fe^{II}(bpy)$_3$]$^{2+}$, (10) [Fe^{II}(5-Cl-phen)$_3$]$^{2+}$, (11) [Ru^{II}(bpy)$_3$]$^{2+}$, (12) ferrocene, (13) bromoferrocene, (14) acetylferrocene, (15) Br$_2$Fc,] to [(N4Py)Mn^{IV}(O)]$^{2+}$ in the absence of Sc^{3+} (black circles) and the presence of 5.0 mM Sc^{3+} (green circles) in CF_3CH_2OH-CH_3CN (v/v = 1:1) at 273 K. The blue, green and black lines are the best fit of the Marcus lines calculated for blue, green and black circles, respectively.

indicates that the sulfoxidation of thioanisoles by [(N4Py)Mn^{IV}(O)]$^{2+}$–(Sc^{3+})$_2$ proceeds via an outer-sphere electron-transfer pathway (Figure 16).

The occurrence of electron transfer was confirmed in the case of *p*-methoxythioanisole in the presence of Sc(OTf)$_3$ (5.0 mM), where the driving force for electron transfer is positive ($-\Delta G_{et}$ = 0.20 eV) (i.e., a thermodynamically favorable process). As shown in Figure 17, the transient absorption band at 580 nm due to *p*-methoxythioanisole radical cation appeared instantly, followed by a relatively slow decay (see ref 30b for the reference spectrum of *p*-methoxythioanisole radical cation). The absorption band at 635 nm due to [(N4Py)Mn^{IV}(O)]$^{2+}$–(Sc^{3+})$_2$ was not detected even with a stopped-flow spectrometer since electron transfer from *p*-methoxythioanisole to [(N4Py)Mn^{IV}(O)]$^{2+}$–(Sc^{3+})$_2$[37] was extremely fast. These results clearly demonstrate that the electron-transfer pathway (ET/OT in Scheme 1) becomes

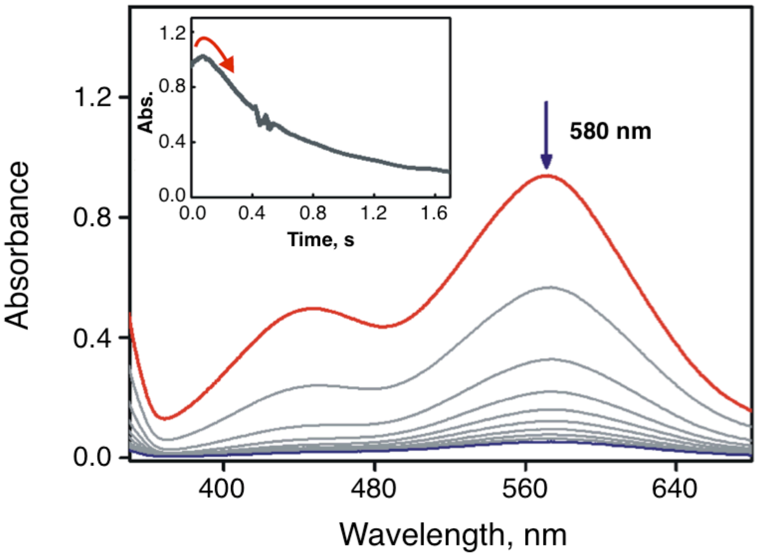

Figure 17. UV-vis spectral changes in the reaction of $[(N4Py)Mn^{IV}(O)]^{2+}$ (6.25×10^{-5} M) with *p*-methoxythioanisole (1.25×10^{-3} M) in the presence of $Sc(OTf)_3$ (6.25×10^{-4} M) in CF_3CH_2OH-CH_3CN (*v*/*v* = 1:1) at 273 K. Inset shows the time course of absorbance at 580 nm due to *p*-methoxythioanisole radical cation.

dominant over the oxygen atom transfer pathway (DOT in Scheme 1) when the sulfoxidation by the manganese(IV)-oxo complex is carried out in the presence of Sc^{3+} ions.

Scheme 1

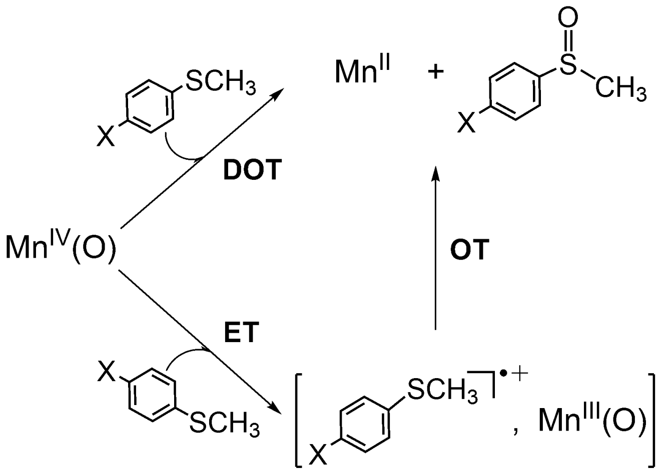

Conclusion

The electron-transfer reactivity of nonheme manganese(IV)-oxo complexes was enhanced as much as 10^7–fold by binding of Sc^{3+} ions. A large positive shift in the one-electron reduction potential was observed by binding of Sc^{3+} ions to $[Mn^{IV}(O)]^{2+}$ (e.g., from 0.80 V of $[(N4Py)Mn^{IV}(O)]^{2+}$ to 1.42 V of $[(N4Py)Mn^{IV}(O)]^{2+}$–$(Sc^{3+})_2$). The reorganization energy of electron transfer becomes smaller by binding of Sc^{3+} ions because of the elongation of Mn^{IV}–O bond, which results in a smaller change in the Mn–O distance upon the electron transfer. Thus, nonheme manganese(IV)-oxo complexes become much stronger oxidants by binding of Sc^{3+} ions, resulting in the change of mechanism in the sulfoxidation of thioanisoles by manganese(IV)-oxo complexes, such as from a direct oxygen atom transfer pathway by $[Mn^{IV}(O)]^{2+}$ to an electron transfer pathway by $[Mn^{IV}(O)]^{2+}$–$(Sc^{3+})_x$. The remarkable enhancement of the electron-transfer reactivity of manganese(IV)-oxo complexes by binding of Sc^{3+} ions may pave a new way to improve the catalytic reactivity of metal-oxo complexes in oxidation reactions.

References

(1) (a) Ortiz de Montellano, P. R. *Cytochrome P450: Structure, Mechanism, and Biochemistry*, 3rd ed.; Kluwer Academic/Plenum Publishers: New York, **2005**. (b) Meunier, B., Ed. *Biomimetic Oxidations Catalyzed by Transition Metal Complexes*; Imperial College Press: London, **2000**. (c) *The Ubiquitous Role of Cytochrome P450 Proteins In Metal Ions in Life Sciences*; Sigel, A., Sigel, H., Sigel, R. K. O., Eds.; John Wiley & Sons Ltd: Chichester, England, **2007**; Vol. 3.

(2) (a) Sono, M.; Roach, M. P.; Coulter, E. D.; Dawson, J. H. *Chem. Rev.* **1996**, *96*, 2841. (b) Watanabe, Y. *J. Biol. Inorg. Chem*. 2001, *6*, 846. (c) Jung, C. *Biochim. Biophys. Acta* **2011**, *1814*, 46. (d) Denisov, I. G.; Makris, T. M.; Sligar, S. G.; Schlichting, I. *Chem. Rev*. **2005**, *105*, 2253.

(3) (a) Rittle, J.; Green, M. T. *Science* **2010**, *330*, 933. (b) Makris, T. M.; von Koenig, K.; Schlichting, I.; Sligar, S. G. *J. Inorg. Biochem*. **2006**, *100*, 507. (c) Groves, J. T. *Proc. Natl. Acad. Sci. U.S.A*. 2003, *100*, 3569. (d) Groves, J. T. *J. Inorg. Biochem*. **2006**, *100*, 434.

(4) (a) Usharani, D.; Janardanan, D.; Li, C.; Shaik, S. *Acc. Chem. Res.* **2013**, *46*, 471. (b) Krebs, C.; Fujimori, D. G.; Walsh, C. T.; Bollinger, J. M., Jr. *Acc. Chem. Res*. **2007**, *40*, 484.

(5) (a) Proshlyakov, D. A.; Henshaw, T. F.; Monterosso, G. R.; Ryle, M. J.; Hausinger, R. P. *J. Am. Chem. Soc.* **2004**, *126,* 1022. (b) Price, J. C.; Barr, E. W.; Hoffart, L. M.; Krebs, C.; Bollinger, J. M., Jr. *Biochemistry* **2005**, *44,* 8138. (c) Price, J. C.; Barr, E. W.; Glass, T. E.; Krebs, C.; Bollinger, J. M., Jr. *J. Am. Chem. Soc.* **2003**, *125,* 13008.

(6) (a) Tinberg, C. E.; Lippard, S. J. *Acc. Chem. Res.* **2011**, *44*, 280. (b) Siewert, I.; Limberg, C. *Chem.–Eur. J.* **2009**, *15*, 10316.

(7) (a) Hammarström, L.; Hammes-Schiffer, S. *Acc. Chem. Res.* **2009**, *42*, 1859. (b) McEvoy, J. P.; Brudvig, G. W. *Chem. Rev.* **2006**, *106*, 4455. (c) Pecoraro, V. L.; Hsieh, W.-Y. *Inorg. Chem.* **2008**, *47*, 1765.

(8) (a) Umena, Y.; Kawakami, K.; Shen, J.-R.; Kamiya, N. *Nature* 2011, *473*, 55. (b) Siegbahn, P. E. M. *Acc. Chem. Res.* 2009, *42*, 1871.

(9) (a) Borovik, A. S. *Acc. Chem. Res.* **2005**, *38*, 54. (b) Benet-Buchholz, J.; Comba, P.; Llobet, A.; Roeser, S.; Vadivelu, P.; Wadepohl, W.; Wiesner., S. *Dalton Trans.* **2009**, 5910. (c) Hohenberger, J.; Ray, K.; Meyer, K. *Nature Commun.* **2012**, *3*, 720.

(10) (a) de Visser, S. P.; Rohde, J.-U.; Lee, Y.-M.; Cho, J.; Nam, W. *Coord. Chem. Rev.* **2012**, *257*, 381. (b) McDonald, A. R.; Que, L., Jr. *Coord. Chem. Rev.* **2013**, *257*, 414.

(11) (a) Meunier, B.; de Visser, S. P.; Shaik, S. *Chem. Rev.* **2004**, *104*, 3947. (b) Shaik, S.; Cohen, S.; Wang, Y.; Chen, H.; Kumar, D.; Thiel, W. *Chem. Rev.* **2010**, *110*, 949. (c) Abu-Omar, M. M.; Loaiza, A.; Hontzeas, N. *Chem. Rev.* **2005**, *105*, 2227. (d) Denisov, I. G.; Makris, T. M.; Sligar, S. G.; Schlichting, I. *Chem. Rev.* **2005**, *105*, 2253. (e) Ortiz de Montellano, P. R. *Chem. Rev.* **2010**, *110*, 932.

(12) (a) Gunay, A.; Theopold, K. H. *Chem. Rev.* **2010**, *110*, 1060. (b) Costas, M. *Coord. Chem. Rev.* **2011**, *255*, 2912.

(13) (a) Yin, G. *Acc. Chem. Res.* **2013**, *46*, 483. (b) Yin, G. *Coord. Chem. Rev.* **2010**, *254*, 1826.

(14) (a) Liua, H.-Y.; HR Mahmooda, M.: Qiuc, S.-X.; Chang, C. K. *Coord. Chem. Rev.* **2013**, *257*, 1306. (b) Goldberg, D. P. *Acc. Chem. Res.* **2007**, *40,* 626.

(15) (a) Cho, J.; Sarangi, R.; Nam, W. *Acc. Chem. Res.* **2012**, *45*, 1321. (b) Cho, J.; Woo, J.; Han, J. E.; Kubo, M.; Ogura, T.; Nam, W. *Chem. Sci.* **2011**, *2*, 2057.

(16) (a) Cho, J.; Jeon, S.; Wilson, S. A.; Liu, L. V.; Kang, E. A.; Braymer, J. J.; Lim, M. H.; Hedman, B.; Hodgson, K. O.; Valentine, J. S.; Solomon, E. I.; Nam, W. *Nature* **2011**, *478*, 502. (b) Rohde, J.-U.; In, J.-H.; Lim, M. H.; Brennessel, W. W.; Bukowski, M. R.; Stubna, A.; Münck, E.; Nam, W.; Que, L., Jr. *Science* **2003**, *299*, 1037.

(17) (a) Nam, W. *Acc. Chem. Res.* **2007**, *40*, 522. (b) Que, L., Jr. *Acc. Chem. Res.* **2007**, *40*, 493.

(18) (a) Gross, Z. *J. Biol. Inorg. Chem.* **2001**, *6*, 733. (b) Kerber, W. D.; Goldberg, D. P. *J. Inorg, Biochem.* **2006**, *100*, 838.

(19) (a) Mayer, J. M. *Acc. Chem. Res.* **2011**, *44*, 36. (b) Che, C.-M.; Lo, V. K.-Y.; Zhou, C.-Y.; Huang, J.-S. *Chem. Soc. Rev.* **2011**, *40*, 1950.

(20) (a) Lubben, M.; Meetsma, A.; Wilkinson, E. C.; Feringa, B.; Que, L., Jr. *Angew. Chem., Int. Ed.* **1995**, *34*, 1512. (b) Kaizer, J.; Klinker, E. J.; Oh, N. Y.; Rohde, J.-U.; Song, W. J.; Stubna, A.; Kim, J.; Münck, E.; Nam, W.; Que, L., Jr. *J. Am. Chem. Soc.* **2004**, *126*, 472. (c) Klinker, E. J.; Kaizer, J.;

Brennessel, W. W.; Woodrum, N. L.; Cramer, C. J.; Que, L., Jr. *Angew. Chem., Int. Ed.* **2005**, *44*, 3690.

(21) (a) Hong, S.; Lee, Y.-M.; Cho, K.-B.; Sundaravel, K.; Cho, J.; Kim, M. J.; Shin, W.; Nam, W. *J. Am. Chem. Soc.* **2011**, *133*, 11876. (b) Tang, H.; Guan, J.; Zhang, L.; Liu, H.; Huang, X. *Phys. Chem. Chem. Phys.* **2012**, *14*, 12863. (c) Kumar, D.; Sastry, G. N.; de Visser, S. P. *J. Phys. Chem. B*, **2012**, *116*, 718.

(22) (a) Arias, J.; Newlands, C. R.; Abu-Omar, M. M. *Inorg. Chem.* **2001**, *40*, 2185. (b) Prokop, K. A.; Neu, H. M.; de Visser, S. P.; Goldberg, D. P. *J. Am. Chem. Soc.* **2011**, *133*, 15874. (c) Fertinger, C.; Hessenauer-Ilicheva, N.; Franke, A.; van Eldik, R. *Chem.–Eur. J.* **2009**, *15*, 13435. (d) Arunkumar, C.; Lee, Y.-M.; Lee, J. Y.; Fukuzumi, S.; Nam, W. *Chem.–Eur. J.* **2009**, *15*, 11482. (e) Kumar, A.; Goldberg, I.; Botoshansky, M.; Buchman, Y.; Gross, Z. *J. Am. Chem. Soc.* **2010**, *132*, 15233. (f) Benet-Buchholz, J.; Comba, P.; Llobet, A.; Roeser, S.; Vadivelu, P.; Wiesner, S. *Dalton Trans.* **2010**, *39*, 3315.

(23) (a) Fukuzumi, S. *Coord. Chem. Rev.* **2013**, *257*, 1564. (b) Lee, Y.-M.; Kotani, H.; Suenobu, T.; Nam, W.; Fukuzumi, S. *J. Am. Chem. Soc.* **2008**, *130*, 434. (c) Fukuzumi, S.; Kotani, H.; Suenobu, T.; Hong, S.; Lee, Y.-M.; Nam, W. *Chem.–Eur. J.* **2010**, *16*, 354. (d) Comba, P.; Fukuzumi, S.; Kotani, H.; Wunderlich, S. *Angew. Chem., Int. Ed.* **2010**, *49*, 2622.

(24) Fukuzumi, S.; Kotani, H.; Prokop, K. A.; Goldberg, D. P. *J. Am. Chem. Soc.* **2011**, *133*, 1859.

(25) (a) Park, M. J.; Lee, J.; Suh, Y.; Kim, J.; Nam, W. *J. Am. Chem. Soc.* **2006**, *128*, 2630. (b) Sastri, C. V.; Lee, J.; Oh, K.; Lee, Y. J.; Lee, J.; Jackson, T. A.; Ray, K.; Hirao, H.; Shin, W.; Halfen, J. A.; Kim, J.; Que, L., Jr.; Shaik, S.; Nam, W. *Proc. Natl. Acad. Sci. U. S. A.* **2007**, *104*, 19181. (c) Jeong, Y. J.; Kang, Y.; Han, A.-R.; Lee, Y.-M.; Kotani, H.; Fukuzumi, S.; Nam, W. *Angew. Chem., Int. Ed.* **2008**, *47*, 7321. (d) Lee, Y.-M.; Dhuri, S. N.; Sawant, S. C.; Cho, J.; Kubo, M.; Ogura, T.; Fukuzumi, S.; Nam, W. *Angew. Chem., Int. Ed.* **2009**, *48*, 1803.

(26) (a) Lee, Y.-M.; Hong, S.; Morimoto, Y.; Shin, W.; Fukuzumi, S.; Nam, W. *J. Am. Chem. Soc.* **2010**, *132*, 10668. (b) Wilson, S. A.; Chen, J.; Hong, S.; Lee, Y.-M.; Clémancey, M.; Garcia-Serres, R.; Nomura, T.; Ogura, T.; Latour, J.-M.; Hedman, B.; Hodfson, K. O.; Nam, W.; Solomon, E. I. *J. Am. Chem. Soc.* **2012**, *134*, 11791.

(27) (a) England, J.; Guo, Y.; Van Heuvelen, K. M.; Cranswick, M. A.; Rohde, G. T.; Bominaar, E. L.; Münck, E.; Que, L., Jr. *J. Am. Chem. Soc.* **2011**, *133*, 11880. (b) Xue, G.; De Hont, R.; Münck, E.; Que, L., Jr. *Nat. Chem.* **2010**, *2*, 400. (c) Xue, G.; Fiedler, A. T.; Martinho, M.; Münck, E.; Que, L., Jr. *Proc. Natl. Acad. Sci. U. S. A.* **2008**, *105*, 20615. (d) Shanmugam, M.; Xue, G.; Que, L., Jr.; Hoffman, B. M. *Inorg. Chem.* **2012**, *51*, 10080.

(28) (a) Gupta R.; A. S. Borovik, A. S. *J. Am. Chem. Soc.* **2003**, *125*, 13234. (b) Pestovsky O,; Bakac, A. *J. Am. Chem. Soc.* **2004**, *126*, 13757. (c) Lam, W. W. Y.; Man, W.-L.; Lau, T,-C. *Coord. Chem. Rev.* **2007**, *251*, 2238. (d) de Visser, S. P. *J. Am. Chem. Soc.* **2010**, *132,* 1087. (e) Prokop, K. A.; de

Visser, S. P.; Goldberg, D. P. *Angew. Chem., Int. Ed.* **2010**, *49*, 5091. (f) Kojima, T.; Nakayama, K.; Ikemura, K,; Ogura, T.; Fukuzumi, S. *J. Am. Chem. Soc*. **2011**, *133*, 11692.

(29) (a) Morimoto, Y.; Kotani, H.; Park, J.; Lee, Y.-M.; Nam, W.; Fukuzumi, S, *J. Am. Chem. Soc*. **2011**, *133*, 403. (b) Park, J.; Morimoto, Y.; Lee, Y.-M.; Nam, W.; Fukuzumi, S. *J. Am. Chem. Soc.* **2011**, *133*, 5236. (c) Park, J.; Morimoto, Y.; Lee, Y.-M.; Nam, W.; Fukuzumi, S. *Inorg. Chem*. **2011**, *50*, 11612. (d) Morimoto, Y.; Park, J.; Kotani, H.; Lee, Y.-M.; Nam, W.; Fukuzumi, S. *Inorg. Chem*. **2012**, *51*, 10025.

(30) (a) Park, J.; Morimoto, Y.; Lee, Y.-M.; Nam, W.; Fukuzumi, S. *J. Am. Chem. Soc*. **2012**, *134*, 3903. (b) Park, J.; Lee, Y.-M.; Nam, W.; Fukuzumi, S. *J. Am. Chem. Soc*. **2013**, *135*, 5052.

(31) (a) Fukuzumi, S. *Bull. Chem. Soc. Jpn*. **1997**, *70*, 1. (b) Fukuzumi, S. *Org. Biomol. Chem*. **2003**, *1*, 609. (c) Fukuzumi, S. *Bull. Chem. Soc. Jpn*. **2006**, *79*, 177. (d) Fukuzumi, S. *Pure Appl. Chem*. **2007**, *79*, 981. (e) Fukuzumi, S. *Prog. Inorg. Chem*. **2009**, *56*, 49. (f) Fukuzumi, S.; Ohkubo, K. *Coord. Chem. Rev*. **2010**, *254*, 372.

(32) (a) Fukuzumi, S.; Ohkubo, K. *Chem.–Eur. J.* **2000**, *6*, 4532. (b) Fukuzumi, S.; Yasui, K.; Suenobu, T. Ohkubo, K.; Fujitsuka, M.; Ito, O. *J. Phys. Chem. A* **2001**, *105*, 10501. (c) Yuasa, J.; Fukuzumi, S. *J. Am. Chem. Soc.* **2006**, *128*, 14281. (d) Yuasa, J.; Yamada, S.; Fukuzumi, S. *J. Am. Chem. Soc.* **2006**, *128*, 14938. (e) Yuasa, J.; Yamada, S.; Fukuzumi, S. *J. Am. Chem. Soc.* **2008**, *130*, 5808. (f) Yuasa, J.; Fukuzumi, S. *J. Phys. Org. Chem.* **2008**, *21*, 886.

(33) (a) Lam, W. W. Y.; Yiu, S.-M.; Lee, J. M. N.; Yau, S. K. Y.; Kwong, H.-K.; Lau, T.-C.; Liu, D.; Lin, Z. *J. Am. Chem. Soc.* **2006**, *128*, 2851. (b) Yiu, S.-M.; Man,W.-L.; Lau, T.-C. *J. Am. Chem. Soc*. **2008**, *130*, 10821. (c) Du, H.; Lo, P.-K.; Hu, Z.; Liang, H.; Lau, K.-C.; Wang, Y.-N.; Lam, W. W. Y.; Lau, T.-C. *Chem. Commun*. **2011**, *47*, 7143.

(34) Fukuzumi, S.; Morimoto, Y.; Kotani, H.; Naumov, P.; Lee, Y.-M.; Nam, W. *Nat. Chem*. **2010**, *2*, 756.

(35) (a) Yocum, C. F. *Coord. Chem. Rev.* **2008**, *252*, 296. (b) Yachandra, V. K.; Yano, J. *J. Photochem. Photobiol. B* **2011**, *104*, 51.

(36) (a) Wiechen, M.; Zaharieva, I.; Dau, H.; Kurz, P. *Chem. Sci*. 2012, *3*, 2330. (b) Han, X.; Zhang, T.; Du, J.; Cheng, F.; Chen, J. *Chem. Sci*. **2013**, *4*, 368. (b) Park, Y. J.; Cook, S. A.; Sickerman, N. S.; Sano, Y.; Ziller, J. W.; Borovik. A. S. *Chem. Sci*. **2013**, *4*, 717.

(37) Chen, J.; Lee, Y.-M.; Davis, K. M.; Wu, X.; Seo, M. S.; Cho, K.-B.; Yoon, H.; Park, H. J.; Fukuzumi, S.; Pushkar, Y. N.; Nam, W. *J. Am. Chem. Soc.* **2013**, DOI: 10.1021/ja312113p.

(38) Leeladee, P.; Baglia, R. A.; Prokop, K. A.; Latifi, R.; de Visser, S. P.; Goldberg, D. P. *J. Am. Chem. Soc*. **2012**, *134*, 10397.

(39) (a) Tsui, E.; Y. Tran, R.; Yano, J.; Agapie, T. *Nat. Chem*. **2013**, *5*, 293. (b) Kanady, J. S.; Mendoza-Cortes, J. L.; Tsui, E. Y.; Nielsen, R. J.; Goddard, W. A., III; Agapie, T. *J. Am. Chem. Soc.* **2013**, *135*, 1073.

(40) Kanady, J. S.; Tsui, E. Y.; Day, M. W.; Agapie, T. *Science* **2011**, *333*, 733.

(41) (a) Wu, X.; Seo, M. S.; Davis, K. M.; Lee, Y.-M.; Chen, J.; Cho, K.-B.; Pushkar, Y. N.; Nam, W. *J. Am. Chem. Soc.* **2011**, *133*, 20088. (b) Yoon, H.; Morimoto, Y.; Lee, Y.-M.; Nam, W.; Fukuzumi, S. *Chem. Commun*. **2012**, *48*, 11187.

(42) Evans, D. F.; Jakubovic, D. A. *J. Chem. Soc. Dalton Trans.* **1988**, 2927.

(43) Fukuzumi, S.; Kondo, Y.; Mochizuki, T.; Tanaka, T. J. *Chem. Soc., Perkin Trans.* 2 **1989**, 1753.

(44) Fukuzumi, S.; Kondo, Y.; Mochizuki, T.; Tanaka, T. J. *Chem. Soc., Perkin Trans.* 2 **1989**, 1753.

(45) A solvent molecule may coordinate to the Sc center. However, a solvent molecule was not incorporated in the present DFT calculations, which were performed to demonstrate that the second Sc^{3+} ion is located at the secondary coordination sphere. The exact structure has yet to be clarified.

(46) The blue-shift in UV-vis indicates an increased energy gap between the HOMO-LUMO orbitals. However, this issue is not directly related to any increase/decrease in E_{red} values, which is a measure of the LUMO orbital energy (not HOMO). The presence of Sc^{3+} can shift the energies of all the orbitals of the $Mn^{IV}O$ moiety (including both HOMO and LUMO orbitals).

(47) (a) Marcus, R. A. *Annu. Rev. Phys. Chem*. **1964**, *15*, 155. (b) Marcus, R. A.; Sutin, N. *Biochim. Biophys. Acta Rev. Bioenerg.* **1985**, *811*, 265. (c) Marcus, R. A. *Angew. Chem. Int. Ed. Engl.* **1993**, *32*, 1111.

(48) Armarego, W. L. F.; Chai, C. L. L. *Purification of Laboratory Chemicals*, 6th ed.; Pergamon Press: Oxford, **2009**.

(49) *Organic Syntheses*; Saltzman, H.; Sharefkin, J. G., Eds.; Wiley: New York, **1973**, Vol. V, pp. 658.

(50) (a) Lubben, M.; Meetsma, A.; Wilkinson, E. C.; Feringa, B.; Que, L., Jr. *Angew. Chem., Int. Ed.* **1995**, *34*, 1512. (b) Duelund, L.; Hazell, R.; McKenzie, C. J.; Nielsen, L. P.; Toftlund, H. *J. Chem. Soc., Dalton Trans.* **2001**, 152. (c) Groni, S.; Dorlet, P.; Blain, G.; Bourcier, S.; Guillot, R.; Anxolabéhère-Mallart, E. *Inorg. Chem.* **2008**, *47*, 3166.

(51) (a) Fussa-Rydel, O.; Zhang, H.-T.; Hupp, J. T.; Leidner, C. R. *Inorg. Chem*. **1989**, *28*, 1533. (b) Fukuzumi, S.; Nakanishi, I.; Tanaka, K.; Suenobu, T.; Tabard, A.; Guilard, R.; Van Caemelbecke, E.; Kadish, K. M. *J. Am. Chem. Soc*. **1999**, *121*, 785.

(52) Frisch, M. J. *et al. Gaussian 09, Revision B.01*, Gaussian Inc.: Wallingford CT, **2009**.

(53) (a) Becke, A. D. *Phys. Rev. A* **1988**, *38*, 3098. (b) Becke, A. D. *J. Chem. Phys*. **1993**, *98*, 1372. (c) Becke, A. D. *J. Chem. Phys*. **1993**, *98*, 5648. (d) Lee, C.; Yang, W.; Parr, R. G. *Phys. Rev. B* **1988**, *37*, 785.

(54) (a) The LACVP and LACV3P^{*+} basis sets uses pople style 6-31G and 6-311+G* basis sets (respectively) on all atoms except transition metals, where an ECP is used as defined in the quantum chemistry program Jaguar, version 7.7, Schrödinger, LLC, New York, NY, **2010**. See also (b) Hay, P. J.; Wadt, W. R. *J. Chem. Phys*. **1985**, *82*, 299. (c) Dyall, K. G. *Theor. Chem. Acc*. **2004**, *112*, 403.

(55) (a) Barone, V.; Cossi, M. *J. Phys. Chem. A*. **1998**, *102*, 1995. (b) Cossi, M.; Rega, N.; Scalmani, G.; Barone, V. *J. Comp. Chem*. **2003**, *24*, 669.

Supporting Information for Chapter 4

Table S1. EXAFS Least Squares Fitting Results**.** Selected Bond Lengths (Å) and Angles (°) for [Mn^{II}(N4Py)(CF$_3$SO$_3$)](CF$_3$SO$_3$).

Complex	Coordination/Path	R(Å)[a]	σ^2(Å^2)[b]	E$_0$ (eV)	*F*[c]
Mn^{IV}(O)–(Sc^{3+})$_1$	1 Mn-O	1.74	640	-3.26	0.42
	4 Mn-N	2.07	575		
	1 Mn-N	2.36	95		
	6 Mn-C	2.94	334		
	12 Mn-C-N	3.32	/334		
	1 Mn-Sc[d]	3.45	160		
	2 Mn-O-Sc[d]	3.59	461		
	4 Mn-C-N	4.37	597		
Mn^{IV}(O)–(Sc^{3+})$_2$	1 Mn-O	1.74	841	-3.78	0.36
	4 Mn-N	2.08	838		
	1 Mn-N	2.27	358		
	6 Mn-C	2.91	410		
	12 Mn-C-N	3.35	/410		
	1 Mn-Sc[d]	3.44	140		
	2 Mn-O-Sc[d]	3.52	139		
	4 Mn-C-N	4.26	619		

[a] The estimated standard deviations for the distances are in the order of ± 0.02 Å. [b] The σ^2 values are multiplied by 10^5. [c] Error is given by $\Sigma[(\chi_{obsd} - \chi_{calcd})^2 k^6]/\Sigma[(\chi_{obsd})^2 k^6]$. [d] / indicates the σ^2 value for the path is linked to the preceding path. The S_0^2 factor was set at 0.95.

Table S2. Selected Geometries in Å.

species	Mn-O	MnO-Sc$_A$	MnO-Sc$_B$	Sc$_A$-Sc$_B$	Mn-Sc$_A$	Mn-Sc$_B$
$[(\text{Bn-TPEN})\text{Mn}^{IV}(\text{O})]^{2+a}$	1.68	---	---	---	---	---
$[(\text{Bn-TPEN})\text{Mn}^{IV}(\text{O})]^{2+}$–$(\text{Sc}^{3+})_1$	1.75	1.94	---	---	3.65	---
$[(\text{Bn-TPEN})\text{Mn}^{IV}(\text{O})]^{2+}$–$(\text{Sc}^{3+})_2$	1.75	1.94	6.11	5.35	3.68	7.09

[a] Values taken from ref 41a in the text.

Table S3. Mulliken Spin Density Distribution.

species	Mn	O	Sc$_A$	Sc$_B$	5 x N	rest of Bn-TPEN	6 x OTf
$[(\text{Bn-TPEN})\text{Mn}^{IV}(\text{O})]^{2+a}$	2.64	0.63	---	---	-0.15	0.02	---
$[(\text{Bn-TPEN})\text{Mn}^{IV}(\text{O})]^{2+}$–$(\text{Sc}^{3+})_1$	3.13	0.27	0.02	---	-0.50	0.06	0.02[b]
$[(\text{Bn-TPEN})\text{Mn}^{IV}(\text{O})]^{2+}$–$(\text{Sc}^{3+})_2$	3.14	0.29	0.01	0.00	-0.54	0.08	0.03

[a] Values taken from ref 41a in the main text. [b] 3 x OTf.

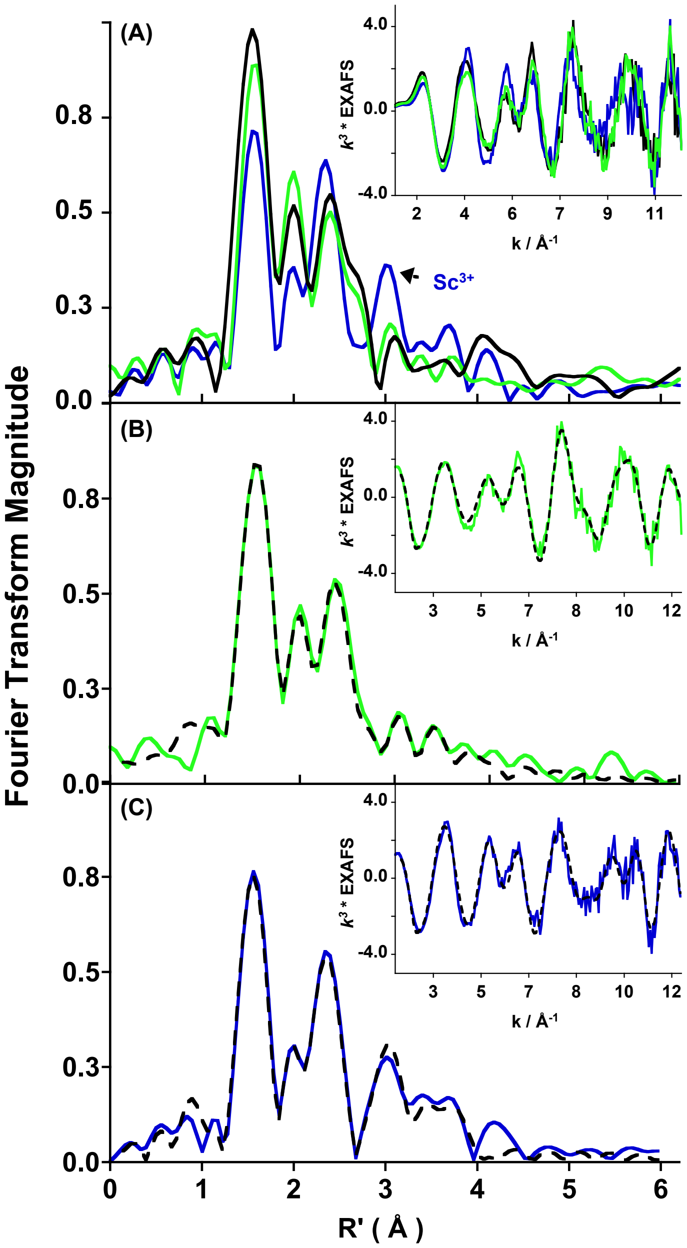

Figure S1. (a) A comparison of the non phase-shift corrected Fourier transforms and the corresponding Mn K-edge EXAFS data (inset) for **1** (—), $Mn^{IV}(O)–(Sc^{3+})_1$ (—) and $Mn^{IV}(O)–(Sc^{3+})_2$ (—). FEFF best-fits (**- - -**) to $Mn^{IV}(O)–(Sc^{3+})_1$ (—) and $Mn^{IV}(O)–(Sc^{3+})_2$ (—) are shown in (b) and (c), respectively. Fits were performed over $k = 2 - 12$ $Å^{-1}$ range.

Chapter 5

Protonated Mononuclear Nonheme Manganese(IV)-Oxo Complexes with Much Enhanced Oxidation Capacity

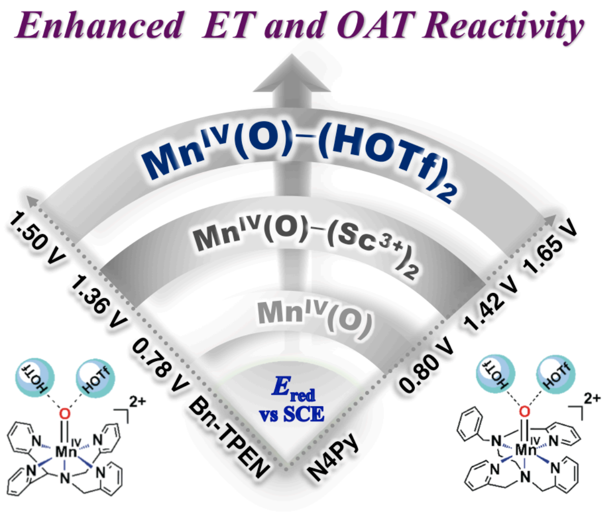

Abstract: Triflic acid (HOTf)-bound nonheme manganese(IV)-oxo complexes, $[(L)Mn^{IV}(O)]^{2+}$–$(HOTf)_2$ (L = N4Py and Bn-TPEN; N4Py = *N*,*N*-bis(2-pyridylmethyl)-*N*-bis(2-pyridyl)methylamine) and Bn-TPEN = *N*-benzyl-*N*,*N*′,*N*′-tris(2-pyridylmethyl)ethane-1,2-diamine), were synthesized by adding HOTf to the solutions of the $[(L)Mn^{IV}(O)]^{2+}$ complexes and were characterized by various spectroscopies. The one-electron reduction potentials of the $Mn^{IV}(O)$ complexes exhibited a significant positive shift upon binding of HOTf. The driving force dependence of electron transfer (ET) from electron donors to the $Mn^{IV}(O)$ and $Mn^{IV}(O)$–$(HOTf)_2$ complexes were examined and evaluated in light of the Marcus theory of ET to determine the reorganization energies of ET. The smaller reorganization energies and much more positive reduction potentials of the $[(L)Mn^{IV}(O)]^{2+}$–$(HOTf)_2$ complexes resulted in much enhanced oxidation capacity towards one-electron reductants and *para*-X-substituted-thioanisoles. The reactivities of the manganese(IV)-oxo complexes were markedly enhanced by binding of HOTf, such as a 6.4×10^5-fold increase in the oxygen atom transfer (OAT) reaction (i.e., sulfoxidation). Such a remarkable acceleration in the OAT reaction results from the enhancement of ET from *para*-X-substituted-thioanisoles to the manganese(IV)-oxo complexes as revealed by the unified ET driving force dependence of the rate constants of OAT and ET

reactions of $[(L)Mn^{IV}(O)]^{2+}$–$(HOTf)_2$. In contrast, deceleration was observed in the rate of H-atom transfer (HAT) reaction of $[(L)Mn^{IV}(O)]^{2+}$–$(HOTf)_2$ complexes with 1,4-cyclohexadiene as compared with those of the $[(L)Mn^{IV}(O)]^{2+}$ complexes. Thus, the binding of two HOTf molecules to the $Mn^{IV}(O)$ moiety resulted in remarkable acceleration of the ET rate when the ET is thermodynamically feasible. When the ET reaction is highly endergonic, the rate of the HAT reaction is decelerated due to the steric effect of the counter anion of HOTf.

Introduction

High-valent metal-oxo species have been invoked as key intermediates in biological and chemical oxidation reactions.[1-5] In particular, high-valent manganese-oxo species have attracted much attention recently as an essential species in oxygen-evolving complex (OEC) in Photosystem II (PS II), which contains a redox-inactive Ca^{2+} ion in addition to redox-active Mn ions as cofactors.[6-8] In biomimetic studies, the reactivities of metal-oxo complexes have been investigated in various oxidation reactions such as oxygen atom transfer (OAT) and hydrogen atom transfer (HAT) reactions.[1-5,9] It has been demonstrated that the reactivities of high-valent metal-oxo complexes are affected by various factors such as the structure and topology of supporting ligands, the identity of axial ligands, and the spin state of metal ions.[9,10] The reactivity of metal-oxo complexes has been further enhanced by binding of redox-inactive metal ions to the metal-oxo moiety, indicating that metal-oxo complexes act as much powerful oxidants by binding of redox-inactive metal ions.[10-13] Binding of a redox-inactive metal ion acting as a Lewis acid to a high-valent metal-oxo complex has been confirmed by the crystal structure of a Sc^{3+} ion–bound nonheme iron(IV)-oxo complex, $[(TMC)Fe^{IV}(O)]^{2+}$ (TMC = 1,4,8,11-tetramethyl-1,4,8,11-tetraazacyclotetradecane).[14] In general, binding metal ions to oxygen and nitrogen atoms of C=O and C=N bonds of organic compounds as well as metal-oxo complexes results in enhancement of their reactivity towards electron donors, caused by a positive shift of the one-electron reduction potentials of metal ion-bound electron acceptors.[15,16] Not only metal ions but also Brønsted acids, such as perchloric acid ($HClO_4$) and trifluoromethanesulfonic acid (HOTf), accelerate electron transfer from electron donors to electron acceptors including metal-oxo complexes when acids bind to the one-electron-reduced species of electron acceptors.[15-18] The acceleration effects of Brønsted acids on the reactivity of electron acceptors towards electron donors are expected to be maximized when electron acceptors are protonated prior to electron transfer.[19] In the catalytic cycles of metalloenzymes, Brønsted acids play a very important role in controlling the reactivity of high-valent metal–oxo intermediates via hydrogen bonding.[20,21] However, evidence for the direct binding of Brønsted acids to high-valent metal-oxo complexes has yet to be obtained.

We report herein the first spectroscopic evidence for binding of two HOTf molecules to mononuclear nonheme manganese(IV)-oxo complexes, $[(\text{N4Py})\text{Mn}^{\text{IV}}(\text{O})]^{2+}$ and $[(\text{Bn-TPEN})\text{Mn}^{\text{IV}}(\text{O})]^{2+}$ (N4Py = *N,N*-bis(2-pyridylmethyl)-*N*-bis(2-pyridyl)methylamine and Bn-TPEN = *N*-benzyl-*N,N′,N′*-tris(2-pyridylmethyl)ethane-1,2-diamine) to produce $[(\text{L})\text{Mn}^{\text{IV}}(\text{O})]^{2+}$–$(\text{HOTf})_2$ (L = N4Py and Bn-TPEN) (see Figure 1). The binding of two HOTf molecules to $[(\text{L})\text{Mn}^{\text{IV}}(\text{O})]^{2+}$ enhanced the reactivity of $[(\text{L})\text{Mn}^{\text{IV}}(\text{O})]^{2+}$ dramatically in electron transfer (ET) reaction with one-electron reductants as well as in OAT reaction with thioanisoles. In contrast, the reactivity of $[(\text{L})\text{Mn}^{\text{IV}}(\text{O})]^{2+}$–$(\text{HOTf})_2$ decreased significantly in the HAT reaction with 1,4-cyclohexadiene. A large positive shift of the one electron reduction potentials of the manganese(IV)-oxo complexes was also observed upon binding of two HOTf molecules to the manganese(IV)-oxo complexes, resulting from the much larger binding constants of HOTf to the one-electron reduced species, ($[(\text{L})\text{Mn}^{\text{III}}(\text{O})]^{+}$), as compared with that of $[(\text{L})\text{Mn}^{\text{IV}}(\text{O})]^{2+}$. A unified ET driving force dependence of the rate constants of ET and OAT reactions of $[(\text{L})\text{Mn}^{\text{IV}}(\text{O})]^{2+}$–$(\text{HOTf})_2$, which were analyzed in light of the Marcus

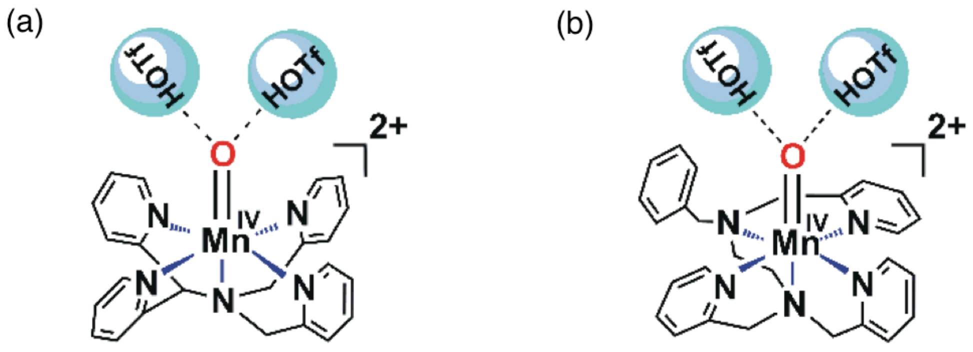

Figure 1. Schematic drawing of the chemical structures of diprotonated $[(\text{N4Py})\text{Mn}^{\text{IV}}(\text{O})]^{2+}$ (a) and $[(\text{Bn-TPEN})\text{Mn}^{\text{IV}}(\text{O})]^{2+}$ (b) species biding two HOTf molecules.

theory of electron transfer,[22] provides valuable insights into the change in the mechanism depending on the ET driving force.

Experimental Section

Materials. Commercially available chemicals were used without further purification unless otherwise indicated. Solvents were dried according to published procedures and distilled under Ar prior to use.[32] Trifluoromethanesulfonic acid (HOTf, OTf = $CF_3SO_3^-$) was purchased from Aldrich and used as received. $H_2{}^{18}O$ (95% ^{18}O-enriched) was purchased from ICON Services Inc. (Summit, NJ, USA). Iodosylbenzene (PhIO), N4Py and Bn-TPEN ligands, and $Mn^{II}(OTf)_2{\cdot}2CH_3CN$ were prepared by literature methods.[10a,33-35] $[(L)Mn^{II}(CF_3SO_3)]^+$ and $[(L)Mn^{IV}(O)]^{2+}$ were prepared by literature methods.[23-25] One-electron reductants, such as $[Fe^{II}(Me_2\text{-bpy})_3]^{2+}$, $[Fe^{II}(phen)_3]^{2+}$, $[Fe^{II}(bpy)_3]^{2+}$, $[Ru^{II}(Me_2\text{-bpy})_3]^{2+}$, $[Ru^{II}(bpy)_3]^{2+}$, $[Ru^{II}(5\text{-Cl-phen})_3]^{2+}$, $[Ru^{II}(5\text{-Br-bpy})_3]^{2+}$ and $[Ru^{II}(5\text{-NO}_2\text{-phen})_3]^{2+}$, were synthesized according to literature methods.[36]

Instrumentation. UV-vis spectra were recorded on a Hewlett Packard 8453 diode array spectrophotometer equipped with a UNISOKU Scientific Instruments Cryostat USP-203A for low-temperature experiments or on a Hi-Tech Scientific (U.K.) SF-61 DX2 cryogenic stopped-flow spectrophotometer equipped with a Xe arc lamp and a KinetaScan diode array rapid scanning unit. The coldspray ionization time-of-flight mass (CSI-TOF MS) spectral data were collected on a JMS-T100CS (JEOL) mass spectrometer equipped with the CSI source. Typical measurement conditions are as follows: needle voltage: 2.2 kV, orifice 1 current: 50-500 nA, orifice 1 voltage: 0 to 20 V, ring lens voltage: 10 V, ion source temperature: 5°C, spray temperature: –40 °C. X-band EPR spectra were recorded at 5 K using X-band Bruker EMX-plus spectrometer equipped with a dual mode cavity (ER 4116DM). Low temperature was achieved and controlled with an Oxford Instruments ESR900 liquid He quartz cryostat with an Oxford Instruments ITC503 temperature and gas flow controller. The experimental parameters for EPR measurement were as follows: Microwave frequency = 9.646 GHz, microwave power = 1.0 mW, modulation amplitude = 10 G, gain = 1×10^3, modulation frequency = 100 kHz, time constant = 40.96 ms, and conversion time = 81.00 ms. ^1H

NMR spectra were measured with a Bruker model digital AVANCE III 400 FT-NMR spectrometer.

EXAFS Measurements. The Mn K-edge X-ray absorption spectra of **3**, $[(N4Py)Mn^{IV}(O)]^{2+}-(HOTf)_2$, were measured at the Stanford Synchrotron Radiation Lightsource (SSRL) on the unfocussed 20-pole 2 T wiggler side-station beam line 7-3 under standard ring conditions of 3 GeV and ~500 mA. A Si(220) double crystal monochromator was used for energy selection. A Rh-coated harmonic rejection mirror was used on beam line 7-3 to reject components of higher harmonics. The monochromator was further detuned by 70% to eliminate higher harmonic and to reduce beam damage on samples. The solution samples for $[(N4Py)Mn^{IV}(O)]^{2+}-(HOTf)_2$ (~120 μL) were transferred into 2 mm delrin XAS cells with 70 m Kapton tape windows under synthesis conditions and were immediately frozen after preparation and stored under liquid N_2. During data collection, samples were maintained at a constant temperature of ~10 – 15 K using an Oxford Instruments CF 1208 liquid helium cryostat. Data were measured to $k = 12$ Å^{-1} (fluorescence mode) using a Canberra Ge 30-element array detector. Internal energy calibration was accomplished by simultaneous measurement of the absorption of a Mn-foil placed between two ionization chambers situated after the sample. The first inflection point of the foil spectrum was fixed at 6539.0 eV. Data presented here are 32-scan average spectra for $[Mn^{IV}(O)]^{2+}-(HOTf)_2$. Data were processed by fitting a second-order polynomial to the pre-edge region and subtracting this from the entire spectrum as background. A four-region spline of orders 2, 3, 3 and 3 was used to model the smoothly decaying post-edge region. The data were normalized by subtracting the cubic spline and assigning the edge jump to 1.0 at 6555 eV using the Pyspline[37] program. Data were then renormalized in Kaleidagraph for comparison and quantitation purposes. Theoretical EXAFS signals $\chi(k)$ were calculated by using FEFF[38-40] (macintosh version). Starting structural models for $Mn^{IV}(O)-(HOTf)_2$ was generated by modifying the crystal structure[23] of $[Mn^{II}(N4Py)(CF_3SO_3)]^+$ in Avogadro.[41] The input structure was improved based on preliminary EXAFS fit parameters to generate more accurate theoretical EXAFS signals. Data fitting was performed in EXAFSPAK.[42] The structural parameters varied during the fitting process were the bond distance (R) and the bond variance σ^2, which is related to the Debye-Waller factor resulting from thermal motion, and static disorder of the absorbing and scattering atoms. The non-structural parameter E_0 (the energy at which $k = 0$) was also allowed to vary but was restricted to a common value for every component in a given fit. Coordination numbers were systematically varied in the course of the fit but were fixed within a given fit.

EXAFS Data Analysis. The k^3 weighted Mn K-edge EXAFS data for **3**, along with their non-phase shift corrected Fourier transforms (FT) (k = 1 - 12 $Å^{-1}$), are shown in Figure 7. The EXAFS data for $[(N4Py)Mn^{IV}(O)]^{2+}$ (**1**) have been previously reported,[23] but were re-measured under the same experimental conditions for direct comparison to proton bound $Mn^{IV}(O)$ complex. FEFF fits to the EXAFS data (Table S1 in SI) were performed to quantitatively understand the differences visually observed in the FT data. It is consistent with a distorted six-coordinate first shell with one short Mn–O (1.74 Å) which is longer than the 1.67 Å observed in $[(N4Py)Mn^{IV}(O)]^{2+}$ (**1**).

Kinetic Measurements. Kinetic measurements were performed on a UNISOKU RSP-601 stopped-flow spectrometer equipped with a MOS-type highly sensitive photodiode array or a Hewlett Packard 8453 photodiode-array spectrophotometer at 298 K. Rates of electron transfer from one-electron donors to $[(N4Py)Mn^{IV}(O)]^{2+}–(HOTf)_2$ (**3**) and oxidation of *para*-X-thioanisoles (X = Me, H, F and Br) by **3** were monitored by the formation of absorption bands due to the one-electron oxidized species and the decay of absorption band due to **3**. Most kinetic measurements were carried out under pseudo-first-order conditions, where concentrations of substrates were maintained to be more than 10-folds excess of that of **3**. Because electron transfer from $Ru(Me_2\text{-bpy})_3]^{2+}$ to **3** was too fast to follow even with stopped-flow equipment under pseudo-first-order conditions, the second-order rate constant was determined under second-order conditions, where the concentrations of $[Ru^{II}(Me_2\text{-bpy})_3]^{2+}$ and **3** were maintained as the same (1.0×10^{-4} M).

Redox Titrations. Electron transfer from $[Ru^{II}(5\text{-}NO_2\text{-phen})_3]^{2+}$ to $[(L)Mn^{IV}(O)]^{2+}–(HOTf)_2$ (5×10^{-4} M) was examined from the spectral change in various concentrations of $[Ru^{II}(5\text{-}NO_2\text{-phen})_3]^{2+}$ (1×10^{-4} M – 1×10^{-3} M) at 273 K using a Hewlett Packard 8453 photodiode-array spectrometer. Typically, a deaerated CH_3CN solution of $[Ru^{II}(5\text{-}NO_2\text{-phen})_3]^{2+}$ (1×10^{-4} M – 1×10^{-3} M) was added to a solution of **3** (5×10^{-4} M) in $CF_3CH_2OH\text{-}CH_3CN$ (*v/v* = 1:1). The concentration of

$[Ru^{III}(5\text{-}NO_2\text{-phen})_3]^{3+}$ was determined from the absorption band at λ_{max} = 650 nm due to $[Ru^{III}(5\text{-}NO_2\text{-phen})_3]^{3+}$ (ε = 1.3 × 10^3 M^{-1} cm^{-1}) and the ε value of $[Ru^{III}(5\text{-}NO_2\text{-phen})_3]^{3+}$ was determined by the electron-transfer oxidation of $[Ru^{II}(5\text{-}NO_2\text{-phen})_3]^{2+}$ with cerium (IV) ammonium nitrate (3 equiv) in the presence of HOTf (30 mM) in $CF_3CH_2OH\text{-}CH_3CN$ (*v/v* = 1:1) at 273 K.

Product Analysis. Products formed in the oxidation of thioanisole by **3** were analyzed by HPLC. Quantitative analysis was performed by comparing the HPLC peak integration of products with its authentic sample. Methyl phenyl sulfoxide was produced as a sole product with 91(4)% yield (based on the concentration of catalyst). In the oxidation of 1,4-cyclohexadiene by **3**, GC and GC-MS were used to analyze products. Benzene was obtained as the sole product with the yield of 48(4)%, as observed in the oxidation of CHD by other metal-oxo complexes including $[(N4Py)Mn^{IV}(O)]^{2+}$, and $[(N4Py)Mn^{IV}(O)]^{2+}\text{–}(Sc^{3+})_2$.[23]

Results and Discussion

Binding of HOTf to Nonheme $Mn^{IV}(O)$ Complexes. Mononuclear high-valent manganese(IV)-oxo complexes, $[(N4Py)Mn^{IV}(O)]^{2+}$ (**1**) and $[(Bn\text{-}TPEN)Mn^{IV}(O)]^{2+}$ (**2**), were generated by reacting $[(N4Py)Mn^{II}]^{2+}$ and $[(Bn\text{-}TPEN)Mn^{II}]^{2+}$ with iodosylbenzene (PhIO), respectively, as reported previously.[23-25] Addition of HOTf to an *in situ* generated solution of **1** in $CF_3CH_2OH\text{-}CH_3CN$ (*v/v* = 1:1) at 273 K afforded a reddish brown solution and resulted in the disappearance of the absorption band at 940 nm due to **1**, accompanied by a new absorption band formation at 550 nm (shoulder, ε = 540 M^{-1} cm^{-1}) (Figure 2). Similar spectral changes were also obtained for **2**, indicating that the absorption band at 1020 nm due to **2** disappeared and concomitantly a new absorption band at 580 nm (ε = 650 M^{-1} cm^{-1}) was generated (Figure 3).

The spectral titration of **1** with HOTf (Figure 2a) exhibits a sigmoidal curvature (inset of Figure 2a), which suggests that more than one HOTf are attached to **1**. In such a case, the absorption change (ΔA) due to binding of n molecules of HOTf to **1** is given by eq 1,

$$\Delta A = \Delta A_0 K[\mathrm{HOTf}]^n/(1 + K[\mathrm{HOTf}]^n) \qquad (1)$$

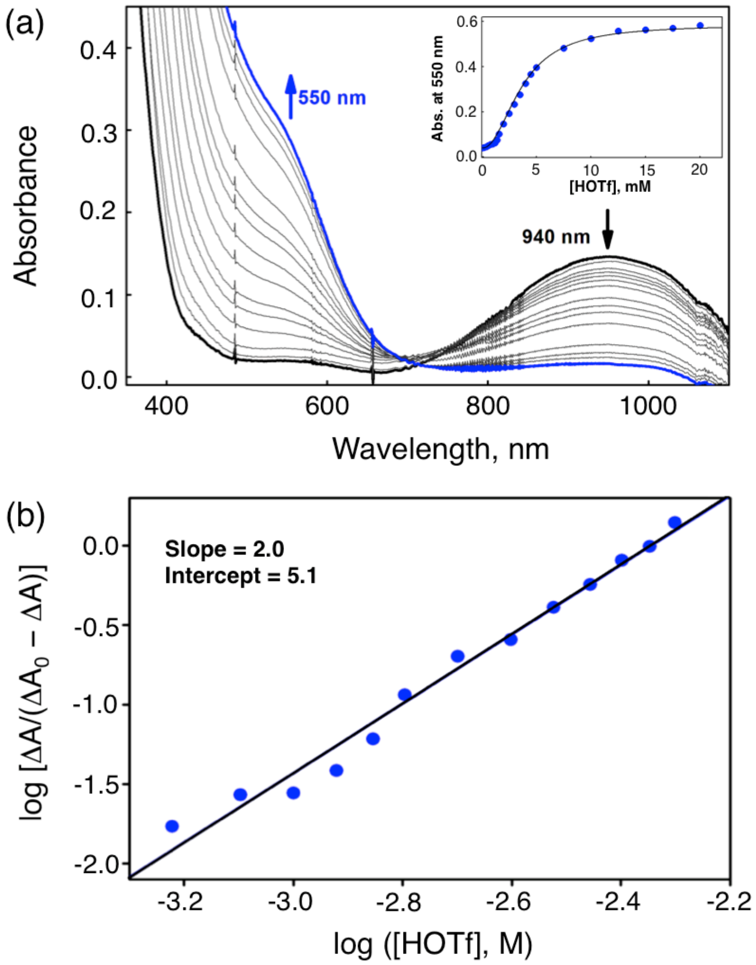

Figure 2. (a) UV-vis spectral changes observed in the titration of **1** (black bold line) with HOTf. HOTf (0 – 20 mM) was added incrementally into the solution of **1** (0.50 mM) in CF_3CH_2OH-CH_3CN (*v/v* = 1:1) at 273 K. Inset shows the spectral titration monitored at 550 nm (blue circles) due to the formation of **3**. (b) Plot of log($\Delta A/(\Delta A_0 - \Delta A)$) against log[HOTf] in the spectral titration of **1** with HOTf. ΔA and ΔA_0 are the absorption change and the final absorption change, respectively, due to binding of n molecules of HOTf to **1** (see eqs 1 and 2 in Text).

where ΔA_0 is the final absorption change due to binding of n molecules of HOTf to **1** and K is the binding constant. Eq 1 is rewritten by eq 2,

$$\log(\Delta A/(\Delta A_0 - \Delta A)) = \log K + n(\log[\mathrm{HOTf}]) \qquad (2)$$

which predicts a linear correlation between log($\Delta A/(\Delta A_0 - \Delta A)$) and log[HOTf] with a slope of n. From a linear correlation of log($\Delta A/(\Delta A_0 - \Delta A)$) vs log[HOTf], the number of HOTf molecules bound to **1** and the biding constant were determined to be 2.0(1) and 1.3(3) × 10^5 M^{-2}, where log$K$ = 5.1(1), respectively (inset of Figure 2a for the

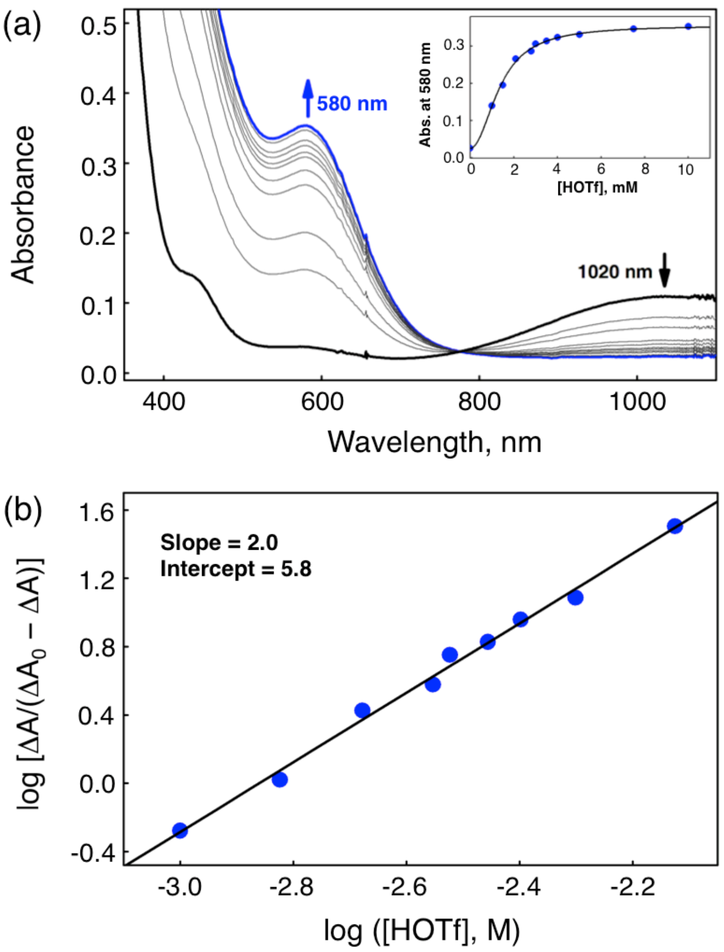

Figure 3. (a) UV-vis spectral changes observed in the titration of **2** (black bold line) with H^+ upon addition of HOTf (0 – 10 mM) into the solution of **2** (0.50 mM) in CF_3CH_2OH-CH_3CN (*v/v* = 1:1) at 273 K. Inset shows the spectral titration monitored at 580 nm (blue circles) due to the formation of **4**. (b) Plot of $\log(\Delta A/(\Delta A_0 - \Delta A))$ against log[HOTf] in the spectral titration of **2** with HOTf. ΔA and ΔA_0 are the absorption change and final absorption change due to binding of n molecules of HOTf to **2** (see eqs 1 and 2 in Text).

fitting of spectral titration data; Figure 2b for linear plot using eq 2). Thus, **1** is bound to two HOTf molecules to afford the HOTf-bound species, $[(\mathrm{N4Py})\mathrm{Mn}^{\mathrm{IV}}(\mathrm{O})]^{2+}$–$(\mathrm{HOTf})_2$ (**3**) (eq 3), which is relatively stable at 273 K ($t_{1/2} \approx 6$ h).

$$[(\mathrm{N4Py})\mathrm{Mn}^{\mathrm{IV}}(\mathrm{O})]^{2+} + 2\mathrm{HOTf} \longrightarrow [(\mathrm{N4Py})\mathrm{Mn}^{\mathrm{IV}}(\mathrm{O})]^{2+}\text{–}(\mathrm{HOTf})_2 \qquad (3)$$

When **2** was bound to two HOTf molecules to form the HOTf-bound species, $[(\mathrm{Bn\text{-}TPEN})\mathrm{Mn}^{\mathrm{IV}}(\mathrm{O})]^{2+}$–$(\mathrm{HOTf})_2$ (**4**), the half-lifetime of **4** was 1.5 h, indicating **4** is

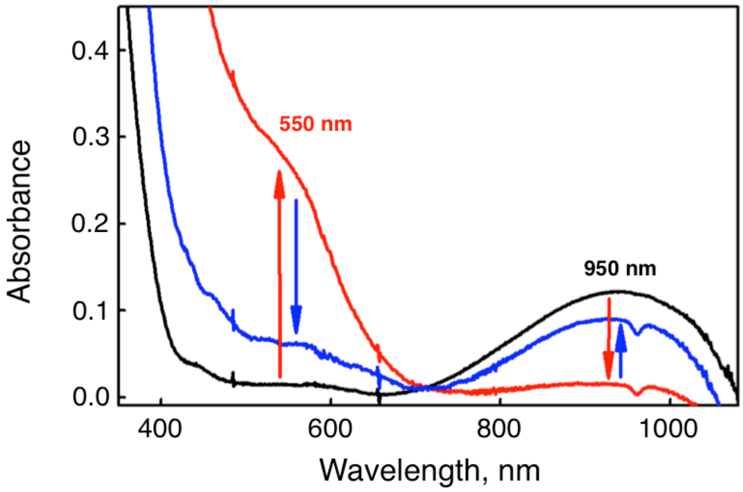

Figure 4. UV-Vis spectra of **1** (0.50 mM; black line) and **3** (0.50 mM; red line) in CF_3CH_2OH-CH_3CN (*v/v* = 1:1) at 273 K. **3** was generated by adding 30 mM of HOTf to a solution of **1**. Blue line shows UV-vis spectrum of **3** (0.50 mM) with triethylamine (30 mM) in CF_3CH_2OH-CH_3CN (*v/v* = 1:1) at 273 K.

somewhat less stable than **3**. It is important to note that **3** and **4** reverted to **1** and **2**, respectively, upon addition of base (i.e., triethylamine) as shown in Figure 4.

The X-band EPR spectrum of **3** exhibits signals that are characteristic of $S = 3/2$ Mn^{IV} ($g_1 = 5.8$, $g_2 = 3.2$ and $g_3 = 2.01$; see Figure 5). The magnetic moment of **3** was also determined to be 4.3 μ_B by the modified ^{1}H NMR technique of Evans,[26] confirming the spin state of $S = 3/2$. The coldspray ionization time-of-flight mass (CSI-TOF MS)

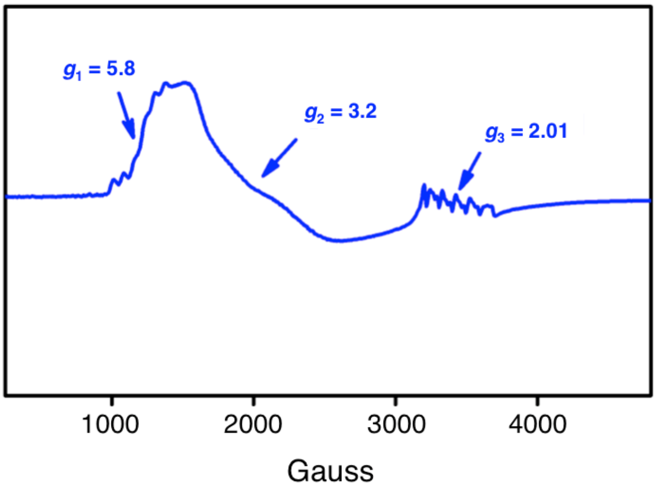

Figure 5. X-band CW-EPR spectrum of $[(N4Py)Mn^{IV}(O)]^{2+}$–$(HOTf)_2$ (**3**) (2.0 mM) in the presence of HOTf (30 mM) in CF_3CH_2OH-CH_3CN (*v/v* = 1:1) in perpendicular mode at 5 K. The signals of $g_1 = 5.8$, $g_2 = 3.2$ and $g_3 = 2.01$ are characteristic of $S = 3/2$ Mn^{IV}.

spectrum of **3** exhibits ion peaks at *m/z* 737.0 and 759.0, which shift to 739.0 and 761.0 upon introduction of ^{18}O during the generation of **3** using PhI^{18}O (Figure 6 for detailed assignments). This ^{18}O-labeled experiment suggests that **3** contains one oxygen atom. It should be noted that a species containing one bound HOTf was detected in CSI-TOF MS spectra, but the species with two bound HOTf molecules was not detected, probably because the binding of HOTf is fragile and easily broken under the CSI-TOF MS conditions.

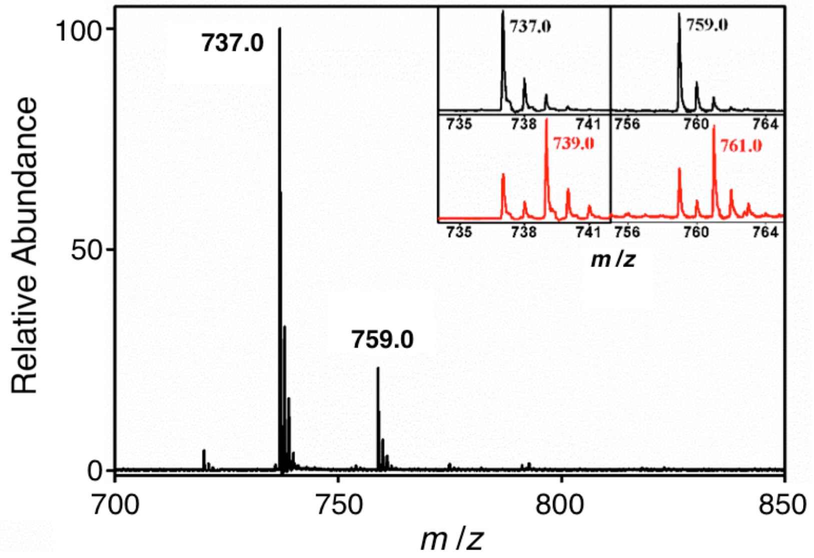

Figure 6. CSI-TOF MS spectrum of **3** with HOTf (30 mM) in CF_3CH_2OH-CH_3CN (*v/v* = 1:1) at 273 K. The mass and isotope distribution patterns of ion peaks at *m/z* = 737.0 and 759.0 correspond to $[Mn^{IV}(O)(N4Py)(CF_3SO_3)(CF_3SO_3H)]^+$ (*calcd. m/z* = 737.1) and $[Mn^{IV}(O)(N4Py)(CF_3SO_3)(NaCF_3SO_3)]^+$ (*calcd. m/z* = 759.0), respectively. Insets show the observed isotope distribution patterns for **3**-^{16}O (upper panel) and **3**-^{18}O (lower panel). **1**-^{16}O (1.0 mM) and **1**-^{18}O (1.0 mM) were prepared by reacting $[(N4Py)Mn(CF_3SO_3)]^+$ (1.0 mM) with PhI^{16}O (4.0 mM) and PhI^{18}O (4.0 mM), respectively, and then **3**-^{16}O and **3**-^{18}O were generated upon addition of HOTf (30 mM) into the solution of **1**-^{16}O (1.0 mM) and **1**-^{18}O (1.0 mM). The peak at 759.0 is assigned to [**1**-$NaCF_3SO_3]^+$, in which the Na^+ ion might be from the CSI-TOF MS conditions.

Comparison of X-ray absorption near edge structure (XANES) at the Mn K-edge for $[(N4Py)Mn^{IV}(O)]^{2+}$ (**1**, red line in Figure 7a) and $[(N4Py)Mn^{IV}(O)]^{2+}$–$(HOTf)_2$ (**3**, black line in Figure 7a) clearly shows a decrease in pre-edge intensity and no change in the rising-edge energy position of **3** relative to **1**, which is consistent with the elongation of the Mn–O bond and unchanged Mn^{IV} oxidation state, also consistent with the EPR results (Figure 5). Extended X-ray absorption fine structure (EXAFS) data as shown in

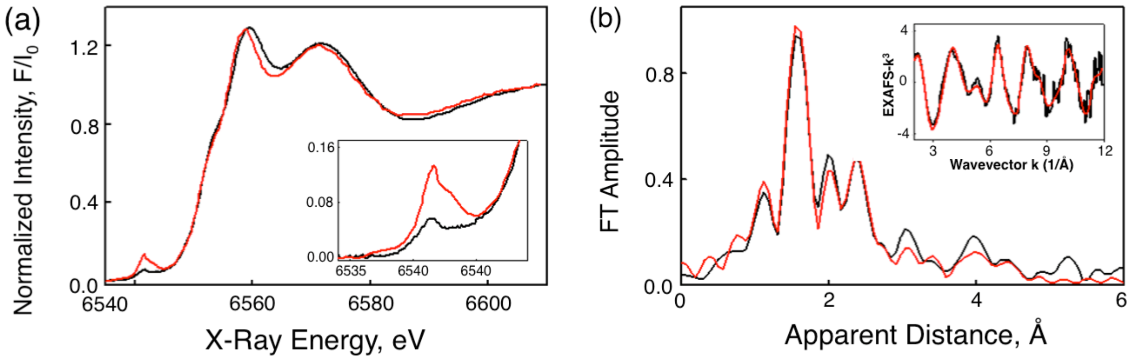

Figure 7. (a) Normalized Mn K-edge XANES of **1** (red line) and **3** with 30 mM of HOTf (black line). Inset shows magnified pre-edge features. (b) Non phase-shift corrected Fourier transforms (black line) and the corresponding Mn K-edge EXAFS data (inset; black line) for **3**. Fits (red lines) were performed in the range of $k = 2 – 12$ Å^{-1}.

Figure 7b indicates a short Mn−O bond distance of 1.74 Å (see Tables S1 and S2 in SI). This is longer than the 1.67 Å observed in [(N4Py)Mn^{IV}(O)]$^{2+}$ (**1**), indicating that the HOTf molecules interact with the oxo moiety of **1**. This Mn-O bond distance in **3** is almost identical to that of the [(N4Py)Mn^{IV}(O)]$^{2+}$ complex binding Sc^{3+} ions.[23,24] It should be noted that protons are not dissociated from the two HOTf moieties in Mn=O···(HOTf)$_2$, instead they are coordinated to the Mn(IV)=O unit by hydrogen bonding interaction. It is distinct from diprotonation, which would yield the putatively unstable [Mn^{IV}(OH$_2$)]$^{4+}$ species. This is evidenced by the small change in Mn=O distance upon binding of two HOTf molecules (less than 0.1 Å). The Mn–O distance of 1.74 Å indicates the double bond character of Mn–O, somewhat weakened by hydrogen bonding.

Thermodynamic and Kinetic Evidence for Binding of HOTf to [(N4Py)Mn^{IV}(O)]$^{2+}$ (1). Binding of two HOTf molecules to **1** was supported by the kinetic studies on the oxidation of *para*-CN-thioanisole by **3**, which was prepared by adding different amounts of HOTf (0 – 50 mM) into a solution of **1** (0.50 mM). The observed second-order rate constants (k_2) were determined by monitoring a decrease in absorption bands at 550 nm due to **3** or 940 nm due to **1**. The dependence of second-order rate constant for the oxidation of *para*-CN-thioanisole on the concentration of HOTf shows a sigmoidal curvature as shown in Figure 8. Such a sigmoidal curvature can be well explained by eq 4,

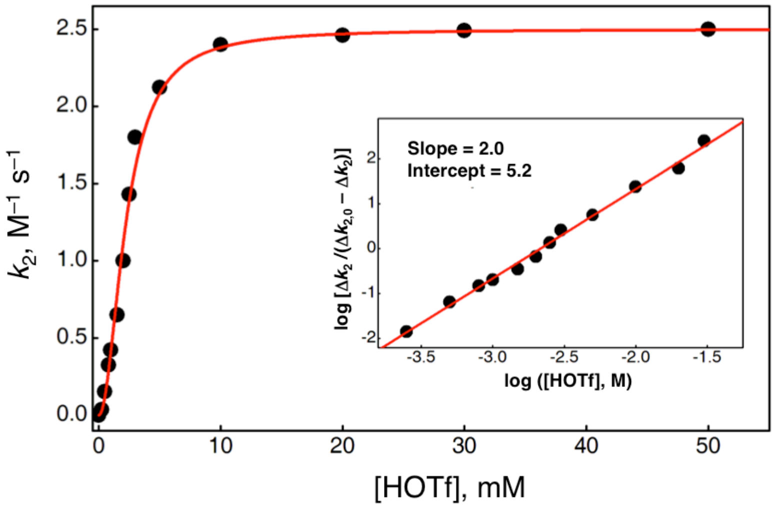

Figure 8. Dependence of the second-order rate constant, k_2, for the oxidation of *para*-CN-thioanisole by **3** (0.50 mM) on [HOTf] (0 – 50 mM) in CF_3CH_2OH-CH_3CN (v/v = 1:1) at 273 K. Inset shows a plot of log[$\Delta k_2/(\Delta k_{2,0} - \Delta k_2)$] vs log[HOTf], where $\Delta k_{2,0}$ is the full change of second-order rate constant.

$$k_2 = k_{ox}K[\mathrm{HOTf}]^2/(1 + K[\mathrm{HOTf}]^2) \qquad (4)$$

where k_{ox} is the rate constant of OAT from **3** to *para*-CN-thioanisole. Eq 4 is rewritten by eq 5, which predicts a linear relation between k_2^{-1}

$$k_2^{-1} = (k_{ox}K)^{-1}[\mathrm{HOTf}]^{-2} + k_{ox}^{-1} \qquad (5)$$

and $[\mathrm{HOTf}]^{-2}$. A linear plot of k_2^{-1} vs $[\mathrm{HOTf}]^{-2}$ (Figure 9) afforded the k_{ox} and K values

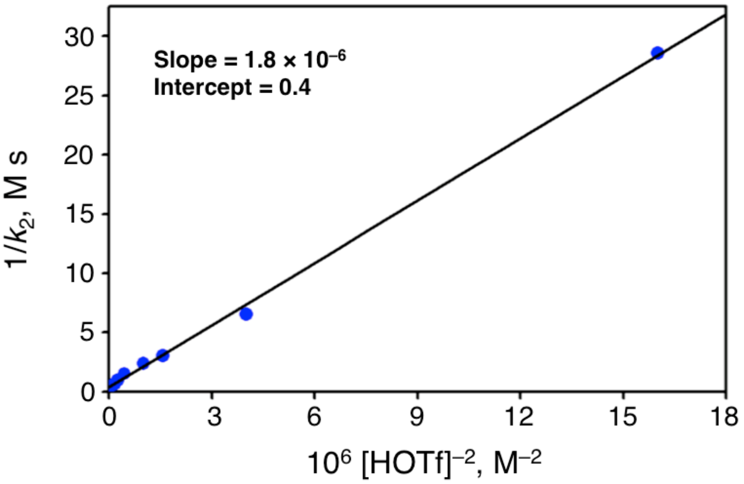

Figure 9. Plot of $1/k_2$ (M s) for sulfoxidation of *para*-CN-thioanisole by **3** (0.50 mM) vs $[\mathrm{HOTf}]^{-2}$.

of 2.5 M^{-1} s^{-1} and 1.6(4) × 10^5 M^{-2} [log$K$ = 5.2(1)], respectively, determined from the slope and intercept. The K value determined from inset of Figure 8 or Figure 9 is quite consistent with the value determined from the spectral titration under the same experimental conditions (Figure 2b). Furthermore, the fitting line in Figure 8 obtained by using the k_{ox} and K values determined is well matched with experimental data points, clearly indicating that two molecules of HOTf are involved in these reactions.

Enhancement of the Oxidation Capacity of the Nonheme Mn^{IV}(O) Complexes by Binding of Two HOTf Molecules. Electron transfer from coordinatively saturated metal complexes to $[Mn^{IV}(O)]^{2+}$–$(HOTf)_2$ complexes, **3** and **4**, were investigated, and these **3** and **4** species were found to perform electron transfer (ET) reaction with the one-electron reductant, $[Ru^{II}(5\text{-}NO_2\text{-phen})_3](PF_6)_2$ (5-NO_2-phen: 5-nitro-1,10-phenanthroline), which has a one-electron oxidation potential as high as

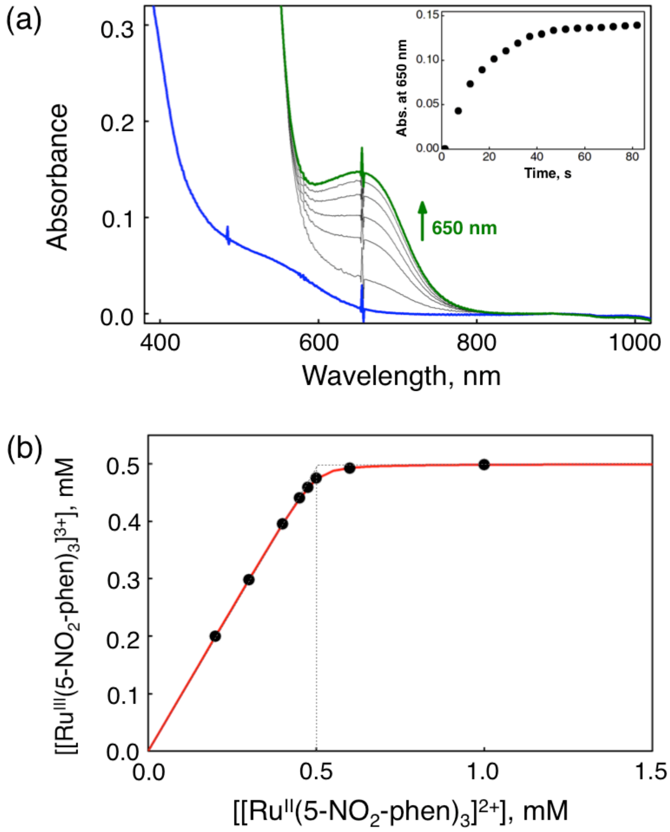

Figure 10. (a) UV-vis spectral changes for 3 (0.10 mM) upon addition of $[Ru^{II}(5\text{-}NO_2\text{-phen})_3](PF_6)_2$ (1.0 mM) in the presence of HOTf (30 mM) in CF_3CH_2OH-CH_3CN (*v/v* =1:1) at 273 K. The inset shows the time trace monitored at 650 nm due to the formation of $[Ru^{III}(5\text{-}NO_2\text{-phen})_3]^{3+}$. (b) Plot of concentration of $[Ru^{III}(5\text{-}NO_2\text{-phen})_3]^{3+}$ produced in electron transfer from $[Ru^{II}(5\text{-}NO_2\text{-phen})_3]^{2+}$ (1.50 V vs SCE) to 3 (0.50 mM) in the presence of HOTf (30 mM) at 273 K.

1.50 V vs SCE, whereas no ET was observed for **1** (E_{red} = 0.80 V vs SCE) and **2** (E_{red} = 0.78 V vs SCE).[24] The redox titration for formation of $[Ru^{III}(5\text{-}NO_2\text{-phen})_3]^{3+}$, as shown in Figure 10, indicates only one-electron reduction of **3** occurred without further reduction by $[Ru^{II}(5\text{-}NO_2\text{-phen})_3]^{2+}$. Upon addition of $[Ru^{II}(5\text{-}NO_2\text{-phen})_3]^{2+}$ into a solution of **3**, the absorption band at 450 nm due to $[Ru^{II}(5\text{-}NO_2\text{-phen})_3]^{2+}$ disappeared (data not shown) and concomitantly the absorption band at 650 nm due to $[Ru^{III}(5\text{-}NO_2\text{-phen})_3]^{3+}$ appeared with an isosbestic point at 550 nm (Figure 10a). By analyzing the resulting solution by EPR, we found that a Mn^{III} species was formed as a major product in the ET reaction by **3** (Figure 11). It should be noted that the second electron transfer could be observed to form the Mn^{II} product when a large excess of $[Ru^{II}(5\text{-}NO_2\text{-phen})_3]^{2+}$ was used; however, the rate of the second ET is much slower than that of the first ET at 273 K. The titration curve of the ET reaction, as shown in Figure 10b, revealed that ET from $[Ru^{II}(5\text{-}NO_2\text{-phen})_3]^{2+}$ to **3** is in equilibrium with back electron transfer from the $[Mn^{III}(O)]^{+}\text{–}(HOTf)_2$ species to $[Ru^{III}(5\text{-}NO_2\text{-phen})_3]^{3+}$ (eq 6, where K_{et} is the electron-transfer equilibrium constant).

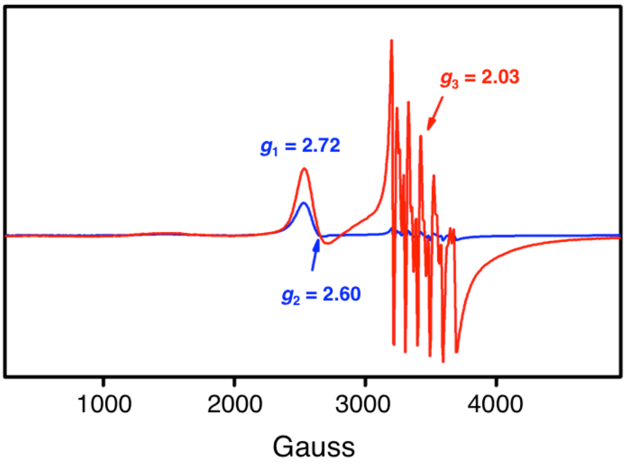

Figure 11. X-band CW-EPR spectra of the resulting solutions obtained in the reactions of **3** (2.0 mM) with $[Ru^{II}(5\text{-}NO_2\text{-phen})_3]^{2+}$ [2.0 mM (blue line) and 20 mM (red line)] after 4 h in the presence of HOTf (30 mM) in $CF_3CH_2OH\text{-}CH_3CN$ (*v/v* = 1:1) at 273 K. EPR spectra were recorded in perpendicular mode at 5 K. The EPR parameters of g_1 = 2.72 and g_2 = 2.60 in blue line are the signals of $[Ru^{III}(5\text{-}NO_2\text{-phen})_3]^{3+}$; however, no signals of Mn^{II} species were detected, indicating Mn^{III} species was formed as a product.

$$E_{red} = E_{ox} + (RT/F)\ln(K_{et}) \qquad (6)$$

By analyzing a linear plot as shown in Figure 12c, which was obtained from the redox titration curve in Figure 10b, the K_{et} value was determined to be 330. The one-electron reduction potential (E_{red}) of **3** in CF_3CH_2OH-CH_3CN (v/v = 1:1) at 273 K

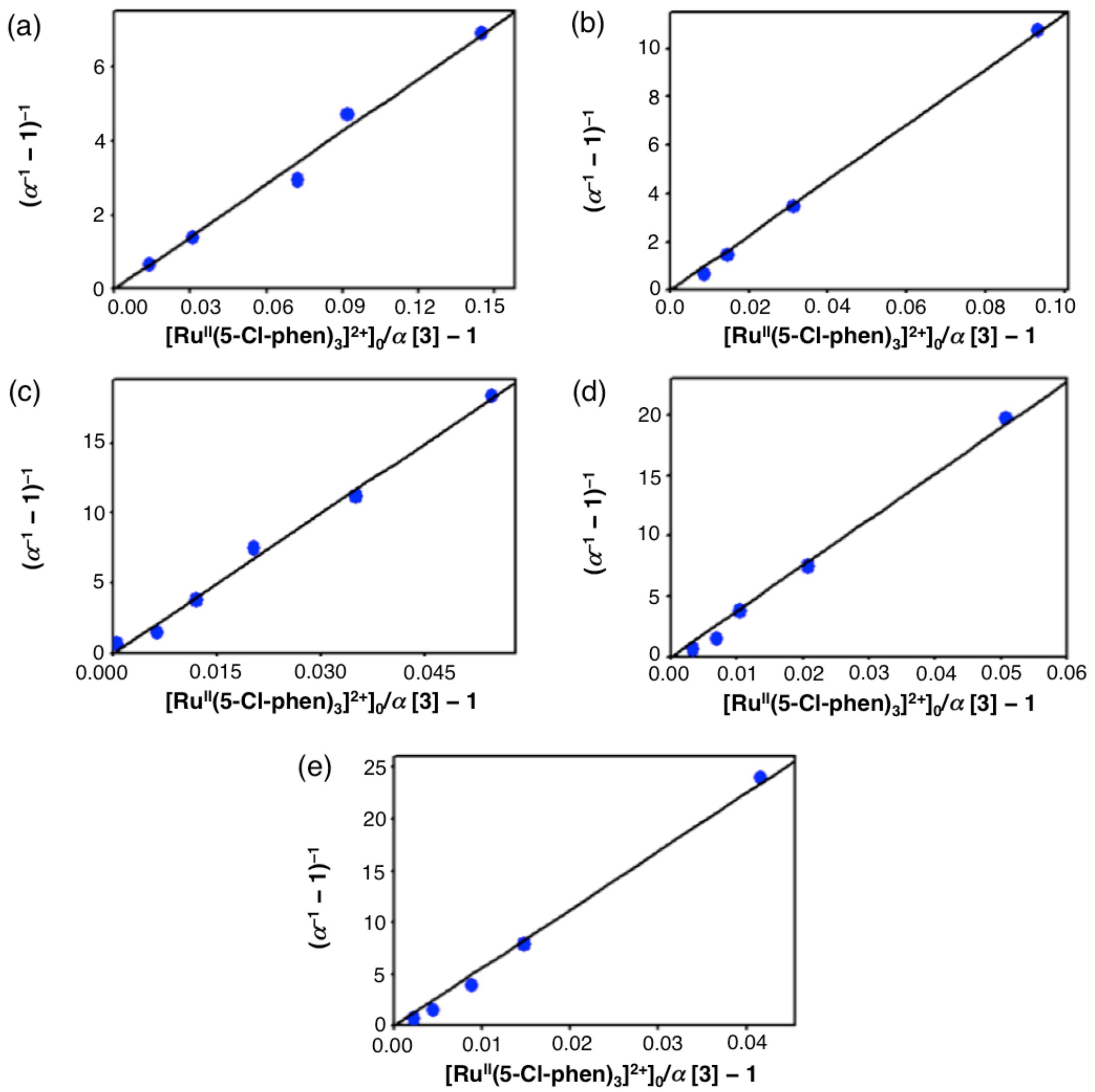

Figure 12. (a) Plot of $(\alpha^{-1} - 1)^{-1}$ vs $[[Ru^{II}(5\text{-Cl-phen})_3]^{2+}]_0/\alpha[\mathbf{3}]_0 - 1$ to determine the equilibrium constant, K_{et} (K_{et} = $[[Ru^{III}]^{3+}][[Mn^{III}(O)]^{+}]/[[Ru^{II}]^{2+}][[Mn^{IV}(O)]^{2+}]$), for electron transfer from $[Ru^{II}(5\text{-Cl-phen})_3]^{2+}$ to **3** upon addition of $[Ru^{II}(5\text{-Cl-phen})_3]^{2+}$ (0 – 1.0 mM) into a solution of **3** (0.50 mM) in the presence of HOTf (10 mM) in CF_3CH_2OH-CH_3CN (v/v = 1:1) at 273 K ($\alpha = [[Ru^{III}]^{3+}]/[\mathbf{3}]_0$). (b, c, d, e) Plots of $(\alpha^{-1} - 1)^{-1}$ vs $[[Ru^{II}(5\text{-NO}_2\text{-phen})_3]^{2+}]_0/\alpha[\mathbf{3}]_0 - 1$ to determine the equilibrium constants for electron transfer from $[Ru^{II}(5\text{-NO}_2\text{-phen})_3]^{2+}$ to **3** upon addition of $[Ru^{II}(5\text{-NO}_2\text{-phen})_3]^{2+}$ (0 – 1.0 mM) into a solution of **3** (0.50 mM) in the presence of HOTf [(b) 20 mM, (c) 30 mM, (d) 50 mM and (e) 80 mM)] in CF_3CH_2OH-CH_3CN (v/v = 1:1) at 273 K ($\alpha = [[Ru^{III}]^{3+}]/[\mathbf{3}]_0$).

was then determined from the K_{et} value and the E_{ox} value of $[\mathrm{Ru^{II}}(5\text{-}\mathrm{NO_2}\text{-phen})_3]^{2+}$ (E_{ox} = 1.50 V vs SCE) using the Nernst equation (eq 7),[27,28] where R is the gas constant, T is the absolute temperature, and F is the Faraday constant, to be 1.65 V vs SCE in the presence of HOTf (30 mM).

$$E_{\mathrm{red}} = E_{\mathrm{ox}} + (RT/F)\ln(K_{\mathrm{et}}) \qquad (7)$$

Similarly, the E_{red} value of **4** was determined from the K_{et} value of 1.2, which was obtained by the redox titration with $[\mathrm{Ru^{II}}(5\text{-}\mathrm{NO_2}\text{-phen})_3]^{2+}$ (see Figure 13), to be 1.50 V

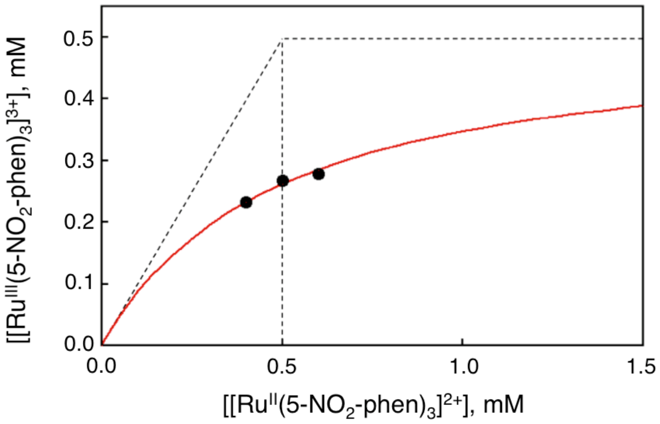

Figure 13. Plot of concentration of $[\mathrm{Ru^{III}}(5\text{-}\mathrm{NO_2}\text{-phen})_3]^{3+}$ produced in electron transfer from $[\mathrm{Ru^{II}}(5\text{-}\mathrm{NO_2}\text{-phen})_3]^{2+}$ (1.50 V vs SCE) to $[(\mathrm{Bn\text{-}TPEN})\mathrm{Mn^{IV}(O)}]^{2+}$ (0.50 mM) in the presence of HOTf (30 mM) in $\mathrm{CF_3CH_2OH\text{-}CH_3CN}$ (v/v = 1:1) at 273 K. The equilibrium constant (K_{et}) is determined to be

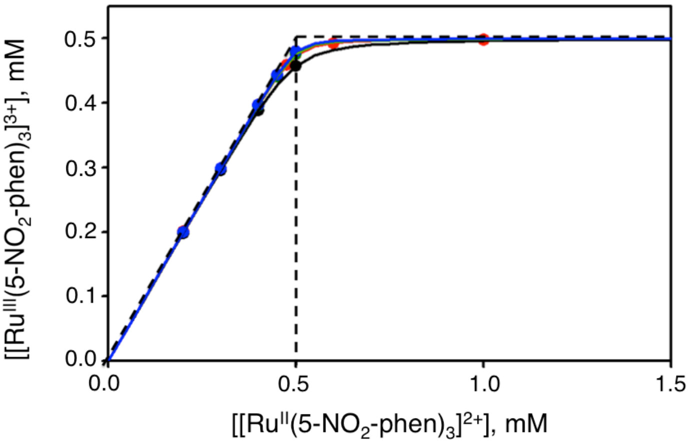

Figure 14. Plots of concentration of $[\mathrm{Ru^{III}}(5\text{-}\mathrm{NO_2}\text{-phen})_3]^{3+}$ produced in electron transfer from $[\mathrm{Ru^{II}}(5\text{-}\mathrm{NO_2}\text{-phen})_3]^{2+}$ (1.50 V vs SCE) to $[(\mathrm{N4Py})\mathrm{Mn^{IV}(O)}]^{2+}$ (0.50 mM) in the presence of various HOTf concentrations (black circles, 20 mM; red circles, 30 mM; green circles, 50 mM; blue circles, 80 mM) vs initial concentrations of $[\mathrm{Ru^{II}}(5\text{-}\mathrm{NO_2}\text{-phen})_3]^{2+}$ in $\mathrm{CF_3CH_2OH\text{-}CH_3CN}$ (v/v = 1:1) at 273 K.

vs SCE in the presence of HOTf (30 mM). Further, the E_{red} values of **3** at different concentrations of HOTf were also determined from the K_{et} values obtained by the redox titrations with $[Ru^{II}(5\text{-Cl-phen})_3]^{2+}$ (5-Cl-phen = 5-chloro-1,10-phenanthroline; E_{ox} = 1.41 V vs SCE) and $[Ru^{II}(5\text{-NO}_2\text{-phen})_3]^{2+}$ (see Figures 12 and 14). Figure 15 shows the dependence of E_{red} of **3** on the concentration of HOTf. The E_{red} value increases with increasing the concentration of HOTf to reach the constant value of 1.65 V vs SCE at more than 30 mM of HOTf at 273 K. The saturated E_{red} value of 1.65 V vs SCE in the presence of a large excess of HOTf corresponds to that of the $[Mn^{IV}(O)]^{2+}–(HOTf)_2$ complex of **3**. There is a large difference (ΔE_{red} = 0.85 V in the case of N4Py) in the E_{red} values between $[Mn^{IV}(O)\ ]^{2+}$ and $[Mn^{IV}(O)]^{2+}–(HOTf)_2$, which indicates that the binding of HOTf to $[Mn^{III}(O)]^{+}$ (the species derived from one-electron reduction of $[Mn^{IV}(O)]^{2+}$) is much stronger than that to $[Mn^{IV}(O)]^{2+}$, as expected from the increased basicity of the oxo moiety in $[Mn^{III}(O)]^{+}$. Thus, the HOTf-bound $Mn^{IV}(O)$ complex acts as the strongest oxidant among the nonheme Mn-oxo complexes bearing the same ligand system.

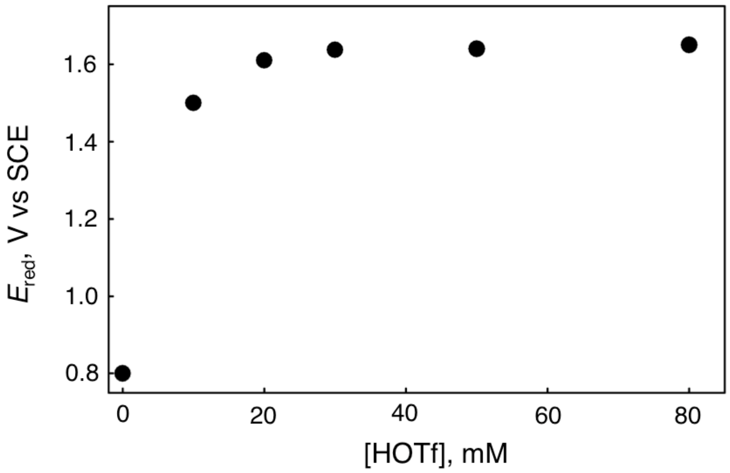

Figure 15. Dependence of E_{red} of $[(N4Py)Mn^{IV}(O)]^{2+}$ on the concentration of HOTf (0 – 80 mM) in CF_3CH_2OH-CH_3CN (*v/v* = 1:1) at 273 K.

As compared with the E_{red} values of $[(N4Py)Mn^{IV}(O)]^{2+}$ (0.80 V vs SCE) and $[(N4Py)Mn^{IV}(O)]^{2+}–(Sc^{3+})_2$ (1.42 V vs SCE),[24] a remarkable positive shift of E_{red} of **3** (1.65 V vs SCE) was observed under the same conditions in CF_3CH_2OH-CH_3CN (*v/v* = 1:1) at 273 K, resulting in significant enhancement of the ET reactivity. Rates of ET from various one-electron donors, coordinatively saturated iron(II) and ruthenium(II)

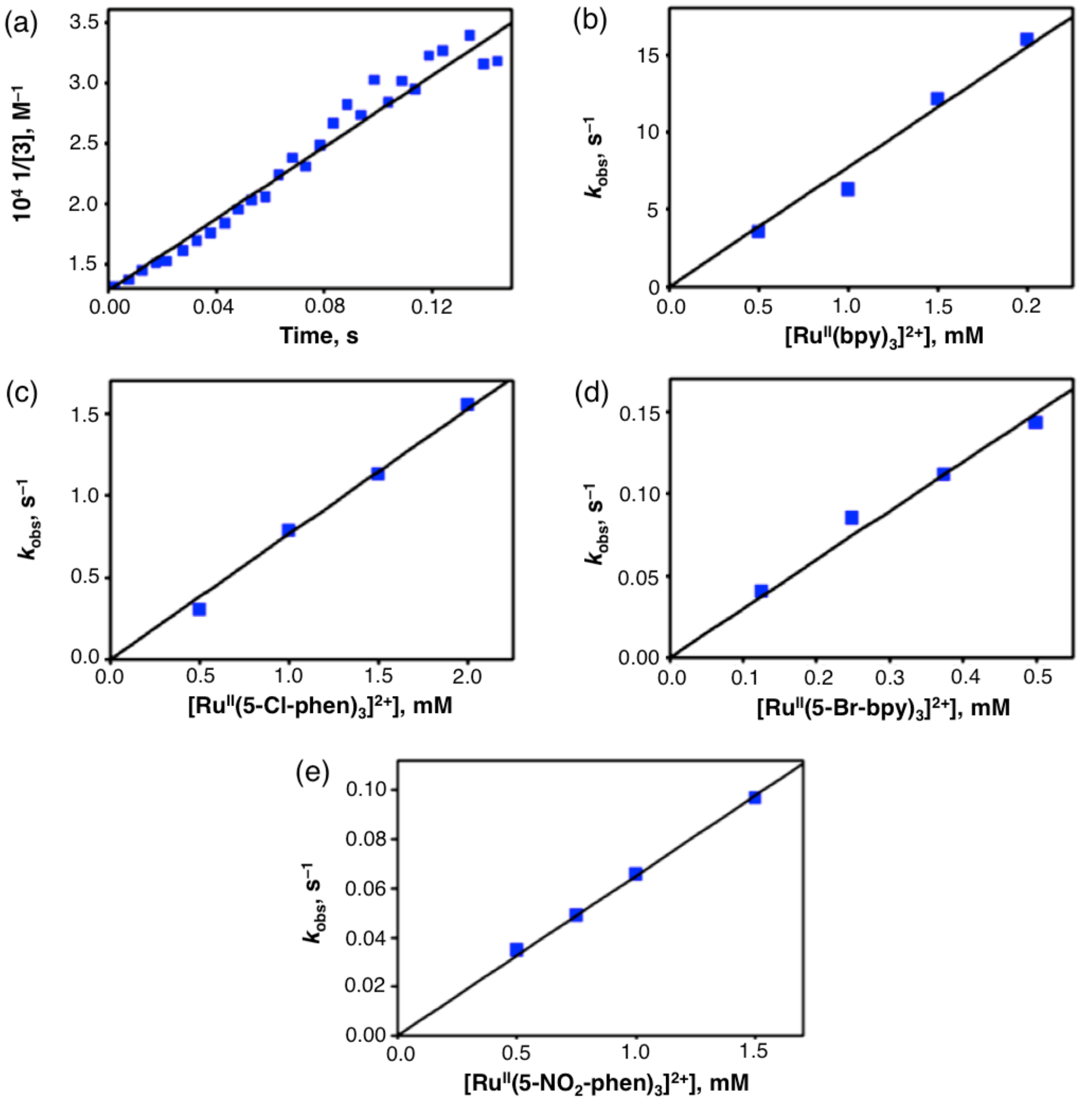

Figure 16. (a) Second-order plot of 1/[**3**] vs time for electron transfer from $[\mathrm{Ru^{II}(Me_2\text{-}bpy)_3}]^{2+}$ (0.10 mM) to **3** (0.10 mM). (b, c, d, e) Plots of k_{obs} against the concentration of one-electron reductants to determine second-order rate constants in the electron transfer reactions from one electron reductants [(b) $[\mathrm{Ru^{II}(bpy)_3}]^{2+}$, (c) $[\mathrm{Ru^{II}(5\text{-}Cl\text{-}phen)_3}]^{2+}$, (d) $[\mathrm{Ru^{II}(5\text{-}Br\text{-}bpy)_3}]^{2+}$ and (e) $[\mathrm{Ru^{II}(5\text{-}NO_2\text{-}phen)_3}]^{2+}$] to **3** in the presence of HOTf (30 mM) in $\mathrm{CF_3CH_2OH\text{-}CH_3CN}$ (*v/v* = 1:1) at 273 K.

complexes, to **3** and **4** were investigated and the rate constants were determined by monitoring the absorbance changes due to the decay of iron(II) or the formation of corresponding ruthenium(III) species. Rates of ET obeyed pseudo-first order or second-order kinetics, and the pseudo-first-order rate constant (k_{obs}) increased linearly with increasing concentrations of electron donors. The second-order rate constants (k_{et}) of ET thus determined are listed in Table 1 together with the one-electron oxidation

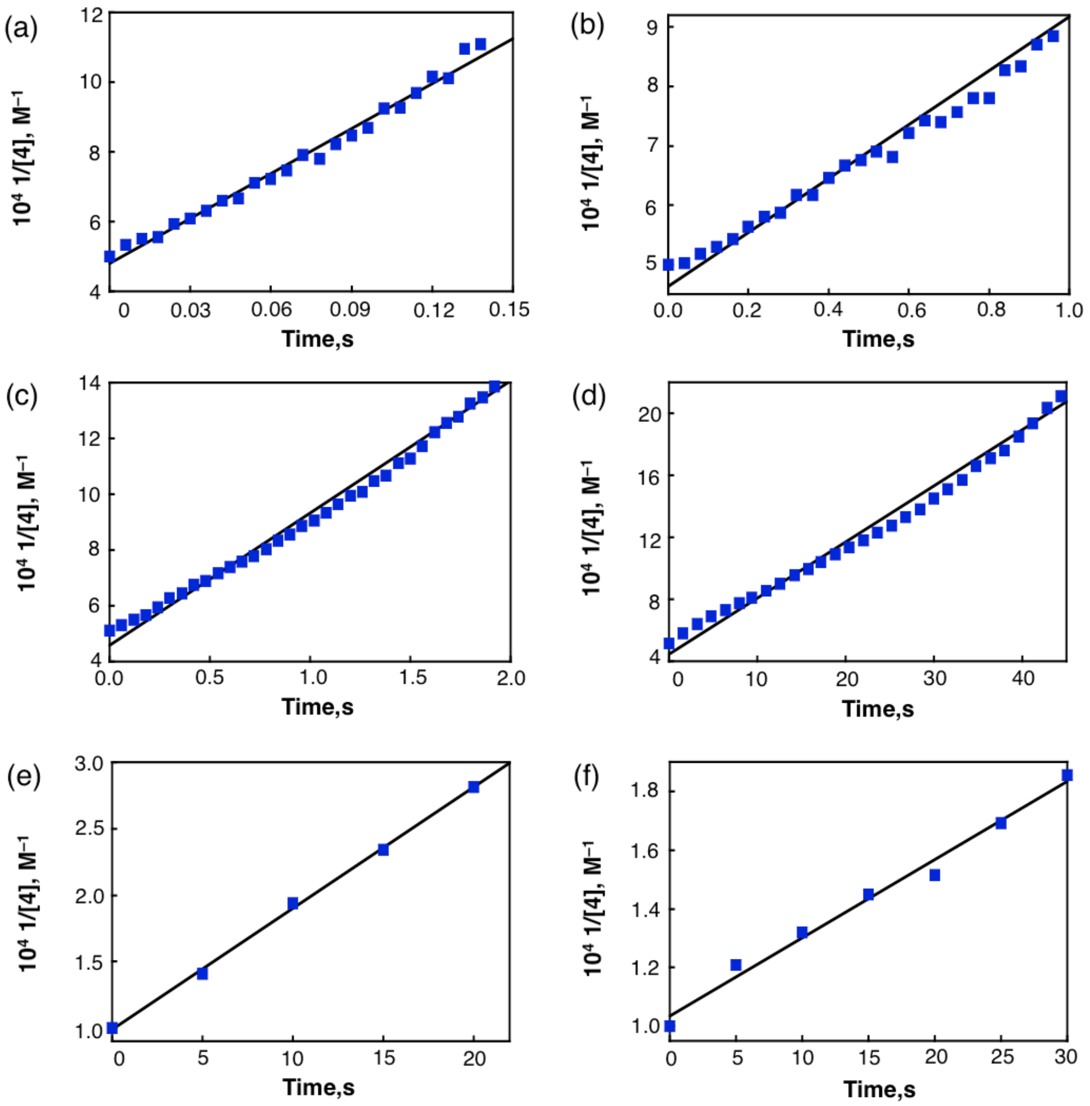

Figure 17. Second-order plots of 1/[**4**] vs time for electron transfer from one electron reductants (0.020 mM; (a) $[Fe^{II}(Me_2\text{-bpy})_3]^{2+}$, (b) $[Fe^{II}(phen)_3]^{2+}$, (c) $[Fe^{II}(bpy)_3]^{2+}$, (d) $[[Ru^{II}(Me_2\text{-bpy})_3]^{2+}$, (e) $[Ru^{II}(5\text{-Br-bpy})_3]^{2}$ and (f) $[Ru^{II}(5\text{-Cl-phen})_3]^{2+}$) to **4** (0.020 mM) in the presence of HOTf (30 mM) in $CF_3CH_2OH\text{-}CH_3CN$ (*v*/*v* = 1:1) at 273 K.

potentials (E_{ox}) of one-electron reductants in $CF_3CH_2OH\text{-}CH_3CN$ (*v*/*v* = 1:1) and the driving force of ET ($-\Delta G_{et}$) (see also Figures 16 and 17 for **3** and **4**, respectively).

Outer-Sphere Electron Transfer of $[Mn^{IV}(O)]^{2+}$–$(HOTf)_2$. The driving force dependence of the rate constants of electron transfer from one-electron reductants to **3** (Figure 18 and Table 1) is well fitted in the light of the Marcus theory of adiabatic outer-sphere electron transfer (eq 8),

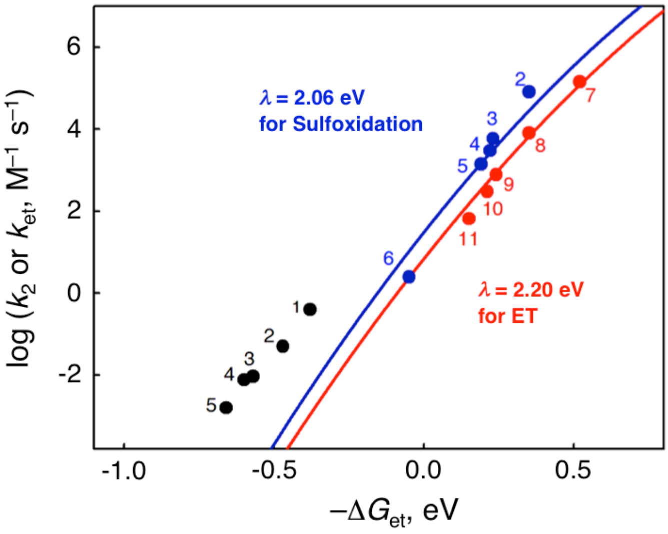

Figure 18. Plots of log k_2 for sulfoxidation of *para*-X-substituted thioanisoles [X = (1) MeO, (2) Me, (3) H, (4) F, (5) Br and (6) CN] by $[(N4Py)Mn^{IV}(O)]^{2+}$ vs the driving force of electron transfer [$-\Delta G_{et}$ = e($E_{red} - E_{ox}$)] from thioanisoles to $[(N4Py)Mn^{IV}(O)]^{2+}$ in the absence of HOTf (black circles)[21,22] and the presence of 30 mM of HOTf (blue circles) in CF_3CH_2OH-CH_3CN (*v/v* = 1:1) at 273 K. The red circles show the driving force dependence of the rate constants (log k_{et}) of ET from one-electron reductants ((7) $[Ru^{II}(Me_2\text{-bpy})_3]^{2+}$, (8) $[Ru^{II}(bpy)_3]^{2+}$, (9) $[Ru^{II}(5\text{-Cl-phen})_3]^{2+}$, (10) $[Ru^{II}(5\text{-Br-bpy})_3]^{2+}$ and (11) $[Ru^{II}(5\text{-NO}_2\text{-phen})_3]^{2+}$ to $[(N4Py)Mn^{IV}(O)]^{2+}$ in the presence of 30 mM of HOTf in CF_3CH_2OH-CH_3CN (*v/v* = 1:1) at 273 K.

$$k_{et} = Z\exp[-(\lambda/4)(1 + \Delta G_{et}/\lambda)^2/k_BT] \qquad (8)$$

where Z is the collision frequency, taken as 1 × 10^{11} M^{-1} s^{-1}, λ is the reorganization energy of electron transfer, k_B is the Boltzmann constant, and T is the absolute temperature. From the fitting of the ET rate constants (red circles in Figure 18), the λ value of ET from one-electron reductants to **3** was determined to be 2.20 ± 0.02 eV. Similarly, the λ value for the ET reaction of **4** with one-electron reductants was determined to be 2.15 ± 0.03 eV (Table 1; see also Figures 17 and 19). Both λ values of the ET reduction of $[(L)Mn^{IV}(O)]^{2+}$–$(HOTf)_2$ (L = N4Py and Bn-TPEN) are smaller than those of $[(L)Mn^{IV}(O)]^{2+}$ in the absence of HOTf,[24,25] since the elongation of the Mn-O bond distance by binding of two HOTf molecules occurs prior to the ET, resulting in smaller change in the Mn-O bond distance after ET reduction. However, the λ values for $[Mn^{IV}(O)]^{2+}$–$(HOTf)_2$ are quite similar to those for $[Mn^{IV}(O)]^{2+}$–$(Sc^{3+})_2$.[22] This result is quite reasonable because, according to the XANES/EXAFS analyses, the elongation of the Mn-O bond due to binding of HOTf is almost identical to the case of the Mn-O species binding Sc^{3+} ions (vide supra).[23]

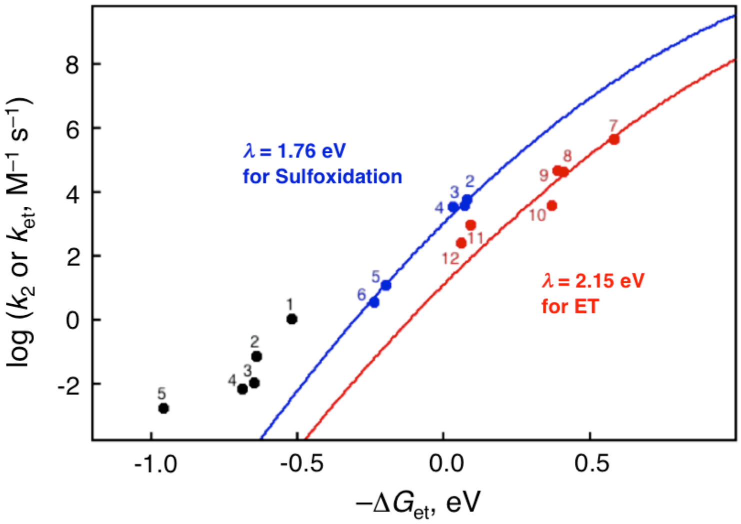

Figure 19. Plots of log k_2 for sulfoxidation of *para*-X-substituted thioanisoles [X = (1) Me, (2) H, (3) F, (4) Br, (5) CN and (6) NO_2] by $[(\text{Bn-TPEN})Mn^{IV}(O)]^{2+}$ (**2**; black circles) and $[(\text{Bn-TPEN})Mn^{IV}(O)]^{2+}-(HOTf)_2$ (**4**; blue circles) vs the driving force of electron transfer [$-\Delta G_{et} = e(E_{red} - E_{ox})$] from thioanisoles to **2** (E_{red} = 0.78 V vs SCE) and **4** (E_{red} = 1.50 V vs SCE) in the presence of HOTf (30 mM) in CF_3CH_2OH-CH_3CN (*v*/*v* = 1:1) at 273 K. The red circles show the driving force dependence of the rate constants (log k_2) of ET from one-electron reductants [(7) $[Fe^{II}(Me_2\text{-bpy})_3]^{2+}$, (8) $[Fe^{II}(bpy)_3]^{2+}$, (9) $[Fe^{II}(phen)_3]^{2+}$, (10) $[Ru^{II}(Me_2\text{-bpy})_3]^{2+}$, (11) $[Ru^{II}(5\text{-Cl-phen})_3]^{2+}$ and (12) $[Ru^{II}(Br\text{-bpy})_3]^{2+}$] to **4** in CF_3CH_2OH-CH_3CN (*v*/*v* = 1:1) at 273 K. The blue and red lines are the Marcus lines calculated with λ values of 1.76 and 2.15 eV, respectively.

Contrasting Effects of Binding of HOTf to on the Reactivity of Nonheme $Mn^{IV}(O)$ Complexes in OAT and HAT Reactions. The reactivity of the HOTf-bound $Mn^{IV}(O)$ complexes, **3** and **4**, was investigated in OAT and HAT reactions. The OAT reaction (e.g., the oxidation of thioanisoles) was markedly influenced by binding of two HOTf molecules to the Mn-oxo moiety (Table 1, Figures 20 and 21 for **3** and **4**, respectively). Upon addition of thioanisole to a solution of **3** (Figure 22), the $Mn^{IV}(O)$ complex reverted back to the starting Mn^{II} complex, which was confirmed by EPR (Figure 23). Product analysis of the reaction solutions revealed the formation of methyl phenyl sulfoxide in a quantitative yield. These results indicate that the oxidation of thioanisole by the HOTf-bound $Mn^{IV}(O)$ complexes, $Mn^{IV}(O)-(HOTf)_2$, occurs via a two-electron oxidation process as reported previously for $Mn^{IV}(O)$ and $Mn^{IV}(O)-(Sc^{3+})_2$.[23,24] The second-order rate constant (5.9×10^3 M^{-1} s^{-1}) determined in the reaction of thioanisole with **3** at 273 K is 6.4×10^5-fold and 3.0×10^2-fold greater than those of **1** (9.2×10^{-3} M^{-1} s^{-1}) and $[(N4Py)Mn^{IV}(O)]^{2+}-(Sc^{3+})_2$ (2.0×10 M^{-1} s^{-1}),[23] respectively, demonstrating that the reactivity of the manganese(IV)-oxo complex in the

Table 1. One-Electron Oxidation Potentials (E_{ox}) of One-Electron Reductants and *para*-X-substituted Thioanisoles and Second-Order Rate Constants of ET and Sulfoxidation Reactions by $[(N4Py)Mn^{IV}(O)]^{2+}$–$(HOTf)_2$ (3) and $[(Bn\text{-}TPEN)Mn^{IV}(O)]^{2+}$–$(HOTf)_2$ (4) with Driving Force of ET ($-\Delta G_{et}$) in the Presence of HOTf (30 mM) in CF_3CH_2OH-CH_3CN (v/v = 1:1) at 273 K.

electron donor	E_{ox}[a] (V vs SCE)	$[(N4Py)Mn^{IV}(O)]^{2+}$–$(HOTf)_2$		$[(Bn\text{-}TPEN)Mn^{IV}(O)]^{2+}$–$(HOTf)_2$	
		k_{et}, M^{-1} s^{-1}	$-\Delta G_{et}$, eV	k_{et}, M^{-1} s^{-1}	$-\Delta G_{et}$, eV
$[Fe^{II}(Me_2\text{-}bpy)_3]^{2+}$	0.92	too fast	0.73	4.3×10^5	0.58
$[Fe^{II}(bpy)_3]^{2+}$	1.09	too fast	0.56	4.5×10^4	0.41
$[Fe^{II}(phen)_3]^{2+}$	1.11	too fast	0.54	4.7×10^4	0.39
$[Ru^{II}(Me_2\text{-}bpy)_3]^{2+}$	1.13	1.4×10^5	0.52	3.6×10^3	0.37
$[Ru^{II}(bpy)_3]^{2+}$	1.30	8.0×10^3	0.35	*c*	0.20
$[Ru^{II}(5\text{-}Cl\text{-}phen)_3]^{2+}$	1.41	7.8×10^2	0.24	9.2×10^2	0.09
$[Ru^{II}(5\text{-}Br\text{-}bpy)_3]^{2+}$	1.44	3.0×10^2	0.21	2.6×10^2	0.06
$[Ru^{II}(5\text{-}NO_2\text{-}phen)_3]^{2+}$	1.50	6.5×10	0.15	too slow	0
X in *para*-X-thioanisole	E_{ox}[b] (V vs SCE)	$[(N4Py)Mn^{IV}(O)]^{2+}$–$(HOTf)_2$		$[(Bn\text{-}TPEN)Mn^{IV}(O)]^{2+}$–$(HOTf)_2$	
		k_2, M^{-1} s^{-1}	$-\Delta G_{et}$, eV	k_2, M^{-1} s^{-1}	$-\Delta G_{et}$, eV
Me	1.30	8.1×10^4	0.35	*c*	0.20
H	1.42	5.9×10^3	0.23	5.5×10^3	0.08
F	1.43	3.0×10^3	0.22	3.8×10^3	0.07
Br	1.47	1.4×10^3	0.18	3.4×10^3	0.03
CN	1.70	2.5	-0.05	1.2×10	-0.20
NO_2	1.74	*c*	-0.09	3.4	-0.24

[a] The one-electron oxidation potentials of coordinatively saturated metal complexes were determined by cyclic voltammetry in CF_3CH_2OH-CH_3CN (v/v = 1:1) containing 0.10 M n-Bu_4NPF_6 as a supporting electrolyte at 298 K. The one-electron oxidation potentials of coordinatively saturated metal complexes in the presence of HOTf (30 mM) were identical to those in the absence of HOTf. [b] The one-electron oxidation potentials of *para*-X-thioanisoles were determined by second harmonic A.C. voltammetry (SHACV) in CF_3CH_2OH-CH_3CN (v/v = 1:1) containing 0.10 M n-Bu_4NPF_6 as a supporting electrolyte at 298 K. [c] Not mearsured.

OAT reaction is markedly enhanced by binding of two HOTf molecules. Much accelerated reactivity of the HOTf-bound $Mn^{IV}(O)$ species was also observed in the reactions of other *para*-X-substituted thioanisoles (Table 1; Figure 20). In addition, a good linear correlation was obtained by plotting the log k_2 values against one-electron oxidation potentials of thioanisoles (Figure 22b). The slope of –11.4(5) in Figure 22b is in between those reported for outer-sphere electron transfer reductions of $[(TMC)Fe^{III}\text{-}OOH]^{2+}$ [slope = –9.7(6)] and $[(TMC)Fe^{III}\text{-}OOC(CH_3)_3]^{2+}$ [slope = –12(1)],[29] suggesting that the rate dependence on the oxidation potential of the reductant

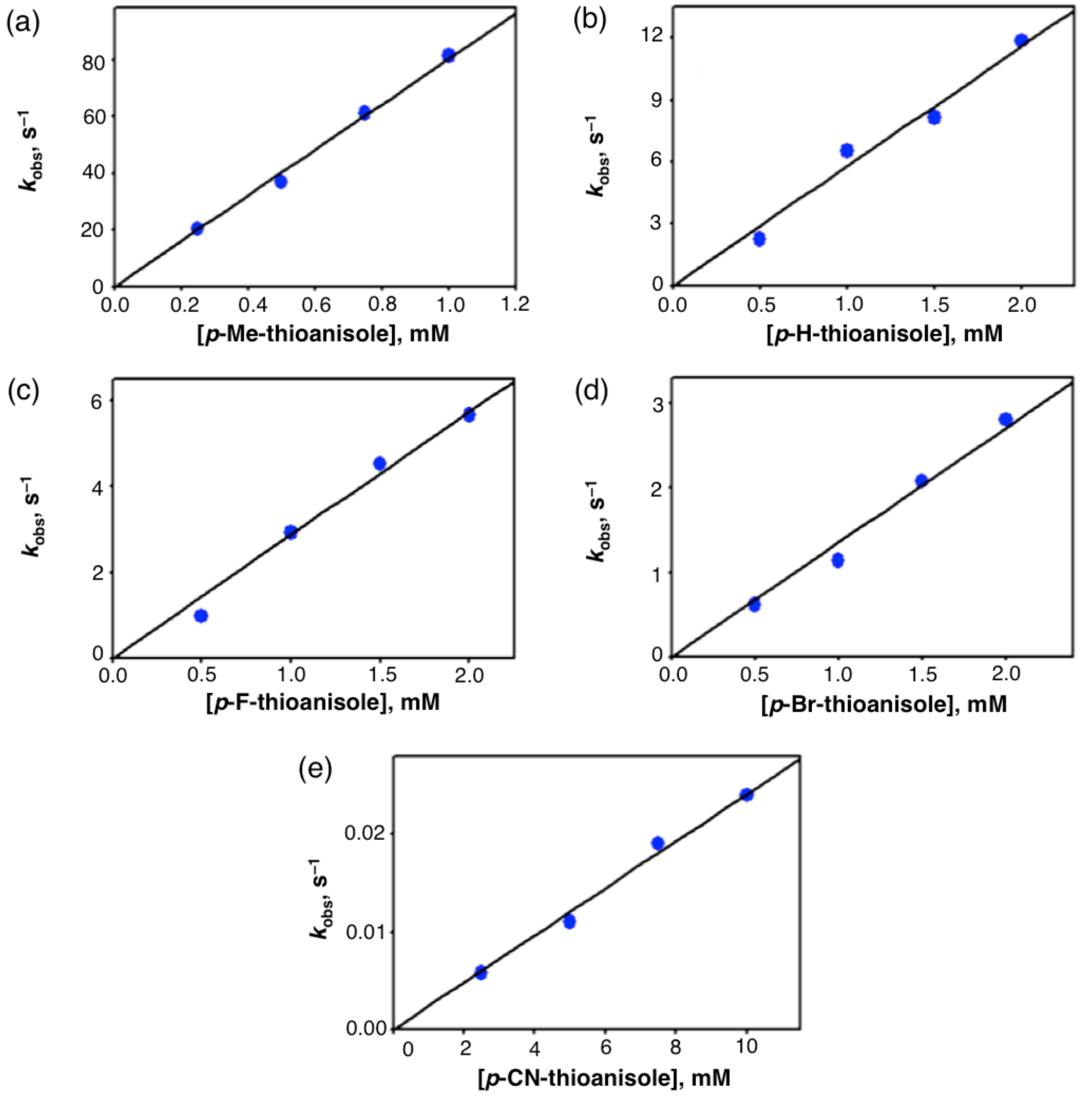

Figure 20. Plots of k_{obs} against the concentration of *para*-X-thioanisoles to determine second-order rate constants (k_2) in the oxidation of *para*-X-thioanisoles [X = (a) Me, (b) H, (c) F, (d) Br and (e) CN] by **3** in the presence of HOTf (30 mM) in CF_3CH_2OH-CH_3CN (v/v = 1:1) at 273 K.

follows the Marcus theory of electron transfer. The remarkable enhancement of the reactivity was also observed in the oxidation of thioanisoles by **4**. The slope in the plot of the log k_2 values against one-electron oxidation potentials of thioanisoles (Figure 24) for **4** was –10.0(6), which is similar to that of **3**, indicating that ET process is involved in the rate determining step. In the OAT reaction by **3**, the rate was dependent on reaction temperature (Figure 25). The activation parameters of $\Delta H^{\ddagger}$ = 15.1 kcal mol^{-1} and $\Delta S^{\ddagger}$ = −1.2 cal mol^{-1} K^{-1} were determined from the slope and intercept in a linear Eyring plot obtained between 253 K and 293 K (Figure 26). The observed activation

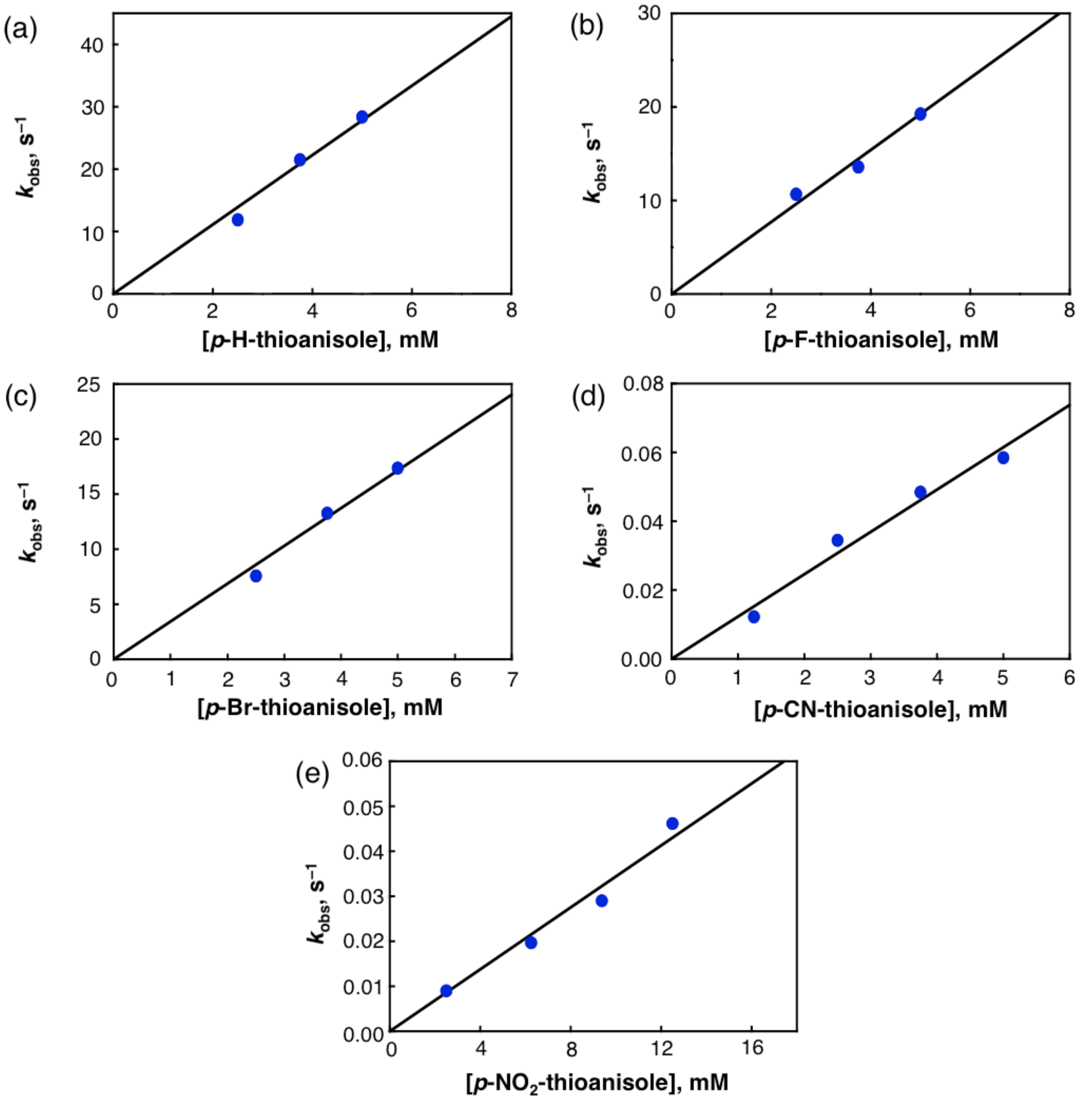

Figure 21. (a) Plots of the pseudo-first-order rate constants (k_{obs}) of *para*-X-substituted thioanisoles [X = (a) H, (b) F, (c) Br, (d) CN and (e) NO_2] at 580 nm due to the decay of $[(Bn\text{-}TPEN)Mn^{IV}(O)]^{2+}$–$(HOTf)_2$ in the presence of HOTf (30 mM) in CF_3CH_2OH-CH_3CN (*v/v* = 1:1) at 273 K.

entropy close to zero is also indicative of those of outer-sphere electron-transfer reactions,[22,27] suggesting that the OAT reaction of **3** occurs via ET from thioanisoles to **3**.

We have shown previously the change of mechanism from a direct oxygen atom-transfer (DOT) pathway by $[(N4Py)Mn^{IV}(O)]^{2+}$ to an electron transfer (ET) pathway by $[(N4Py)Mn^{IV}(O)]^{2+}$ binding two Sc^{3+} ions in the sulfoxidation of thioanisoles.[24] As shown in Figure 18, the electron-transfer driving force dependence of log k_2 for the oxidation of thioanisoles by **3** (blue circles) exhibits virtually the same

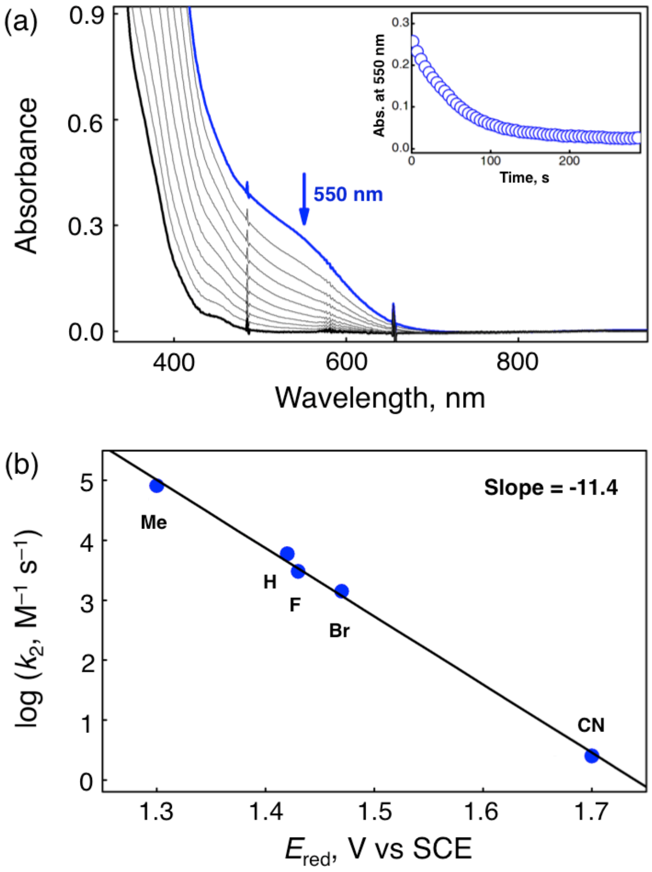

Figure 22. (a) UV-vis spectral changes of **3** (0.50 mM) upon addition of *p*-CN-thioanisole (5.0 mM) in the presence of HOTf (30 mM) in CF_3CH_2OH-CH_3CN (*v/v* = 1:1) at 273 K. Inset shows the time trace monitored at 550 nm. (b) Plot of the log k_2 against one-electron oxidation potentials of *para*-X-thioanisoles (X = MeO, Me, H, F, Br, and CN) for the oxidation of thioanisole derivatives by **3** in the presence of HOTf (30 mM) in CF_3CH_2OH-CH_3CN (*v/v* = 1:1) at 273 K.

relationship with the driving force dependence of log k_{et} of electron-transfer reactions of **3** (red circles), whereas a huge deviation from the ET line for those of **1** (black circles) was shown. This result together with the slope in the plot of the log k_2 values against one-electron oxidation potentials of thioanisoles and the activation parameters (vide supra) strongly indicates that the oxidation of thioanisoles by $Mn^{IV}(O)-(HOTf)_2$ intermediates proceeds via an outer-sphere electron-transfer pathway.[25]

The reactivities of the HOTf-bound Mn-oxo species, **3** and **4**, were also investigated kinetically in HAT, such as the C-H bond activation of 1,4-cyclohexadiene (CHD). Outer-sphere electron transfer from CHD to **3** is highly endergonic and thereby unlikely to occur judging from the more positive one-electron oxidation potential of CHD (E_{ox} = 1.89 V vs SCE)[30] than the one-electron reduction potential of **3** (E_{red} = 1.65 V vs SCE).

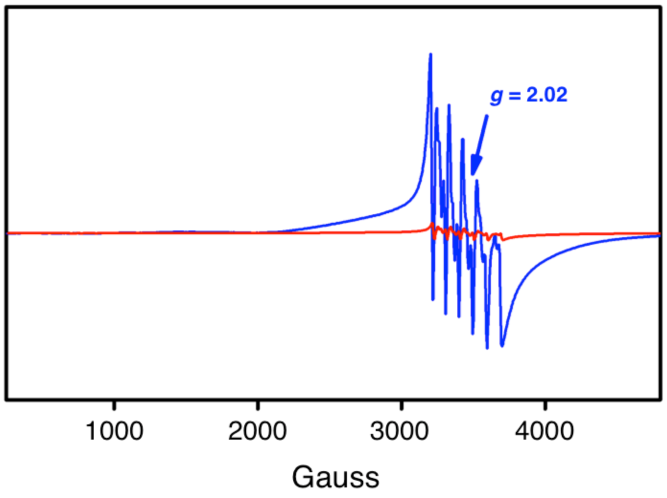

Figure 23. X-band EPR spectra of reaction solutions of $[(N4Py)Mn^{IV}(O)]^{2+}$–$(HOTf)_2$ (**3**, 2.0 mM) with thioanisole (20 mM; blue line) and 1,4-cyclohexadiene (20 mM; red line) in the presence of HOTf (30 mM) in CF_3CH_2OH-CH_3CN (*v/v* = 1:1) at 273 K and 298 K, respectively. EPR spectra were recorded in perpendicular mode at 5 K.

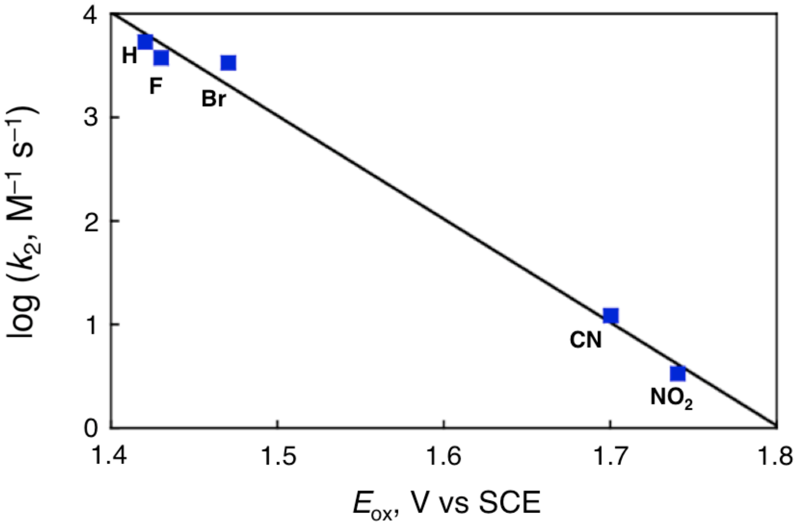

Figure 24. Plot of log k_2 against the one-electron oxidation potentials (E_{ox}) of *para*-X-thioanisoles (X = H, F, Br, CN and NO_2) by $[(Bn\text{-}TPEN)Mn^{IV}(O)]^{2+}$– $(HOTf)_2$ [slope = –10.0(6)] in the presence of HOTf (30 mM) in CF_3CH_2OH-CH_3CN (*v/v* = 1:1) at 273 K.

As shown in Figure 27a, addition of CHD to a solution of **3** in CF_3CH_2OH-CH_3CN (*v/v* = 1:1) at 298 K afforded the decay of absorption band at 550 nm due to **3**. Analysis of the resulting solution with EPR, GC and GC-MS showed that the major product was a Mn^{III} species, which is EPR silent (Figure 23 for EPR),[23] and that benzene was obtained as the sole organic product with a yield of 48% based on the concentration of **3**, similar

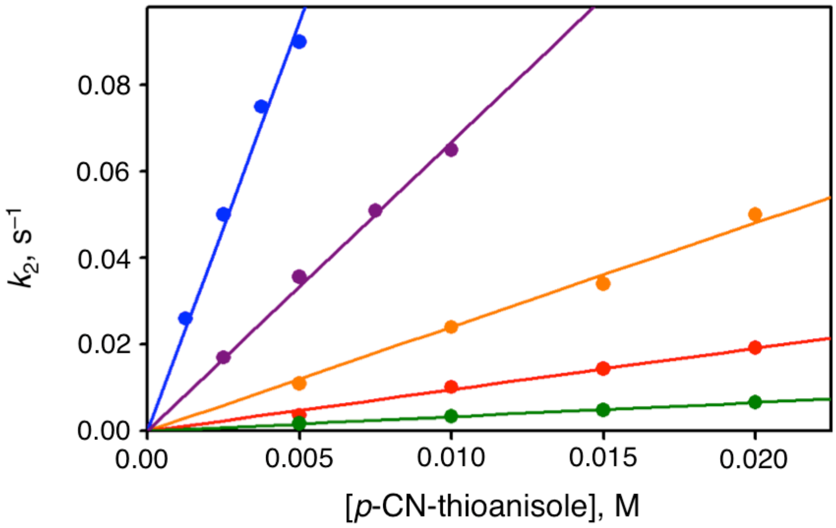

Figure 25. Plots of k_{obs} against the concentration of *para*-CN-thioanisole to determine second-order rate constants (k_2) in the presence of HOTf (30 mM) in CF_3CH_2OH-CH_3CN (*v/v* = 1:1) at various temperature [293 K (blue), 283 K (violet), 273 K (orange), 263 K (red) and 253 K (green)].

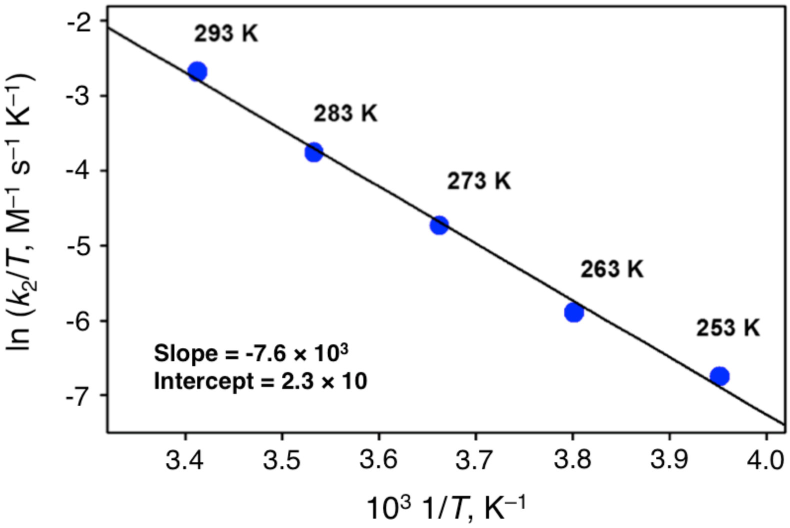

Figure 26. Eyring plot to determine activation parameters for the reaction of **3** with *para*-CN-thioanisole in the presence of HOTf (30 mM) in CF_3CH_2OH-CH_3CN (*v/v* = 1:1).

to that observed in the oxidation of CHD by nonheme $Mn^{IV}(O)$, $Mn^{IV}(O)$–$(Sc^{3+})_2$ and other nonheme metal-oxo species.[23,31] The second-order rate constant (9.2×10^{-1} M^{-1} s^{-1}) determined in the oxidation of CHD by **3** was smaller, by a factor of ~4, than that for **1** (3.5 M^{-1} s^{-1}) at 298 K (Figure 27b), indicating that the reactivity of the $Mn^{IV}(O)$ complex is diminished by binding of two HOTf molecules to the $Mn^{IV}(O)$ moiety. As

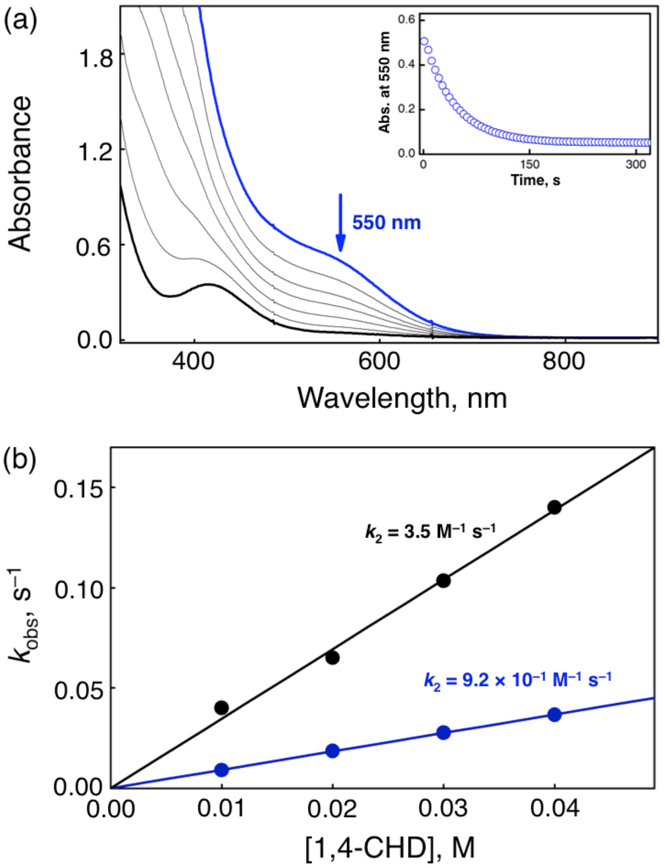

Figure 27. (a) UV-vis spectral changes of **3** (0.50 mM) upon addition of *p*-CN-thioanisole (5.0 mM) in the presence of HOTf (30 mM) in CF_3CH_2OH-CH_3CN (*v/v* = 1:1) at 273 K. Inset shows the time trace monitored at 550 nm. (b) Plot of the log k_2 against one-electron oxidation potentials of *para*-X-thioanisoles (X = MeO, Me, H, F, Br, and CN) for the oxidation of thioanisole derivatives by **3** in the presence of HOTf (30 mM) in CF_3CH_2OH-CH_3CN (*v/v* = 1:1) at 273 K.

reported previously, the reactivity of the $Mn^{IV}(O)$ complex in the oxidation of CHD was diminished by a factor of ~180 upon binding of two Sc^{3+} ions and the reason of the significant deceleration of the rate was proposed to be owing to the steric effect of the Sc^{3+} ions.[23] The smaller deceleration (~4-fold) due to HOTf binding, as compared to the $Sc(OTf)_3$ binding, may be explained by the smaller molecular size of HOTf than that of $Sc(OTf)_3$. The $Mn^{IV}(O)$ moiety in $[Mn^{IV}(O)]^{2+}$–$(HOTf)_2$ can provide suitable interaction with substrate, but the interaction was slightly hindered by binding of HOTf. However, the interaction between substrate and intermediate was more hindered by binding of Sc^{3+} ions, which has a relatively bigger size, to $Mn^{IV}(O)$ moiety, leading to the more diminished reactivity in HAT reactions. Similarly, in the reaction of **4** with CHD, a deceleration of ~9-fold was detected by comparison of the reactivity of **2** (Figure 28).

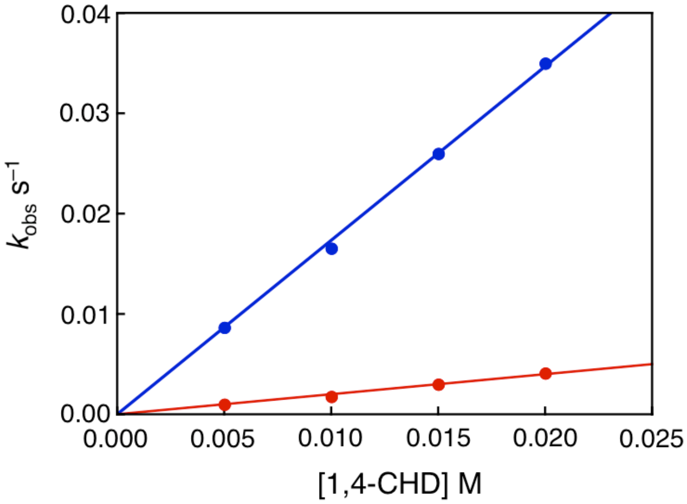

Figure 28. Plots of k_{obs} against the concentration of 1,4-cyclohexadiene (CHD) to determine the second-order rate constants in the oxidation of CHD by **2** (0.25 mM) and **4** (0.25 mM) in CF_3CH_2OH-CH_3CN (v/v = 1:1) at 273 K, respectively. Deceleration (~9-fold) of C-H bond activation by $[(\mathrm{Bn\text{-}TPEN})\mathrm{Mn}^{\mathrm{IV}}(\mathrm{O})]^{2+}$–$(\mathrm{HOTf})_2$ can be explained as prohibiting suitable interaction between Mn(IV)-oxo moiety and CHD.

The contrasting effects by binding of two HOTf molecules observed in OAT and HAT reactions were brought to light for the first time experimentally in the study of the effect of Brønsted acid. In agreement with the result reported for the promotion effect of Lewis acid in the reaction of $[(\mathrm{N4Py})\mathrm{Fe}^{\mathrm{IV}}(\mathrm{O})]^{2+}$, our results also have shown that Brønsted acid has the ability to promote the ET reaction intensely efficient, but relatively, the possibility of steric hindrance caused by binding of two HOTf molecules to the metal-oxo group should also be taken into consideration when the Brønsted acid is involved in a reaction system.

Conclusion

Mononuclear nonheme manganese(IV)-oxo complexes binding protons were generated for the first time and characterized by various spectroscopic techniques. Their reactivities on electron transfer (ET), oxygen atom transfer (OAT) and hydrogen atom transfer (HAT) reactions were investigated. Binding of protons to the manganese-oxo moiety leads to a more positive shift of the one-electron reduction potential and a contrasting effect on the reactivities in OAT and HAT reactions. The reactivity of the nonheme manganese(IV)-oxo complexes was markedly enhanced by the diprotonation;

6.4×10^5-fold increase in OAT reaction (i.e., oxygenation of thioanisole), whereas deceleration was observed in the rate of HAT reaction of $Mn^{IV}(O)-(HOTf)_2$ complexes with CHD relative to that of the corresponding manganese(IV)-oxo complexes. However, HAT was faster compared to that of the Sc^{3+} ion-bound complex, which may be explained by the relatively smaller molecular size of HOTf compared with that of $Sc(OTf)_3$, when the interaction between manganese(IV)-oxo and substrate required for HAT reactions would be less hindered. Thus, the diprotonation of the manganese(IV)-oxo moiety with HOTf resulted in remarkable acceleration of the ET rate, when thermodynamically feasible. When the ET reaction is highly endergonic as with CHD, the rate of HAT is decelerated due to steric effects of the counter anion of HOTf.

References

(1) (a) Meunier, B.; de Visser, S. P.; Shaik, S. *Chem. Rev.* **2004**, *104*, 3947. (b) Abu-Omar, M. M.; Loaiza, A.; Hontzeas, N. *Chem. Rev.* **2005**, *105*, 2227. (c) Denisov, I. G.; Makris, T. M.; Sligar, S. G.; Schlichting, I. *Chem. Rev.* **2005**, *105*, 2253. (d) Groves, J. T. *J. Inorg. Biochem*. **2006**, *100*, 434. (e) Ortiz de Montellano, P. R. *Chem. Rev*. **2010**, *110*, 932.

(2) (a) Shaik, S.; Cohen, S.; Wang, Y.; Chen, H.; Kumar, D.; Thiel, W. *Chem. Rev*. **2010**, *110*, 949. (b) Usharani, D.; Janardanan, D.; Li, C.; Shaik, S. *Acc. Chem. Res*. **2013**, *46*, 471.

(3) (a) Krebs, C.; Fujimori, D. G.; Walsh, C. T.; Bollinger, J. M., Jr. *Acc. Chem. Res.* **2007**, *40*, 484. (b) Que, L., Jr. *Acc. Chem. Res*. **2007**, *40*, 493. (c) Nam, W. *Acc. Chem. Res.* **2007**, *40*, 522. (d) Borovik, A. S. *Acc. Chem. Res.* **2005**, *38*, 54 ㅗ간. (e) Borovik, A. S. *Chem. Soc. Rev.* **2011**, *40*, 1870. (f) Hohenberger, J.; Ray, K.; Meyer, K. *Nat. Commun.* **2012**, *3*, 720.

(4) (a) Comba, P.; Kerscher, M.; Schiek, W. *Prog. Inorg. Chem.* **2007**, *55*, 613. (b) Bakac, A. *Coord. Chem. Rev.* **2006**, *250*, 2046. (c) Espenson, J. H. *Coord. Chem. Rev.* **2005**, *249*, 329. (d) Fujii, H. *Coord. Chem. Rev*. **2002**, *226*, 51.

(5) (a) Solomon, E. I.; Brunold, T. C.; Davis, M. I.; Kemsley, J. N.; Lee, S.-K.; Lehnert, N.; Neese, F.; Skulan, A. J.; Yang, Y.-S.; Zhou, J. *Chem. Rev.* **2000**, *100*, 235. (b) Costas, M.; Mehn, M. P.; Jensen, M. P.; Que, L., Jr. *Chem. Rev*. **2004**, *104*, 939. (c) Tshuva, E. Y.; Lippard, S. J. *Chem. Rev.* **2004**, *104*, 987. (d) Decker, A.; Solomon, E. I. *Curr. Opin. Chem. Biol.* **2005**, *9*, 152. (e) Solomon, E. I.; Wong, S. D.; Liu, L. V; Decker, A.; Chow, M. S. *Curr. Opin. Chem. Biol.* **2009**, *13*, 99.

(6) (a) Najafpour, M. M.; Moghaddam, A. N.; Allakhverdiev, S. I.; Govindjee, *Biochim. Biophys. Acta Bioenerg.* **2012**, *1817*, 1110. (b) Loll, B.; Kern, J.; Saenger, W.; Zouni, A.; Biesiadka, J. *Nature* **2005**, *438*, 1040.

(7) (a) Aromi, G.; Brechin, E. K. *Struct. Bonding* **2006**, *122*, 1. (b) Bagai, R.; Christou, G. *Chem. Soc.*

Rev. **2009**, *38*, 1011. (c) Mullins, C. S.; Pecoraro, V. L. *Coord. Chem. Rev.* **2008**, *252*, 416. (d) Iwata, S.; Barber, J. *Curr. Opin. Struct. Biol.* **2004**, *14*, 447. (e) Barber, J. *Phil. Trans. R. Soc. B* **2008**, *363*, 2665.

(8) (a) Umena, Y.; Kawakami, K.; Shen, J.-R.; Kamiya, N. *Nature* **2011**, *473*, 55. (b) Kawakami, K.; Umena, Y.; Kamiya, N.; Shen, J.-R. *J. Photochem. Photobiol. B* **2011**, *104*, 9.

(9) Nam, W.; Lee, Y.-M.; Fukuzumi, S. *Acc. Chem. Res*. **2014**, *47*, 1146.

(10) (a) Kaizer, J.; Klinker, E. J.; Oh, N. Y.; Rohde, J.-U.; Song, W. J.; Stubna, A.; Kim, J.; Münck, E.; Nam, W.; Que, L., Jr. *J. Am. Chem. Soc*. **2004**, 126, 472. (b) Seo, M. S.; Kim, N. H.; Cho, K.-B.; So, J. E.; Park, S. K.; Clémancey, M.; Garcia-Serres, R.; Latour, J.-M.; Shaik, S.; Nam, W. *Chem. Sci.* **2011**, *2*, 1039. (c) Hong, S.; Lee, Y.-M.; Cho, K.-B.; Sundaravel, K.; Cho, J.; Kim, M. J.; Shin, W.; Nam, W. *J. Am. Chem. Soc.* **2011**, *133*, 11876.

(11) (a) Morimoto, Y.; Kotani, H.; Park, J.; Lee, Y.-M.; Nam, W.; Fukuzumi, S. *J. Am. Chem. Soc.* **2011**, *133*, 403. (b) Park, J.; Morimoto, Y.; Lee, Y.-M.; Nam, W.; Fukuzumi, S. *J. Am. Chem. Soc.* **2011**, *133*, 5236. (c) Park, J.; Morimoto, Y.; Lee, Y.-M.; You, Y.; Nam, W.; Fukuzumi, S. *Inorg. Chem*. **2011**, *50*, 11612. (d) Morimoto, Y.; Park, J.; Suenobu, T.; Lee, Y.-M.; Nam, W.; Fukuzumi, S. *Inorg. Chem*. **2012**, *51*, 10025.

(12) Leeladee, P.; Baglia, R. A.; Prokop, K. A.; Latifi, R.; de Visser, S. P.; Goldberg, D. P. *J. Am. Chem. Soc*. **2012**, *134*, 10397.

(13) (a) Tsui, E. Y.; Tran, R.; Yano, J.; Agapie, T. *Nat. Chem*. **2013**, *5*, 293. (b) Kanady, J. S.; Mendoza-Cortes, J. L.; Tsui, E. Y.; Nielsen, R. J.; Goddard, W. A., III; Agapie, T. *J. Am. Chem. Soc.* **2013**, *135*, 1073. (c) Kanady, J. S.; Tsui, E. Y.; Day, M. W.; Agapie, T. *Science* **2011**, *333*, 733..

(14) Fukuzumi, S.; Morimoto, Y.; Kotani, H.; Naumov, P.; Lee, Y.-M.; Nam, W. *Nat. Chem*. **2010**, *2*, 756.

(15) (a) Fukuzumi, S. *Prog. Inorg. Chem.* **2009**, *56*, 49. (b) Fukuzumi, S. *Bull. Chem. Soc. Jpn.* **1997**, *70*, 1. (c) Fukuzumi, S.; Ohkubo, K. *Coord. Chem. Rev.* **2010**, *254*, 372. (d) Fukuzumi, S. *Chem. Lett.* **2008**, *37*, 808. (e) Fukuzumi, S.; Ohtsu, H.; Ohkubo, K.; Itoh, S.; Imahori, H. *Coord. Chem. Rev.* **2002**, *226*, 71. (f) Fukuzumi, S.; Itoh, S. *Antioxid. Redox Signal.* **2001**, *3*, 807.

(16) (a) Fukuzumi, S. *Pure Appl. Chem.* **2003**, *75*, 577. (b) Fukuzumi, S. *Electron Transfer in Chemistry*, vol. 4, ed. V. Balzani; Wiley-VCH: Weinheim, Germany, 2001, pp 3–59. (c) Fukuzumi, S.; Ohkubo, K.; Morimoto, Y. *Phys. Chem. Chem. Phys*. **2012**, *14*, 8472.

(17) (a) Park, J.; Morimoto, Y.; Lee, Y.-M.; Nam, W.; Fukuzumi, S. *J. Am. Chem. Soc*. **2012**, *134*, 3903. (b) Park, J.; Lee, Y.-M.; Nam, W.; Fukuzumi, S. *J. Am. Chem. Soc*. **2013**, *135*, 5052.

(18) (a) Taylor, M. S.; Jacobson, E. N. *Angew. Chem., Int. Ed.* **2006**, *45*, 1520. (b) Akiyama, T. *Chem. Rev*. **2007**, *107*, 5744.

(19) Yuasa, J.; Suenobu, T; Fukuzumi, S. *ChemPhysChem* **2006**, *7*, 942.

(20) (a) Yosca, T. H.; Behan, R. K.; Krest, C. M.; Onderko, E. L.; Langston, M. C.; Green, M. T. *J. Am.*

Chem. Soc. **2014**, *136*, 9124. (b) Yosca, T. H.; Rittle, J.; Krest, C. M.; Onderko, E. L.; Silakov, A.; Calixto, J. C.; Behan, R. K.; Green, M. T. *Science* **2013**, *342*, 825.

(21) (a) Widger, L. R.; Davies, C. G.; Yang, T.; Maxime A. Siegler, M. A.; Troeppner, O.; Jameson, G. N. L.; Ivanović-Burmazović, I.; Goldberg, D. P. *J. Am. Chem. Soc*. **2014**, *136*, 2699. (b) Latifi, R.; Sainna, M. A.; Rybak-Akimova, E. V.; de Visser, S. P. *Chem.–Eur. J.* **2013**, *19*, 4058.

(22) (a) Marcus, R. A. *Annu. Rev. Phys. Chem*. **1964**, *15*, 155. (b) Marcus, R. A.; Sutin, N. *Biochim. Biophys. Acta Rev. Bioenerg.* **1985**, *811*, 265. (c) Marcus, R. A. *Angew. Chem., Int. Ed. Engl*. **1993**, *32*, 1111.

(23) Chen, J.; Lee, Y.-M.; Davis, K. M.; Wu, X.; Seo, M. S.; Cho, K.-B.; Yoon, H.; Park, Y. J.; Fukuzumi, S.; Pushkar, Y. N.; Nam, W. *J. Am. Chem. Soc*. **2013**, *135*, 6388.

(24) Yoon, H.; Lee, Y.-M.; Wu, X.; Cho, K.-B.; Sarangi, R.; Nam, W.; Fukuzumi, S. *J. Am. Chem. Soc.* **2013**, *135*, 9186.

(25) (a) Wu, X.; Seo, M. S.; Davis, K. M.; Lee, Y.-M.; Chen, J.; Cho, K.-B.; Pushkar, Y. N.; Nam, W. *J. Am. Chem. Soc.* **2011**, *133*, 20088. (b) Yoon, H.; Morimoto, Y.; Lee, Y.-M.; Nam, W.; Fukuzumi, S. *Chem. Commun*. **2012**, *48*, 11187.

(26) Evans, D. F.; Jakubovic, D. A. *J. Chem. Soc. Dalton Trans.* **1988**, 2927.

(27) Fukuzumi, S. *Coord. Chem. Rev*. **2013**, *257*, 1564.

(28) Lee, Y.-M.; Kotani, H.; Suenobu, T.; Nam, W.; Fukuzumi, S. *J. Am. Chem. Soc*. **2008**, *130*, 434.

(29) Bang, S.; Park, S.; Lee, Y.-M.; Hong, S.; Cho, K.-B.; Nam, W. *Angew. Chem., Int. Ed.* **2014**, *53*, 7843.

(30) Fukuzumi, S.; Itoh, S.; Komori, T.; Suenobu, T.; Ishida, A.; Fujitsuka, M.; Ito, O. *J. Am. Chem. Soc.* **2000**, *122*, 8435.

(31) Cho, K.-B.; Wu, X.; Lee, Y.-M.; Kwon, Y. H.; Shaik, S.; Nam, W. *J. Am. Chem. Soc.* **2012**, *134*, 20222.

(32) Armarego, W. L. F.; Chai, C. L. L. *Purification of Laboratory Chemicals*, 6th ed.; Pergamon Press: Oxford, 2009.

(33) Saltzman, H.; Sharefkin, J. G., Eds.; *Organic Syntheses;* Wiley: New York, 1973, Vol. V, p 658.

(34) Dixon, N. E.; Lawrance, G. A.; Lay, P. A.; Sargeson, A. M.; Taube, H. *Inorg. Synth.* **1990**, *28*, 70.

(35) (a) Lubben, M.; Meetsma, A.; Wilkinson, E. C.; Feringa, B.; Que, L., Jr. *Angew. Chem., Int. Ed.* **1995**, *34*, 1512. (b) Duelund, L.; Hazell, R.; McKenzie, C. J.; Nielsen, L. P.; Toftlund, H. *J. Chem. Soc., Dalton Trans.* **2001**, 152. (c) Groni, S.; Dorlet, P.; Blain, G.; Bourcier, S.; Guillot, R.; Anxolabéhère-Mallart, E. *Inorg. Chem.* **2008**, *47*, 3166.

(36) (a) Fussa-Rydel, O.; Zhang, H.-T.; Hupp, J. T.; Leidner, C. R. *Inorg. Chem*. **1989**, *28*, 1533. (b) Fukuzumi, S.; Nakanishi, I.; Tanaka, K.; Suenobu, T.; Tabard, A.; Guilard, R.; Van Caemelbecke, E.; Kadish, K. M. *J. Am. Chem. Soc*. **1999**, *121*, 785. (c) Lin, C-T.; Bottcher, W.; Chou, M.; Creutz, C.; Sutin, N. *J. Am. Chem. Soc*. **1976**, *98*, 6536.

(37) Tenderholt, A.; Hedman, B.; Hodgson, K. O. *PySpline: A Modern, Cross-Platform Program for the Processing of Raw Averaged XAS Edge and EXAFS Data; X-ray Absorption Fine Structure - XAFS13*, **2007**, *882*, 105.

(38) Zabinsky, S. I.; Rehr, J. J.; Ankudinov, A.; Albers, R. C.; Eller, M. J. *Phys. Rev. B: Condens. Matter* **1995**, *52*, 2995.

(39) Mustre de Leon, J.; Rehr, J. J.; Zabinsky, S. I.; Albers, R. C. *Phys. Rev. B: Condens. Matter* **1991**, *44*, 4146.

(40) Rehr, J. J.; Mustre de Leon, J.; Zabinsky, S. I.; Albers, R. C. *J. Am. Chem. Soc.* **1991**, *113*, 5135.

(41) *Avogadro: an open-source molecular builder and visualization tool*. Version 1.1.0. http://avogadro.openmolecules.net/.

(42) George, G. N. *EXAFSPAK and EDG-FIT*, Stanford Synchrotron Radiation Laboratory, Stanford Linear Accelerator Center, Stanford, CA, 2000.

Supporting Information for Chapter 5

Table S1. EXAFS Least Squares Fitting Results**.** Selected Bond Lengths (Å) and Angles (°) for $[Mn^{II}(N4Py)(CF_3SO_3)](CF_3SO_3)$.

complex	coordination/path	R(Å)[a]	σ^2(Å^2)[b]	E_0 (eV)	F[c]
3	1 Mn-O	1.74	331	-3.53	0.26
	5 Mn-N	2.00	747		
	6 Mn-C	2.96	1326		
	8 Mn-C-N	3.16	264		
	8 Mn-C-N	3.33	264[d]		
	8 Mn-C	4.25	914		
	6 Mn-C-N	4.71	233		

[a]The estimated standard deviations for the distances are in the order of ± 0.02 Å. [b]The σ^2 values are multiplied by 10^5. [c]Error is given by $\Sigma[(\chi_{obsd} - \chi_{calcd})^2 k^6]/\Sigma[(\chi_{obsd})^2 k^6]$. [d]/ indicates the σ^2 value for the path is linked to the preceding path. The S_0^2 factor was set at 0.95.

Table S2. Mn-O and Mn-N Distances (Å) Determined by EXAFS Measurements.

coordination/path	**1**	$[(N4Py)Mn^{IV}(O)]^{2+}–(Sc^{3+})_2$	**3**
Mn-O	1.70[a] (1.67)[b,c]	1.74[a] (1.74)[a,b]	1.74
$Mn-N_{avg}$[d]	2.00[a] (2.01)[b,c]	2.00[a] (2.01)[a,b]	2.00

[a] Taken from ref 23 in Text. [b]The values in parenthesis were determined by DFT calculation. [c]Taken from reference, Cho, K.-B.; Shaik, S.; Nam, W. *J. Phys. Chem. Lett.* **2012**, *3*, 2851. [d]Average value of Mn-N distances.

Concluding Remarks

This thesis focuses on synthesis and characterization of highly reactive nonheme manganese(IV)-oxo complexes. In addition, tuning reactivity and mechanisms of oxidation with nonheme manganese(IV)-oxo complexes have been successfully accomplished by binding of Lewis acids (i.e., Sc^{3+} and proton) to the oxo moiety of the nonheme manganese(IV)-oxo complexes, which resulted in remarkable enhancement of the electron acceptor ability.

Electron-transfer properties of $[(L)Mn^{IV}(O)]^{2+}$ (L = Bn-TPEN and N4Py) are clarified to obtain the one-electron reduction potential values, which were found to be significantly higher than those of iron(IV)-oxo complexes. Thus, hydride transfer from $AcrH_2$ to manganese(IV)-oxo complexes occurs via rate-determining ET with no KIE due to the energetically feasible electron transfer from $AcrH_2$ to manganese(IV)-oxo complexes. This thesis also reports the first spectroscopic evidence for the Sc^{3+} ions bound and diprotonated a mononuclear manganese(IV)-oxo complexes, which were well characterized by using various spectroscopic techniques. The E_{red} values of the manganese(IV)-oxo complexes showed significant positive shifts on the binding of Lewis acids (i.e., Sc^{3+} and HOTf). The reactivities of the manganese(IV)-oxo complexes are markedly enhanced by binding Lewis acid in OAT reactions of thioanisole (i.e., OAT), which proceed via ET from thsianisoles to Lewis acids-bound manganese(IV)-oxo complexes. In the case of HAT from 1,4-cyclohexadiene to Lewis acids-bound manganese(IV)-oxo complexes in which ET is endergonic, significant deceleration was observed due to the steric effect of the counter anions. Such contrasting effects by binding of metal ions and protons observed in OAT and HAT reactions provides valuable insights into fine control of the reactivity of metal-oxo complexes, which is certianly requried to develop efficient catalytic oxidation sytems including water oxidation.

Publication List

Publication

1. **Electron-Transfer Properties of a Nonheme Manganese(IV)–Oxo Complex Acting as a Stronger One-Electron Oxidant than the Iron(IV)-Oxo Analogue**
   Heejung Yoon, Yuma Morimoto, Yong-Min Lee, Wonwoo Nam and Shunichi Fukuzumi
   Chem. Commun. **2012**, *48*, 11187-11189.

2. **Mononuclear Non-Heme Manganese(IV)–Oxo Complex Binding Redox-Inactive Metal Ions**
   Junying Chen, Yong-Min Lee, Katherine M. Davis, Xiujuan Wu, Mi Sook Seo, Kyung-Bin Cho, Heejung Yoon, Young Jun Park, Shunichi Fukuzumi and Wonwoo Nam
   J. Am. Chem. Soc. **2013**, *135*, 6388-6391.

3. **Enhanced Electron-Transfer Reactivity of Nonheme Manganese(IV)–Oxo Complexes by Binding Scandium Ions**
   Heejung Yoon, Yong-Min Lee, Xiujuan Wu, Kyung-Bin Cho, Ritimukta Sarangi, Wonwoo Nam and Shunichi Fukuzumi
   J. Am. Chem. Soc. **2013**, *135*, 9186-9194.

4. **Hydride Transfer from NADH Analogues to a Nonheme Manganese(IV)–Oxo Complex *via* Rate-Determining Electron Transfer**
   Heejung Yoon, Yong-Min Lee, Wonwoo Nam and Shunichi Fukuzumi
   Chem. Commun. **2014**, *50*, 12944-12946.

5. **Triflic Acid-Bound Mononuclear Nonheme Manganese(IV)-Oxo Complexes with Much Enhanced Oxidation Capacity**
   Junying Chen, Heejung Yoon, Yong-Min Lee, Ritimukta Sarangi, Shunichi Fukuzumi and Wonwoo Nam
   J. Am. Chem. Soc. **in revision**.

Supplementary

1. **Reactivity Comparison of High-Valent Iron(IV)–Oxo Complexes Bearing *N*-Tetramethylated Cyclam Ligands with Different Ring Size**
   Seungwoo Hong, Hee So, Heejung Yoon, Kyung-Bin Cho, Yong-Min Lee, Shunichi Fukuzumi and Wonwoo Nam
   Dalton. Commun. **2013**, *42*, 7842-7845.

2. **Tuning the Redox Properties of Nonheme Iron(III)-Peroxo Complex Binding Redox-Inactive Zn Ion by Water Molecules**
   Yong-Min Lee, Suhee Bang, Heejung Yoon, Seong Hee Bae, Seungwoo Hong, Kyung-Bing Cho, Ritimukta Sarangi, Shunichi Fukuzumi and Wonwoo Nam
   J. Am. Chem. Soc. **in revision**.

Presentation at International Conference

The 7th International Conference on Porphyrins and Phthalocyanines (ICPP-7)
Fundamental Electron Transfer Properties of Oxomanganese(IV) Complexes in the Absence and Presence of Redox-Inactive Metal Ion
Heejung Yoon, Ari Kim, Yong-Min Lee, Shunichi Fukuzumi and Wonwoo Nam

The International Conference on Biological Inorganic Chemistry (ICBIC 16)
Enhanced Electron-Transfer Reactivity of Nonheme Manganese(IV)-Oxo Complexes by Binding Scandium Ions
Heejung Yoon, Yong-Min Lee, Wonwoo Nam and Shunichi Fukuzumi

Acknowledgements

I am very delighted to express my gratitude to Prof. Shunichi Fukuzumi for his valuable guidance, educational instruction, and encouragement throughout my Ph. D. study.

I heartily thank Prof. Wonwoo Nam and Dr. Yong-Min Lee for their warm teaching and excellent suggestions throughout my study. From my master to doctoral courses, I was always dependent on your valuable advice that helped me along the way. Thanks to your continuous encouragement, I was able to grow in my knowledge of the field.

And I would also like to express my gratitude to Prof. Youngmin You, Prof. Jaeheung Cho, Dr. Kyung-Bin Cho, Dr. Seungwoo Hong, Dr. Suenobu Tomoyoshi, Dr. Kei Ohkubo, and Prof. Yusuke Yamada for their constant guidance.

And to my dear Fukuzumi Lab members, thank you for being wonderful colleagues and friends. Your help and support made my life in Japan much more warm and memorable.

I also want to thank the JSPS of the Ministry of Education, Culture, Sports, Science and Technology of Japan for the great support through my scholarships.

And finally, to my beloved mom and dad! Your unconditional love always makes me have faith in myself and gives me strength to pursue my dreams. Love you very much! And to dear Hyosup, I could not have done anything without your constant love and support. Thank you and love you very much!

Thank you all for your support throughout my studies.

Heejung Yoon

Laboratory of Physical Chemistry for Life Science,
Department of Material and Life Science,
Division of Advanced Science and biotechnology,
Graduate School of Engineering, Osaka University